Universiteit Antwerpen

Faculteit Wetenschappen

Departement Fysica

# Two- and three-dimensional transmission electron microscopy of colloidal nanoparticles: from structure to composition

# Twee- en driedimensionale transmissie-elektronenmicroscopie van colloidale nanodeeltjes: van structuur tot samenstelling

Proefschrift voorgelegd tot het behalen van de graad van

Doctor in de Wetenschappen

aan de Universiteit Antwerpen, te verdedigen door

Eva Bladt

Promotor

Prof. Dr. Sara Bals

Antwerpen, 2017

De kandidaat werd financieel gesteund door het Fonds voor Wetenschappelijk Onderzoek – Vlaanderen (FWO Vlaanderen).

The candidate was financially supported by the Research Foundation Flanders.

fwo Research Foundation
Flanders
Opening new horizons

## Doctoral Committee

### Chairman

Prof. Dr. Joris Dirckx, University of Antwerp – Belgium

### Promotor

Prof. Dr. Sara Bals, University of Antwerp – Belgium

### Members

Prof. Dr. Joost Batenburg, Leiden University – The Netherlands

Prof. Dr. Erik Neyts, University of Antwerp – Belgium

Prof. Dr. Sandra Van Aert, University of Antwerp – Belgium

Prof. Dr. Marijn Van Huis, University of Utrecht – The Netherlands

### Contact information

Eva Bladt

University of Antwerp – Department of Physics

EMAT – Electron Microscopy for Materials Science

Groenenborgerlaan 171

B-2020 Antwerp

Belgium

eva.bladt@uantwerpen.be

# Contents

**Preface ........................................................................................ VI**

**Nederlandstalige samenvatting .................................................. VIII**

**List of abbreviations ........................................................................ XIV**

**Chapter 1 - Introduction to functional nanoparticles ....................................1**

1. Nanoparticles ........................................................................ 2
2. Metallic nanoparticles ........................................................................ 3
   2.1. Au nanoparticles ........................................................................ 3
   2.2 Au/Ag core/shell nanoparticles ........................................................................ 5
3. Semiconductor nanoparticles ........................................................................ 6
   3.1. CdSe nanoplatelets ........................................................................ 6
   3.2. CdSe/CdS nanocrystals ........................................................................ 8
   3.3. $CuInSe_2/CuInS_2$ nanocrystals ........................................................................ 9
   3.4. Metal halide perovskite nanoparticles ........................................................................ 10
      3.4.1. Organic-inorganic lead halide perovskites ........................................................................ 10
      3.4.2. Cesium lead halide perovskites ........................................................................ 11
4. Catalytic nanoparticles ........................................................................ 11
   4.1. Ceria-zirconia nanostructures ........................................................................ 11
5. Characterization of nanoparticles ........................................................................ 13

**Chapter 2 - Introduction to electron tomography ........................................15**

1. Introduction to transmission electron microscopy ........................................................................ 16
   1.1. A brief history of TEM ........................................................................ 16
   1.2. The build-up of a TEM ........................................................................ 17
   1.3. Different TEM techniques ........................................................................ 17
      1.3.1. Bright field transmission electron microscopy ........................................................................ 17
      1.3.2. High angle annular dark field scanning transmission electron microscopy ........................................ 19
      1.3.3. Energy dispersive X-ray imaging ........................................................................ 21
      1.3.4. Electron energy loss spectroscopy ........................................................................ 21
2. Imaging in three dimensions ........................................................................ 22

3. History of electron tomography 23
4. Tomography in practice 25
  4.1. Acquisition of the tilt series 25
    4.1.1 Imaging modes in electron tomography 25
    Bright field transmission electron microscopy 25
    High angle annular dark field scanning transmission electron microscopy 27
    Energy dispersive X-ray imaging 29
    4.1.2. Tilt schemes 29
    Single tilt axis acquisition 31
    Dual tilt axis acquisition 33
    On-axis tilt axis acquisition 33
    4.1.3. Automated acquisition 33
  4.2. Alignment of the tilt series 34
  4.3 Reconstruction of a tomographic tilt series 36
    4.3.1 Theory behind tomography 36
    The Radon transform 36
    Fourier slice theorem 38
    4.3.2. Modern reconstruction techniques 41
    Filtered back projection 41
    Simultaneous iterative reconstruction technique 41
    Total variation minimization technique 44
  4.4. Visualization and quantification of a tomographic reconstruction 45
    4.4.1. Isosurface rendering 45
    4.4.2. Voltex rendering 46
    4.4.3. Orthoslices 47
    4.4.4. Segmentation 47

**Chapter 3 - Investigation of semiconductor nanoplatelets by 2D and 3D electron microscopy 49**
1. Introduction 50
2. CdSe flat nanoplatelets: 2D problem 50
  2.1. Facet determination 51
  2.2. Thickness determination 56
3. CdSe nanohelices: 3D problem 57
  3.1. Native state 57

3.2. Thickness determination ........ 61
3.3. Folding formation ........ 63
3.4. Helicity of the nanoplatelets ........ 65
4. Conclusion ........ 67

**Chapter 4 - 2D investigation of beam sensitive perovskite nanostructures 69**

1. Introduction ........ 70
2. Atomic resolution imaging techniques ........ 70
2.1. High resolution HAADF-STEM imaging ........ 71
2.2. Exit wave reconstruction ........ 71
3. Lead cesium halide perovskite nanostructures ........ 72
3.1. Nanoparticles ........ 72
3.2. Nanowires ........ 77
3.2.1. Oriented attachment ........ 77
3.2.2. Halide ion exchange reaction ........ 79
4. Organolead iodide perovskites at the atomic scale ........ 82
5. Outlook towards alternative techniques ........ 86
6. Conclusion ........ 87

**Chapter 5 - Characterization of core/shell semiconductor nanoparticles...89**

1. Introduction ........ 90
2. Binary core/shell nanostructures ........ 90
2.1. Characterization of the morphology ........ 91
2.2. Identification of the core location ........ 92
2.3. Facet determination ........ 95
3. Ternary core/shell nanostructures ........ 100
3.1. Characterization of the morphology ........ 100
3.2. Identification of the core location ........ 105
4. Conclusion ........ 107

**Chapter 6 - Energy dispersive X-ray tomography ........ 109**

1. Introduction ........ 110
2. EDX from 2D to 3D ........ 110
2.1. 2D EDX mapping ........ 110
2.2. Practical aspects of EDX tomography ........ 111
2.2.1. Detector set-up ........ 111

2.2.2. Acquisition of tilt series of EDX maps .......... 112
Acquisition methodology .......... 113
Quantification of tilt series .......... 116
2.2.3. Alignment of tilt series .......... 118
3. Investigation of Au/Ag core/shell nanoparticles .......... 118
3.1. Qualitative results .......... 119
3.2. Quantitative results .......... 121
4. Conclusion .......... 125

**Chapter 7 - A neural network filtered back projection approach .......... 127**
1. Introduction .......... 128
2. Neural network filtered back projection method: structural characterization .......... 129
2.1. Method .......... 131
2.1.1. Reconstruction phase .......... 131
2.1.2. Learning phase .......... 132
2.2. Results .......... 134
2.2.1. Qualitative results .......... 134
2.2.2. Quantitative results .......... 136
2.2.3. Statistical results .......... 142
3. Neural network filtered back projection method: chemical characterization .......... 145
3.1. HAADF-STEM tomography .......... 145
3.1.1. Method and results .......... 146
3.2. EDX tomography .......... 149
3.2.1. Method and results .......... 150
4. Conclusion .......... 153

**Chapter 8 - Outlook towards a 3D chemical characterization at the atomic scale .......... 155**
1. Introduction .......... 156
2. Ceria-zirconia nanocrystals at the atomic scale .......... 156
3. Extension to 3D .......... 159
4. Conclusion .......... 162

**Chapter 9 - Outlook ........................................................................163**

1. Conclusion ........................................................................164
2. The study of beam sensitive materials ........................................................................164
3. Novel reconstruction algorithms for spectroscopic tomography ........................................................................165
4. The extension towards a 3D chemical characterization at the atomic level........................................................................166

**References ........................................................................168**

**List of scientific contributions........................................................................180**

**Dankwoord ........................................................................184**

# Preface

To understand the structure-property relationship of nanomaterials and to trigger the synthesis of novel nanomaterials with predefined properties, a 3D investigation at the nanoscale and below is of key importance. To reach this goal, electron tomography is required. The technique has progressed significantly the last decade, but progress in materials science is leading to even higher demands concerning characterization. The growing interest in hetero-nanostructures requires clear knowledge on both the shape and chemical nature of the structure in 3D. Therefore, a need for spectroscopic electron tomography emerges. The ever increasing complexity in composition of novel nanostructures is often accompanied by an increasing sensitivity towards the electron beam. Depending on the degree of sensitivity, the conventional acquisition of a single projection image is already troublesome and low dose techniques are required. When expanding the investigation to 3D, the acquisition of a (large) set of images necessary for an electron tomography experiment is far from straightforward. Finally, although electron tomography yields very precise and local information in 3D of nanoparticles, a major drawback remains that it is not straightforward to perform statistically relevant studies in 3D as the technique is quite time-consuming. Therefore, one of the emerging challenges in the field is to increase the throughput of 3D reconstructions of nanoparticles.

**Chapter 1** starts with a short introduction on functional nanoparticles. The different nanoparticles, which are studied in the thesis, and their properties are introduced in this chapter. In **Chapter 2**, an introduction on electron tomography is presented. After the motivation to perform electron tomography, a short historical overview of the development of the technique is presented. The remainder of the chapter focuses on the practical aspects of electron tomography. In **Chapter 3**, a 2D and 3D structural characterization of semiconductor CdSe nanoplatelets is performed. The use of

HAADF-STEM tomography enables us to characterize these nanoplatelets in 3D and to elucidate on the helicity of nanohelices. Different beam sensitive perovskite nanocrystals are investigated in **Chapter 4**. The use of alternative techniques emerges as specific perovskite nanomaterials do not even withstand the acquisition of a single HAADF-STEM projection image. Different techniques are used to study the atomic structure of these perovskite nanomaterials. With the growing interest in the use of core/shell semiconductor nanoparticles, a 3D characterization of both the structure as the chemical nature of the nanoparticles emerges. The results of such full 3D characterizations of several core/shell semiconductor nanoparticles are presented in **Chapter 5**. Here, the use of HAADF-STEM tomography is sufficient to perform both a structural as a chemical characterization since the difference in atomic number of the core and the shell is sufficiently large and will result in different intensity values for the core and the shell in the projection images. To perform a 3D chemical characterization for samples in which different components with comparable atomic numbers are present, the use of EDX tomography is proposed. In **Chapter 6**, the practical aspects of EDX tomography will be discussed and different acquisition approaches will be applied to metallic Au/Ag core/shell nanoparticles. During EDX tomography experiments, only a limited number of projection images can be acquired. This complicates an accurate and reliable 3D reconstruction of the chemical nature of a nanoparticle. Therefore, there is a need for the development of reconstruction algorithms which can handle such limited amount of projection images. A neural network based reconstruction algorithm is presented in **Chapter 7**. This reconstruction algorithm obtains reliable 3D reconstructions of highly limited HAADF-STEM tomography data. An extension towards chemical 3D characterizations is also discussed. In **Chapter 8**, the ceria layer of a ceria-zirconia nanoparticle is investigated by high resolution EDX mapping. We aim for an atomically resolved EDX map as we want to reveal the chemical nature of each atom in the nanomaterial and retrieve the atomic thickness of the ceria layer. The applicability of such atomic resolution EDX maps for atom-counting is evaluated by the study of a ceria nanoparticle. We believe that the use of atom-counting will open up possibilities towards the 3D atomic resolution chemical characterization of hetero-nanostructures.

# Nederlandstalige samenvatting

Om de relatie tussen de morfologie en de eigenschappen van nanomaterialen te onderzoeken en de synthese van nieuwe nanomaterialen te leiden, is een driedimensionale (3D) karakterisering van deze nanomaterialen uitermate belangrijk. Conventionele transmissie-elektronenmicroscopie (TEM) is echter niet voldoende om een materiaal in 3D te karakteriseren aangezien deze techniek enkel tweedimensionaal (2D) beelden levert van een 3D object. Daarom wordt elektronentomografie gebruikt, een methode om een 3D reconstructie te verkrijgen uit een set van 2D projectiebeelden. Hoewel deze techniek enorm geëvolueerd is de laatste jaren, duiken nieuwe uitdagingen op. De groeiende interesse in hetero-nanostructuren, bijvoorbeeld, vereist kennis over zowel de morfologie als de chemische aard van de nanostructuur in 3D. Om deze uitdaging aan te gaan, moeten spectroscopische technieken gecombineerd worden met elektronentomografie. De groeiende complexiteit van de samenstelling van nieuwe nanostructuren gaat vaak gepaard met een toename in bundelgevoeligheid. Het onderzoeken van zo'n bundelgevoelige materialen in 2D vormt vaak al een obstakel. Daarom moeten alternatieve lage elektronendosis technieken uitgevoerd worden met het oog op de karakterisering van deze materialen in 3D. Tenslotte, hoewel elektronentomografie precieze en lokale 3D informatie van nanodeeltjes levert, is het verkrijgen van statistisch relevante informatie in 3D niet eenduidig aangezien de techniek tijdsrovend is. Het reduceren van de tijd, die nodig is om een elektronentomografie experiment uit te voeren, vormt een grote uitdaging.

In **hoofdstuk 1** worden de verschillende functionele nanodeeltjes, die in de thesis bestudeerd worden, besproken. Drie klassen van nanodeeltjes worden geïntroduceerd: metallische, halfgeleider en katalytische nanomaterialen. Een korte bespreking over de groei, eigenschappen en toepassingen van de nanodeeltjes wordt besproken in dit hoofdstuk.

**Hoofdstuk 2** geeft een inleiding over elektronentomografie. Vooraleer elektronentomografie uitvoerig word besproken, wordt een korte inleiding over transmissie-elektronenmicroscopie gegeven. Vervolgens, na een korte historische kadering, worden de verschillende stappen van een elektronentomografie experiment uitgelegd. Een elektronentomografie experiment bestaat uit de volgende stappen: opname van een tilt serie, de tilt serie uitlijnen ten opzichte van een gemeenschappelijke tilt-as, reconstrueren van het 3D volume en visualizeren en/of quantificeren. Elke stap wordt uitvoerig besproken in dit hoofdstuk.

In **hoofdstuk 3**, wordt de karakterisering van halfgeleider CdSe nanoplaatjes behandeld in 2D en 3D. Twee types worden bestudeerd: dunne nanoplaatjes met laterale dimensies van enkele nanometers en dunne nanoplaatjes met laterale dimensies van een honderdtal nanometer. De rol van azijnzuur zout op de groei van het eerste type CdSe nanoplaatjes werd onderzocht aan de hand van hoge resolutie TEM. Het gebruik van cadmiumacetaat leverde diverse nanoplaatjes op, waarbij zowel de vorm als het type van de oppervlakte facetten varieerde. Door het cadmiumacetaat te vervangen door natriumacetaat werden CdSe nanoplaatjes gevormd met {110} facetten. Aangezien meer acetaat vrijkomt bij natriumacetaat, zal een stijgende selectieve groei van de facetten waargenomen worden en enkel de {110} facetten komen tot uiting. De CdSe nanoplaatjes met grotere laterale afmetingen worden opgerold waargenomen. Door middel van cryogene elektronentomografie werd de opgerolde morfologie van deze nanostructuren bevestigd. Cryogene elektronenmicroscopie wordt echter bemoeilijkt door de aanwezigheid van een ijslaag rond de nanostructuren en zal zorgen voor een gelimiteerde spatiale resolutie. Om de morfologie van deze nanoplaatjes grondiger te bestuderen werden ze daarom ingekapseld in een silica laag. Deze silica laag heeft geen invloed op de opgerolde morfologie van de nanoplaatjes en laat een elektronenmicroscopie onderzoek toe op kamertemperatuur. Het onderzoeken van de heliciteit van deze opgerolde CdSe nanoplaatjes kan niet aan de hand van 2D beeldvorming. Een 2D beeld van een links- of rechtshandige helix zal geen verschil tonen. Daarom werden ze hier met *high angle annular dark field scanning transmissie-*

*electronmicroscopy* (HAADF-STEM) tomografie onderzocht, aangezien een 3D reconstructie ons zal toelaten om de heliciteit te bestuderen.

In **hoofdstuk 4** worden perovskiet nanostructuren onderzocht waarbij de karakterisering sterk bemoeilijkt wordt door de bundelgevoeligheid van de nanomaterialen. Een 2D karakterisering op atomair niveau wordt uitgevoerd op twee types perovskieten: cesium lood halogenide en organische-inorganische lood halogenide perovskiet nanomaterialen. Cesium lood halogenide perovskieten werden onderzocht aan de hand van hoge resolutie HAADF-STEM beelden waarbij de verschillende types atoomkolommen bepaald konden worden. De karakterisering van organische-inorganische lood halogenide perovskieten vormt een grotere uitdaging aangezien deze materialen instantaan vervormen onder de elektronenbundel. Door middel van het gebruik van HAADF-STEM met een beperkte elektronendosis, werden beelden met een erg lage kwaliteit opgenomen. Een *template-matching* procedure werd vervolgens toegepast op deze beelden om een uitgemiddelde templaat te bekomen. Door deze uitmiddeling, neemt de kwaliteit van het templaat toe en kan de atomaire structuur van de organische-inorganische perovskiet gevisualiseerd worden. Deze aanpak geeft echter enkel een gemiddeld beeld van de atomaire structuur, lokale defecten kunnen hier bijvoorbeeld niet mee onderzocht worden. Het gebruik van *exit wave reconstruction* wordt toegepast om opnieuw de volledige structuur van de perovskiet te onderzoeken. Een 3D karakterisering blijft nog een uitdaging door de extreme bundelgevoeligheid van deze perovskieten.

Halfgeleider materialen worden vaak gebruikt om kern/schil nanodeeltjes met geoptimaliseerde eigenschappen te groeien. Het bepalen van de locatie van de kern in het kern/schil deeltje is noodzakelijk om de groei van deze nanodeeltjes te onderzoeken en begrijpen. De combinatie van een kern en een schil bemoeilijkt echter de karakterisering aangezien deze onderscheiden moeten worden. Zowel de morfologie van het kern/schil nanodeeltje als zijn samenstelling moet gekarakteriseerd worden. In **hoofdstuk 5** worden twee types halfgeleider kern/schil nanodeeltjes onderzocht: CdSe/CdS en $CuInSe_2/CuInS_2$. Aangezien in beide nanostructuren de kern Se bevat, kan deze gelokaliseerd worden door middel van HAADF-STEM tomografie. De Se-bevattende kern zal intenser gevisualiseerd worden aangezien dit atoomtype zwaarder is dan S. Het verschil is echter niet al te groot waardoor de kern zwak waar te nemen is in de 3D reconstructie. Door het toepassen van een geavanceerde reconstructietechniek wordt de kern duidelijker gedecteerd in de 3D reconstructie.

HAADF-STEM kan enkel gebruikt worden om spectoscopische informatie te verkrijgen als het atoomnummer van de kern en de schil erg verschilt. Het uitbreiden van spectroscopische elektronentomografie vereist een techniek die geen voorwaarde legt op het atoomnummer van de verschillende componenten in het nanomateriaal. In **hoofdstuk 6** wordt *energy dispersive X-ray* (EDX) tomografie geïntroduceerd en worden de praktische aspecten van deze techniek besproken. De techniek was tot voor kort erg beperkt aangezien de detector enkel voldoende signaal opving bij bepaalde hoeken, wat een betrouwbare elektronentomografie experiment bemoeilijkt. De ontwikkeling van een nieuw detectorsysteem, waar vier detectoren symmetrisch opgesteld worden boven het specimen, verhogen de efficiëntie van de detector. Deze nieuwe set-up vereist een grondig onderzoek, waarbij moet nagegaan worden of elektronentomografie op een betrouwbare wijze kan uitgevoerd worden. Hiervoor worden metallische Au/Ag kern/schil nanodeeltjes onderzocht aan de hand van verschillende opname procedures. De resultaten van deze verschillende procedures worden zowel kwalitatief als kwantitatief vergeleken. De opname van een EDX tilt serie voor elektronentomografie bevat een beperkt aantal projectiebeelden in vergelijking met een conventionele HAADF-STEM tilt serie. Het ontwikkelen van reconstructie-algoritmen die betrouwbare resultaten opleveren bij een beperkt aantal beelden wordt daardoor noodzakelijk.

In **hoofdstuk 7** wordt een neuraal netwerk gebaseerde reconstructietechniek geïntroduceerd waarbij betrouwbare 3D reconstructies van Au nanodeeltjes behaald worden op basis van sterk gelimiteerde tilt series. Deze reconstructietechniek werkt met een leer fase en een reconstructie stap, waarbij in de leer fase 3D reconstructies van 151 HAADF-STEM projectiebeelden worden gebruikt. Na deze procedure, wordt het bekomen reconstructie-algoritme toegepast op een nanodeeltjes van dezelfde samenstelling waarbij enkel 10 projectiebeelden beschikbaar zijn. De 3D reconstructies worden vergeleken met een standaard experiment zowel kwalitatief als kwantitatief. Een uitbreiding van deze reconstructietechniek om kern/schil hetero-nanostructuren te bestuderen wordt besproken.

**Hoofdstuk 8** bespreekt, tot slot, de uitbreiding van een chemische karakterisering in 3D tot op atomair niveau. Eerst worden ceria-zirconia nanodeeltjes onderzocht in 2D. De synthese van deze katalytische nanodeeltjes tracht nanodeeltjes te produceren met een erg dunne ceria laag. Aangezien de katalytische reactie plaatsvindt aan het oppervlak van de nanostructuren, moet ceria enkel aanwezig zijn als een oppervlaktelaag. Aangezien de hoeveelheid ceria erg laag is, neemt de opname tijd van een EDX map enorm toe. Aan de hand van twee orthogonale EDX mappen, wordt de aanwezigheid van de ceria laag rond de zirconia nanodeeltjes bevestigd op nanometer niveau. Om de exacte dikte van deze dunne ceria laag te bepalen moeten we echter een atomaire resolutie EDX map opnemen. De opnamen van een hoge resolutie EDX map vereist extreme stabiliteit van de elektronenmicroscoop aangezien een opname tijd van enkele minuten nodig is. We konden besluiten dat de ceria laag enkel twee atoomlagen dik is, na een succesvolle opname van een atomaire resolutie EDX map. Een volgende uitdaging is het uitbreiden van atomaire chemische karakterisering in 3D. Een combinatie van de lage detectie-efficiëntie en bundelgevoeligheid van de nanostructuren bemoeilijkt het opnemen van een tilt serie van EDX mappen op atomair niveau. Daarom stellen we hier voor om de toepasbaarheid van deze mappen voor *atom-counting* te onderzoeken. Op basis van *statistical parameter estimation theory* kan het aantal atomen in een atoomkolom bepaald worden in een hoge resolutie HAADF-STEM projectiebeeld. Op deze manier kan 3D informatie bekomen worden uit een 2D beeld. In dit hoofdstuk wordt op basis van een ceria nanodeeltje bevestigd dat atomaire resolutie EDX mappen gebruikt kunnen worden voor *atom-counting*. Dit resultaat zal de deuren openen naar een 3D atomaire resolutie chemische karakterisering van hetero-nanostructuren.

In **hoofdstuk 9** wordt een vooruitzicht van de resterende uitdagingen gegeven. Verder onderzoek en verdere ontwikkelingen zijn vereist om bundelgevoeldige materialen in 3D te onderzoeken en om een 3D atomaire resolutie chemische karakterisering van hetero-nanostructuren te bekomen.

# List of abbreviations

| | |
|---|---|
| 0D | Zero-dimensional |
| 1D | One-dimensional |
| 2D | Two-dimensional |
| 3D | Three-dimensional |
| ADF | Annular dark field |
| BF | Bright field |
| CCD | Charged coupled device |
| DART | Discrete algebraic reconstruction technique |
| DF | Dark field |
| EDX | Energy dispersive X-ray |
| EELS | Electron energy loss spectroscopy |
| EFTEM | Energy filtered transmission electron microscopy |
| ESEM | Environmental scanning electron microscopy |
| FBP | Filtered back projection |
| FFT | Fast Fourier transform |
| FIB | Focused ion beam |
| HAADF | High angle annular dark field |
| NN-FBP | Neural network filtered back projection |
| PXRD | Powder X-ray diffraction |
| SAD | Selected area diffraction |
| SEM | Scanning electron microscopy |
| SILAR | Successive ion layer adhesion and reaction |
| SIRT | Simultaneous iterative reconstruction technique |

| | |
|---|---|
| SRMO | Severe reduction followed by mild oxidation |
| STEM | Scanning transmission electron microscopy |
| TEM | Transmission electron microscopy |
| TVM | Total variation minimization |
| WDX | Wavelength dispersive X-ray |

# Chapter 1

## Introduction to functional nanoparticles

## 1. Nanoparticles

A ‘nanomaterial’ typically corresponds to a material in which at least one of the three dimensions is ranging from 1 to approximately 100 nm. A length scale is presented in Figure 1.1, in which the size of a nanomaterial is compared to the size of cells, the diameter of a human hair and a tennis ball for example. According to this definition, nanomaterials can be divided in three main classes: two-dimensional (2D) nanomaterials, such as thin films, are confined along one direction, but the second and third dimension can exceed the upper limit of 100 nm. Nanorods, nanowires and nanotubes are examples of one-dimensional (1D) nanomaterials, which yield only one dimension that is not restricted up to 100 nm. The last class of nanomaterials yields three confined dimensions and corresponds to zero-dimensional (0D) nanomaterials or nanoparticles. Nanomaterials are of specific interest as they exhibit unique properties that differ from the properties of their bulk counterparts. For example, the surface-to-volume ratio of a nanoparticle is much higher in comparison to the bulk material. Such high surface-to-volume ratios are therefore beneficial in e.g. catalytic applications, since the catalytic reaction occurs at the surface of the material. Another example corresponds to the colour of nanoparticles, which can change depending on the size. The absorbed wavelengths will be defined by the size of the nanoparticle, resulting in a certain colour appearance.

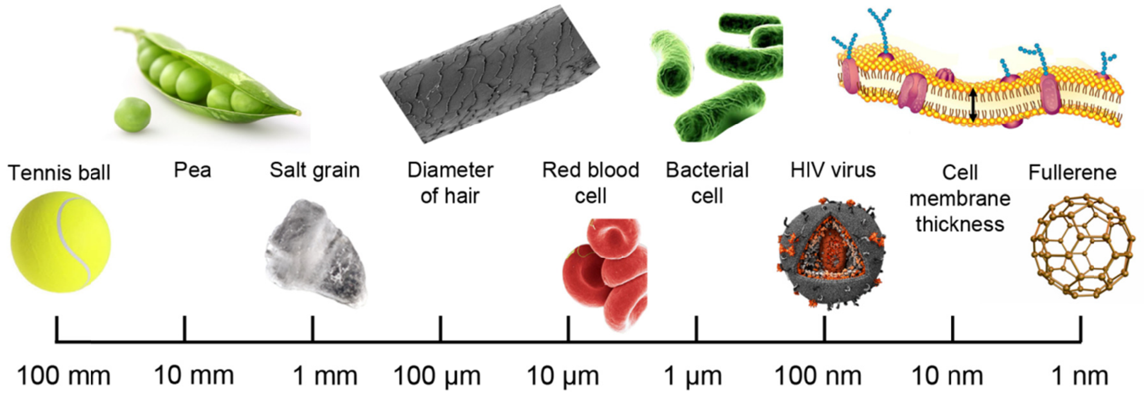

**Figure 1.1.** Length scale illustrating the size range of nanomaterials.

Nowadays, a wide variety of nanoparticles can be produced by different synthesis approaches using numerous starting material. Depending on the material, nanoparticles such as e.g. magnetic, metallic, photonic, polymeric or semiconducting nanoparticles can be obtained. Understanding the connection between the physical properties and the local structure or composition of nanoparticles is of crucial importance to provide the necessary input for predicting the properties and to guide the synthesis of novel nanomaterials with predefined properties. In the remainder of this chapter, the classes of nanoparticles which will be investigated in this thesis will be introduced and the motivation for their characterization will be discussed. It should be noted that the nanoparticles are introduced in different categories: metallic, semiconductor and catalytic nanoparticles; however, this is not the order in which they will be presented in the thesis.

## 2. Metallic nanoparticles

Metallic nanoparticles are among the most widely studied systems in nanoscience as they exhibit totally different properties when downsized to the nanometer level. For example, Au nanoparticles can be used as active catalysts for oxidation reactions while their bulk counterpart is inactive. The investigated metallic nanoparticles in this thesis are Au and Au/Ag core/shell nanoparticles.

### 2.1. Au nanoparticles

Throughout history, gold (Au) has been a popular subject of investigation in science. Since the properties of Au nanoparticles greatly differ from the properties of bulk Au, their study has emerged in nanoscience and nanotechnology. In addition to their stability, Au nanoparticles exhibit size-related electronic, magnetic and optical properties and are therefore ideal for numerous applications such as photovoltaics, optoelectronics, catalysis and biomedicine[1–5].

Over the last decade, there has been a tremendous progress in the synthesis of Au nanoparticles of various sizes and shapes with a good yield and monodispersity[6–14]. Figure 1.2 shows bright field transmission electron microscopy (BF-TEM) images of Au nanoparticles with different shapes obtained using different chemical environments. The synthesis of Au nanoparticles with a certain

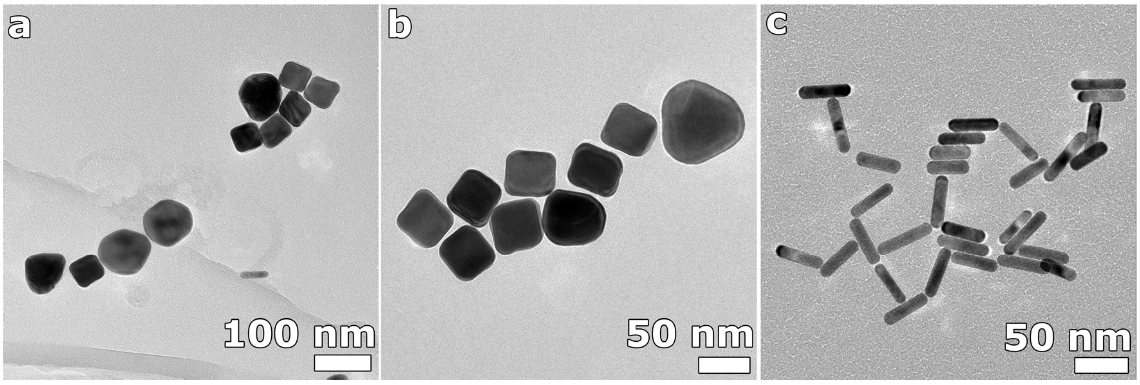

**Figure 1.2.** BF-TEM images of Au nanoparticles yielding different shapes.

shape is typically achieved through a two-step procedure, referred to as a "seed-mediated growth"[15–18]. The conditions which are necessary for nucleation of nanoseeds are opposite to those required for the selective growth of facets. Indeed, small seed Au particles are formed under conditions which ensure rapid growth of all crystal surfaces. To control the morphology, the reaction conditions are altered afterwards: e.g. more Au ions are added, or a different reductant and/or a shape templating surfactant are used. This approach will lead to the growth of larger Au nanoparticles with a particular morphology. Currently, the growth of Au nanorods (Figure 1.2.c) is the most mature synthesis procedure for Au nanoparticles in terms of monodispersity as well as the degree of control over the size and aspect ratio.

Although Au nanoparticles can be prepared with almost any desired shape, the synthesis procedures have evolved empirically and so far, there is no accepted general understanding which explains the fundamental mechanisms behind the shape control of Au nanoparticles. Therefore, a lot of research is still carried out to study the growth mechanism of Au nanoparticles for different synthesis methods. In Chapter 7, the shape of different Au nanoparticles (nanorods, nanospheres and nanotriangles) is examined and an approach to reduce the amount of necessary projection images in an electron tomography experiment is examined.

## 2.2 Au/Ag core/shell nanoparticles

The size- and shape-dependent optical properties of Au and Ag nanoparticles make them ideal candidates for several applications in fields such as sensing, biomedicine and imaging[19,20]. Au is often more suited for biomedical applications due to its chemical stability, biocompatibility and easy surface modification[4], whereas the use of Ag is more attractive for optoelectronic and photovoltaic applications[21,22]. The synthesis of bimetallic Au/Ag core/shell nanostructures provides additional flexibility, stability and even novel properties in comparison to their monometallic counterparts. Au/Ag core/shell nanoparticles can be used in electro-optical devices[23,24], for applications in surface-enhanced Raman scattering and as contrast agents in biomedical applications[25,26]. Nowadays, Au/Ag core/shell nanoparticles with different sizes and shapes can be synthetized. In Figure 1.3, high angle annular dark field scanning transmission electron microscopy (HAADF-STEM) images of different Au/Ag core/shell nanoparticles are visualized. To understand the property-structure relation and tailor the properties, a thorough knowledge of the structure and the chemical composition of the nanoparticles is required. A 3D chemical characterization will be obtained by the use of EDX tomography in Chapter 6. As EDX tomography is a more recently developed technique, the practical aspects will be discussed as well. In Chapter 7, a novel reconstruction algorithm is evaluated using these core/shell nanoparticles.

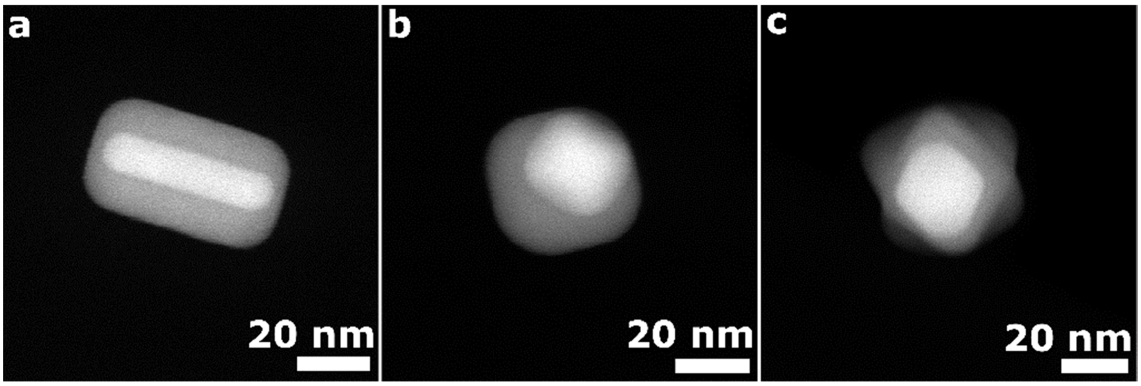

**Figure 1.3.** HAADF-STEM images of Au core / Ag shell nanoparticles with different shapes: (a) Au rod core / Ag cube shell nanoparticle, (b) Au octahedron core / Ag cube shell nanoparticle and (c) Au octahedron core / Ag star-shaped shell nanoparticle.

## 3. Semiconductor nanoparticles

Semiconductor materials are frequently present in everyday life and are used in many technologies. Colloidal semiconductor nanocrystals have gained significant interest because of the possibility to precisely tune their optoelectronic properties, by exploiting the quantum confinement effect[27–29]. This effect states that the properties of a semiconductor material will drastically change with size if the material has dimensions of only a few nanometers. For example, colloidal CdSe nanospheres with different sizes will have different photoluminescence energies and thereby different colours. By varying the size of these CdSe nanospheres from approximately 6 to 2 nm, the photoluminescence can be tuned from the red (6 nm) to the blue light (2 nm). The easy tunability of these CdSe nanocrystals makes them extremely interesting and show potential use in applications such as solar cells[30] and light-emitting diodes[31]. The semiconductor nanoparticles which have been studied in the thesis are Cd-based, CuIn-based and Pb-based nanocrystals.

### 3.1. CdSe nanoplatelets

Recently, a lot of work has been reported concerning the growth of 0D and 1D colloidal semiconductor nanomaterials in solution[27,32,33]. The synthesis of such 2D nanomaterials requires a high level of control since the growth in the basal direction needs to be hindered where the growth in the lateral dimensions needs to be promoted. Novel developments in colloidal synthesis have enabled the synthesis of 2D colloidal semiconductor nanocrystals with well-defined atomic thickness[34–39]. A commonly used synthesis technique was proposed by Itthuria *et al* [34] in which Cd myristate is mixed with a powder of Se in octadene and heated to 240°. When a temperature of 180° is reached, an acetate salt, mostly Cd acetate, is added and CdSe nanoplatelets form. A HAADF-STEM image of such a CdSe nanocrystal is presented in Figure 1.4.a. In the case of CdSe, these nanocrystals, or so-called nanoplatelets, are often only a few CdSe units thick with lateral dimensions in the range of nanometers. Extension of the lateral dimensions is of key importance for their use in devices. The combination of a limited thickness and larger lateral dimensions leads to CdSe nanosheets with a remarkably strong luminescence and an extremely narrow emission spectrum[40,41]. Measurements of the radiative fluorescent lifetime of such CdSe nanoplatelets show that the lifetime decreases with temperature and reaches two orders of magnitude less than for spherical CdSe nanoparticles. These measurements prove that the CdSe nanoplatelets are currently the fastest colloidal fluorescent emitters available[40].

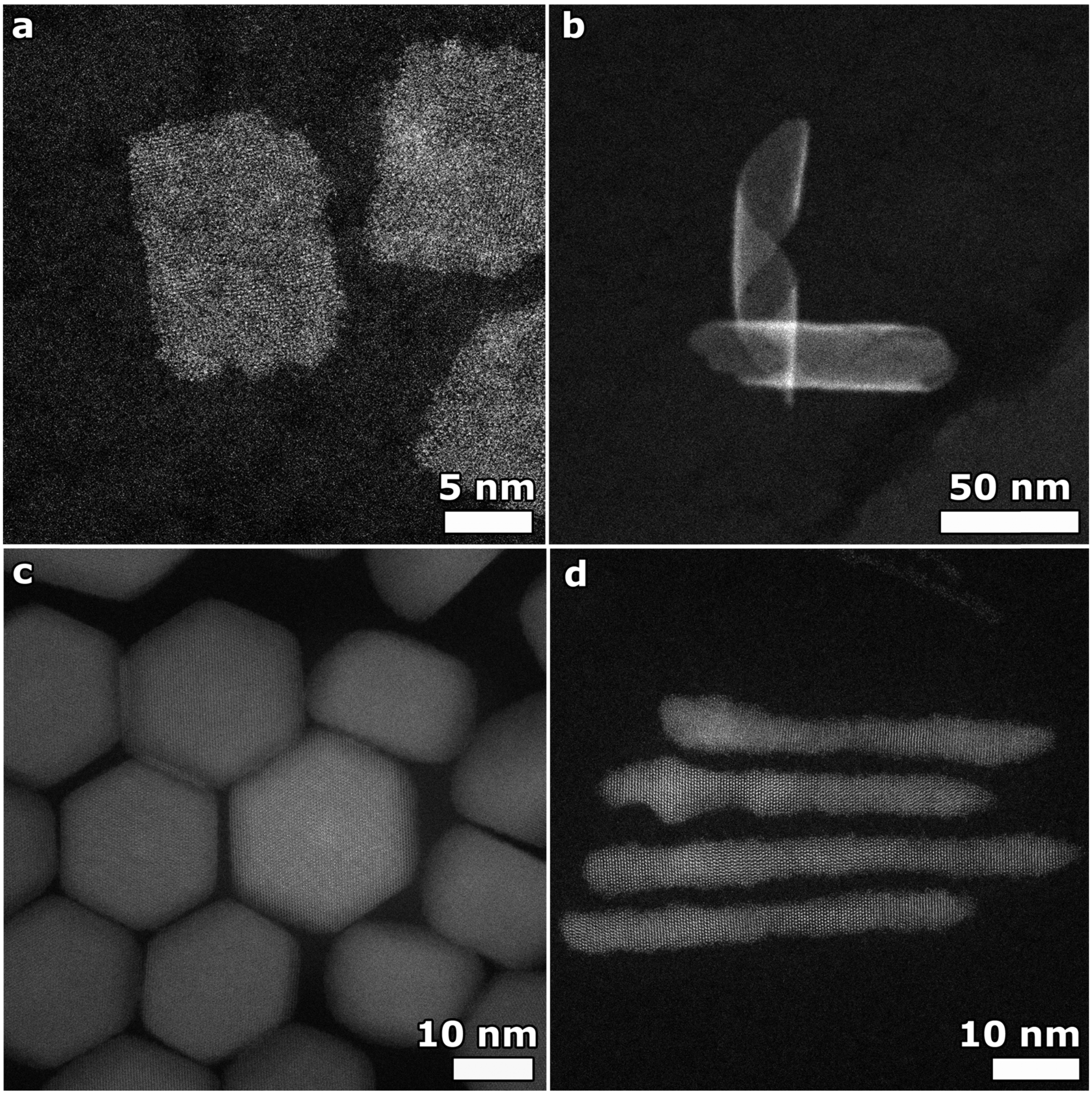

**Figure 1.4.** HAADF-STEM images of (a) a CdSe nanoplatelet, (b) a CdSe ultrathin nanoplatelet, or so-called nanohelix, which seems to be rolled up, (c) CdSe/CdS nanocrystals with an anisotropic shape and (d) CdSe/CdS nanorods.

When the lateral dimensions increase (in the order of hundreds of nanometer), the ultrathin CdSe nanoplatelets are often observed to be rolled up[34,35,38,42,43] or strongly wrinkled[36,38,44]. However, it remains unclear whether this wrinkled conformation is the native or colloidal state of such ultrathin CdSe nanoplatelets. In Figure 1.4.b a CdSe nanoplatelet is shown which seems to be rolled up. However, no conclusions on the shape can be made from this 2D image, which only represents a 2D projection of a 3D object. In order to study the helicity of a nanohelix, electron tomography is required. Therefore, these nanoplatelets and their conformation are studied by electron tomography in Chapter 3. The sample preparation for a TEM investigation needs to be optimized in such a manner that it has no effect on the conformation of the nanoplatelets.

### 3.2. CdSe/CdS nanocrystals

The properties and applicability of semiconductor nanocrystals is limited by the presence of dangling bonds at the surface of the nanocrystal. The growth of a shell of a higher band gap semiconductor around a semiconductor nanocrystal can thereby greatly improve the optical properties. More specific, both the photoluminescence quantum yield and the stability of the full system will enhance[45,46]. Due to these advances, core/shell nanostructures are frequently used as luminescent biological probes and as active materials in light-emitting diodes and optoelectronic devices[47–49].

However, the complex synthesis of these core/shell structures, in which multiple precursors need to controlled simultaneously, remains a major drawback. A first difficulty is the lattice mismatch between the core and the shell of the structures. This mismatch will introduce crystal defects at the core/shell interface and will prevent the growth of the shell when a large lattice mismatch occurs[50,51]. In addition, the possible diffusion of cations[52] and anions[53] which may occur during the shell growth, prevent the growth of a sharp interface. An additional parameter which should be controlled during the shell growth is the addition of ligands. The type of ligands which are used for the shell growth can influence the shape of the final nanostructure[54,55] and the crystal structure of the shell, which can be different than the crystal structure of the core[56,57]. An accurate characterization of the nanostructure therefore emerges to guide and optimize the synthesis procedure.

For colloidal CdSe nanocrystals, it has been demonstrated that the growth of a shell of a higher bandgap semiconductor, such as ZnS and CdS, improves its properties. In Figure 1.4.c and d, CdSe/CdS core/shell nanocrystals with a different shape are shown. In Chapter 5, CdSe (core) / CdS (giant shell) nanocrystals are characterized since they have remarkable optical properties and are therefore of scientific and technological importance. In addition to a more complicated synthesis procedure, the characterization of these core/shell structures is more demanding since the core and the final nanostructure need to be studied. The growth of such core/shell nanostructures is initiated at the position of the core. Therefore, characterizing the position of the core in the nanostructure will lead to insights in their growth process.

### 3.3. $CuInSe_2/CuInS_2$ nanocrystals

As pointed out in the previous section, the combination of two (or more) different semiconductors offers a lot of possibilities to improve the properties of such semiconductor systems. By tailoring both the composition, size and shape of each component and the full architecture of the system, the final properties can be optimized in a controlled manner[29]. Over the last decades, Cd- and Pb-chalcogenides (CdX and PbX, with X = S, Se, Te) have been studied extensively and a high degree of precision has been achieved in the synthesis of these hetero-nanocrystals[29,55,57,58]. Although these materials exhibit exceptional optical properties[57,59–61], large scale deployment of these nanocrystals is limited by the toxicity of Cd and Pb. This encouraged a worldwide research effort to produce alternative materials which have comparable photoluminescence properties and a low toxicity level.

A suitable candidate was found in $CuInX_2$ nanocrystals as their photoluminescence can be tuned from the visible to near-infrared light. This tunability is relevant for applications such as light-emitting devices or biomedical imaging[62–66]. The synthesis of such ternary nanocrystals, however, is very challenging as multiple precursor reactivities must be controlled in a simultaneous manner, which hampers a direct synthesis protocol for colloidal $CuInX_2$ nanocrystals[43,67–71]. In Chapter 5, colloidal $CuInX_2$ nanorods which were developed using a novel method based on sequential cation exchange reactions are fully characterized by advanced 2D and 3D electron microscopy to evaluate the synthesis procedure.

### 3.4. Metal halide perovskite nanoparticles

The development of metal halide perovskites was originally driven by scientific curiosity. Over the past few years, it became clear that these materials can be incorporated in photovoltaic technologies. Their outstanding optoelectronic properties have brought them to the forefront of many research fields such as solar cells, light-emitting diodes, lasers and photodetectors[72,73]. The power conversion of metal halide perovskite solar cells has increased from approximately 3% to 20% in the last four years[72,74–76]. Most studies have concentrated on the development and optimization of hybrid organic-inorganic lead halides, more specific mainly on $CH_3NH_3PbX_3$ (X = Cl, Br, I). A closely related family of materials have gained interest in the last years, which are cesium lead halide ($CsPbX_3$) perovskites. A short introduction on both types is given in the next sections.

### 3.4.1. Organic-inorganic lead halide perovskites

The high absorption coefficient at visible wavelengths of organic-inorganic lead halide perovskites[72,77], which is attractive for solar energy conversion, has been the driving force for their synthesis. Planar perovskite-based photovoltaic devices consist of a thin perovskite $CH_3NH_3PbX_3$ (X = Cl, Br, I) layer in between conductive scaffolds. Recent studies have shown that these devices exhibit power conversion efficiencies exceeding 20%[78,79]. The morphology and crystallinity of the perovskite layer are known to be crucial as they influence the device performance[80–83]. Nevertheless, the conventional synthesis methods produce perovskite films with large variations in grain morphology. The high defect density in a polycrystalline film is generally disadvantageous for charge carrier dynamics[84,85]. Therefore, the synthesis of high quality monocrystalline inorganic-organic lead halide perovskites is currently of high interest and could form the cornerstone of fundamental studies or large-scale application in perovskite-based devices. In Chapter 7, these planar $CH_3NH_3PbX_3$ perovskites are investigated down to the atomic scale to investigate their crystallinity. The organic component in these perovskites makes a characterization study very challenging as the electron beam does not strongly interact with the organic component, which hampers a clear visualization.

### 3.4.2. Cesium lead halide perovskites

The synthesis of purely inorganic cesium-based perovskites is less straightforward as these ternary compounds are far less soluble in common solvents contrary to $CH_3NH_3PbX_3$, which is necessary to form colloidal nanocrystals. Although the potential of $CsPbX_3$ (X= Cl, Br, I) was already reported more than 50 years ago[86], their colloidal synthesis has only been recently demonstrated[87–91]. In Figure 1.5, BF-TEM images of $CsPbBr_3$ and $CsPbI_3$ nanocrystals with a monodisperse shape are shown. These colloidal $CsPbX_3$ nanocrystals exhibit high photoluminescence quantum yields, narrow emission line widths and considerable air stability. An advantage of these systems is the tunability of their bangap by altering their size and halide (X) composition. The tunable bandgap energies cover the entire visible spectral region with narrow and bright emission. Nowadays, alternative synthesis approaches are investigated to prepare high quality nanocrystals and to develop synthesis approaches which can tune the halide composition in a straightforward manner. In Chapter 4, colloidal $CsPbX_3$ nanocubes and nanowires are investigated at the atomic level by TEM.

## 4. Catalytic nanoparticles

### 4.1. Ceria-zirconia nanostructures

Ceria-zirconia mixed oxides have shown great potential as catalysts for a variety of chemical processes related to environmental catalysis, the production of hydrogen for fuel cells and the production of other chemicals[92]. A new route in the synthesis of heterogeneous catalysts is the development of materials with reduced amount of noble metals and lanthanides. The reduction of

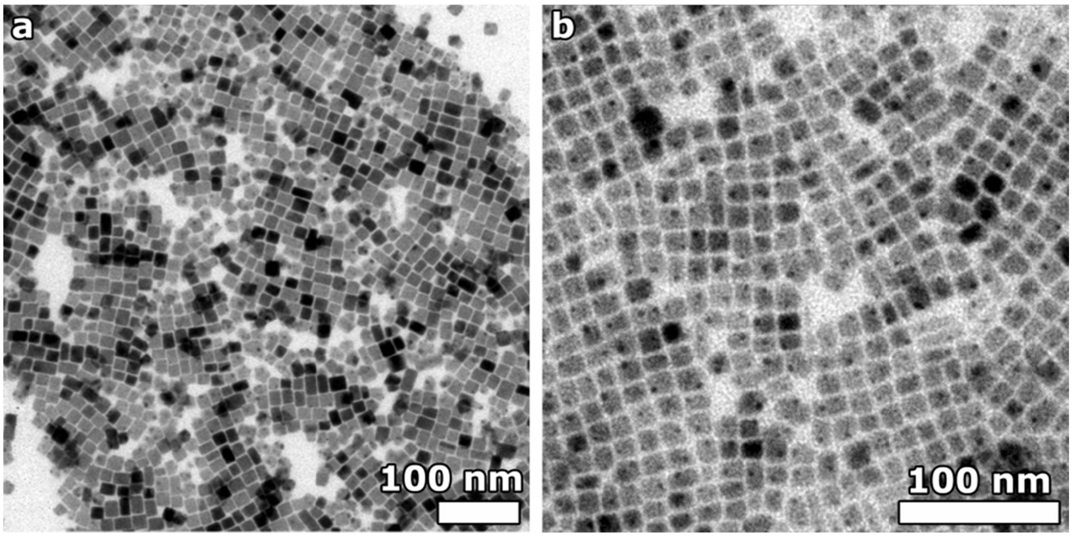

**Figure 1.5.** BF-TEM images of multiple (a) $CsPbBr_3$ and (b) $CsPbI_3$ nanocrystals. The exchange of Br into I results in a red shift of the photoluminescence emission.

these components is relevant from both an economic and geo-strategic point of view. For the synthesis of ceria-zirconia catalysts, this translates in the optimization of the amount of ceria. One of the key properties of ceria-zirconia oxides is their ability to exchange lattice oxygen with reactants, usually referred to as oxygen storage capacity[93,94]. The oxygen storage capacity is coupled to the $Ce^{4+}/Ce^{3+}$ redox exchange, which equals to the reducibility of the oxide. The exact capacity is dependent on structural and compositional factors, which are closely related to each other[95–97]. In Figure 1.6, HAADF-STEM images of ceria-zirconia nanocrystals are shown, where ceria is present as islands on the surface of the nanocrystal which are indicated by the white arrows in Figure 1.6.b. Understanding the complex relationship between these factors and the properties has been the focus of intense research and has allowed foreseeing new synthesis routes towards novel ceria-zirconia materials. The requirements for these novel materials are very high oxygen storage capacity values in the whole temperature range, low ceria content and the absence of noble metals. These novel ceria-zirconia nanocrystals and their ceria content are investigated in Chapter 8 to relate their properties to the final structure.

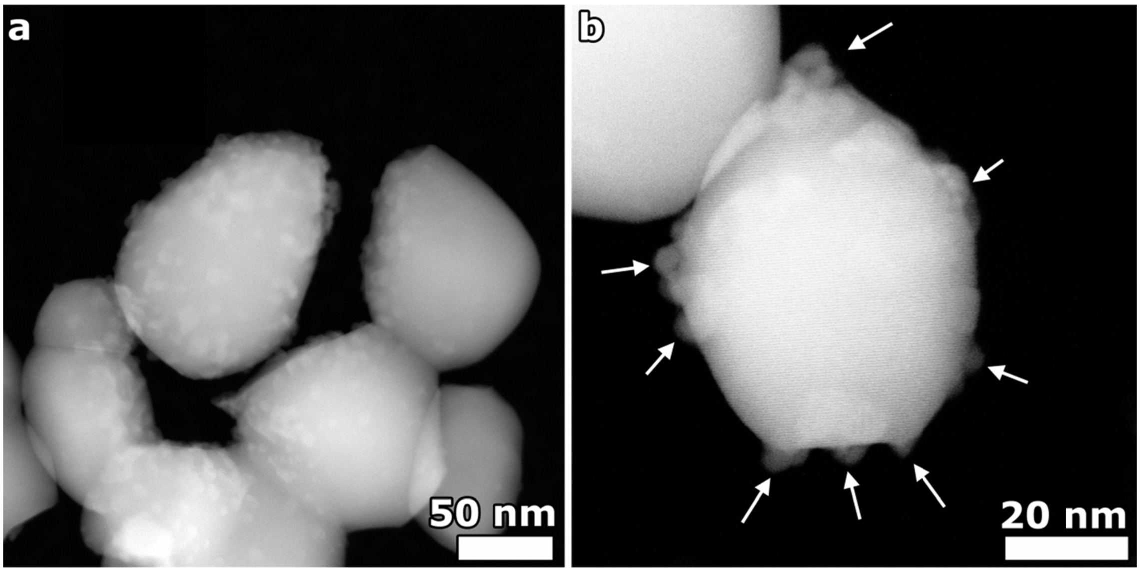

**Figure 1.6.** HAADF-STEM images of (a) multiple ceria-zirconia nanostructures and (b) a single ceria-zirconia nanocrystal. The white arrows indicate the presence of ceria containing islands.

## 5. Characterization of nanoparticles

From the previous sections, it has become clear that nanomaterials play a key role in modern technology because of their unique physical and chemical characteristics. The specific properties of nanoparticles are strongly related to their shape, size and composition. Therefore, in order to understand this property-structure relation, a thorough and precise structural and chemical characterization is of utmost importance. Techniques such as powder X-ray diffraction (PXRD), scanning electron microscopy (SEM) and transmission electron microscopy (TEM) are used for the characterization of nanoparticles at the nanometer level and below.

From a PXRD pattern, one can identify the particular phase of the material as the position and the relative intensities of the peaks provide a unique “finger print”. Additionally, the lattice parameters, size and strain can be obtained for the overall powder. The technique is non-destructive and there is no need for an extensive sample preparation. However, only global information can be retrieved, a single nanoparticle characterization cannot be obtained.

SEM uses a focused electron beam (up to a few nanometers) to scan the surface of the sample. The interaction of the beam with the sample generates a lot of different signals, the most commonly detected signal are the secondary electrons which are emitted by the atoms excited within the sample. The detection of these secondary electrons yields information on the topography of the sample. Also, analytical information can be obtained by the use of an energy dispersive X-ray (EDX) or wavelength dispersive X-ray (WDX) spectroscopy system. Nowadays, the ability of an investigation at environmental conditions is possible with the use of an environmental SEM (ESEM). The use of an ESEM can eliminate the need for conductive coating and will thereby open a new route towards the investigation of soft matter surfaces. However, SEM is limited to the investigation of the surface of a nanomaterial and will not provide one with information on the internal structure. Additionally, the spatial resolution of a SEM is far from optimal to study nanoparticles at the atomic level.

TEM is an excellent technique to investigate nanomaterials. By using different TEM techniques, structural, chemical and even electronic information can be obtained on single nanostructures. The benefit of TEM, in comparison to PXRD, is that one is able to investigate single nanoparticles and that by the use of different TEM techniques a thorough characterization can be performed. Nevertheless, one should not forget that TEM images are only 2D projections of three-dimensional (3D) objects. Therefore, TEM has been expanded to 3D, which is referred to as "electron tomography"[98,99]. Most results have been achieved at the nanometer level[100–105], but currently, imaging individual atoms in 3D is possible for model-like systems[106–108].

Throughout this thesis, the aim is to characterize different functional nanoparticles in 2D and 3D to understand their structure-to-properties connection. Therefore, different TEM techniques are applied and optimized to extract reliable structural and chemical information. In the next chapter, electron tomography will be extensively discussed as this technique will enable a 3D characterization, which forms the basis of this thesis.

# Chapter 2

## Introduction to electron tomography

## 1. Introduction to transmission electron microscopy

Prior to introducing electron tomography, a brief overview of transmission electron microscopy (TEM) is given. A brief history of TEM, the build-up of a TEM and different TEM techniques are discussed.

### 1.1. A brief history of TEM

Ernst Ruska stated in 1930 that a TEM can be built using the same principle as for an optical microscope by only replacing the glass lenses by electromagnetic lenses[109,110]. The use of TEM enables us to acquire images with a spatial resolution which cannot be obtained using an optical microscope. The resolution of an optical instrument is determined as the ability to distinguish separate points of an object that are located at a small angular distance. The resolution of an optical microscope is limited by the wavelength of its radiation source, which is typically $400-700\,nm$. The wavelength of accelerated electrons in a TEM depends on their energy $E$. When neglecting relativistic effects, de Broglie's equation is given by:

$$\lambda = \frac{1.22}{E^{1/2}} \tag{2.1}$$

with $E$ in electron volts and $\lambda$, the wavelength, in nm. Typically, electrons in a TEM are accelerated by high acceleration voltages of $100-300\,kV$ and result in electron wavelengths of approximately $2-4\,pm$, which is several magnitude orders smaller in comparison to an optical microscope. However, the resolution of a TEM is not only limited by the wavelength of the electrons, but also by the aberrations of the electromagnetic lenses in the microscope, which restricts the practical resolution to approximately $1-2$ Å. Spherical aberration is the most prominent aberration which results in a focus difference for electrons which deviate from the optical axis. The idea of a TEM by Ruska was commercialised by Siemens and Halske in 1939. Ernst Ruska received the Noble Prize in Physics in 1986 for his contribution to electron optics.

## 1.2. The build-up of a TEM

As pointed out in section 1.1, the principle of a TEM is comparable to the principle of an optical microscope. From top to bottom, a TEM consists of an illumination system, a condensor lens system, the stage where the specimen is located and the imaging lens system. The electrons are generated by an electron source which is either a thermionic gun or a field emission gun, which is currently more often used. The required size, intensity and convergence angle of the electron beam are formed by the condensor system. By a set of electromagnetic lenses, the appropriate electron beam to investigate the sample is formed. A condensor aperture can be inserted to select the electrons that follow a path close to the optical axis, which will reduce the effect of the aberrations caused by the lenses in the condensor system. After passing the condensor system, the electrons interact with the specimen which is inserted with the use of a dedicated TEM holder. The objective lens, located close to the specimen, disperses the electrons and yields a diffraction pattern in the back focal plane of the objective lens. The diffracted beams recombine and form an enlarged image in the image plane of the objective lens. The use of an objective aperture in the back focal plane of the objective lens can reduce the effect of lens aberrations of the objective lens and/or select specific spots in the diffraction pattern. A selected area diffraction (SAD) aperture can be inserted in the image plane of the objective lens, which selects a specific region of the specimen from which information will be extracted. The projector lens system will form the final magnified projection image, which either uses the back focal plane or the image plane of the objective lens as its object plane. A fluorescent viewing screen or a charged coupled device (CCD) is located at the bottom of the TEM and will visualize the image.

## 1.3. Different TEM techniques

### 1.3.1. Bright field transmission electron microscopy

When applying BF-TEM, the specimen is illuminated by a parallel beam of electrons. Figure 2.1 represents a schematic overview of the electron ray diagram for BF-TEM imaging. In this imaging mode, elastically scattered electrons contribute to the image formation and two main mechanisms occur: mass-thickness and diffraction contrast. When amorphous or non-crystalline specimens are imaged, thicker regions of the specimen will appear darker in the image (mass-thickness mechanism). For crystalline specimens, the incident parallel electron beam is diffracted by the crystal lattice of the specimen and the formed contrast is referred to as diffraction contrast. By using an objective aperture, either the direct beam or a diffracted beam is selected. If the diffracted beam(s) is used for the image formation, the technique is referred to as dark field (DF) imaging. The selection of the direct, undiffracted beam results in a bright field (BF) image. In Figure 2.2.a, a BF-TEM image of a Au nanotriangle is shown.

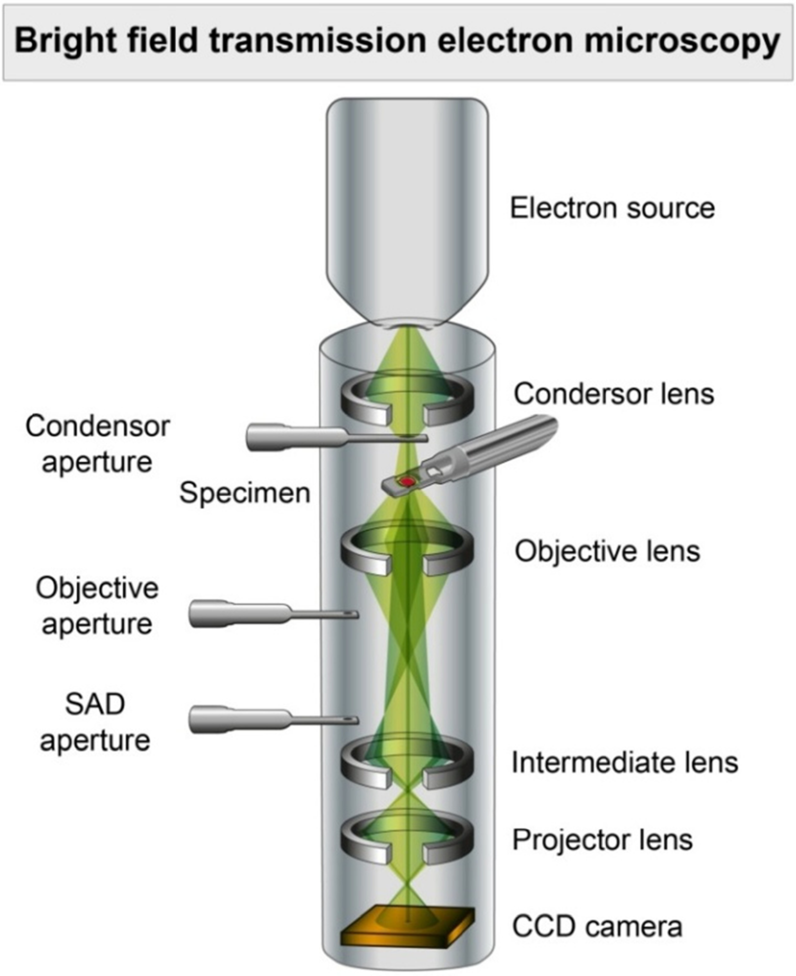

**Figure 2.1.** Schematic overview of the electron ray diagram for BF-TEM.

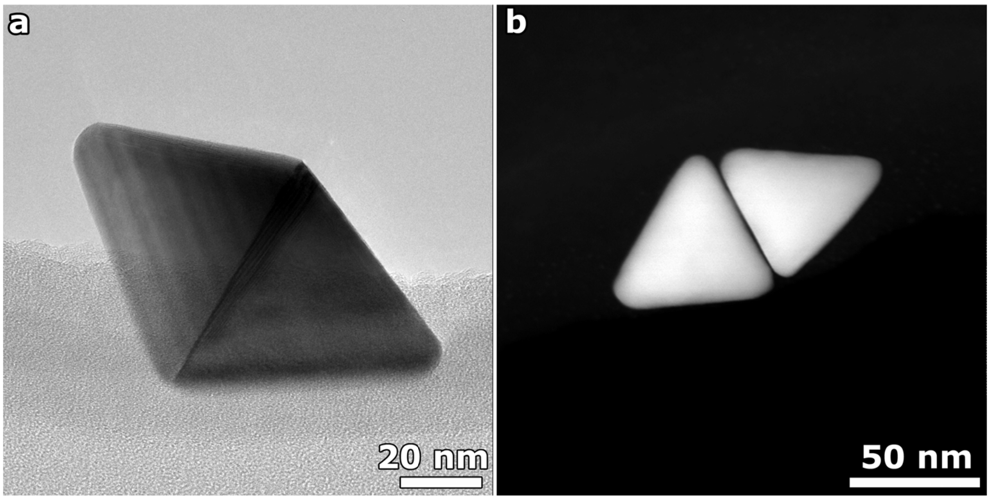

**Figure 2.2.** (a) BF-TEM and (b) HAADF-STEM image of two Au nanotriangles.

### 1.3.2. High angle annular dark field scanning transmission electron microscopy

In scanning transmission electron microscopy (STEM), the electron beam is focused into a fine probe (probe sizes of << 1 nm) by the lenses of the illumination system, as visualized in Figure 2.3. The region of interest is scanned line by line by the use of deflection coils. At each position, a signal is generated and for each pixel, the number of electrons scattered to an annular detector is detected. The quality of the image is only affected by the aberrations of the electron probe and possible scan noise during the acquisition. In STEM mode, the selection of the electrons for imaging is based on their scattering angle. The electrons scattered to a specific angular range from $\theta_{in}$ (inner angle) to $\theta_{out}$ (outer angle) are detected using an annular detector. The inner and outer angles can be adjusted by adapting the physical camera length at which the annular detector is positioned with respect to the specimen. The most widely used detector in STEM is an annular detector. Annular dark field STEM (ADF-STEM) collects the electrons scattered to an angle between 10 and 50 mrad when a long camera length is used. When a small camera length is used, electrons scattered to high angles (> 50 mrad) are collected and the technique is referred to as high angle annular dark field STEM (HAADF-STEM). An example of a HAADF-STEM image is shown in Figure 2.2.b. In this case, scattering is associated with the interaction close to the nucleus of the atoms of the investigated specimen and the collected electrons can be considered as Rutherford scattered particles. The intensity of the formed

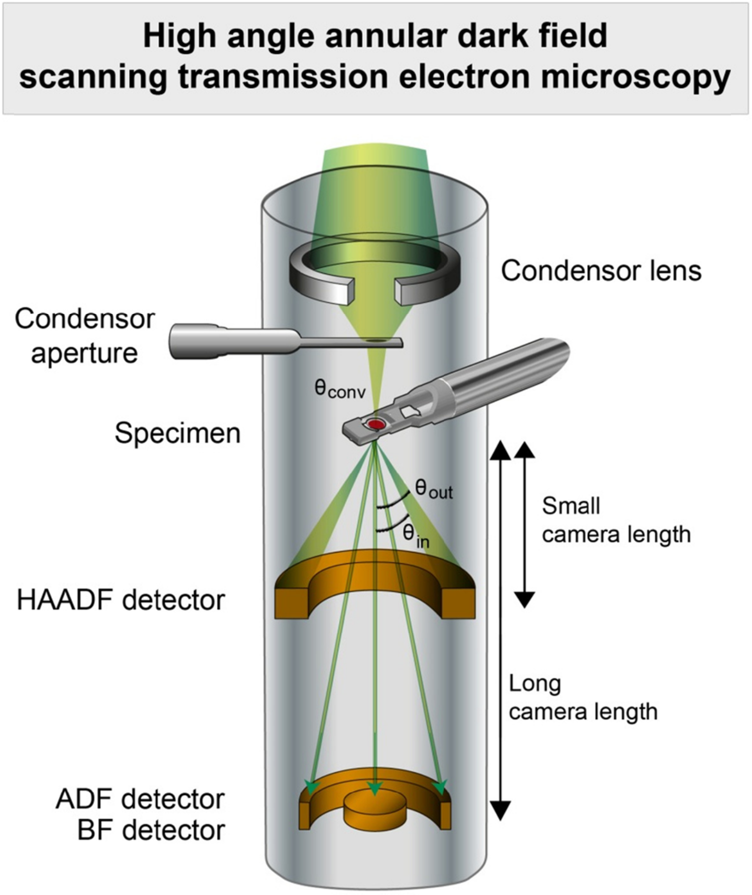

**Figure 2.3.** Schematic overview of the microscope setup for STEM imaging. The convergent electron beam is used to scan the specimen and the electrons which are scattered to a specific angular range (from $\theta_{in}$ to $\theta_{out}$) are detected using an annular detector. By changing the camera length of the detector, the angular range can be adjusted.

images is proportional to $Z^n$ (the atomic number), with $1.6 < n < 2$, of the elements under investigation and of the projected thickness of the specimen[111]. The presence of diffraction contrast is minimized since most of the diffracted electrons have a scattering angle less than $\theta_{in}$ and thereby pass through the hole of the annular detector.

### 1.3.3. Energy dispersive X-ray imaging

Energy dispersive X-ray (EDX) spectroscopy is used in a TEM to map the chemical elements present in a specimen. Incoming electrons of the beam can excite inner shell electrons of an atom in the specimen, which will generate X-rays and create an electron hole. A higher energy electron from an outer shell will then fill this vacancy and an X-ray will be emitted with the difference energy. The specific energies of these X-rays are characteristic for the chemical elements that are present in the specimen. Thereby, the obtained characteristic X-ray spectrum can be used for a chemical characterization. Such a spectrum consists of a superposition of a background signal caused by Bremsstrahlung and the characteristic X-ray peaks. As the background signal is rather constant throughout the energy window, it is straightforward to extract a spectrum only consisting of the characteristic peaks. When EDX is combined with STEM imaging, a complete 2D elemental map can be obtained since each pixel in the 2D image contains a measured spectrum. In Figure 2.4 a schematic overview of the position of the EDX and HAADF-STEM detector are shown. The spectrum in each pixel can be evaluated and the characteristic X-ray peaks can be selected by an energy window around the characteristic energy to obtain 2D elemental maps.

### 1.3.4. Electron energy loss spectroscopy

Electron energy loss spectroscopy (EELS) is another technique, which can provide chemical information. Incoming electrons in a TEM can lose part of their energy due to interactions with the specimen. The energy loss of the scattered electrons can be recorded on a CCD. After interaction with the specimen, the electrons are deflected by a magnetic prism, before reaching the CCD. The radius of the deflection is dependent on the remaining electron energy which results in an energy dispersive plane. The electrons are then directed to the CCD camera by a drift tube and set of lenses. An energy slit in the energy dispersive plane can now be used to select a specific energy window, which will result in an image of a specific energy loss corresponding to a specific chemical element. This technique is referred to as “energy filtered TEM” (EFTEM). It is also possible to obtain an elemental map of a recorded EELS spectrum, as such a spectrum can be acquired pixel-by-pixel. Unfortunately,

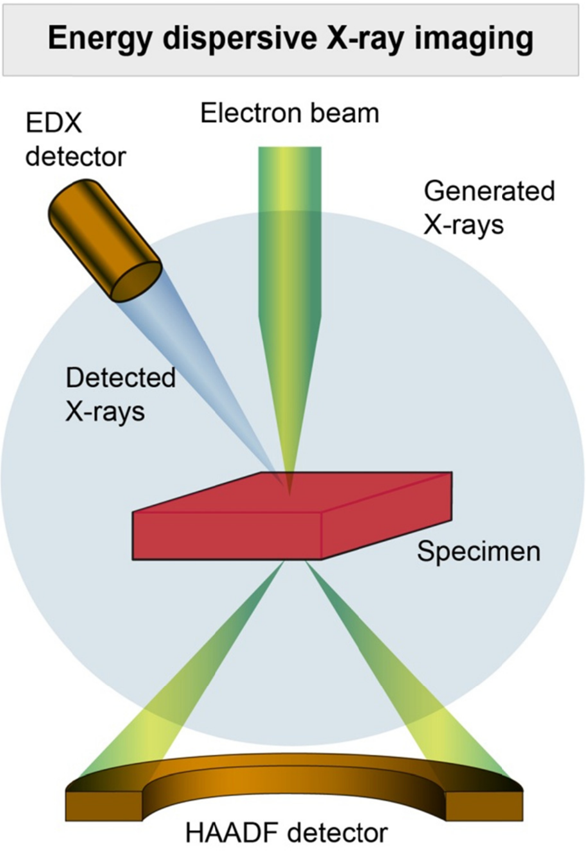

**Figure 2.4.** Specimen detector geometry for a conventional EDX detector in a TEM. While X-rays are collected by the EDX detector, a HAADF-STEM image can be acquired simultaneously.

the dominant background signal in an EELS spectrum complicates a straightforward chemical characterization. Therefore, the background signal needs to be removed using model fitting techniques in order to obtain reliable chemical maps.

## 2. Imaging in three dimensions

For tens of years, structural, chemical and electronic information of a nanoscale object can be retrieved using different TEM techniques. However, the majority of these techniques provides only 2D information on the investigated 3D object. 2D imaging may be sufficient when investigating isotropic or periodic nanostructures, but may lead to an incomplete and unreliable characterization for highly asymmetric nanostructures. For example, as mentioned in section 3.1 of Chapter 1, retrieving the helicity of CdSe nanohelices is impossible using 2D imaging or understanding the growth process of core/shell nanostructures requires obtaining the 3D location of the core in the nanostructure. A 3D investigation of such materials is crucial to understand the relationship between the physical properties and the structure of these nanomaterials. To perform such studies, "electron tomography" is required, a technique from which a 3D reconstruction can be computed from a series of 2D projection images. The four steps of an electron tomography experiment are schematically visualized in Figure 2.5. The first step corresponds to the acquisition of a tilt series of projection images of the investigated object over an angular range as large as possible, with tilt increments of typically 1° or 2°. After the acquisition, the tilt series of projection images is aligned with respect to a common tilt axis to eliminate relative shifts and rotations between the successive images. In the next step, a mathematical reconstruction algorithm is used to compute the 3D reconstruction. Nowadays, advanced reconstruction algorithms are often used, which benefit from prior knowledge concerning the specimen under investigation. During a last step, the outcome of the electron tomography experiment is analyzed, preferentially in a quantitative manner.

## 3. History of electron tomography

In 1917, Johan Radon outlined the mathematical principles behind the tomography technique[112]. Before the idea of Radon was adopted in materials science, Cormack proposed the idea of an X-ray tomography scanner (CAT-scan) for 3D medical imaging[113], which was built by Hounsfield in 1971 and for which they received a shared Nobel prize in 1979[114,115]. The first applications of tomography in electron microscopy were published in 1968. Rosier and Klug determined the structure of a biological macromolecule of which a single projection was sufficient for a 3D representation due to its helical symmetry[116]. Next, Hoppe showed that with a sufficient number of projection images, it is possible to retrieve the 3D morphology of a fully asymmetrical system[117]. In a third paper by Hart[118], it was demonstrated that the quality of a tomographic reconstruction depends on the number of

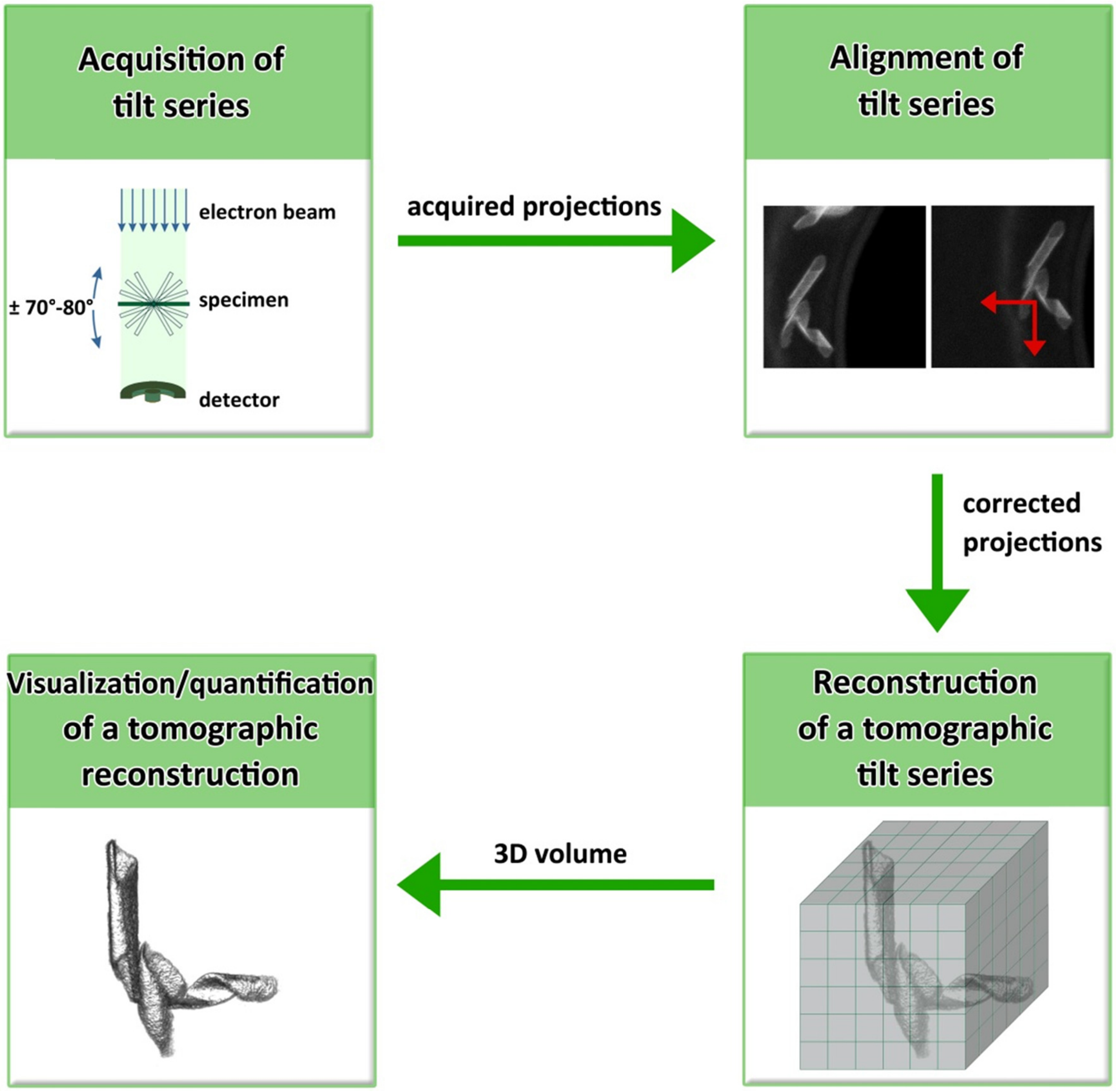

**Figure 2.5.** Schematic overview of the different steps in an electron tomography experiment.

projection images used during the reconstruction. Due to practical limitations such as beam damage, limited tilt range and the lack of computer processing power, it took more than a decade before the first experimental results became available in biological science. It took considerably longer for the first application of electron tomography in the materials science field was obtained. Indeed, when investigating biological samples, BF-TEM imaging is used. However, this imaging technique is not suitable to perform electron tomography on crystalline samples. Since the technique does not fulfil the so-called “projection requirement”, which states that the intensity in a projection image must be a monotonic function of a physical property of the investigated object integrated along the thickness of the specimen in the projection direction[119]. Different imaging modes and their applicability to electron tomography will be further discussed in section 4.1.1.

## 4. Tomography in practice

### 4.1. Acquisition of the tilt series

As illustrated in Figure 2.5, an electron tomography experiment starts with the acquisition of a tilt series of projection images. Figure 2.6 shows a schematic overview of the acquisition procedure of an electron tomography experiment, where the sample is tilted with respect to the electron beam and a tilt series of projection images is acquired. This section will first discuss the applicability of different TEM imaging modes to electron tomography. Next, different tilt schemes for the acquisition of a tilt series and the possibility of the use of an automated acquisition procedure will be discussed.

### 4.1.1 Imaging modes in electron tomography

As discussed above, the projection images of a tilt series need to satisfy the projection requirement in order to be usable as input for the tomography experiment. In materials science, a broad range of nanostructures is investigated. Depending on the type of nanomaterial and the information which one wants to obtain, different imaging modes are better suited. In the next part of this section, the applicability of BF-TEM, HAADF-STEM and EDX mapping to electron tomography are discussed.

#### Bright field transmission electron microscopy

As discussed in section 1.3.1, the electron beam in BF-TEM mode is diffracted by the crystal lattice of the crystalline specimen. Due to the presence of such diffraction contrast in a BF-TEM image when imaging a crystalline specimen, the intensity in the image is not only related to the projected thickness of the specimen, but also depends on the orientation of the specimen. From Figure 2.2.a, it is clear that the intensity throughout the crystalline Au nanoparticles is not homogeneous, which is due to the

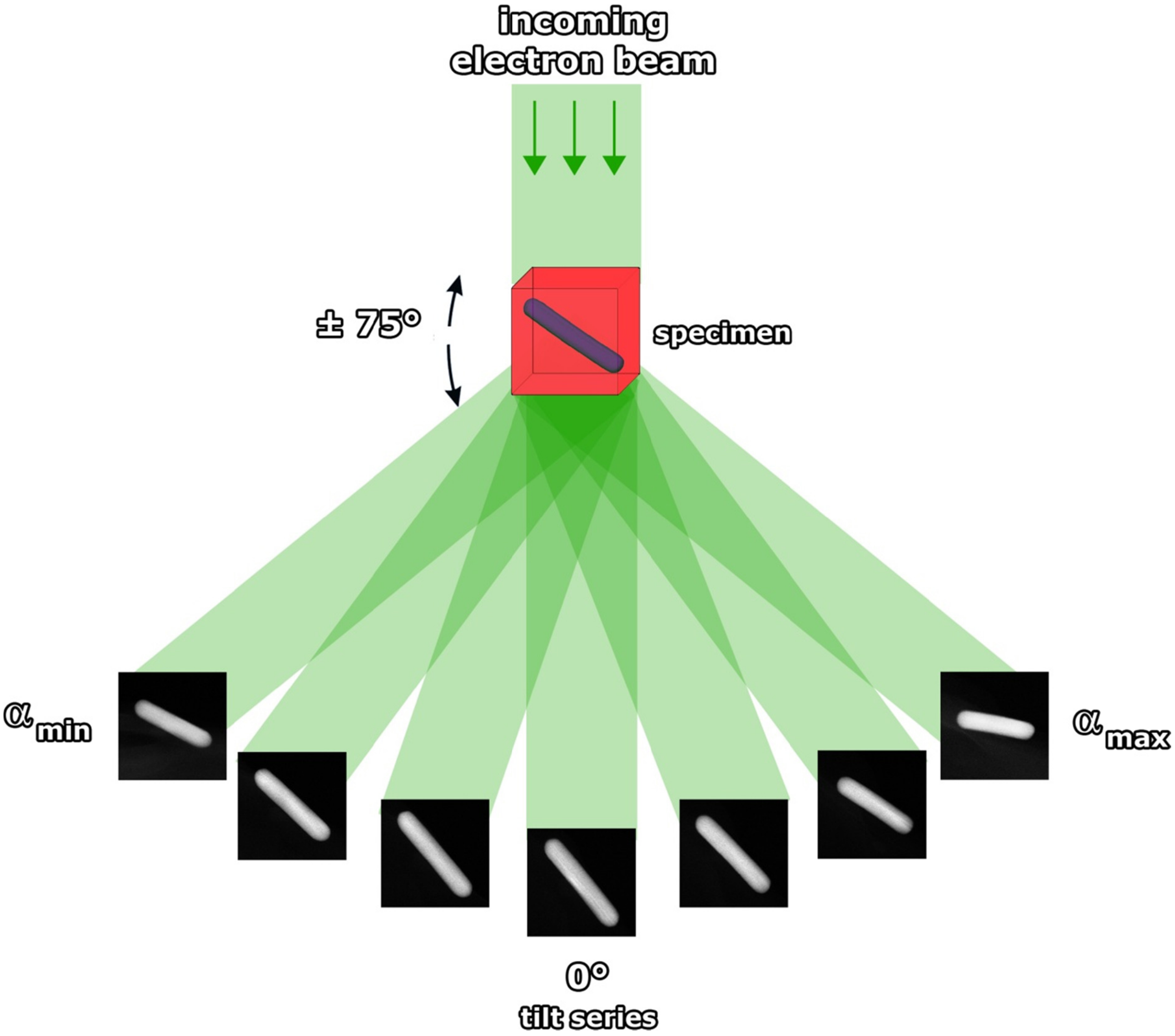

**Figure 2.6.** Illustration of the acquisition of a tilt series in an electron tomography experiment. While tilting over an angular range of typically ± 75° in certain tilt increments, a series of projected images of the object under investigation is acquired. The design of the microscope, the support grid and location of the object on the grid determine the angular range that can be reached.

presence of diffraction contrast. Consequently, the relation between the acquired intensity in the projection images and the thickness of the specimen does not fulfil the projection requirement, which makes BF-TEM imaging less favourable when an electron tomography experiment is applied to a crystalline specimen[120,121].

**High angle annular dark field scanning transmission electron microscopy**

In order to evaluate whether HAADF-STEM images fulfil the projection requirement, we need to investigate the dependence of the detected intensity to the thickness of a specimen. A HAADF-STEM image of two Au nanotriangles is shown in Figure 2.2.b. When multiple scattering is ignored, the intensity in a HAADF-STEM image increases with the thickness of the investigated specimen. As illustrated in Figure 2.7, a uniform sample build-up of layers with a thickness $dt$ is considered.

Each individual layer scatters the same amount of incoming electrons to an angle larger than $\theta_{in}$. The decrease in transmitted electrons due to scattering to angles smaller than $\theta_{in}$ from the layer with thickness $dt$ is equal to[122]:

$$dI = -I_0 \mu dt \quad \text{with} \quad \mu = n\sigma \tag{2.2}$$

in which $I_0$ corresponds to the intensity of the unscattered incoming electron beam, $n$ is the number atoms per unit of volume, $\sigma$ is the Rutherford scattering cross-section for angles larger than $\theta_{in}$ and $\mu$

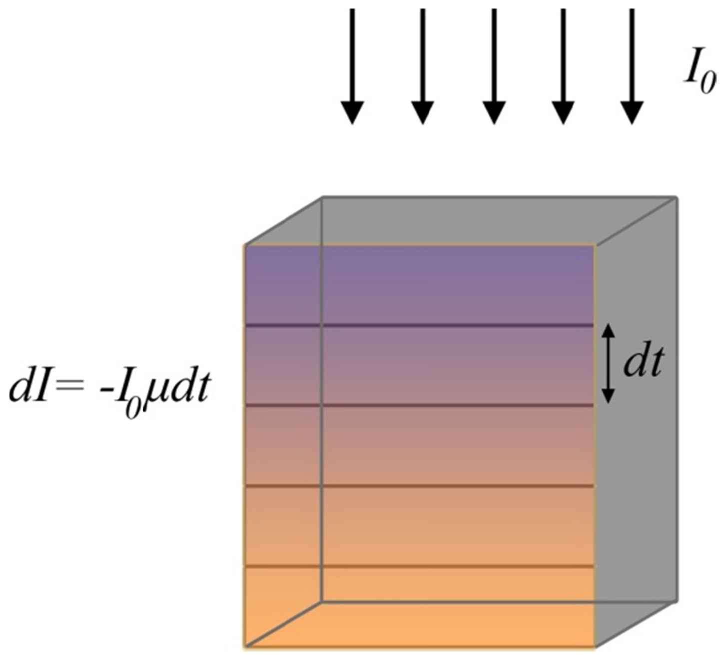

**Figure 2.7.** Schematic representation of a uniform sample build-up of layers. Scattering of electrons at a layer with thickness $dt$ results in a decrease of the transmitted intensity of $I_0\mu dt$.

is the attenuation coefficient. Integration over the total thickness $t$ of the specimen results in:

$$I' = I_0 e^{-\mu t} \tag{2.3}$$

and shows that the amount $I'$ of the electrons scattered to angles smaller than $\theta_{in}$ decreases exponentially with thickness $t$. If it is assumed that the outer radius of the annular detector approaches infinity and that all the electrons, which reach the detector, are recorded, the measured intensity equals:

$$I_{det} = I_0 - I' \tag{2.4}$$

$$= I_0(1 - e^{-\mu t}) \tag{2.5}$$

$$\cong I_0 \mu t - \frac{1}{2} I_0 \mu t^2 \tag{2.6}$$

The first order approximation of the Taylor expansion shows that the detected intensity in an HAADF-STEM image is proportional to the thickness $t$ of the specimen. However, this first order approximation will only hold for thin samples. If the specimen thickness increases, the higher order terms are no longer negligible and damping occurs[123]. In Figure 2.8, the relative intensity of a Au slab is illustrated in function of the thickness.

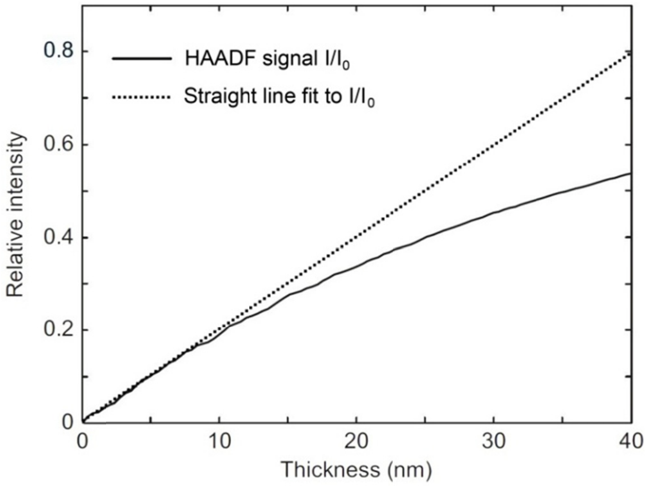

**Figure 2.8.** HAADF-STEM signal $\frac{I}{I_0}$ (full line) and straight line fit to $\frac{I}{I_0}$ between 0 and 5 nm (dotted line) as a function of thickness of a Au slab[124]. Damping of the signal occurs when the thickness increases.

Thereby, it can be concluded that the projection requirement is satisfied for thin samples as the intensity scales with the thickness of the specimen. Due to the relation between the intensity and the average integrated atomic number of the elements in the specimen, relative chemical information can also be obtained. HAADF-STEM tomography was first introduced in materials science in 2003, which was used to study metal nanoparticles in a mesoporous silica support matrix[125]. Since then, a broad variety of specimens has been investigated successfully with HAADF-STEM tomography[103,120,126–129].

**Energy dispersive X-ray imaging**

The intensity of a characteristic X-ray peak of an element present in the specimen in an EDX spectrum scales with the weight fraction, the fluorescence yield and the ionization cross-section of the element. Therefore, a 2D EDX map can in principle be used as a projection image for tomography[130,131]. In the past, the combination of tomography and EDX mapping was hampered by the directionality and inefficiency of the sample-detector geometry. Since the EDX detector is typically placed under a specific tilt angle of the specimen, only a maximum efficiency is obtained when the specimen is tilted towards the detector. At other angles, shadowing occurs and part of the generated X-rays does not reach the detector. With this set-up, only needle-shaped samples, where shadowing is avoided during the acquisition, were suitable for EDX tomography[132–135]. Recently, a new detector system was developed to reduce the X-ray blocking. The detector geometry uses four detectors which are symmetrically placed around the sample[136], which is schematically presented in Figure 2.9. With the development of this geometry, EDX tomography becomes within reach[137–140]. The application of EDX tomography of nanoparticles will be discussed in Chapter 6.

### 4.1.2. Tilt schemes

As discussed in Section 4.1 of this chapter, a tilt series of multiple projection images needs to be acquired in the first step of an electron tomography experiment. As schematically depicted in Figure

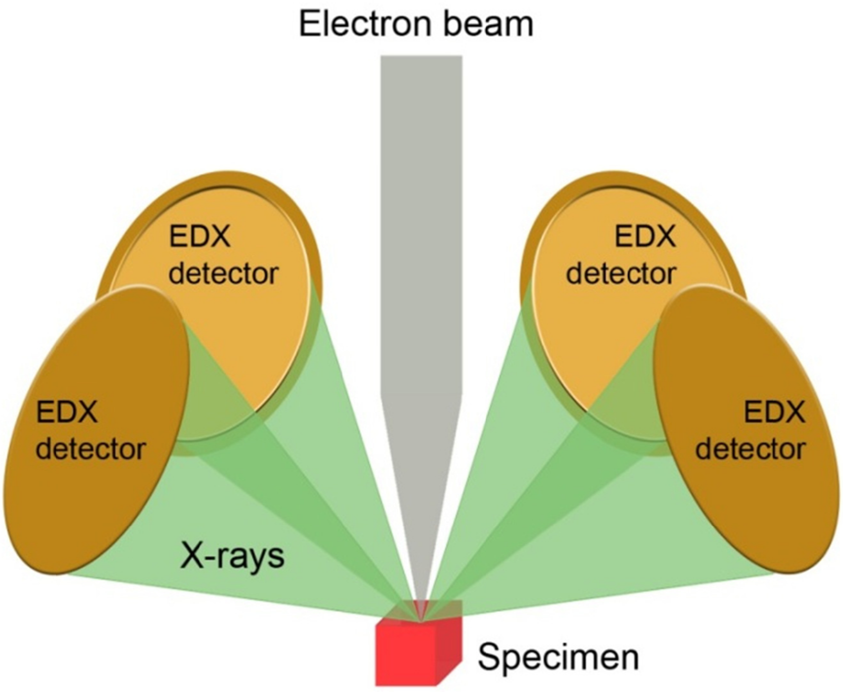

**Figure 2.9.** Super-X detection system which has four X-ray detectors symmetrically placed around the specimen.

2.6, by tilting a dedicated tomography holder with respect to the electron beam, different projection images of a sample are obtained at different tilt angles. Conventionally, the quality of a tomographic reconstruction is strongly related to the number and the angular range of the obtained projections.

However, due to shadowing effects of the grid and the sample holder at high tilt angles, the tilt range is typically restricted to ± 75°. Both the tip of a regular double tilt holder (Figure 2.10.a) and a dedicated tomography holder (Figure 2.10.b) are shown in Figure 2.10. Due to the special design of the dedicated tomography holder, the tilt range has increased a lot in comparison to the range of the double tilt holder. Still, the gap of missing information in the angular range will lead to a so-called "missing wedge" of information in the projection data. A representation of the missing wedge/pyramid is shown in Figure 2.11 for both a single tilt axis and a dual tilt axis geometry, which will be discussed further in this section. As a result, artefacts will occur in the final reconstruction such as fanning artefacts and an elongation in the direction of the optical axis. Figure 2.12 shows the effect of the missing wedge on the Shepp Logan phantom, from which it is clear that a larger missing wedge causes missing details and more elongation in the vertical direction.

**Single tilt axis acquisition**

A single tilt axis acquisition is the most general and most commonly used acquisition scheme. Hereby, the specimen is tilted around the eucentric axis of the microscope stage with a constant angular tilt increment over an as large as possible angular range. In some cases, a Saxton step increment[141], which corrects for thickness variations in slab geometries throughout the tilt series, is preferred. Here, a smaller step size at higher tilt angles is used to compensate for this uneven sampling due to thickness variations.

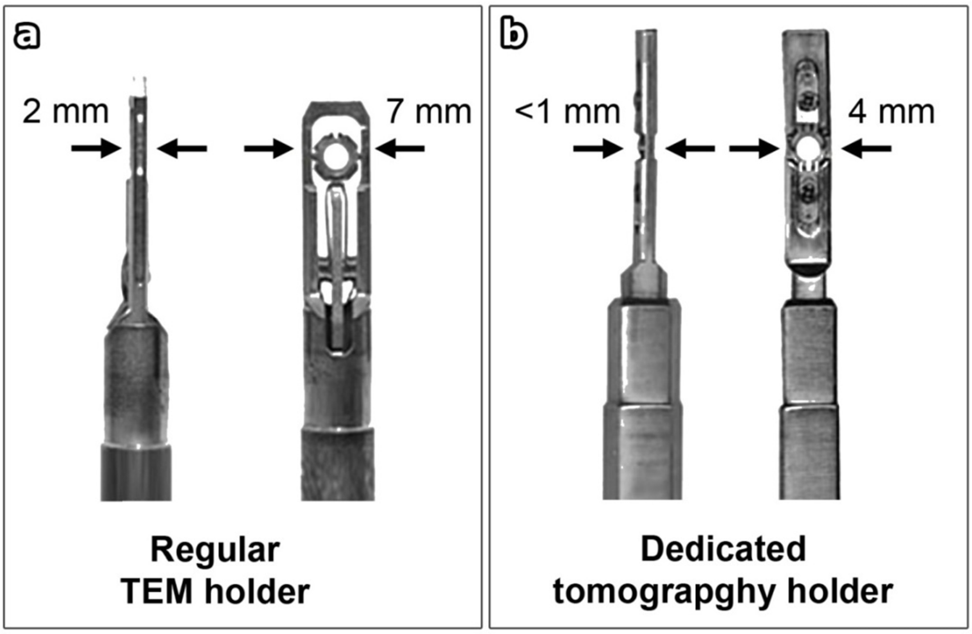

**Figure 2.10.** (a) Regular double tilt holder which can be tilted to approximately ± 40° between the polepieces of the electron microscope. (b) Dedicated tomography holder which can be tilted to ± 70° – 80°, due to the narrow tip of the holder.

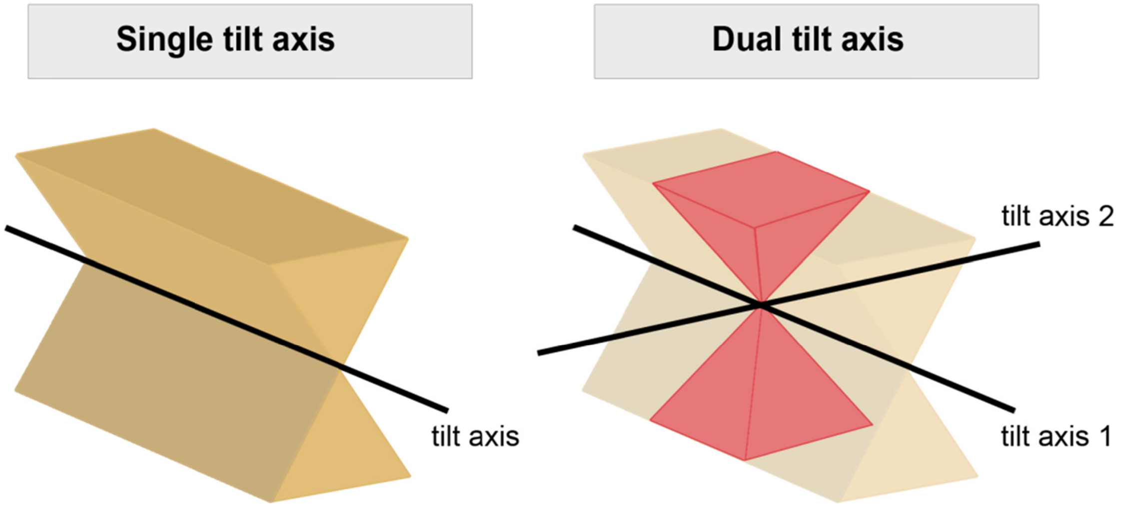

**Figure 2.11.** Representation of the missing wedge of information in the Fourier space for a single tilt axis and dual tilt axis scheme. The dual tilt axis geometry can be used to reduce the missing wedge to a missing pyramid.

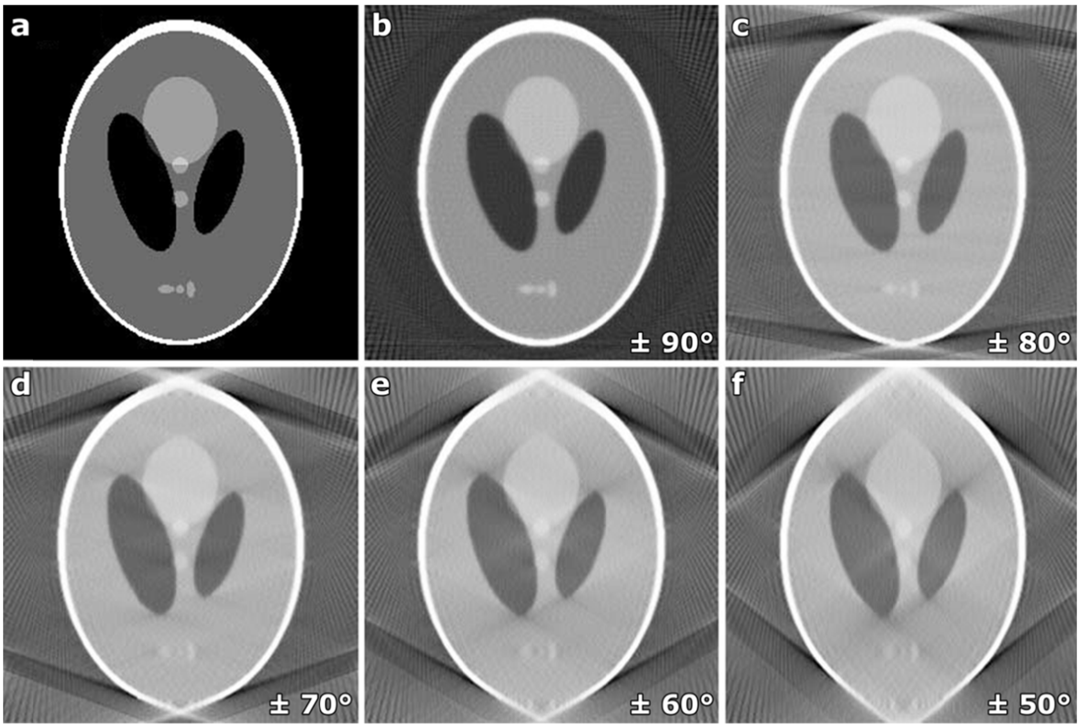

**Figure 2.12.** Visualization of the effect of the missing wedge on the Shepp Logan phantom image (a). A tilt series is simulated for the phantom image and a reconstruction is calculated using different missing wedges (b-f). An elongation in the vertical direction can clearly be detected in the images. The elongation increases with decreasing angular range of the tilt series.

### Dual tilt axis acquisition

Multiple tilt series of the same object can be used to reduce missing wedge artefacts in the final reconstruction[142,143]. When a dual tilt axis geometry is used, two tilt series of the same object are acquired. The tilt axis of the second tilt series is perpendicular to the tilt axis of the first tilt series, which is represented in Figure 2.11. From this Figure, it is also clear that the missing wedge of information in Fourier space is reduced to a missing pyramid. However, the need for a longer total exposure time and the time-consuming alignment and reconstruction of such acquisition schemes make these schemes less favourable. In addition, the sensitivity of the specimen to the electron beam limits the applicability of the dual tilt axis acquisition as degradation of the specimen can occur. Therefore, only single tilt axis acquisition schemes are used in this thesis.

### On-axis tilt axis acquisition

A dedicated on-axis tomography holder has been developed to enable tilting of needle-shaped samples over a full tilt range of ± 180°. The possibility of acquiring a full range tilt series completely eliminates the missing wedge artefacts[144,145]. Such needle-shaped samples are prepared by focused ion beam (FIB) milling and afterwards the sample is mounted on the dedicated rod-shaped on-axis tomography holder. The quality of the 3D reconstruction will improve due to the elimination of any missing wedge artefacts. However, the technique remains less popular as the sample preparation is challenging, especially to prepare needle-shaped samples for nanoparticles[146].

### 4.1.3. Automated acquisition

The acquisition of a tilt series requires a number of steps, which can be performed by the use of an automated acquisition software. It is important that the specimen is positioned at the correct eucentric height beforehand, to minimize the movement between successive tilt angles as tilting the dedicated holder results in a movement of the imaging field. It is however impossible to completely avoid these shifts, therefore a correction for these small shifts is necessary to track the investigated nanostructure and keep it in the field of view during the acquisition. The correction is calculated by cross correlation methods and a band-pass filter can be applied to enhance the success of a reliable correction. A detailed description of the cross correlation will be explained in the following section. After centering the region of interest, the image needs to be focused. During the focus procedure implemented in the automated software, several images are acquired at different focus values. The variance in each image is measured and the image with the maximum variance is finally acquired as it holds the optimal focus. After the acquisition, the sample is tilted to the next tilt angle and the previous steps are repeated. Performing such an automated acquisition requires a careful choice of different parameters such as acquisition time for the different steps (tracking, focus, and final acquisition), focus interval and step size, image filters, maximum tilt angle and other parameters that are used during the acquisition process. These parameters should be optimized for each individual experiment as the automated acquisition needs to be finalized before beam damage occurs. Different types of automated acquisition software have been developed over the last years[100,147–149]. Here, the Xplore3D program from the FEI Company was used for the acquisition of the tilt series.

### 4.2. Alignment of the tilt series

During the acquisition of the tilt series, the dedicated tomography holder needs to make a mechanical rotation of a few degrees. With this rotation of the holder, a shift in the field of view will occur. The specimen is tracked back into the field of view at each tilt angle, which will induce local shifts between successive images. These relative shifts are measured and corrected for in the whole tilt series during the alignment. In practice, the shifts are measured by calculating the normalized cross correlation image between two succeeding projection images, which is illustrated in Figure 2.13. Such a cross correlation image is formed by calculating the inverse Fourier transform of the product of the Fourier transform of the first projection image and the complex conjugate of the Fourier transform of the second projection image. The position of the maximum intensity in this cross correlation image presents the relative shift between the two original projection images. As the two projection images are acquired at two different tilt angles, the correlation will not completely coincide. In order to improve the determination of the peak position, band-pass filters and morphological filters may be

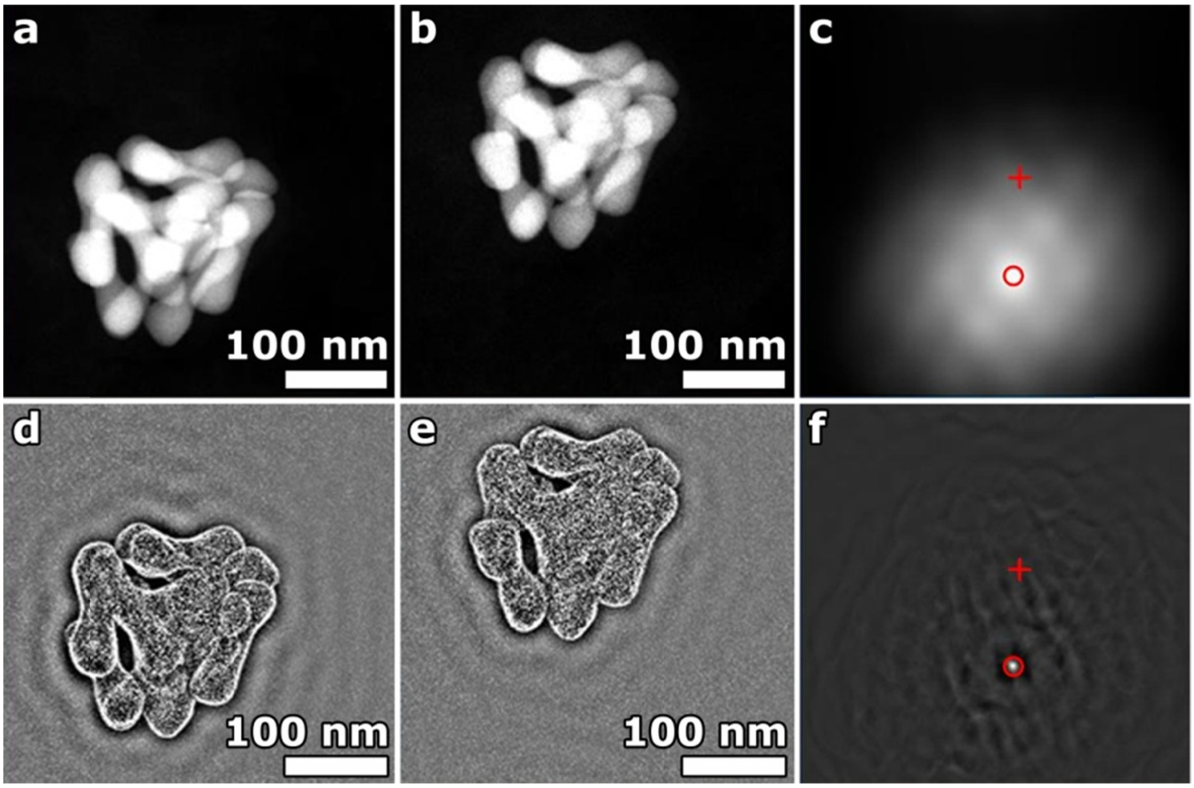

**Figure 2.13.** The position of the maximum intensity in the cross correlation image (c) of two successive projection images of an assembly of Au dumbbells (a and b) is indicated by a red circle. The position resembles the relative shift between the two projections. The use of a band-pass and a morphological filter enhances the image features in the projection images (d and e) and improves the location of the maximum in the resulting cross correlation image (f).

applied to the original projections (Figure 2.13.d and e). In this manner, a lack of projection images can also complicate the alignment procedure as two successive images will differ greatly.

In a second step, the direction of the tilt axis is estimated so that the tilt axis corresponds to the original tilt axis of the experimental tilt series during the acquisition. The tilt axis is shifted and rotated in order to minimize the arc shaped artefacts in the final reconstruction[125]. In this thesis, the alignment was mostly performed in a commercial program, Inspect3D. For more challenging tilt series, a manual tilt alignment can be applied using the Midas software.

## 4.3 Reconstruction of a tomographic tilt series

### 4.3.1 Theory behind tomography

#### The Radon transform

In the remainder of this chapter, the mathematical principles of electron tomography are explained by considering a 2D object and its 1D projections. The extension to a 3D object is straightforward since a 3D object can be regarded as a set of independent 2D slices.

The Radon transform, which was introduced by Johan Radon in 1917, forms the basis of the mathematical principles for most tomographic techniques[112,150,151]. This transform describes the projection of an object $f(x,y)$, which is equivalent to a line integral through $f$ by a Radon transform $R$, as:

$$Rf = F(t,\theta) = \int_L f(x,y)ds\,, \tag{2.6}$$

where the function $f$ is integrated along $L$ with respect to line length. The $(t,\theta)$-coordinates of the Radon transform of function $f(x,y)$ represent the projection angle $(\theta)$ and the distance of the projection line from the origin $(t)$. Figure 2.14 shows examples of a sphere (Figure 2.14.a) and a set of shapes (Figure 2.14.b) and their Radon transforms. A set of projections is also referred to as a sinogram. By taking the inverse Radon transform of the projections, the reconstruction of the object $f(x,y)$ can be retrieved. However, the inverse Radon transform is an integral transform, which requires an infinite number of projection images. As an infinite collection of projection images is experimentally impossible, this technique cannot be used in a straightforward manner on experimental data. Furthermore, this procedure can only be applied on parallel beam geometries as it utilizes a transformation along parallel lines. Due to these constraints, other reconstruction procedures were explored.

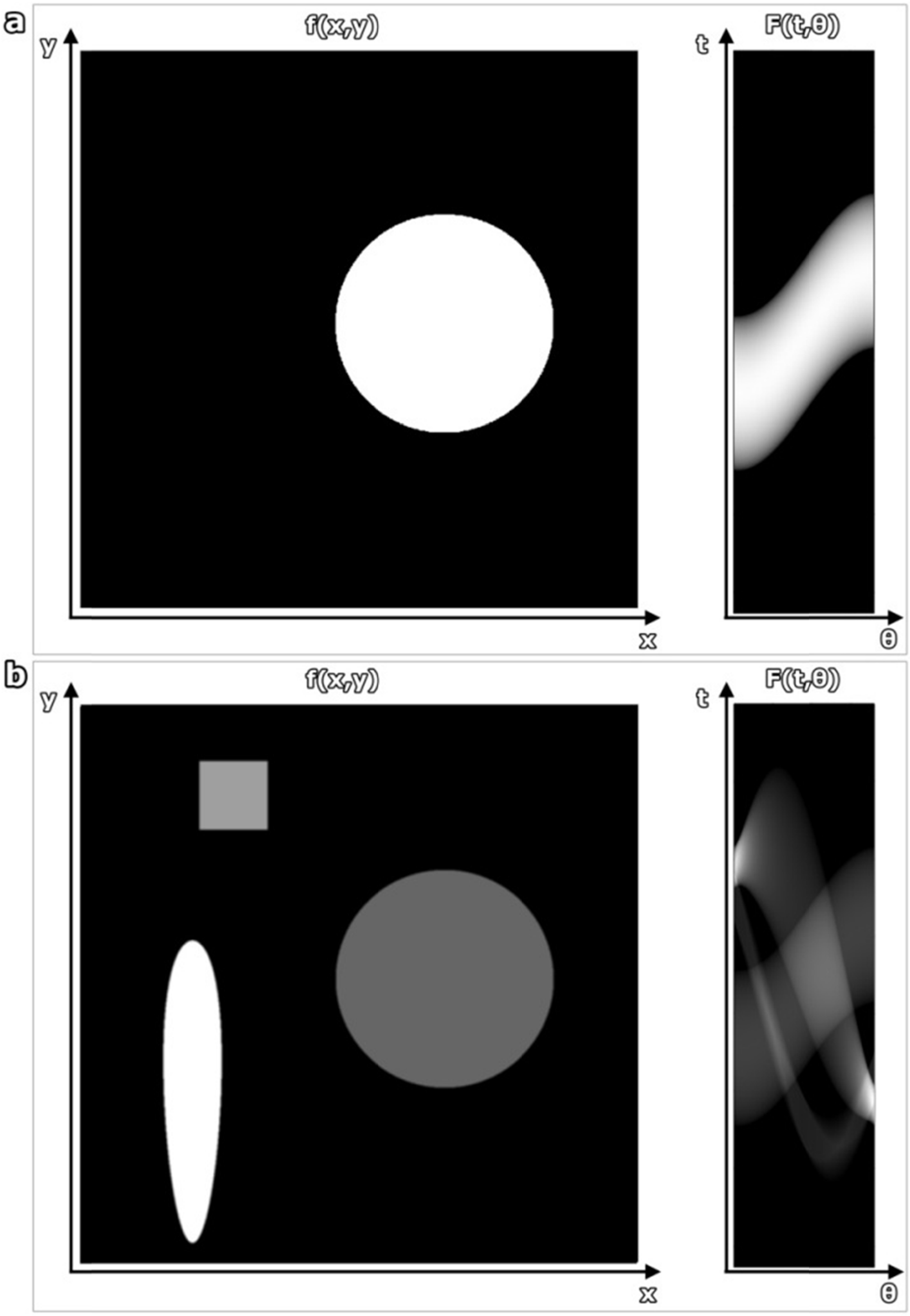

**Figure 2.14.** (a) Image of a sphere and its Radon transform. (b) Image of multiple shapes (sphere, rod and cube) and its Radon transform.

### Fourier slice theorem

The Fourier slice theorem describes the relationship between the projections in real space and Fourier space. It states that the 1D Fourier transform of a projection of a 2D object is equal to a line through the 2D Fourier transform of that object. The line crosses the origin of the Fourier space and its direction is perpendicular to the projection direction. The Fourier slice theorem is illustrated in Figure 2.15.

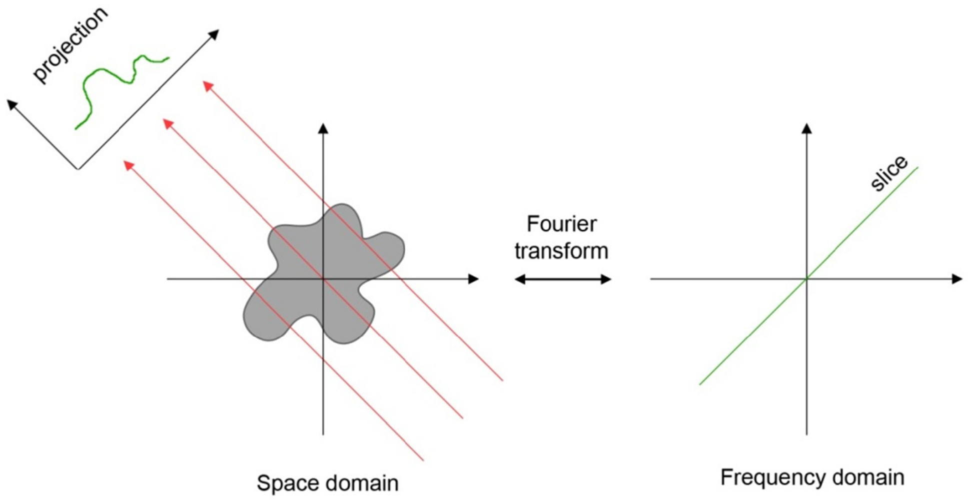

**Figure 2.15.** Illustration of the Fourier slice theorem which states that a projection at a certain angle at the space domain corresponds to a central section through the Fourier transform of that object.

The proof of the Fourier slice theorem is straightforward when a 2D object $f(x, y)$ and its projection along the $y$ direction are considered. The derivation however can be extended to higher dimensions as well. The projection through the 2D object can be described as:

$$p(x) = \int_{-\infty}^{+\infty} f(x, y) dy \tag{2.7}$$

The Fourier transform of the object $f(x, y)$ is defined as:

$$F(u, v) = \int_{-\infty}^{+\infty} \int_{-\infty}^{+\infty} f(x, y) e^{-2\pi i(xu+yv)} dx dy \tag{2.8}$$

Choosing the slice perpendicular to the projection direction ($v = 0$) through this Fourier transform is then given by:

$$F(u,0) = \int_{-\infty}^{+\infty} \left[ \int_{-\infty}^{+\infty} f(x,y)dy \right] e^{-2\pi i(xu)}dx \tag{2.9}$$

$$= \int_{-\infty}^{+\infty} p(x)e^{-2\pi i(xu)}dx \tag{2.10}$$

which equals the Fourier transform of the measured projection $p(x)$. When the proof needs to be generalized for an arbitrary direction, a rotation of axes needs to be included. By summing all the lines through the Fourier space of the object and calculating its inverse Fourier transform, a reconstruction can be obtained. However, it is not possible to sample over the full Fourier space because only a finite number of projections can be obtained in practice. As the projections are acquired at discrete angles, there are regular gaps in the Fourier space, which will hamper a perfect reconstruction of the investigated object. Additionally, this approach will lead to blurry reconstructions due to low frequency oversampling in Fourier space, which is illustrated in Figure 2.16. The overestimation of the low frequencies can be compensated by using a weighting filter. The most commonly used filters are Hamming or Hann filters[152,153] (Figure 2.17), which are more advantageous than a ramp filter. These filters simultaneously compensate for oversampling of the low frequencies and reduce the noise stemming from the higher frequencies. It must be noted that here an interpolation in Fourier space is required due to its radial symmetry to reconstruct the object. The interpolation becomes problematic when only a limited number of projections is used, which is the main reason that this approach becomes less popular in practical tomography applications.

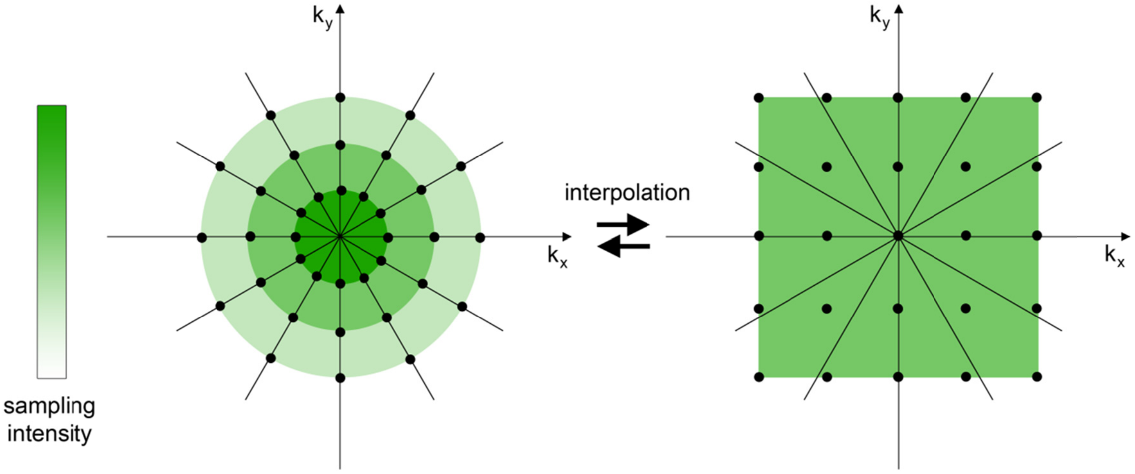

**Figure 2.16.** Due to the radial acquisition geometry, low frequencies will be oversampled in the Fourier space of the object in comparison to higher frequency values, which can be visualized by the closely packed black dots of the dark green circle close to the center of the Fourier domain. To convert this radial lattice to a Cartesian grid an interpolation is required before the inverse Fourier transform can be calculated.

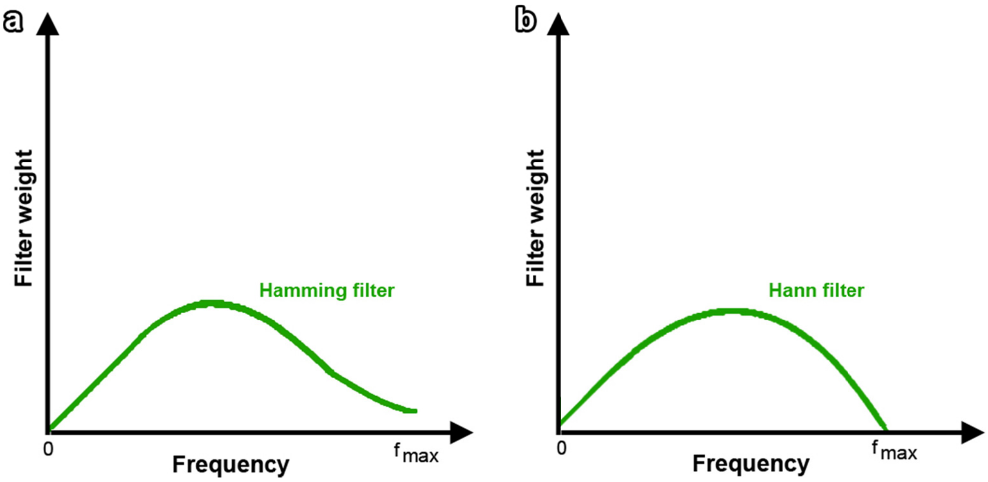

**Figure 2.17.** (a) Hamming and (b) Hann weighting filters to compensate the oversampling at the lower frequencies and to reduce the noise present in the high frequencies.

### 4.3.2. Modern reconstruction techniques

#### Filtered back projection

The filtered back projection (FBP) technique is an analytical reconstruction technique where the acquired projection images are convoluted with a weighting filter and afterwards reprojected in their original projection directions[154]. The weighting filter reduces blurring in real space due to an uneven sampling of the spatial frequencies in Fourier space, which was explained in the previous section. This technique provides reliable results when a lot of projection images are obtained over a large tilt range. Therefore, the technique is nowadays standardly used for X-ray tomography. However, only a limited number of projection images are acquired over a limited tilt range during an electron tomography experiment, which makes the use of the FBP technique less accurate and thereby less favourable. Additionally, the presence of noise in the individual projection images further complicates the reconstruction process. As a result, iterative reconstruction techniques have been developed as they are more robust to noise and do not require an infinite number of projection images. Nowadays, such algorithms are commonly used for electron tomography investigations in materials science.

#### Simultaneous iterative reconstruction technique

The simultaneous iterative reconstruction technique (SIRT) is based on the Riemann back projection principle[151]. In the first step, the preliminary reconstruction is obtained by a regular back projection reconstruction. Next, this first reconstruction is reprojected along the original tilt directions which were used during the acquisition of the tilt series. These reprojections are then all compared simultaneously to the original acquired projection images. The difference or ratio between them is calculated for an additive SIRT algorithm (aSIRT) or a multiplicative SIRT algorithm (mSIRT), respectively. A reconstruction of the result is obtained and added (aSIRT) or multiplied (mSIRT) to the previous reconstruction. The final reconstruction is obtained in an iterative manner until convergence is reached. The number of necessary iterations is highly influenced by the presence of noise in the projection images and needs to be adjusted independently for each tomography experiment[155].

When approaching the SIRT algorithm in a more mathematical manner, the following projection equation needs to be addressed:

$$W\boldsymbol{x} = \boldsymbol{p} \tag{2.11}$$

where $W$ is the projection matrix, $\boldsymbol{p}$ are the projections and $\boldsymbol{x}$ is the investigated object. The projection geometry for a tomographic experiment is schematically shown in Figure 2.18.

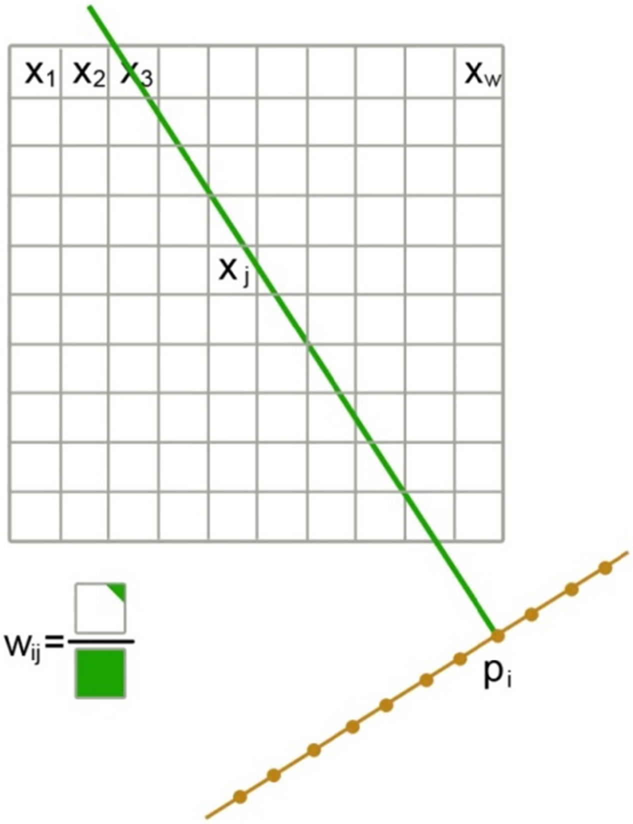

**Figure 2.18.** Projection geometry for a tomographic experiment. The vector $\boldsymbol{x}$ represents the imaged object. The element $w_{ij}$ of the weight or projection matrix $W$ equals the contribution of element $x_j$ to the recorded projection intensity $p_i$.

It is however not straightforward to solve this equation as it is underdetermined due to the limited number of projection images. In addition, the projection matrix is often large and not sparse which makes a simple inversion to obtain a reconstruction impossible. By running the SIRT algorithm, the difference between the left hand side and the right hand side of the projection equation is minimized. This difference is also referred to as the "projection distance". The projection distance, when using aSIRT, is calculated by an iterative element wise update scheme where $x^k_j$ represents the current ($k^{th}$) estimate of the intensity of the $j^{th}$ pixel[156]:

$$\forall j: x_j^{(k+1)} - x_j^{(k)} = \frac{\sum_i \left[ w_{ij} \left( p_i - \sum_h w_{ih} x_h^{(k)} \right) \Big/ \sum_h w_{ih} \right]}{\sum_i w_{ij}} \qquad (2.12)$$

In this equation, $p_i$ represents the recording of the $i^{th}$ projection and $w_{ij}$ is the contribution of the $j^{th}$ voxel to the $i^{th}$ projection ray. The reconstruction of the projection distance is then calculated by performing an unfiltered back projection and added to the previous reconstruction. The final reconstruction is obtained by iterating this process until convergence is reached (Figure 2.19).

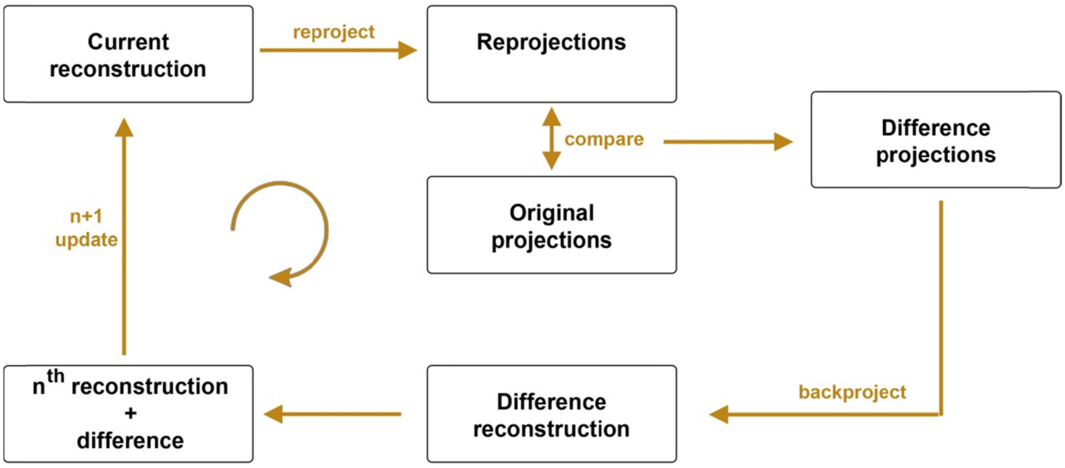

**Figure 2.19.** Schematic overview showing the principle of SIRT with n iterations.

### Total variation minimization technique

Recently, a lot of efforts were made to develop reconstruction techniques which reduce the missing wedge artefacts, which limit the quality of the final reconstruction. One of these new techniques is the total variation minimization (TVM) reconstruction technique[157,158]. TVM is an iterative technique which is based on the assumption that the reconstructed object has a sparse representation in the gradient domain. The reconstructed object itself is not sparse, but the gradient of the object needs to have sharp grey value transitions and is thereby sparse. The Shepp Logan phantom and its gradient image are shown in Figure 2.20. From this example it is clear that although the object itself is not sparse, the gradient is.

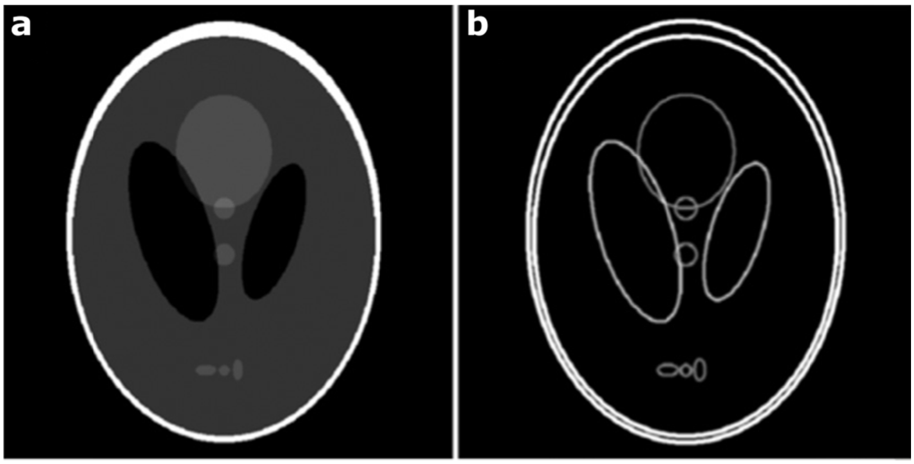

**Figure 2.20.** (a) Shepp Logan phantom object and (b) its gradient image. It is clear that the gradient image is a sparse representation of the original object.

The TVM algorithm finds the solution to the reconstruction problem, $W\boldsymbol{x} = \boldsymbol{p}$, where both the projection distance and the total variation are minimized. To retrieve the lowest total variation solution, the projection distance and the total variation of the reconstructed object are simultaneously minimized:

$$x = arg_x min\left[TV(x) + \frac{\mu}{2}\|Ax - b\|_2^2\right]$$

in which the total variation is computed as the norm of the discrete gradient of the reconstructed object and the projection distance is preceded by a regularization parameter $\mu$. A large value of $\mu$ will lead to a result which closely resembles a SIRT reconstruction and will thereby introduce noise and missing wedge artefacts in the final reconstruction. When $\mu$ is chosen too small, the high frequency details of the object will be lost in the reconstruction. Based on simulation studies, it was shown that $\mu = 0.5$ is considered as a good starting value[157]. Additional to the reduction of missing wedge artefacts, the segmentation of a TVM reconstruction can be performed in a more objective manner, in comparison to segmentations of FBP and SIRT reconstructions[159]. An explanation of the segmentation is given in the following section.

### 4.4. Visualization and quantification of a tomographic reconstruction

During the final step of an electron tomography experiment, a visualization and/or quantification of the 3D reconstruction is performed. To obtain a 3D visualization, three main techniques are often used: the isosurface, the voltex rendering and/or orthoslices. This last quantification step is far from straightforward and requires a segmentation of the reconstruction. During this segmentation, voxels with a certain intensity value are assigned to a specific class. It should be performed in a careful manner as an incorrect segmentation can lead to incorrect conclusions on the 3D character of the specimen under investigation.

#### 4.4.1. Isosurface rendering

An isosurface rendering corresponds to a surface from a specific 3D dataset obtained by connecting all the voxels which have an equal grey value. In this manner, the 3D volume is reduced to a 2D surface, which can easily be inspected along different viewing directions. Due to the data reduction, the calculation of an isosurface rendering only requires a few seconds. In Figure 2.21, an example of an isosurface rendering of an Au core / Ag shell nanostructure is presented.

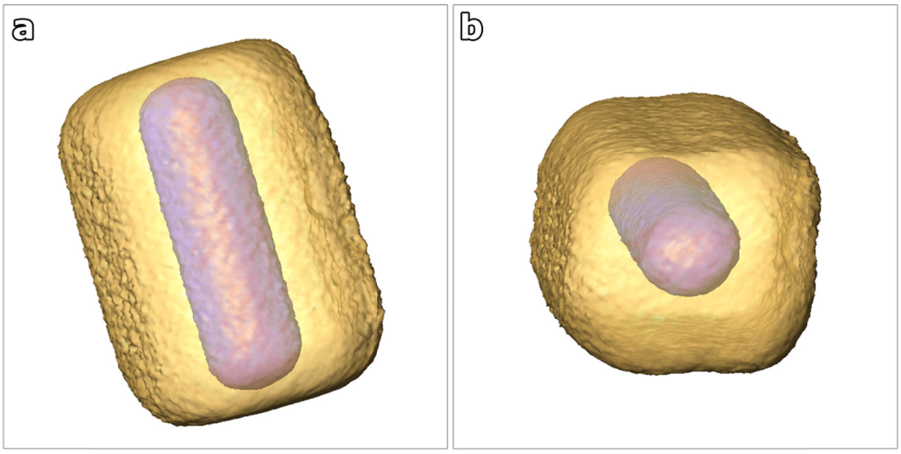

**Figure 2.21.** Isosurface rendering of an Au core / Ag shell nanostructure in two directions.

### 4.4.2. Voltex rendering

A voltex rendering of a reconstructed dataset reprojects the 3D dataset on the computer screen. The intensity, colour and transparency of this reprojected visualization can be adjusted for every voxel in the reconstructed volume. It allows us to highlight certain details in the reconstruction, which is an advantage in comparison to the isosurface rendering. A disadvantage of the voltex rendering is that this method is very time-consuming.

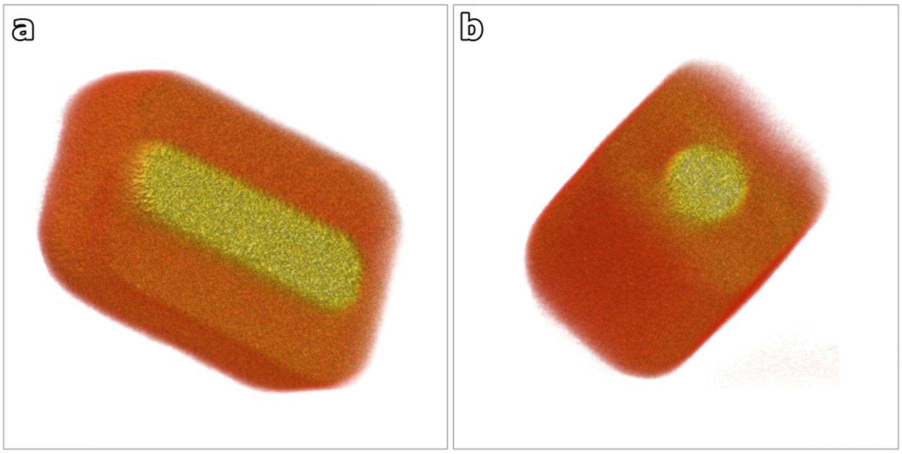

**Figure 2.22.** Voltex rendering of an Au core / Ag shell nanostructure in two directions, where it is clear that each voxel is visualized and not only the surface of the nanostructure.

### 4.4.3. Orthoslices

Performing an electron tomography experiment does not only enable us to study the 3D shape of the investigated nanostructure, but also allow us to investigate its internal structure. We can virtually slice through our object and study the inner structure in different directions (Figure 2.23). The visualization of orthoslices is the most objective visualization, in comparison to the rendering methods, as it does not require any parameter based calculation in which the parameter is chosen by the user.

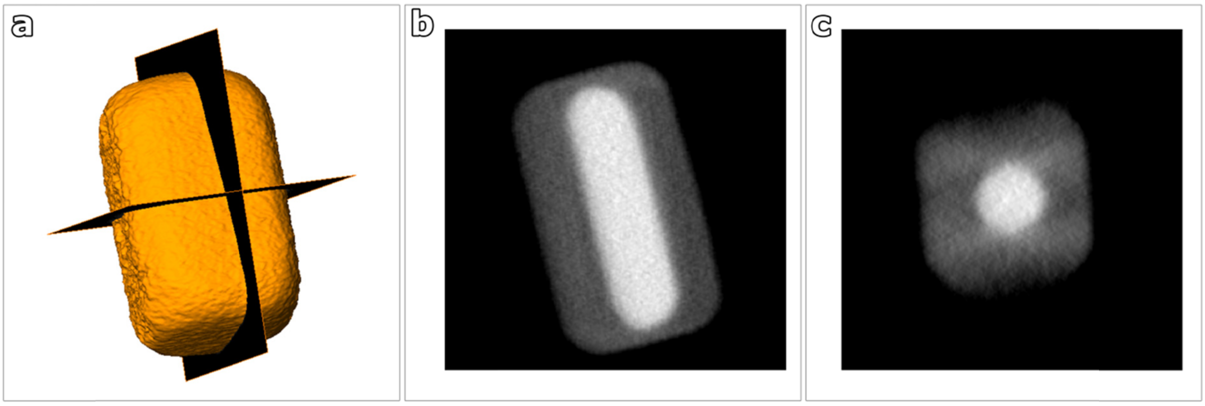

**Figure 2.23.** (a) The location of the two orthoslices (b, c) through the Au core / Ag shell nanostructure is visualized.

### 4.4.4. Segmentation

Quantification of a 3D volume of the reconstructed nanomaterial is based on the segmentation in which a range of voxels values is assigned to a specific class. If we are, for example, investigating a core/shell nanostructure, we would like to separate the core from the shell, which can be done with such a segmentation. The core voxels can be assigned to a first class and the shell voxels to another class. All the voxels in one class obtain the same value and a colour can be addressed to this class. A segmentation of different components in a material can be of great use when we want to investigate the volume of the different components. In the example in Figure 2.24, a first class contains the Ag shell voxels and a second class the Au core voxels. A visualization of both classes, Ag and Au, is shown in Figure 2.24.a and b, respectively.

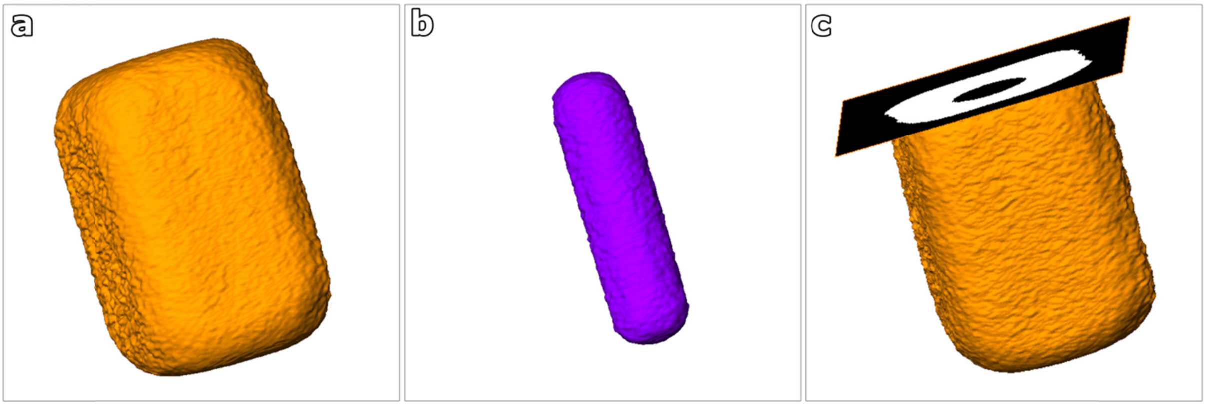

**Figure 2.24.** Segmentation of (a) the Ag shell and (b) the Au core. (c) An orthoslice through the Ag segmentation is shown to indicate that only the Ag voxels are classified and the Au voxels are not present in this segmentation.

An automatic segmentation based on thresholding at different grey levels yields reliable quantitative results in case of a full tilt series of projection images[128]. Artefacts caused by the missing wedge of information will influence the quality of the reconstruction and complicate a straightforward automatic segmentation. Therefore, a careful manual segmentation needs to be performed. However, such a manual segmentation is highly subjective and time-consuming. The use of more advanced reconstruction algorithms, such as TVM, will result in a more straightforward segmentation and quantification of the reconstructed datasets.

# Chapter 3

## Investigation of semiconductor nanoplatelets by 2D and 3D electron microscopy

This chapter is based on: Hutter, E. M., Bladt, E., Goris, B., Pietra, F., Van Der Bok, J. C., Boneschanscher, M. P., de Mello Donegá, C., Bals, S., Vanmaekelbergh, D. *Conformal and atomic characterization of ultrathin CdSe platelets with a helical shape.* Nano Letters, 14 (2015) 6257–6262.

Own contribution: Responsible for all the TEM acquisition and analysis.

## 1. Introduction

Nowadays, ultrathin colloidal CdSe semiconductor nanoplatelets and their optical properties, including high fluorescence quantum yield[34] and ultrafast fluorescence liftetime[40], are the subject of extensive research[37,160–164]. The development of 2D semiconductor nanostructures is of technological interest for the development of miniaturized electronic[165,166] and optoelectronic devices[167]. To implement these 2D structures efficiently in device fabrication, different synthesis procedures aim to obtain colloidal 2D structures with tunable lateral dimensions and preferably of a few hundred nanometers. Therefore, a structural characterization of the nanoplatelets is of key importance to evaluate the outcome of different synthesis approaches and guide those towards a desirable conformation. Here, we investigate ultrathin CdSe nanoplatelets with lateral dimensions in the order of tens of nanometer, which show a flat conformation. Next, the lateral dimensions of the ultrathin nanoplatelets are extended (in the order of hundreds of nanometer) but seem to lose their flat conformation[34,35,42,43,168]. Both types of CdSe nanoplatelets are studied in this chapter using 2D and 3D TEM.

## 2. CdSe flat nanoplatelets: 2D problem

In a first investigation, CdSe nanoplatelets with lateral dimensions in the order of tens of nanometer were studied by TEM. A commonly used synthesis technique was proposed by Itthuria *et al* [34] in which Cd myristate and a powder of Se in octadene are mixed and heated at 240°. When 180° is reached, an acetate salt is added and CdSe nanoplatelets form with {001} basal facets. The acetate salt is required for the formation of 2D CdSe nanostructures[34]. The final geometry of the nanoplatelets can be tuned to different morphologies using different acetate salts, as they have different ionizing capacities. Therefore, the acetate ion will have different binding properties and favour the growth of specific types of crystal facets. The aim of these synthesis methods in solution is to develop techniques which are easily processable and reproducible. The synthesis of nanoplatelets which are monodisperse in thickness, lateral dimensions, crystal structure and surface facets are favoured, as it confirms the high level of control of the synthesis procedure. Here, the effect of Cd acetate and Na acetate on the growth of the nanoplatelets is evaluated. The questions which need to be resolved in order to fully characterize these platelets are:

1. Which surface facets are favoured when using specific acetate salts during the growth reaction?
2. How uniform are the obtained surface facets?
3. What is the thickness of these ultrathin nanoplatelets?

To answer these different questions, the nanoplatelets, produced with the use of these different acetate salts, are studied by TEM and the synthesis methods are evaluated based on the diversity in the synthesized nanostructures.

## 2.1. Facet determination

We will investigate the type of surface facets for two main reasons. The determination of the types of surface facets is of key importance in order to control and understand the growth process of the nanoplatelets. In addition, synthesis methods aim for the production of nanoplatelets with specific types of surface facets, as they influence the selectivity towards ligand binding. The acetate salt, which is used during the growth process, will selectively bind to certain types of facets and therefore their further growth will be hindered, resulting in the growth of the other specific type of facets. This kind of selective growth of facets can contribute to the synthesis of certain anisotropic hetero-nanostructures for example CdSe/CdS or CdSe/PbSe, which are optoelectronically important materials. Additionally, monodispersity is required as this confirms a high level of control of the synthesis.

The colloidal CdSe nanoplatelets are synthesized in solution, which is dropcasted onto a carbon-coated support grid in order to investigate the structures by TEM. As a result, the CdSe nanoplatelets mostly spread out flat on the TEM grid, as visualized in Figure 3.1. In this manner, the surface facets can be investigated in a rather straightforward manner by 2D TEM.

By analyzing the Fourier transform of high resolution HAADF-STEM images, both the lateral facets and the crystal structure can be identified. In Figure 3.2, high resolution HAADF-STEM images acquired along the basal planes of CdSe nanoplatelets ([001] direction) synthesized using Cd acetate are visualized. The nanoplatelets have either a rectangular (Figure 3.2.a and b) or a truncated rectangular shape (Figure 3.2.c and d). The fourfold symmetry of the diffraction patterns, shown in the insets, confirms that the nanoplatelets have a zinc blende structure and the presence of {001} basal facets. Further analysis confirms that the nanoplatelets exhibit different types of lateral surface facets: {100} and {110} facets.

The rectangular nanoplatelets exhibit different types of surface facets, both {100} and {110} facets. The truncated rectangular nanoplatelets are build-up by a combination of {100} and {110}. The observed lateral facets are not atomically sharp, however this could be caused by the interaction with the electron beam. Indeed, since the nanoplatelets are ultrathin, they tend to degrade under the electron beam. This degradation starts at the edges of the nanoplatelets.

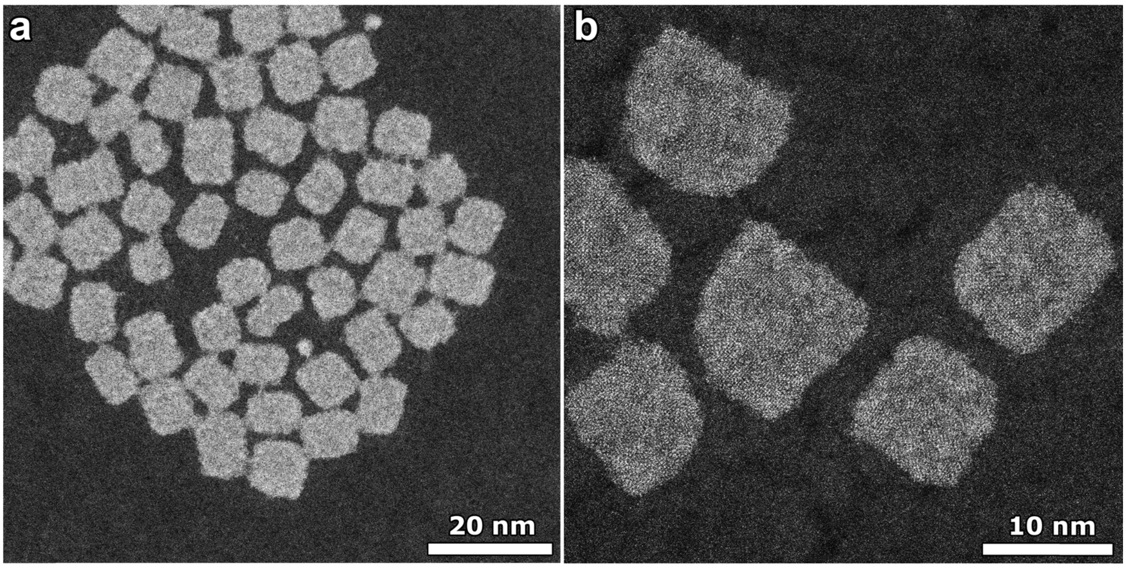

**Figure 3.1.** (a,b) Overview HAADF-STEM images of Cdse nanoplatelets. It can be observed that the ultrathin platelets tend to dry flat onto the TEM support grid.

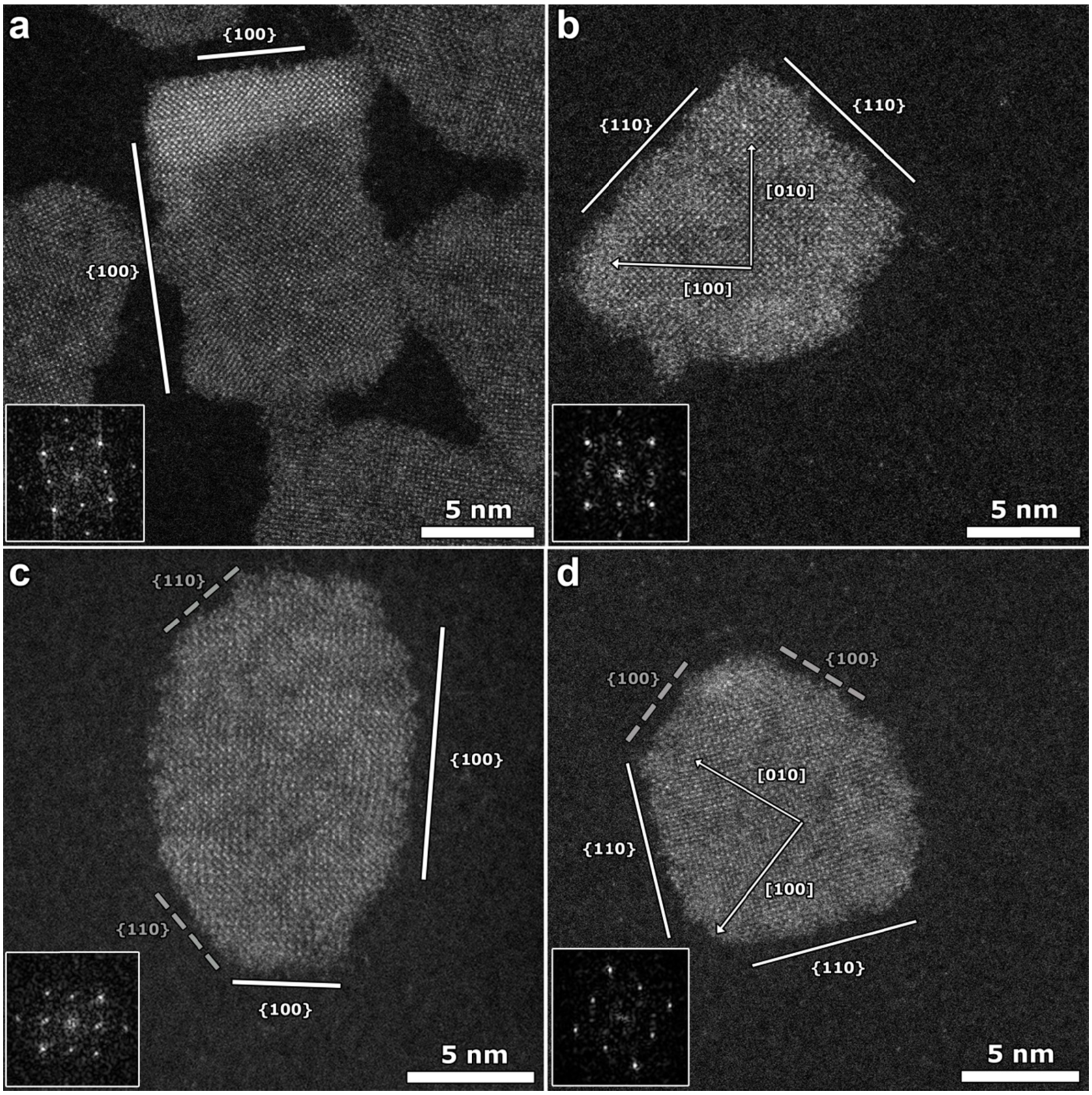

**Figure 3.2.** CdSe nanoplatelets synthesized in the presence of Cd acetate with different surface facets: (a) {100}, (b) {110} and (c, d) a combination of both {100} and {110} facets.

From this visual inspection, we can already state that the nanoplatelets synthesized using Cd acetate do not have a uniform shape or type of surface facet. To investigate whether the use of Cd acetate in the synthesis favours the growth of specific lateral facets, the facets of 80 nanoplatelets were examined by high resolution HAADF-STEM. We found that 54% of the nanoplatelets have {100} as main edges whereas 46% have {110} edges (Figure 3.3.a). We thus conclude that when Cd acetate is used, both facets grow together, as they have comparable stability, which leads to polydiverse nanoplatelets regarding shape and surface facets.

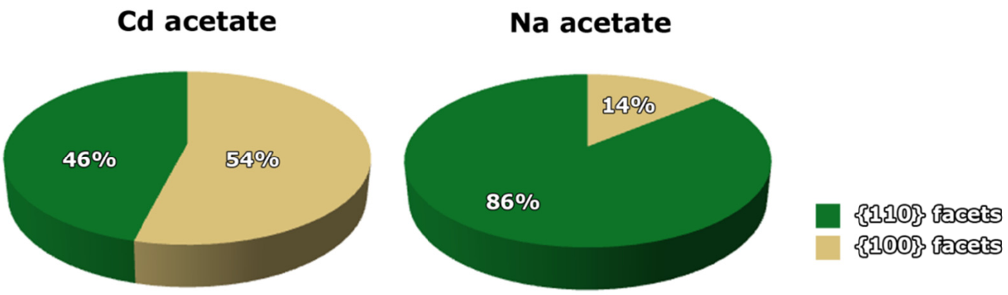

**Figure 3.3.** Graph of the surface facets of the CdSe nanoplatelets, synthesized by two different methods: in the presence of Cd or Na acetate.

Since Cd acetate does not yield monodisperse types of surface facets, the use of another acetate salt is evaluated as it determines the obtained facets. By replacing Cd acetate by Na acetate, the aim is to reduce the diversity of the types of lateral surface facets of the CdSe nanoplatelets. The nanoplatelets developed with this synthesis method are visualized in Figure 3.4. The images are all acquired along the [001] direction, which indicate the presence of {001} basal facets. Additionally, these images show that the nanoplatelets exhibit different types of lateral surface facets. To determine whether a certain type of surface facet is favoured, 43 nanoplatelets were investigated by high resolution HAADF-STEM. The result is visualized in Figure 3.3.b. We found that 86% of the nanoplatelets has a very well pronounced rectangular shape and prominent {110} facets. The minority of the nanoplatelets (14%) exhibits both {100} and {110} facets, an example is shown in Figure 3.4.c. From this statistical analysis we can conclude that, in the presence of Na acetate, {110} facets are the most stable type of facet, which is formed of a mixture of Cd and Se atoms. The CdSe nanoplatelets are more uniform in comparison to the procedure in the presence of Cd acetate, as indicated in the graph in Figure 3.3.

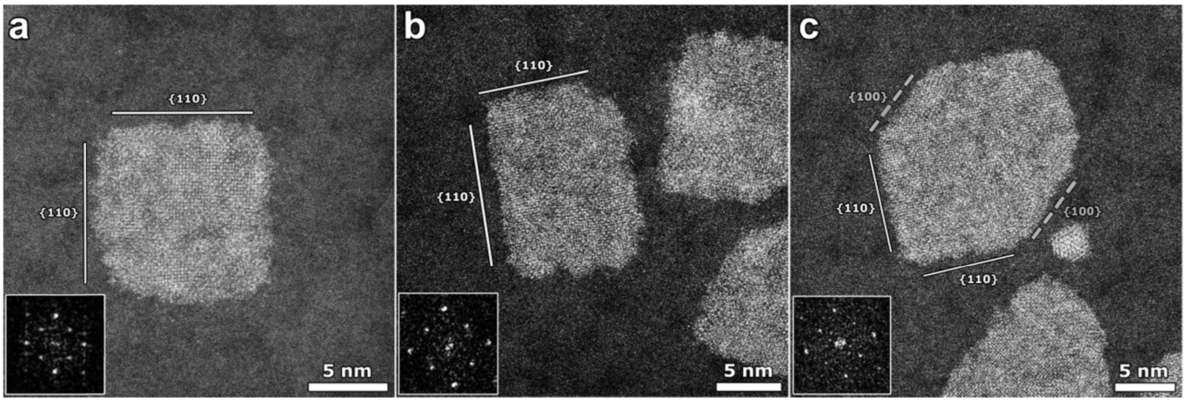

**Figure 3.4.** High resolution HAADF-STEM images of CdSe nanoplatelets synthesized in the presence of Na acetate with (a, b) {110} facets and (c) a combination of both {100} and {110} facets.

By TEM, we could determine the effect of the acetate salt on the type of surface facets, but the exact role of the acetate salt remains a topic of debate, as there is even no general consensus on its role[43]. In this case, the two acetate salts have different ionizing capacities, where Na acetate will produce more acetate ions in comparison to Cd acetate. Therefore, the selective binding of the acetate is possible in case of the Na acetate, which is less probable for Cd acetate. Hence, shape control during the growth is possible with Na acetate and less with Cd acetate as there is less selectivity and therefore different types of surface facets grows equally. The presence of {001} basal surface facets and {110} lateral surface facets, however, make these CdSe nanoplatelets suitable for the growth of anisotropic hetero-nanostructures. Since, the optical properties of core-only semiconductor nanostructures are greatly improved when a semiconductor hetero-nanostructure is grown as a shell or anisotropically[45,46], core/shell nanostructures are of high interest. As two types of surface facets are present, certain ligands will bind selectively to one or the other type of facet, guiding the growth process in the lateral or basal direction. A successful growth of a CdS or CdZnS shell around a CdSe nanoplatelet has been reported by Mahler *et al* [44].

### 2.2. Thickness determination

The optical properties of the CdSe nanoplatelets are mainly dependent on the thickness, therefore a high level of control is of key importance. In order to answer question 3, electron tomography is, in principle, the ideal technique since a 3D reconstruction allows us to study the thickness of these nanoplatelets. However, due to the sensitivity of the ultrathin nanoplatelets towards the electron beam, it was not possible to acquire a reliable tilt series.

After a careful observation of the nanoplatelets on the support grid, some standing nanoplatelets were found. These standing nanoplatelets enable a direct visualization of the thickness as observed in Figure 3.5. These two standing CdSe nanoplatelets are synthesized in the presence of Na acetate. The integrated line profiles in the inset show that both nanoplatelets consist of six Cd atomic planes. A distinct intensity decrease can be observed in the inset of Figure 3.5.b, which is caused by the degradation at the edges of the nanoplatelet.

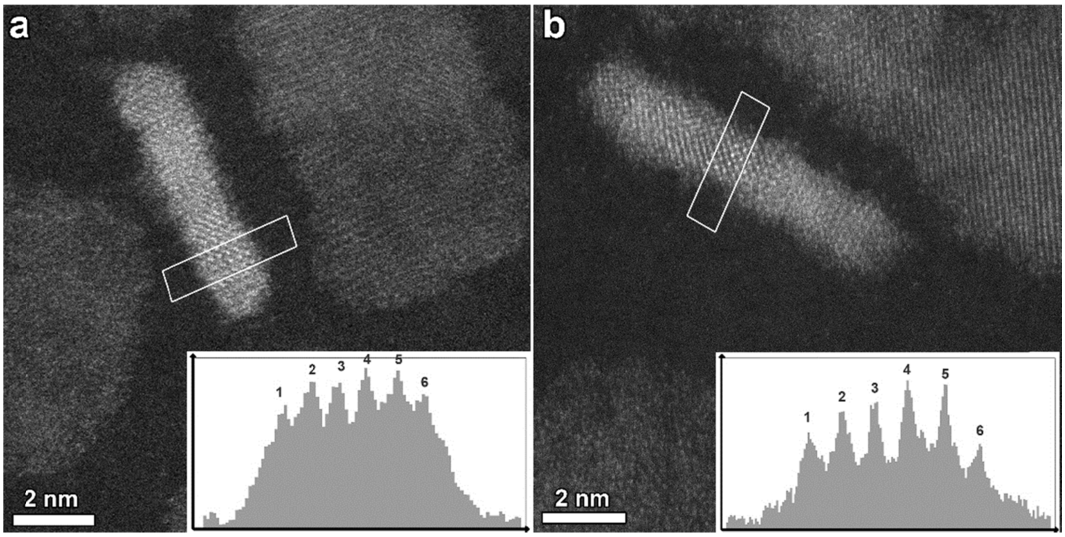

**Figure 3.5.** High resolution HAADF-STEM images of standing CdSe nanoplatelets, from which the atomic thickness can be studied. The nanoplatelets have a thickness of six Cd atomic layers.

# 3. CdSe nanohelices: 3D problem

The applicability of 2D nanoplatelets in diverse applications drives their synthesis from nanoplatelets to nanosheets with large lateral dimensions. Recently, such ultrathin colloidal CdSe nanoplatelets with large lateral dimensions and a uniform thickness, controllable up to the atomic scale, were prepared. Such nanoplatelets often form scrolls of a few nanometers in diameter[34,35,169,170,168]. In order to evaluate the native conformation, when suspended in the organic solvent, of these nanoplatelets and to understand the structure-property relation, HAADF-STEM is used to reveal their native morphology and atomic arrangement. Therefore, a number of questions need to be resolved:

1. Is the rolled-up morphology the native state of these nanoplatelets?
2. Can we measure the thickness of these nanohelices?
3. How are the nanohelices folded from a rectangular sheet into a helix?
4. Are both left- and right-handed helices present? Or is there a preferential helicity?

## 3.1. Native state

As the conformal state of these CdSe nanoplatelets has not yet been precisely determined, it remains unclear whether this rolled-up conformation is their native state (in the organic solvent). When conventional TEM or STEM techniques are used, the colloidal suspension is dropcasted on a support grid and drying effects can alter the conformation of the nanoplatelets. Therefore, the nanoplatelets were investigated by cryo-TEM as rapid freezing of a colloidal suspension should reveal the native morphology of the suspended nanoplatelets.

To perform a cryo-TEM study, the nanoplatelets are encapsulated in a thin layer of vitreous ice. The freezing procedure takes place fast and at very low temperatures, initiating an instantaneous freezing of the solution that inhibits any structural change. In this manner, the freezing procedure will encapture the nanoplatelets in their native state as illustrated in Figure 3.6 and the helical shape of the nanoplatelets was confirmed. This helical conformation is however not ideal for its applicability in certain devices, as the use of nanosheets is preferred. We believe that a complete characterization of

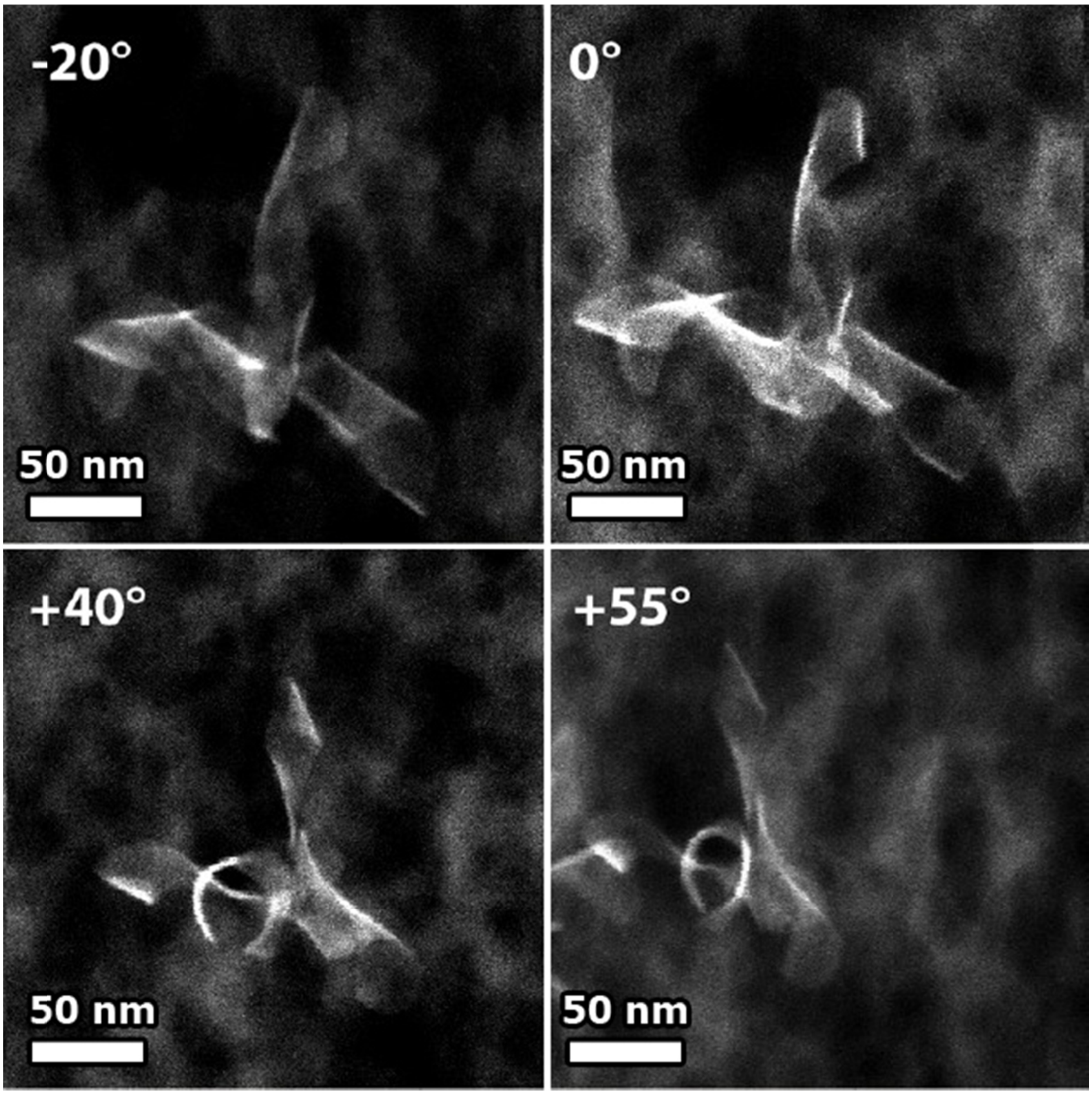

**Figure 3.6.** Cryo-TEM images of a group of CdSe nanoplatelets acquired at different angles.

these nanohelices is of large importance for the further processing of suspensions of 2D semiconductors into material systems and for further understanding of their optical properties. Unfortunately, cryo-TEM is less suitable to study the nanohelices in detail as the spatial resolution is hampered by the thickness of the ice layer and the low dose imaging conditions, which are required to maintain the ice layer. Additionally, by dropcasting the colloidal suspension on a support grid, drying effects can alter the native conformation of the nanoplatelets. With this in mind, the CdSe nanoplatelets were incorporated in an amorphous silica shell using the reverse water-in-oil microemulsion method[171–176], which immobilizes their conformation. We will first study the effect of a rigid silica shell on the native morphology of the nanoplatelets to ensure that the growth of such a shell does not change the morphology of the platelets. HAADF-STEM images in Figure 3.7.a-c show that the helical shape is perfectly preserved if the nanoplatelets are coated with silica inside a microemulsion with 29.9 wt % ammonia in the aqueous phase. One can observe that the nanoplatelets are rolled-up, but the type of helicity cannot be identified from these 2D images (Figure 3.7.a-c). We can however already observe that the nanoplatelets in Figure 3.7.a and in 3.7.c have a different morphology. As the silica shell is quite thick (up to 20 nm) under these growth conditions, relatively mild conditions (3.0 wt % ammonia) were also used to coat the helical nanoplatelets with an ultrathin uniform silica shell to facilitate the characterization study of the CdSe nanoplatelets. From Figure 3.7.d it is clear that the native helical shape is still preserved under these mild conditions. Interestingly, if the incorporation process is slowed down even more (1.5 wt % ammonia), the nanoplatelets are flattened after encapsulation in silica (Figure 3.7.e).

In general, the growth of a silica shell is not expected on a facet that is completely Se-terminated, since the negatively charged silica precursor preferentially attaches to Cd[177]. Considering that the initial growth is based on surface attachment of the negatively charged silica precursor[176], the growth of a silica shell on both sides indicates that Cd atoms should be accessible for the silica precursor both on the inner and the outer surface. In this respect, a rearrangement of the atoms on the Se-terminated surface is required[169]. We believe that the change in surface energy resulting from this surface rearrangement is the cause of the observed helix conformation. Therefore, the observation that both the inside and the outside of the helical nanoplatelets are covered with silica indicates the accessibility of Cd on both these facets. It is clear that also for the CdSe nanoplatelets, grown at 3.0 wt % ammonia conditions, both the inner and the outer facet of the nanoplatelet are covered with a silica shell, which is visible in Figure 3.8. From this image, it can be concluded that the silica shell is between 1 and 2 nm thick. Further investigations are focused on ultrathin CdSe helical nanoplatelets, grown at 3.0 wt % ammonia conditions.

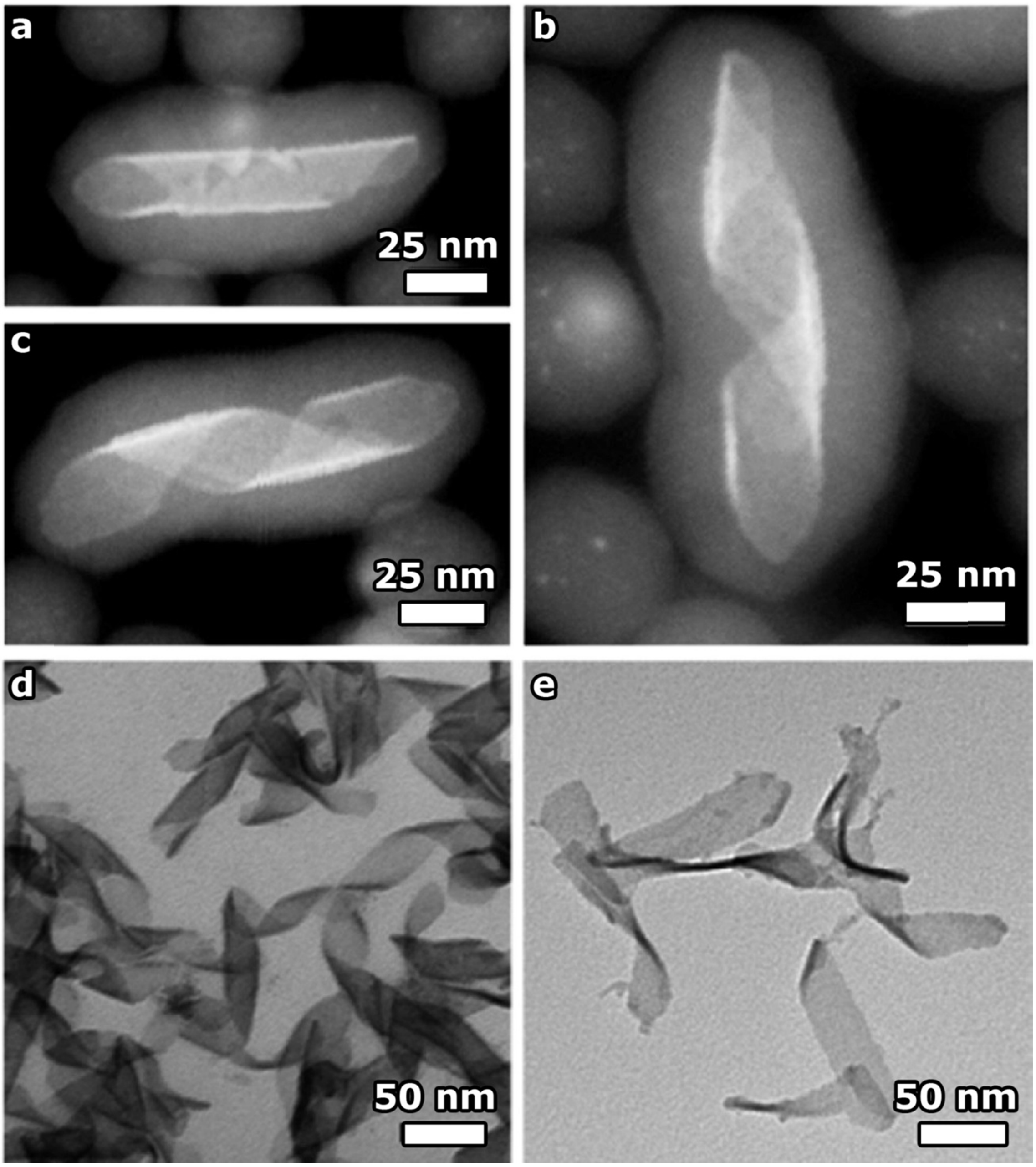

**Figure 3.7.** Images of CdSe nanoplatelets coated with silica shells of different thickness. (a-c) HAADF-STEM images of silica-coated CdSe nanoplatelets, quenched after 1 day of silica growth in a microemulsion to which 29.9 wt % ammonia was added. (d,e) TEM images of CdSe nanoplatelets coated with silica in a microemulsion with 3.0 wt % (d) and 1.5 wt % (e) ammonia, quenched after 3 h of growth.

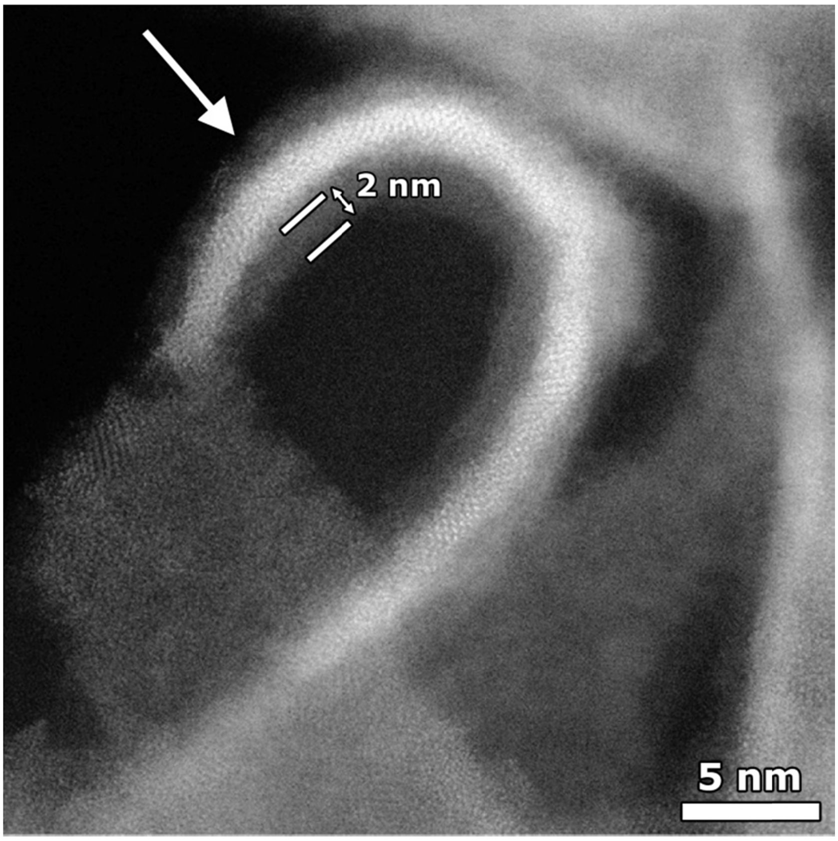

**Figure 3.8.** Top view of a folded nanoplatelet which was encapsulated with a silica shell with 3.0 wt % ammonia conditions. This image indicates the presence of silica at the inner and outer surface. The silica shell has a similar thickness on both sides (~2 nm).

## 3.2. Thickness determination

The acquisition of standing nanoplatelets with high resolution HAADF-STEM enables us to characterize the atomic thickness of the platelets. In Figure 3.9, a high resolution HAADF-STEM image acquired along the [110] direction of a standing CdSe nanoplatelet is shown. The atomic columns present in the image represent the heavier Cd atomic columns (in comparison to Se). The atomic arrangement, illustrated in the insets in Figure 3.9.a and c, shows that the helical CdSe platelets are four monolayers thick. Assuming that these nanoplatelets are stoichiometric, this corresponds to a thickness of two CdSe unit cells. Due to the encapsulation by the silica shell, the CdSe helices do not amorphize and therefore the thickness can be determined in a reliable manner.

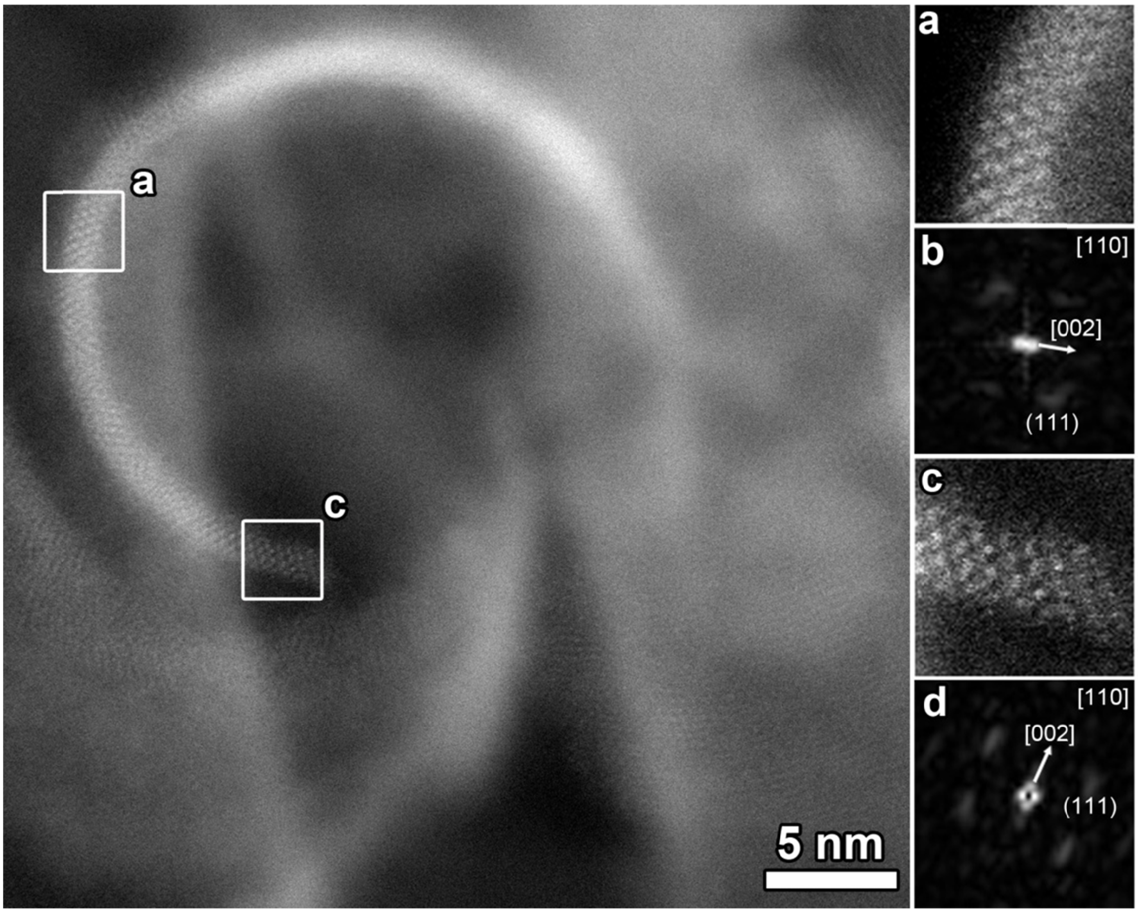

**Figure 3.9.** High-resolution HAADF-STEM image acquired along the [110] direction. (a,c) Detailed images showing that the nanoplatelets consist of 2 CdSe units in their short direction (the white dots show the stronger scattering Cd atoms). (b,d) Fourier transforms of the highlighted regions (a,c) confirming that the nanoplatelets fold along the [110] direction. The vector from the curved structure toward the center always points in a [002] direction.

Considering these results, the pristine crystallographic structure of a CdSe nanoplatelet with a thickness of four monolayers is shown in Figure 3.10. If we take a closer look at the Cd atoms viewed from the top of the helix in Figure 3.9.a and c, we find that they show an asymmetric hexagonal arrangement. This perfectly corresponds to the ⟨110⟩ direction of the zinc blende structure; see Figure 3.10.d. Note that this is not the [111] direction, in which the Cd atoms are arranged in a symmetric hexagon.

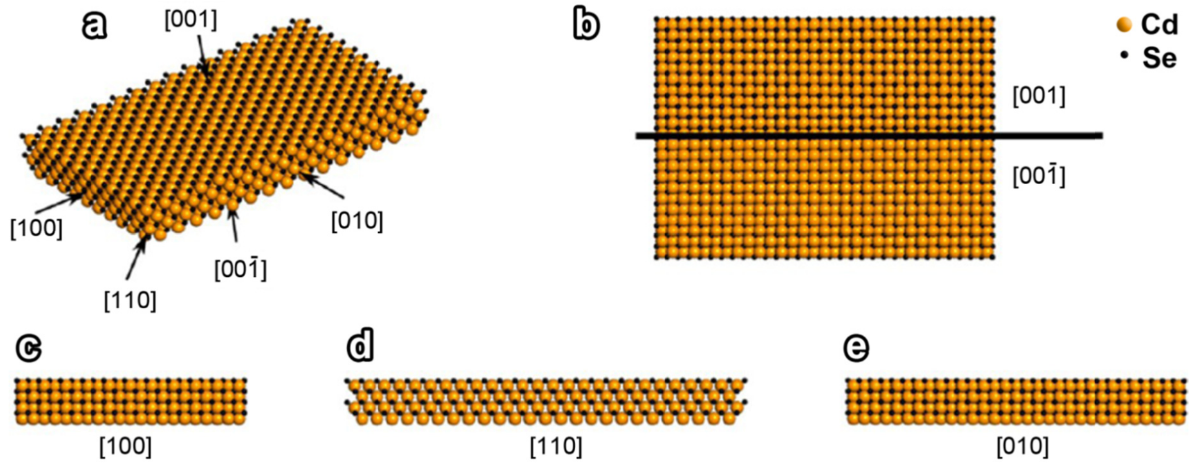

**Figure 3.10.** Crystallographic structure of a zinc blende CdSe nanoplatelet with a thickness of 4 monolayers, corresponding to 2 CdSe unit cells, with lateral dimensions of 10 × 15 unit cells (a). The larger Se atoms and smaller Cd atoms are represented by yellow and black spheres, respectively. In (b), the top (Cd-terminated) and bottom (Se-terminated) surfaces are shown, corresponding to the inner and outer surface of the helices. Different side views of the nanoplatelet are shown in (c–e). Note that the hexagonal arrangement of the Cd atoms in the [110] direction (d) is in agreement with the one observed in Figure 3.9.

### 3.3. Folding formation

High resolution HAADF-STEM imaging is used to investigate the folding formation of the nanohelices. Figure 3.11 presents a high resolution HAADF-STEM projection image showing the crystal lattice in the [001] viewing direction. Based on its Fourier transform (inset of Figure 3.11.b), it can be concluded that this nanoplatelet is folded along the [110] zone axis. Similar results obtained with other nanoplatelets confirm that the platelets always fold along the [110] direction. In Figure 3.7.a-c, we could already differentiate two types of morphologies. A helical morphology is observed for the nanoplatelets in Figure 3.7.b and c. In Figure 3.7.a, a nanoplatelet which resembles an envelope-rolled morphology is visualized. Considering these helical and envelope-rolled

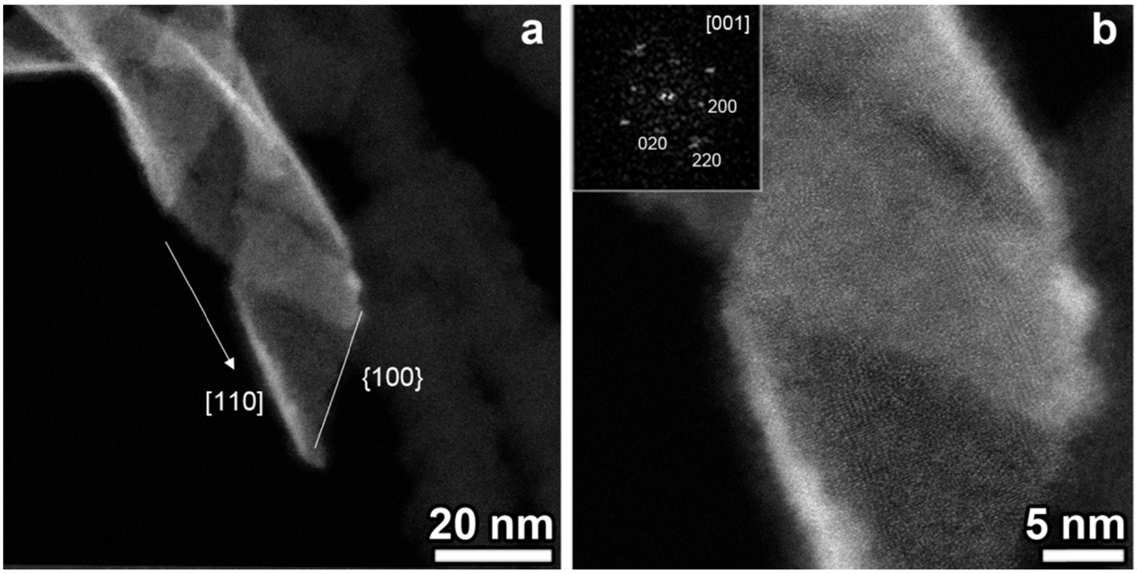

**Figure 3.11.** High-resolution HAADF-STEM images of silica-coated CdSe nanoplatelets (3.0 wt % ammonia). (a,b) HAADF-STEM projection showing that the NPL folds along the [110] direction and that the large end-facets of the helical structures are {100} facets. Inset: FT of the lower part.

morphologies of the silica-coated nanoplatelets, together with the high resolution projection images, we can propose the following model of folding as presented in Figure 3.12. For both morphologies, a flat rectangular nanoplatelet curls along the [110] zone axis. Given that this axis forms a 45° angle with the [100] and [010] axes, the nanoplatelet now folds into (i) a helix if the [010] is short compared to the [100] and vice versa or (ii) an envelope-like structure if the lateral dimensions are closer in length, i.e., if the nanoplatelet shape becomes closer to a square, which is illustrated in Figure 3.12.b. As most of our CdSe nanoplatelets were rectangular rather than square-shaped, their native conformation in solution is closer to a helix.

Additionally, the high resolution HAADF-STEM image in Figure 3.9 confirms that the nanoplatelets are folded around the [110] direction. The folding along the [110] direction is further proven by the fact that the vector from the edge of the nanostructure toward the center of the curvature always corresponds to a [002] direction (Figure 3.9.b and d).

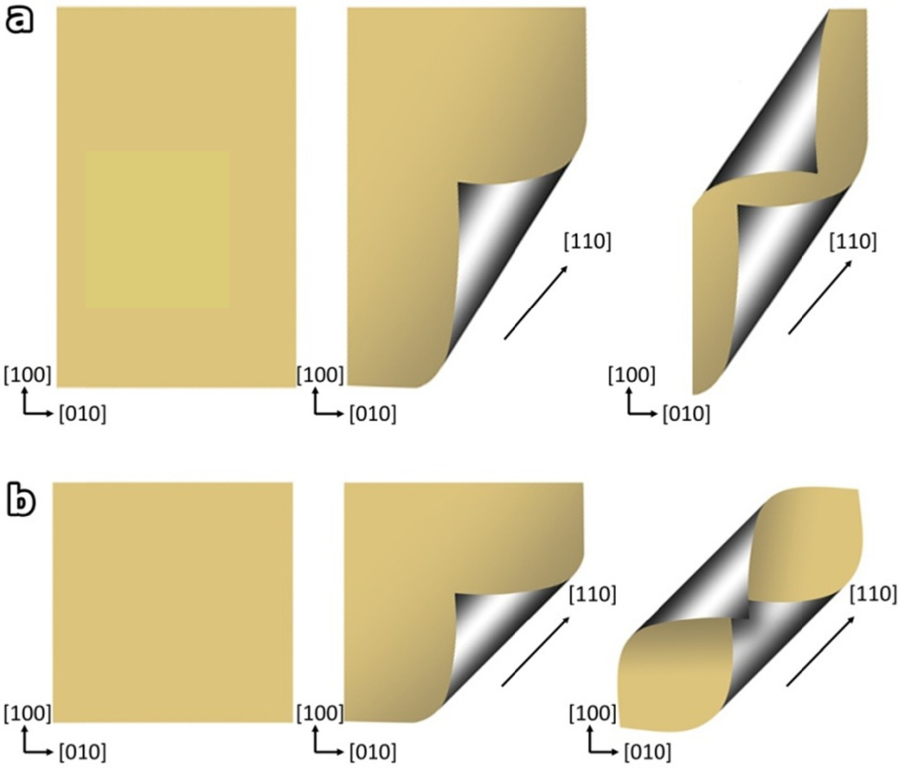

**Figure 3.12.** Model showing the folding of the nanoplatelets, starting from (a) a rectangular sheet and (b) a square-shaped sheet. The folding occurs along a [110] zone axis as visible in Figure 3.9.

### 3.4. Helicity of the nanoplatelets

By 2D high resolution HAADF-STEM imaging in different zone axes, we were able to solve the first questions concerning the thickness and the folding formation of the CdSe helical nanoplatelets. 2D imaging is however not sufficient to answer the remaining question:

4. Are both left- and right-handed helices present? Or is there a preferential helicity?

For example, the helicity of the nanoplatelet in Figure 3.9.a cannot be determined from this image, it could either be a left- or a right-handed helix. From this viewing direction, we can only state the structure appears to be rolled up. Any statement on the helicity cannot be made. To characterize the helicity, electron tomography is required. A tilt series of 37 HAADF-STEM projection images was acquired with an angular range of -70° to +74°, with a tilt increment of 4°. In Figure 3.13.a, the

HAADF-STEM projection image at 2° of a set of helices is shown. The result of the electron tomography experiment is presented in Figure 3.13.b-d, where 3D visualizations from different viewing directions are shown. The 3D tomographic reconstruction confirms that the observed helices are indeed 2D nanoplatelets fully rotated over a diameter of approximately 20−25 nm, and hence most of the helices only make 1−1.5 twists. Furthermore, regarding the helicity of the nanoplatelets we can

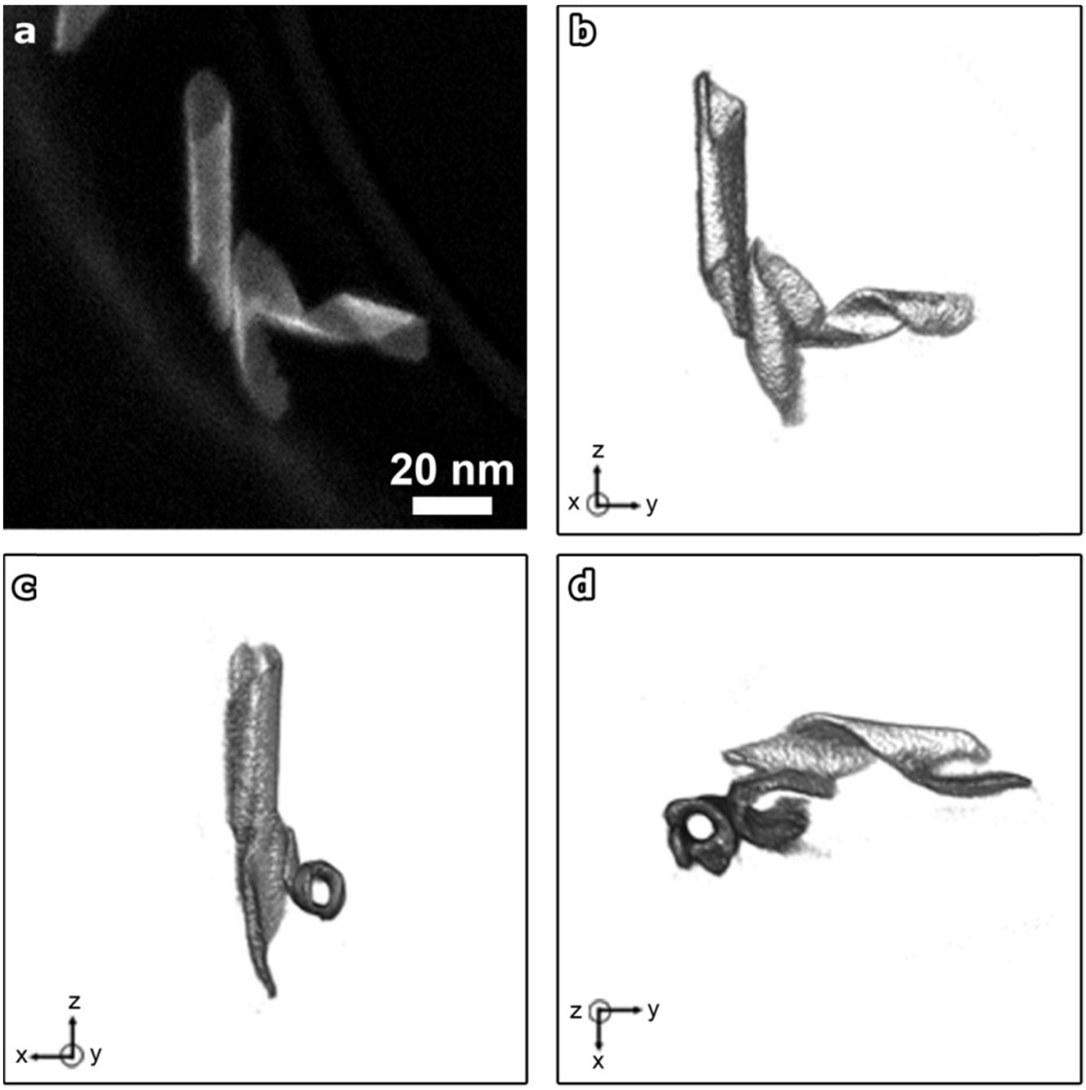

**Figure 3.13.** HAADF-STEM image and its 3D tomographic rendering at different viewing angles of silica-coated CdSe helices (3.0 wt % ammonia, 3 h of growth). An angle of 90° is present between two connected helical structures. Both left- and right-handed helices are observed.

conclude that the helices are not preferentially left- or right-handed. Both types of helicity are found throughout the sample. In Figure 3.13.b, the nanoplatelet along the z-direction (on the left) is a right-handed helix and the nanoplatelet along the y-direction (on the right) is a left-handed helix. Along this viewing direction we can also remark that both nanoplatelets have a different folding formation. The nanoplatelet along the z-direction folds into an “envelope” conformation, as well as the one shown in Figure 3.7.a. From this reconstruction, we can also observe that the two helices are mutually orthogonal attached to each other, which is often observed.

## 4. Conclusion

By high resolution HAADF-STEM imaging, both the thickness as well as the surface facets of the flat ultrathin colloidal CdSe semiconductor nanoplatelets was determined. We could conclude that when Cd acetate is used, there is no preferential growth direction which leads to polydiverse nanoplatelets. The synthesis in presence of Na acetate yields more uniform nanoplatelets with {110} facets and a controllable thickness.

The native morphology of ultrathin colloidal CdSe nanoplatelets with lateral dimensions in order of hundreds of nanometer was revealed by cryo-TEM. After a successful encapsulation in a silica shell, the thickness and folding formation of the helical nanoplatelets was determined by high resolution HAADF-STEM imaging. We confirmed the presence of both left- and right-handed helices by the use of electron tomography.

The degradation at the edges of the CdSe nanoplatelets upon scanning of the electron beam complicated the acquisition of high resolution HAADF-STEM images. However, we were still able to acquire such images as there was sufficient time before the degradation occurred. In the next chapter, 2D investigation studies of highly beam sensitive semiconductor perovskite nanostructures are carried out. These studies require alternative imaging techniques as the degradation or alteration of the nanostructure occurs faster.

# Chapter 4

## 2D investigation of beam sensitive perovskite nanostructures

This chapter is based on: Tong, Y., Bladt, E., Aygüler, M. F., Manzi, A., Milowska, K. Z., Hintermayr, V. A., Docampo, P., Bals, S., Urban, A. S., Polavarapu, L., Feldmann, J. *Highly Luminescent Cesium Lead Halide Perovskite Nanocrystals with Tunable Composition and Thickness by Ultrasonication*. Angewandte Chemie International Edition, 55 (2016) 13887–13892;

Debroye, E., Yuan, H., Bladt, E., Baekelant, W., Van der Auweraer, M., Hofkens, J., Bals, S., Roeffaers M. B. J. *Facile Morphology-Controlled Synthesis of Organolead Iodide Perovskite Nanocrystals Using Binary Capping Agents*. ChemNanoMat, 3 (2017) 223-227.

Tong Y., Bohn B. J., Bladt E., Wang K., Müller-Buschbaum P., Bals S., Urban A. S., Polavarapu L., Feldmann J. *Precursor Powders-to-$CsPbX_3$ Perovksite Nanowires: One-Pot Synthesis, Growth Mechanism and Oriented Self-assembly.* Angewandte Chemie International Edition (in press)

Own contribution: Responsible for all TEM acquisition and analysis.

## 1. Introduction

The outstanding optoelectronic properties of metal halide perovskites have brought them to the forefront of many research fields such as solar cells, light-emitting diodes, lasers and photodetectors[72,73]. Perovskite solar-cell efficiencies have gone from 3% to over 20% in the last four years[72,74–76]. It took decades for silicon solar cells to make that efficiency increase. Additionally, perovskite nanomaterials can be grown at room temperature, which is significant for low cost production. Two types are currently a topic of investigation: cesium lead halide perovskites ($CsPbX_3$) and organic-inorganic lead halide perovskites ($CH_3NH_3PbX_3$) (X = Cl, Br, I). By changing the halide composition, the bandgap energy can be tuned in the entire visible spectral region. Nowadays, different synthesis approaches are investigated to prepare high quality colloidal nanocrystals. An additional aim is to control and convert the halide composition in a straightforward and reproducible manner. The development of new synthesis approaches requires a thorough characterization of the obtained nanostructures. The perovskite nanostructures are investigated by high resolution HAADF-STEM imaging and exit wave reconstruction to elucidate on the atomic structure of the nanostructures. The investigation of these materials is hampered by their sensitivity to the electron beam, which restricts the characterization to 2D. The organic-inorganic lead halide perovskites require even more care as the structures almost instantaneously change upon illumination. The use of dose limited TEM techniques emerges to reveal their atomic structure.

## 2. Atomic resolution imaging techniques

Different TEM imaging techniques can be used to obtain 2D images that yield atomic resolution. Depending on the information we want to retrieve, one technique can be more suitable than others. In this section, different high resolution imaging techniques will be discussed and their advantages/disadvantages will be explained.

## 2.1. High resolution HAADF-STEM imaging

The intensity in a HAADF-STEM image is related to the projected thickness and the average atomic number of the specimen along the projection direction. When investigating small nanoparticles (approximately < 20 nm), the integrated intensity of each projected atomic column in a high resolution HAADF-STEM image scales linearly with the thickness of the specimen. This linear relation enabled the application of statistical parameter estimation methods to determine the number of atoms in each projected atomic column in a nanomaterial[178–180]. Additionally, the intensity-atomic number relation can be exploited to identify atomic columns based on their composition. A chemical characterization, however, can only be applied when the atomic number between different components is sufficiently large. Additionally, we have to keep in mind that we only observe the averaged intensity of all the different atoms in an atomic column, which complicates the identification of mixed columns.

## 2.2. Exit wave reconstruction

Information at the atomic scale can be provided by the use of exit wave reconstruction. An exit wave contains all the information about the specimen as it is the wave obtained after propagation of the electron beam through the specimen. Different to other imaging techniques, there is no direct inspection of the result of such an experiment as the exit wave cannot be directly measured in the electron microscope. In order to recover the exit wave, a focal series of BF-TEM images needs to be acquired[181]. A focal series consists of a large number of images acquired at a different focus value at the region of interest. Studies show that the phase of the exit wave is related to the thickness of the specimen and that, thereby, the number of atoms in an atomic column can be estimated using an Argand plot[182,183]. Such an Argand plot is a complex plane in which the real and imaginary parts of the complex pixel values of the exit wave are plotted in a Cartesian coordinate system. The need of a post-treatment of the focal series of BF-TEM images is a disadvantage in comparison to a direct visualization of the atomic structure, which is possible with high resolution HAADF-STEM. However, the use of a BF-TEM based technique could be advantageous towards investigating the atomic structure of beam sensitive samples. The use of a parallel electron beam spreads the electron dose equally over the full field of view which causes less local damage -when working at high magnification- in comparison to STEM imaging where the dose is focused into one point by the convergent beam.

## 3. Lead cesium halide perovskite nanostructures

First synthesis approaches were focused on the production of perovskite nanocubes, which aim for a straightforward and reproducible approach. In section 3.1, $CsPbBr_3$ nanocubes and their transformation into $CsPbI_3$ after a halide ion exchange reaction are investigated. The use of perovskite nanowires is desired for their use in devices and therefore a straightforward synthesis is the next step after synthesizing nanocubes. High resolution HAADF-STEM imaging is used to evaluate a novel synthesis approach of $CsPbBr_3$ nanowires in section 3.2. As the properties of these perovskite structures are tunable by their halide composition, a successful halide ion exchange reaction is desirable for the nanowires. The obtained $CsPbCl_3$ and $CsPbI_3$ nanowires after the exchange reaction are studied by high resolution HAADF-STEM imaging. The use of exit wave reconstruction is discussed as their sensitivity to the electron beam requires alternative techniques.

### 3.1. Nanoparticles

Recently, the investigation of hybrid metal halide perovskites has gained interest as they exhibit outstanding optoelectronic properties. Since these materials are inexpensive and solution-processable, they are attractive for a broad range of applications such as light-emitting diodes and lasers[72,73]. The success of these materials has led to the synthesis of inorganic cesium-based perovskite nanocrystals ($CsPbX_3$)[87–91]. A new single-step approach for the synthesis of these highly luminescent $CsPbX_3$ perovskite nanocrystals and nanoplatelets controls both the halide composition (X = Cl, Br, I) and the thickness. By tuning the nanoplatelet thickness, the relation to the optical properties can be investigated. By adjusting the halide content, the optical band gap energy can be tuned across almost the entire visible light range (approximately 410-700 nm), which is visualized in Figure 4.1.

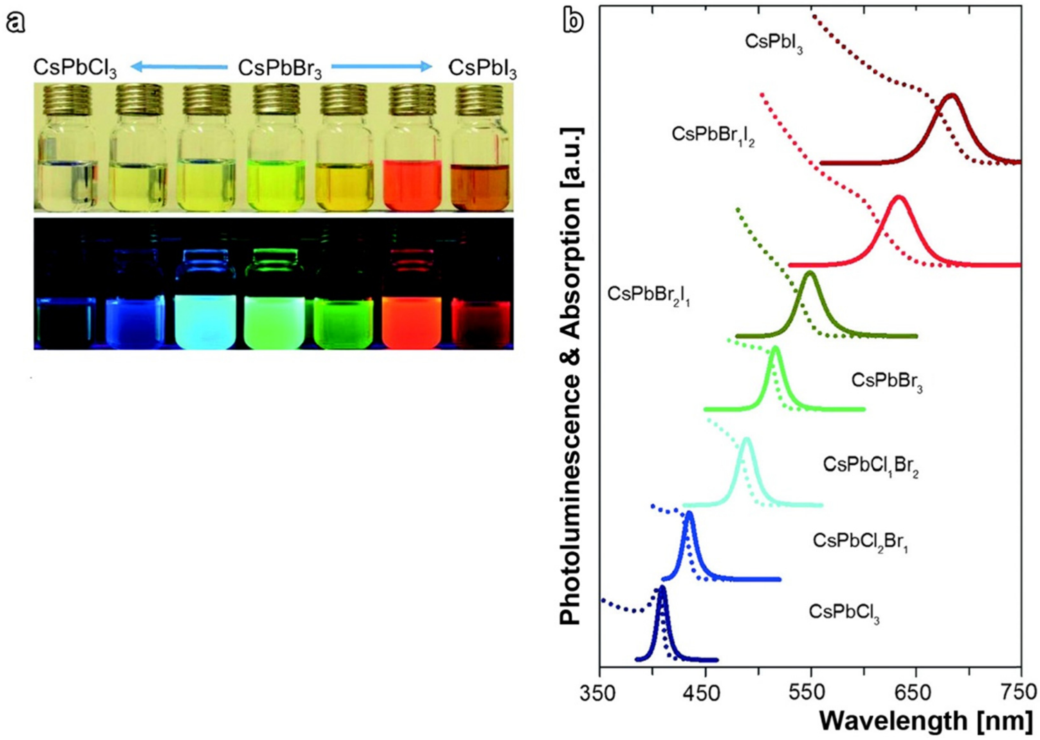

**Figure 4.1.** Photographs of colloidal dispersions of $CsPbX_3$ nanocrystals with different halide (X=Cl, Br, and I) compositions in hexane under room light (top) and UV light with $\lambda$ = 367 nm (bottom) and (b) their corresponding UV/Vis and photoluminescence spectra.

The quality of the perovskite nanocrystals is investigated by high resolution HAADF-STEM imaging. The lead halide perovskite nanocrystals containing only Br and I are of most interest as they exhibit high photoluminescence quantum yields of over 90%. In Figure 4.2.a and d, BF-TEM overview images of both the $CsPbBr_3$ and $CsPbI_3$ perovskite nanocubes are shown. The images show the presence of well-defined cubic and rectangular projected shapes. From these low magnification images, we can examine their dimensions and conclude that their lateral dimensions are rather monodisperse with an average size of 15 ± 2 nm for the Br containing perovskite nanocrystals. To study the nanocrystals in more detail and to determine for example the crystallinity, the nanocrystals are investigated by high resolution HAADF-STEM. Figure 4.2.b and e show atomic resolution HAADF-STEM images of a $CsPbBr_3$ and a $CsPbI_3$ perovskite nanocube, respectively. Both images are acquired along the [100] axis and show a cubic arrangement of the atomic columns. It is well known that $CsPbX_3$ nanocrystals can crystallize in cubic, tetragonal and orthorhombic polymorphs of the perovskite crystal lattice[184]. After an analysis of multiple nanocrystals with high resolution HAADF-STEM, we can conclude that all of the nanocrystals are single crystals and mostly adopt the cubic perovskite phase regardless of the composition. In these high resolution images, the atomic column distances, and thereby lattice spacing, can be investigated. For the $CsPbBr_3$ perovskite nanocrystals, a lattice spacing of approximately 5.9 Å is measured. By substitution of Br into I, the lattice spacing increases to approximately 6.3 Å. Next to the determination of the position of the different atomic columns, their intensity can be studied to identify the different elements present in the atomic columns. The perovskite nanocrystals are built up out of two types of atomic rows in the [100] zone. The different atomic rows of the $CsPbI_3$ perovskite nanocrystal in Figure 4.2.e are indicated by a purple and a white arrow in Figure 4.2.f. In Figure 4.3.a, the integrated line profile

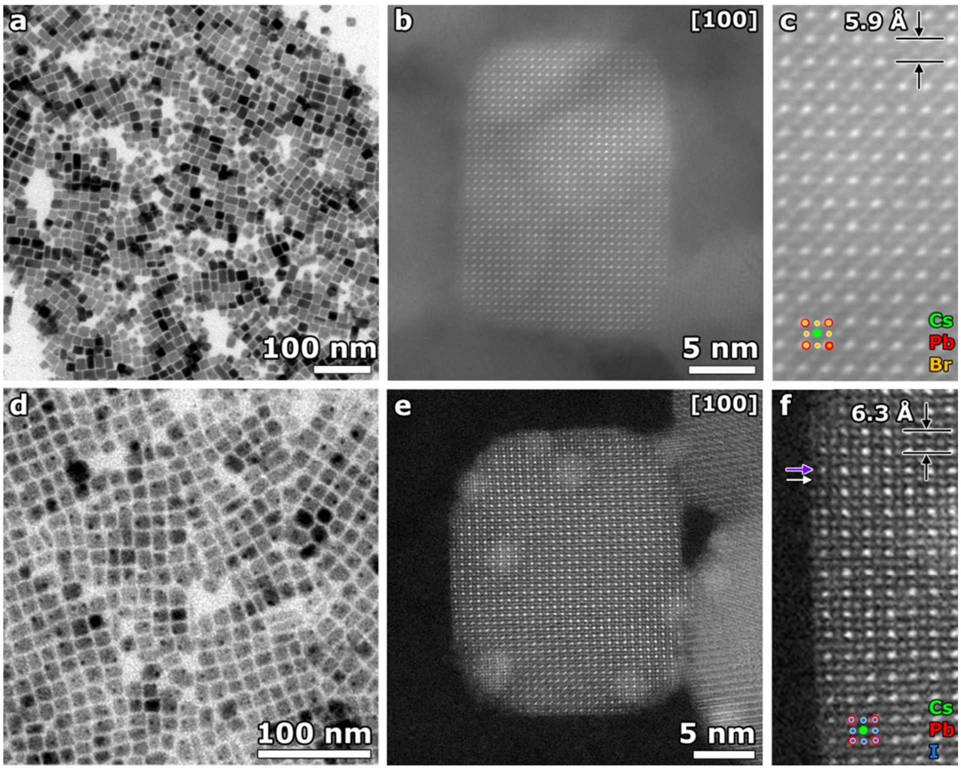

**Figure 4.2.** (a,d) BF-TEM overview images of $CsPbBr_3$ and $CsPbI_3$ NCs, respectively. (b,e) Atomically resolved high resolution HAADF-STEM images of single $CsPbBr_3$ and $CsPbI_3$ nanocrystals with more detailed views shown in (c) and (f), respectively.

through the first type of atomic row (indicated by the purple arrow in Figure 4.2.f) is shown. From a visual inspection of the HAADF-STEM image and the line profile, it is clear that one atomic column is much brighter than the neighbouring atomic column. The cubic unit cell of a perovskite structure $ABX_3$ has type 'A' atoms at the cube corner positions (0, 0, 0), type 'B' atoms at the body center position $(\frac{1}{2}, \frac{1}{2}, \frac{1}{2})$ and the 'X' type atoms at the face centered positions $(\frac{1}{2}, \frac{1}{2}, 0)$, which form $BX_6$ octahedra. We should note that a unit cell with A in the body center, B at the corners and X in the mid-edges are equivalent to the above described unit cell. Therefore, we expect in a $CsPbI_3$ perovskite nanocrystal that the Pb and I form the $PbI_6$ octahedra and that the Cs atoms are located in the center of these octahedra. In these perovskite nanocrystals, Pb are the heaviest atoms ($Z_{Pb} = 82$) followed by Cs and I which have a comparable atomic number ($Z_{Cs} = 55$, $Z_I = 53$). In this manner, the bright atomic columns in the [100] zone are mixed Pb-I columns with an average atomic number of 67,5. As the structure consists of $PbI_6$ octahedra, the neighbouring atomic columns in this row (Figure 4.3.a) are pure I columns. The I columns will appear less bright in a HAADF-STEM projection image due to its lower atomic number, which is confirmed by the integrated line profile in Figure 4.3.a. Investigation of the adjacent atomic rows (indicated by a white arrow in Figure 4.2.f) in Figure 4.3b shows comparable intensity values for neighbouring columns as these columns consist of Cs and I which have only a small difference in atomic number. We can only identify one column from another by a joint inspection of the adjacent atomic row. The Cs atomic columns are present in the center of four $PbI_6$ octahedra in this projected view which is indicated in Figure 4.3.b. Based on the intensity difference and the prior knowledge on the cubic perovskite unit cell, all the atomic columns could be identified in this high resolution HAADF-STEM image. The significant difference in atomic number between Pb and the other two elements (Cs and I) makes HAADF-STEM imaging a suitable technique for elemental identification at the atomic level. From this image, important information

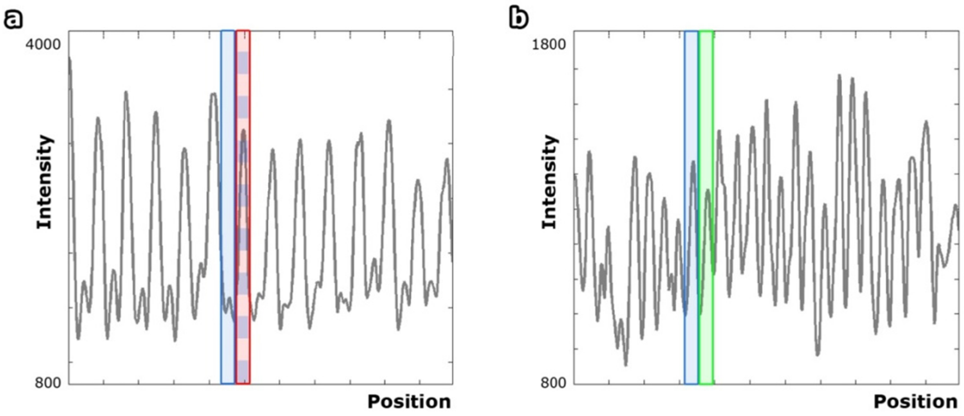

**Figure 4.3.** Integrated line profiles from the different atomic rows: (a) alternating Pb and mixed Pb-I columns and (b) alternating Cs and I columns.

with regard to the surface termination can be obtained. The outer surface layer can be identified as an atomic row containing Cs and I atomic columns (Figure 4.2.f). As the crystal is terminated with Cs atoms, it is most likely that the nanocrystals are passivated by Cs-bound alkyl chains. An enlarged image is shown in Figure 4.4, from which the surface termination can be clearly observed.

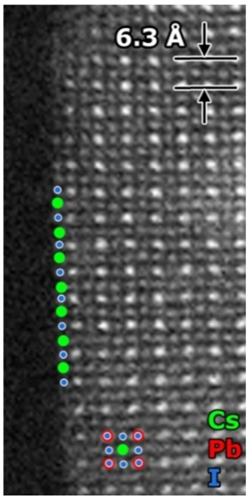

**Figure 4.4.** (a) High resolution HAADF-STEM image of the $CsPbI_3$ nanocrystal showing a more detailed view from which it is clear that the outer surface ends in Cs-I atomic columns.

## 3.2. Nanowires

Over the past two decades, semiconductor nanowires have gained an important role in the evolution of nanodevice technologies for a wide range of applications such as sensing, optoelectronics, lasers, light-emitting diodes and photovoltaics[185]. Despite great progress in the synthesis of semiconductor nanowires, full tunability of the absorption and photoluminescence remains challenging. As discussed in section 3.1, the optical band gap energy of $CsPbX_3$ perovskite nanocrystals can be tuned by controlling the halide composition. In fact, the direct conversion of precursor powders into $CsPbX_3$ nanocubes can significantly reduce the fabrication time, laborious effort and thus costs of production, which are key factors for commercialization. In addition to shape-controlled synthesis, self-assembly of nanocrystals is a crucial step for integrating them into devices. Although self-assembly of conventional semiconductor and metal nanocrystals have been widely demonstrated by various techniques[186,187], it has not yet been explored for perovskite nanocrystals. However, it is a promising research field with great potential, considering their broad range of applications in optical and optoelectronic devices.

Here, we investigate a new synthesis approach in which a conversion of precursor powders into crystalline $CsPbBr_3$ perovskite nanowires by ultrasonication is aimed for. The emission colour of the nanowires can be tuned across the full visible spectrum by applying halide ion (Cl and I) exchange reaction on $CsPbBr_3$ nanowires. Mechanistic studies revealed that nanowires are most likely formed through the oriented attachment of initially formed nanocubes. The oriented attachment of nanocubes into nanowires is investigated by HAADF-STEM imaging of an intermediate sample. Afterwards, the effect of the halide ion exchange reaction on the atomic structure of the nanowires will be studied.

### 3.2.1. Oriented attachment

The synthesis of colloidal $CsPbBr_3$ perovskite nanowires was carried out by adapting the ultrasonication-assisted synthesis of perovskite nanocubes. A prolonged ultrasonication under similar reaction conditions leads to the evolution of nanowires together with a few percent of nanocubes, which can be easily purified by centrifugation to obtain only the nanowires. A BF-TEM image of the obtained nanowires is shown in Figure 4.5. Since, the prepared nanowires tend to form bundles in the colloidal solution due to strong hydrophobic interactions between ligand molecules, they tend to settle down at the bottom of the glass bottle due to heavy mass. Therefore, the nanowires are easily obtained by centrifugation.

The growth process of the $CsPbBr_3$ perovskite nanowires is studied by a BF-TEM investigation of intermediate samples at different stages of the reaction (Figure 4.6.a-f). It is clear from this study that in a first stage $CsPbBr_3$ perovskite nanocubes are formed after ultrasonication of 10 minutes (Figure 4.6.b). With further increase of the reaction time, a gradual transformation of nanocubes into nanowires is obtained, which can be clearly seen in the BF-TEM images in Figures 4.6.b-f. After an ultrasonication of 60 minutes, mostly nanowires are visualized (Figure 4.6.f). A schematic overview of the formation of nanowires by ultrasonication is provided in Figure 4.6.g. High resolution HAADF-STEM images of the intermediate sample, sonicated for 20 minutes, provide a visual confirmation of the oriented attachment in Figure 4.6.h and **i**. The images show the oriented attachment of a $CsPbBr_3$ nanocube to the end of an intermediate $CsPbBr_3$ perovskite nanowire, which is indicated by the arrows.

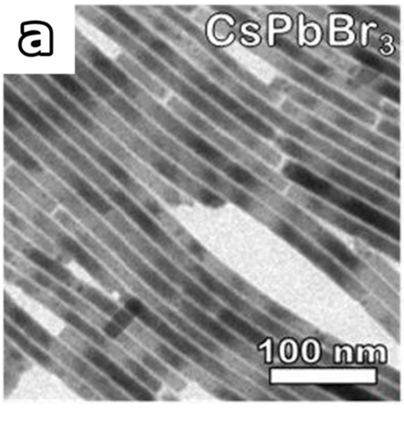

**Figure 4.5.** (a) BF-TEM image of colloidal $CsPbBr_3$ perovskite nanowires obtained by a prolonged ultrasonication.

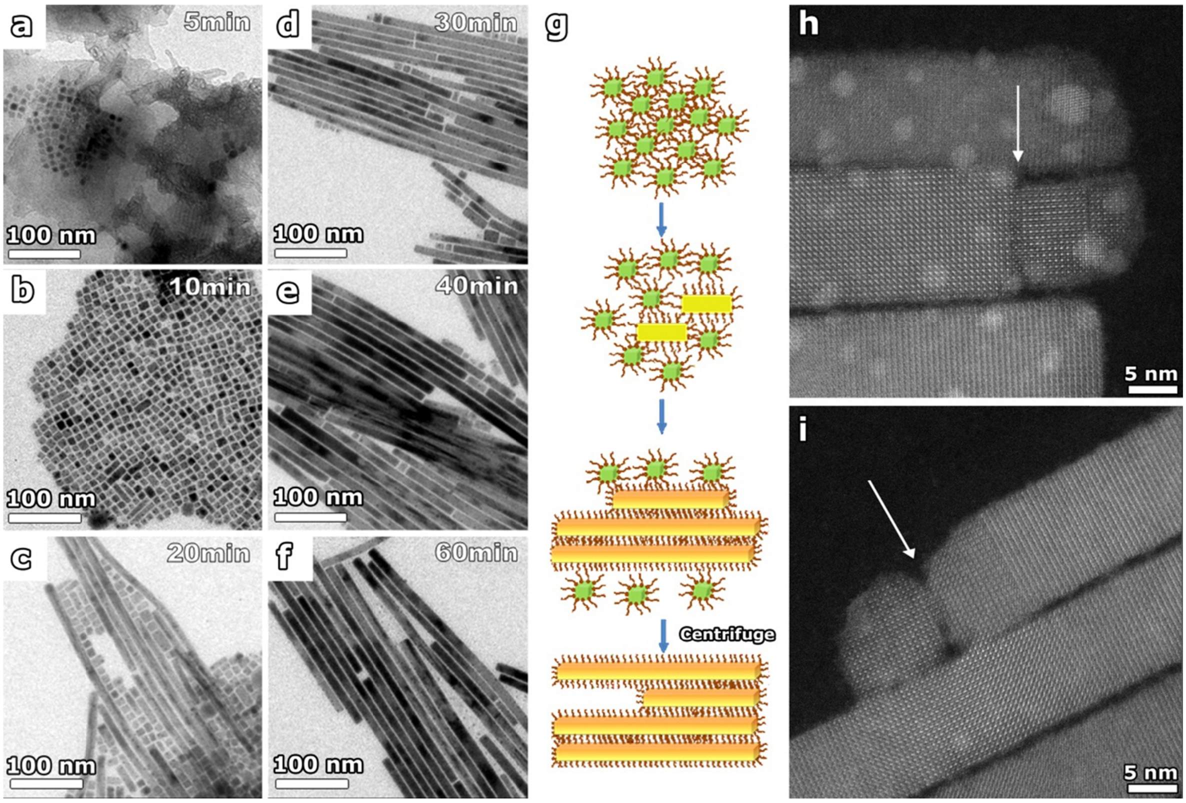

**Figure 4.6.** (a-f) BF-TEM images of colloidal $CsPbBr_3$ perovskite nanocrystals obtained at different reaction times during the transformation of precursor powders into nanowires. (g) Schematic illustration of the transformation of precursor powders into nanowires by ultrasonication, in which initially formed $CsPbBr_3$ nanocubes transformed into nanowires. (h,i) High resolution HAADF-STEM images in which oriented attachment of a nanocube to a nanowire is indicated by the arrow.

### 3.2.2. Halide ion exchange reaction

Unlike the synthesis of $CsPbX_3$ nanocubes of different halide compositions (X = Cl, Br, I), the reaction described above is unable to produce $CsPbCl_3$ and $CsPbI_3$ nanowires from $CsPbCl_3$ and $CsPbI_3$ nanocubes under prolonged ultrasonication. In section 3.1, $CsPbI_3$ nanocubes were successfully formed by a halide ion exchange reaction, starting from the $CsPbBr_3$ nanocubes. The same procedure is used here to obtain $CsPbCl_3$ and $CsPbI_3$ perovskite nanowires. The BF-TEM images in Figure 4.7.a and c show that the halide ion exchange reaction is also successful for both the production of $CsPbCl_3$ and $CsPbI_3$ nanowires. A high resolution HAADF-STEM investigation is performed to study the atomic structure of the nanowires after the halide ion exchange reaction.

To study the effect of the halide ion exchange reaction on the obtained atomic structure, statistical parameter estimation theory[180] is used to retrieve the positions of the atomic columns in the high resolution HAADF-STEM images of the different nanowires. The atomic column positions of the Cs and Pb atomic columns are retrieved and from these obtained positions, we calculate the displacements of the Cs atomic columns. The deviation of the Cs atomic column from the center between four adjacent Pb atomic columns is referred to as the displacement. From these calculations, it is clear that the positions of the Cs atomic columns in the $CsPbBr_3$ nanowire show small displacements in a random orientation (Figure 4.8.b). The displacements are indicated by the arrows in Figure 4.8. The length of the arrows is dependent on the amount of the displacement. When the Br halide ions are exchanged by Cl ions, the displacements remain small (0.16 ± 0.01 Å). There is no

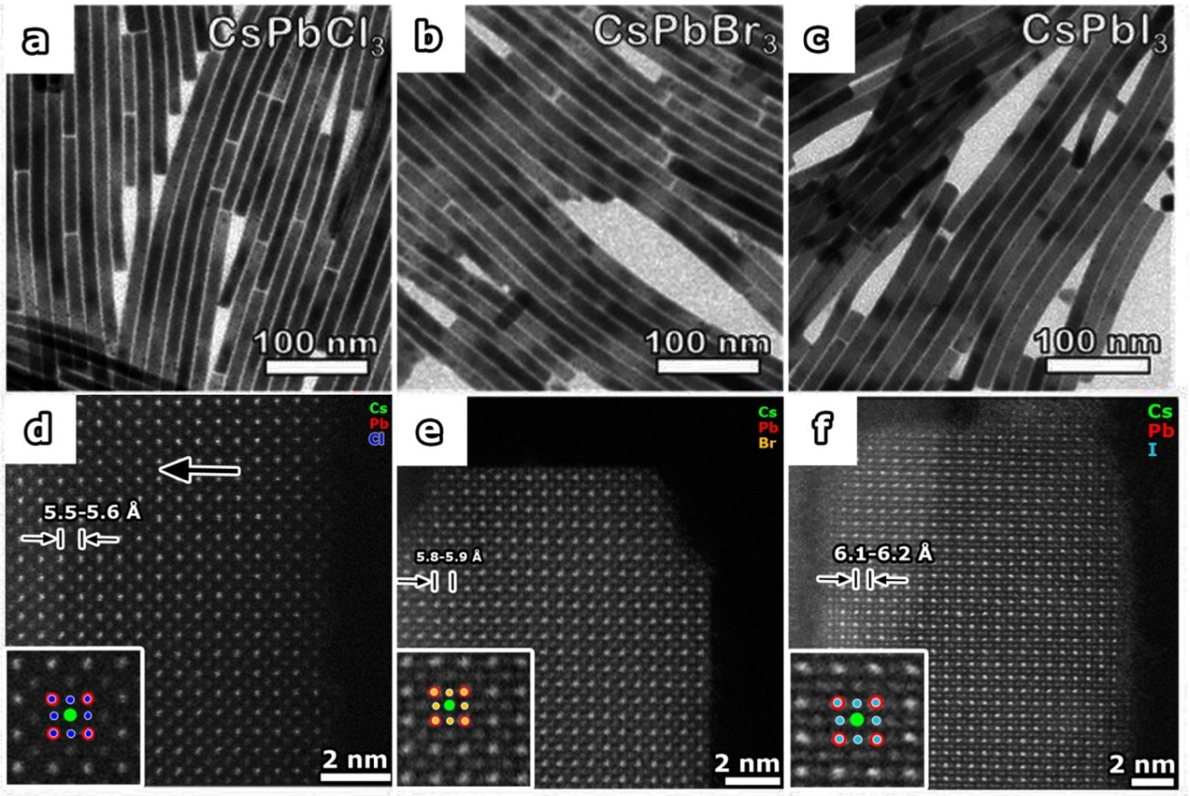

**Figure 4.7.** (a-c) BF-TEM and (d-f) high resolution HAADF-STEM images of $CsPbCl_3$, $CsPbBr_3$ and $CsPbI_3$ nanowire, respectively.

general trend observed for the orientation of the displacement. The displacements of the Cs atomic columns in a $CsPbI_3$ perovskite nanowire in Figure 4.8.c show a significant increase to an average displacement of 0.40 ± 0.01 Å. Additionally, the displacement map shows that the displacements have an alternation direction along the growth direction of the nanowire, which is indicated by the blue and red arrows. It seems that the crystal structure of the obtained $CsPbI_3$ perovskite nanowires deviates from a perfect cubic structure. The Goldschmidt's tolerance factor[188], which indicates the distortion of the crystal structure, was calculated for the different nanowires:

$$t = \frac{r_{Cs} + r_{Pb}}{\sqrt{2}(r_{Pb} + r_X)} \tag{4.1}$$

where $r_{Cs}$ is the radius of the Cs cation, $r_{Pb}$ is the radius of the Pb-cation and $r_X$ is the radius of the halide anion (Br, Cl or I). A cubic crystal structure has a tolerance factor between 0.9 and 1.

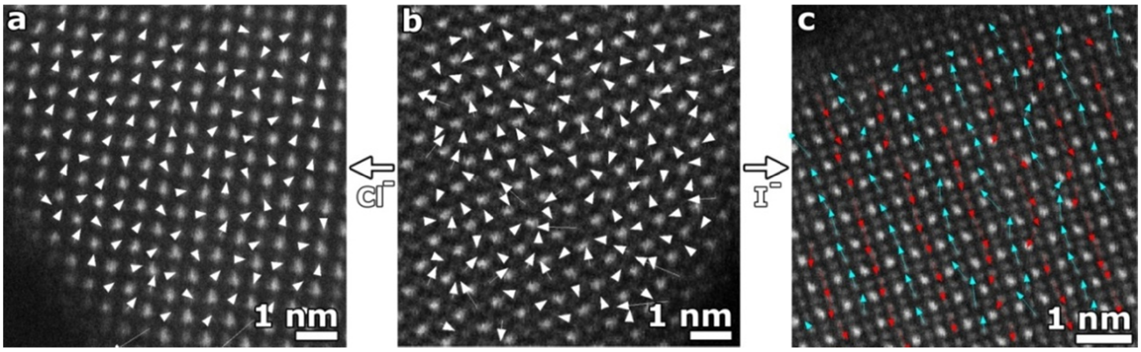

**Figure 4.8.** Displacement map of the Cs atomic columns for (a) a $CsPbCl_3$, (b) a $CsPbBr_3$ and (c) a $CsPbI_3$ perovskite nanowire. In (a) the average Cs atomic column displacement in the $CsPbCl_3$ nanowire equals 0.16 ± 0.02 Å. The orientation of the displacements does not show a general trend. The Cs atomic column displacements in (b) have a random orientation and the average displacement equals 0.16 ± 0.01 Å. The Cs atomic column displacements in (c) have an alternating direction along the growth direction of the nanowire, which is indicated by red and blue arrows. The average displacement equals 0.40 ± 0.01 Å.

The calculated tolerance factors for $CsPbBr_3$, $CsPbCl_3$ and $CsPbI_3$ equal approximately 0.81, 0.82 and 0.81, respectively and clearly show a deviation from the cubic tolerance factor. This means that $Cs^+$ cation seems to be too small for the cuboctahedral voids of the perovskite framework, especially for $CsPbI_3$, which could explain the displacements of the $Cs^+$ cation. The coexistence of both the cubic and the orthorhombic phase was already observed for $CsPbBr_3$ perovskites[189]. The orthorhombic phase of $CsPbBr_3$ shows however a tilting of the $PbBr_6$ octahedrons, which is not observed here.

## 4. Organolead iodide perovskites at the atomic scale

Next to cesium lead halide pervoskites, organolead halide perovskites have attracted attention because of their high absorption coefficient at visible wavelengths[72,77]. In combination with long-range electron-hole diffusion, they are ideal for solar energy conversion applications. The crystallinity and morphology of the organolead perovskite layer are known to have a significant impact on their device performance[80–83]. The development of such perovskite films is still at a first stage where they in general exhibit grain morphology. Similar to the cesium lead halide perovskites, a high defect density in a polycrystalline film is detrimental for the charge carrier dynamics and potential improvements can be offered by the use of monocrystalline organolead crystals. A recent morphology-controlled synthesis of methylammonium lead iodide ($CH_3NH_3PbI_3$ or $MAPbI_3$) perovskite nanocrystals obtains nanocrystals with improved stability in suspension. Scanning electron microscopy and photoluminescence spectroscopy revealed that the suspension of these organolead halide perovskites is stable for months in dark at room temperature. Here, high resolution imaging is used to examine the crystallinity of the nanocrystals. In comparison to the previous study on cesium lead halide perovskite nanocrystals, these $MAPbI_3$ nanocrystals are extremely sensitive to the electron beam. A time series of EDX maps was acquired at the same region of interest in which multiple organolead perovskite nanocrystals were present. Upon scanning, both the I and N content seem to decrease (Figure 4.9). Additional to this spectroscopic investigation, HAADF-STEM imaging at the nanoscale shows that the nanostructures deform upon interaction with the highly energetic electron beam, which is clearly visible in Figure 4.10. Therefore, in order to perform an investigation at the atomic level, a relatively low electron dose needs to be applied to study the native structure of the $MAPbI_3$ nanostructures. A low-dose high resolution HAADF-STEM image of a single $MAPbI_3$ nanocrystal is visualized in Figure 4.11.a. The low electron dose condition leads to a low signal-to-noise ratio and will therefore hamper the quality of the HAADF-STEM image. To improve the signal-to-noise ratio, a part of the HAADF-STEM image is statistically averaged by the use of a template-matching procedure, which was previously used in the investigation of silver clusters confined in zeolites[190]. In this template-matching routine, specific regions are searched for in a given image that corresponds to a template. The result of such a procedure yields an averaged template image with an improved signal-to-noise ratio. In Figure 4.11.b, the template is shown from which a proper analysis is hampered by the low signal-to-noise ratio. After application of the template-matching procedure, the perovskite lattice is clearly visible in the averaged template in Figure 4.11.c. The averaged template image shows that the synthesized nanocrystals have a crystalline structure with a lattice parameter of approximately 6.4 Å, measured in the [100] zone. The different atomic columns can be identified by their intensity differences due to significant differences in the atomic number between the types of elements (Figure 4.12). The bright atomic columns at the corners of the unit cell are mixed Pb-I columns. As the perovskite structure contains $PbI_6$ octahedra, the lighter atomic columns located at the mid-edges consist of I. A very low intensity value is measured in the center of the cubic unit cell, which corresponds to the methylammonium. As the methylammonium is an organic component –only consisting of light elements–, the atomic columns in a HAADF-STEM image will appear very faint (Figure 4.12.d).

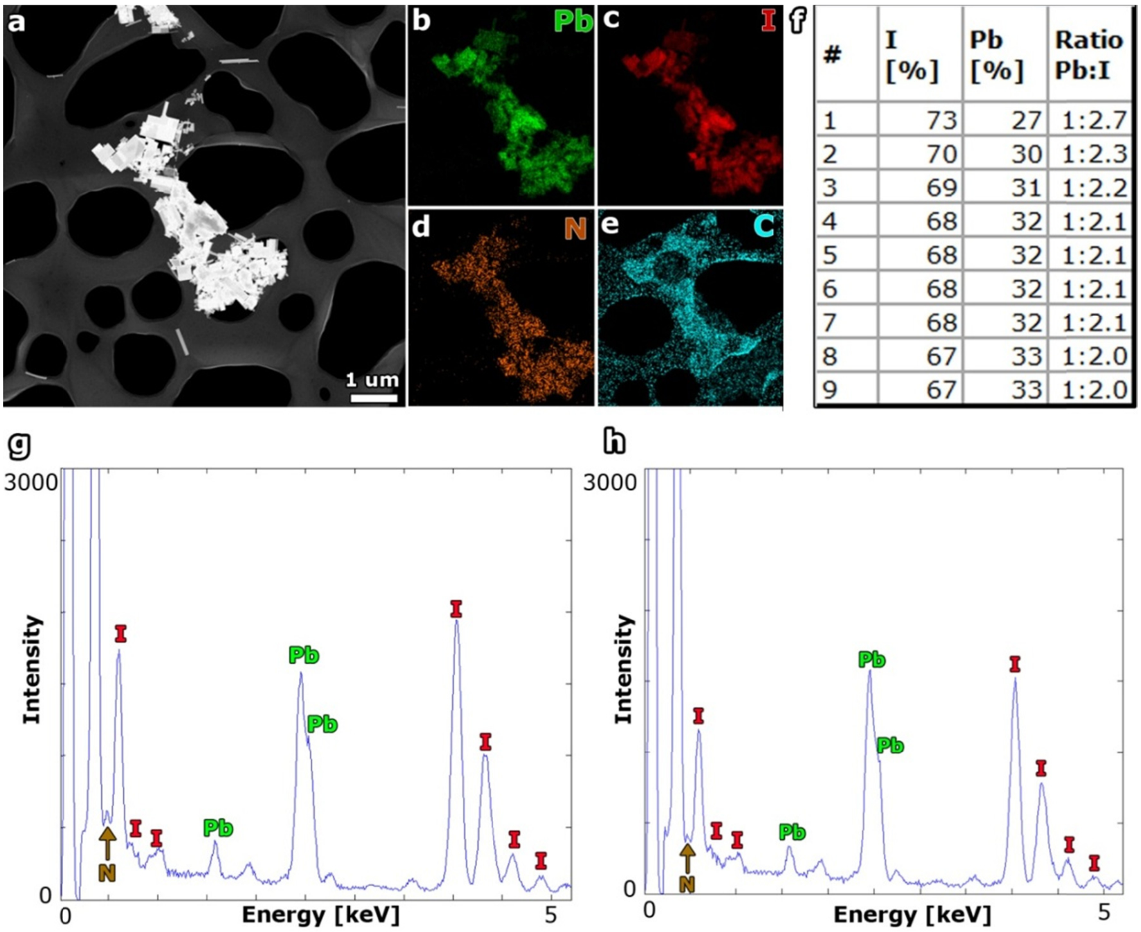

| # | I [%] | Pb [%] | Ratio Pb:I |
|---|---|---|---|
| 1 | 73 | 27 | 1:2.7 |
| 2 | 70 | 30 | 1:2.3 |
| 3 | 69 | 31 | 1:2.2 |
| 4 | 68 | 32 | 1:2.1 |
| 5 | 68 | 32 | 1:2.1 |
| 6 | 68 | 32 | 1:2.1 |
| 7 | 68 | 32 | 1:2.1 |
| 8 | 67 | 33 | 1:2.0 |
| 9 | 67 | 33 | 1:2.0 |

**Figure 4.9.** (a) HAADF-STEM overview image of several $MAPbI_3$ nanostructures of which a series of 9 EDX maps was acquired for 5 minutes each at a low magnification. Elemental maps of Pb (b), I (c), N (d) and C (e) are shown. Both the signal of Pb and I are very prominent. (f) Table depicting the atomic percentage and the relative ratio of Pb and I through the time series. A spectrum of (g) the first map and (h) the final map from 0 to 5 keV are visualized, where a decrease in both the I and N can be observed in the later.

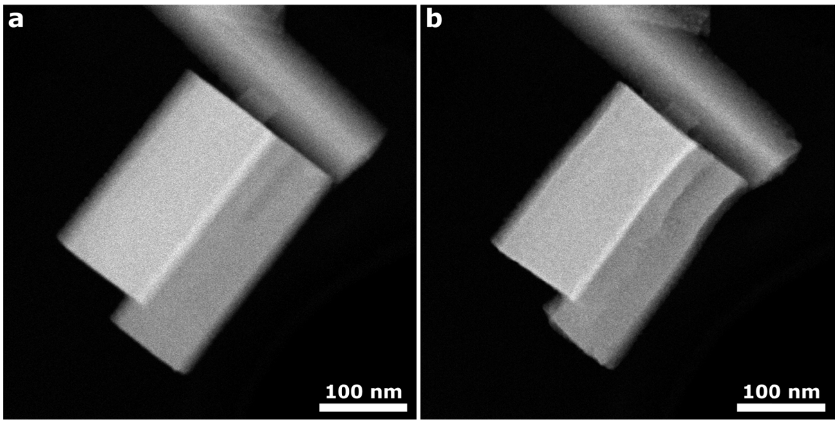

**Figure 4.10.** HAADF-STEM images of MAPbI$_3$ nanostructures (a) before and (b) after the high resolution HAADF-STEM investigation, which show some deformation.

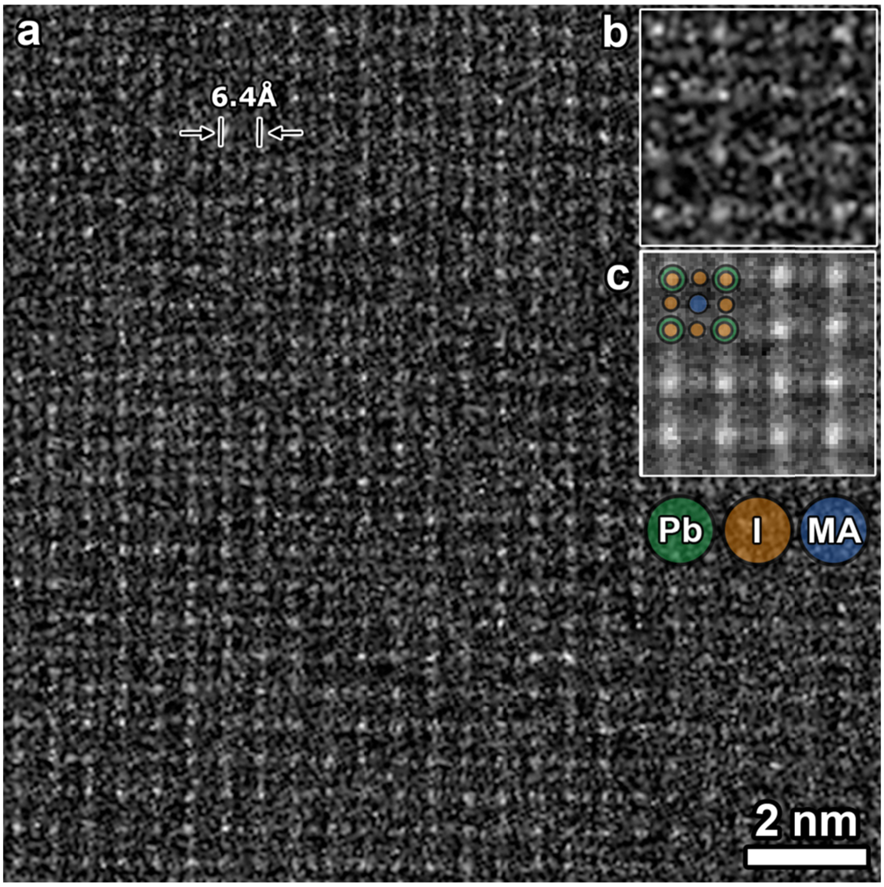

**Figure 4.11.** (a) High-resolution HAADF-STEM image of a MAPbI$_3$ nanocrystal which was acquired with a low electron dose. (b) The quality of the selected template is hampered by the low signal-to-noise ratio. (c) After template-matching, the atomic arrangement of the nanocrystal is resolved in the averaged template. The lattice parameter is approximately 6.4 Å.

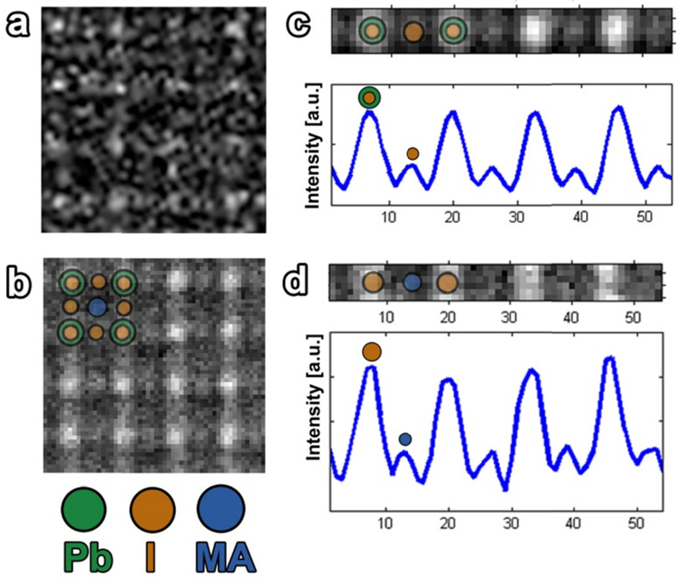

**Figure 4.12.** (a) The selected template from the low-dose high resolution HAADF-STEM image and (b) its averaged template after the template-matching procedure. In (c) and (d) an integrated line profile of each type of atomic row of the averaged template is visualized. Based on the intensity values, the atomic columns are identified.

## 5. Outlook towards alternative techniques

With the use of low dose HAADF-STEM imaging, we were able to retrieve the atomic structure of a $MAPbI_3$ nanocrystal. However, we are only able to retrieve an average visualization of the atomic structure with this approach. Investigating local defects or the surface termination of a nanocrystal is not possible using this technique. Therefore, alternative techniques are necessary to obtain a thorough characterization of such beam sensitive nanostructures.

As discussed in section 2.2, exit wave reconstruction is an alternative technique to investigate the atomic structure of (beam sensitive) nanostructures. In Figure 4.13, a HAADF-STEM image and a phase image of a $CsPbBr_3$ nanowire are shown. A series of 15 BF-TEM images was recorded with a starting defocus of 3 nm and an equidistant focal decrease of 2 nm. The actual reconstruction of the exit wave was carried out using the TrueImage software. There is no degradation at the edges of the

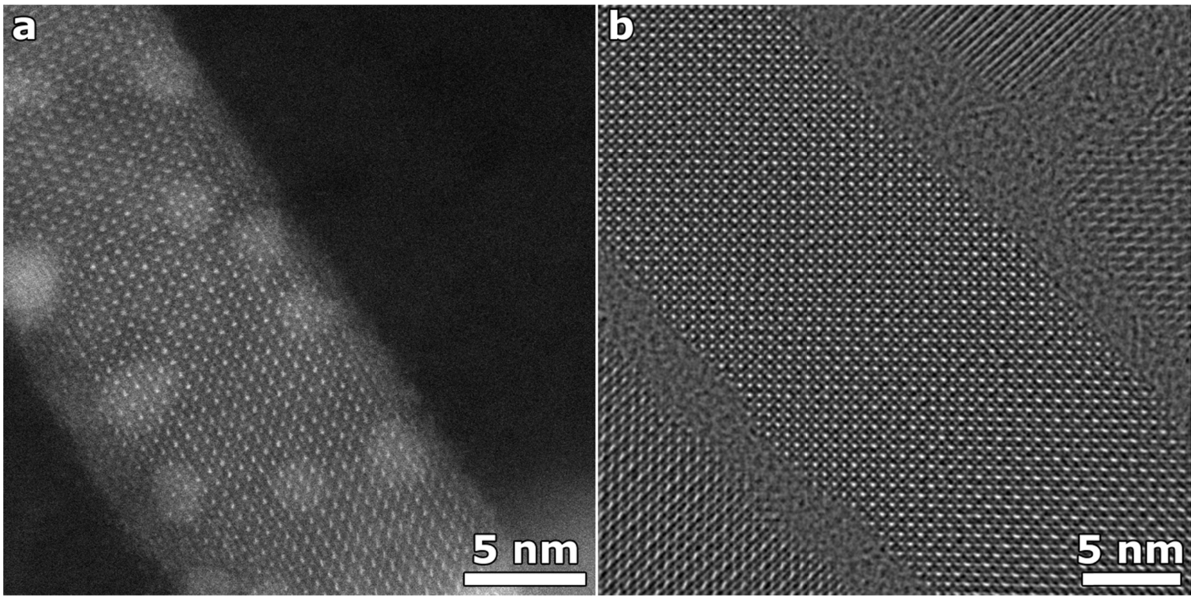

**Figure 4.13.** (a) High resolution HAADF-STEM image and (b) phase image of a $CsPbBr_3$ nanowire. In (a) a clear degradation at the edges can be observed, which does not appear during the acquisition of the focal series (b).

nanowire present in the resulting phase image (Figure 4.13.b), which is detectable in the high resolution HAADF-STEM image (Figure 4.13.a). Additionally, upon the acquisition of a focal series, the formation of Pb clusters is highly reduced in comparison to the formation upon scanning. Pb clusers can be observed as bright sports in Figure 4.13.a. We foresee an extension of this technique in 3D to study the atomic structure of beam sensitive nanostructures in 3D.

## 6. Conclusion

The atomic structure of lead cesium halide perovskite nanocrystals was characterized by the use of high resolution HAADF-STEM. Additionally, the oriented attachment from such nanoparticles into nanowires was visualized and displacements of the Cs atomic columns were detected upon a halide exchange reaction from Br to I. The investigation of organolead iodide perovskite nanocrystals was performed by low-dose HAADF-STEM imaging as these structures are extremely beam sensitive. The atomic structure of such perovskite nanocrystals was revealed by a template-matching procedure. Exit wave reconstruction is an alternative technique which can be used to study these beam sensitive perovskite nanomaterials. However, due to the sensitivity of these different perovskites, characterization studies are currently limited to 2D.

Nowadays, the development of more complex core/shell semiconductor nanocrystals is emerging. To investigate these core/shell nanostructures, both a 3D characterization on the structure and chemical nature becomes necessary. The extension of a chemical characterization with the use of HAADF-STEM tomography is discussed in the next chapter.

# Chapter 5

## Characterization of core/shell semiconductor nanoparticles

This chapter is based on: Bladt, E., van Dijk-Moes, R. J. A., Peters, J., Montanarella, F., de Mello Donega, C., Vanmaekelbergh, D., Bals, S. *Atomic structure of wurtzite CdSe (core)/CdS (giant Shell) nanobullets related to epitaxy and growth*. Journal of the American Chemical Society, 138 (2016) 14288–14293.

van der Stam, W., Bladt, E., Rabouw, F. T., Bals, S., & de Mello Donega, C. *Near-Infrared Emitting CuInSe 2 /CuInS 2 Dot Core/Rod Shell Heteronanorods by Sequential Cation Exchange.* ACS Nano, 9 (2015) 11430–11438.

Own contribution: Responsible for all TEM acquisition, analysis and interpretation.

## 1. Introduction

In Chapter 3, it has been shown that the use of HAADF-STEM tomography is valuable to obtain 3D structural information of nanomaterials. With the growing interest in complex hetero-nanostructures and more specific core/shell nanostructures, a next challenge towards a full characterization is the identification of different chemical components in the nanostructure. As pointed out in Chapter 2, the intensity in a HAADF-STEM image does not only scale with the projected thickness of the investigated nanostructure, but also with the atomic numbers of the elements present in that structure. Therefore, HAADF-STEM imaging can provide us information on the presence of different elements in a material. The only requirement is that the difference in atomic number between the elements is sufficient in order to visualize an intensity difference in the HAADF-STEM images. If this requirement is satisfied, we can extend the 3D characterization from structural to chemical by applying HAADF-STEM tomography, which makes the technique suitable for the investigation of complex hetero-nanostructures.

In this chapter, two types of semiconductor core/shell nanostructures will be characterized in 3D and both structural as well as chemical information will be acquired. In the first part, the investigation of binary core/shell nanostructures will be carried out and a second part will focus on ternary semiconductor nanocrystals.

## 2. Binary core/shell nanostructures

Semiconductor colloidal nanocrystals consisting of different compositions are of great interest since their properties can be tailored by controlling the composition, size and shape of each semiconductor component[29]. Over the last decades, a remarkable degree of precision has been achieved in the synthesis of core/shell hetero-nanostructures based on Cd- and Pd-chalcogenides (CdX and PbX with X = S, Se, Te)[29,55,57,58]. These Cd-chalcogenides hetero-nanostructures have been studied extensively as they exhibit promising photoluminescence quantum yields for the application of phosphors and biological labels[46,57,191–194]. As a spin-off of this extensive research, it also became clear that the exciton wave functions and related optical properties could be engineered by the chemical composition and dimensions of the shell. In such a manner, CdSe/CdS hetero-nanostructures were reported that (i) displayed a spatial separation of the electron and the hole wave functions[195,196], (ii) reduced Auger recombination under high excitation densities[197,198], (iii) reduced blinking when measured on the single quantum dot level[199,200]. This so-called wave function engineering demands a high control of the atomic epitaxy of the shell material on the CdSe core and of the growth of the shell material in case of thicker shells[201–203]. For small PbSe (core) / CdSe (shell) hetero-nanostructures, it has been shown that a 3D atomic characterization of the hetero-interface can be obtained by HAADF-STEM tomography[106]. This was enabled by the relative small size of the PbSe/CdSe hetero-nanostructures and the large contrast between atomic columns containing Pb or Cd. It is however far from straightforward to determine the 3D atomic structure for much larger hetero-nanostructures, e.g. consisting of a core and a giant shell as well as for structures of which the expected contrast between the two materials when imaging in HAADF-STEM mode is not strong.

In order to understand the initial growth, it is of crucial importance to locate the CdSe core in the hetero-nanostructure. In previous studies of CdSe/CdS core/shell nanorods, the location of the CdSe core could be retrieved from 2D TEM techniques such as strain analysis applied to high resolution TEM images[55] and high resolution phase imaging[204]. Due to the large size and anisotropic shape of the bullets investigated here, 2D techniques can no longer be used.

### 2.1. Characterization of the morphology

Figure 5.1.a shows a HAADF-STEM overview image of the as synthesized CdSe (core) / CdS (giant shell) hetero-nanostructures. It is clear that the CdSe/CdS core/shell hetero-nanostructures have an anisotropic shape, with hexagonal and bullet-like projections. In Figure 5.1.b two hexagonal projections of the hetero-nanostructures are presented in more detail and an intensity difference in the center can be observed. This is further illustrated by the line profiles in Figure 5.1.c and d obtained along the white rectangles indicated in Figure 5.1.b. Two different types of profiles were observed:

Type 1 shows a decrease of the intensity in the center, whereas a higher intensity is observed for type 2. Since the intensity in HAADF-STEM images scales with sample thickness, the presence of a brighter region could be related to an increment in the projected thickness of the hetero-nanostructure. However, the intensity in HAADF-STEM also scales with the atomic number Z. Intensity changes may therefore also be related to the presence of the CdSe core. In order to elucidate the origin of the intensity changes, we applied HAADF-STEM electron tomography. Tilt series of HAADF-STEM images were acquired for each type of nanoparticle over a range of ± 70°.

In Figure 5.1.e-h, the 3D reconstructions are presented, showing two different bullet-type crystal shapes: both have a hexagonal base (Figure 5.1.g and h), but at the other end either a dip (Figure 5.1.e) or a tip (Figure 5.1.f) is observed. This explains the intensity differences in the center of the hetero-nanostructures observed in the 2D HAADF-STEM images. It must be noted that 2D overview images enable us to estimate that both types of crystal shape are roughly equally present in the samples that we investigated.

### 2.2. Identification of the core location

Previous work on CdSe/CdS core/shell nanorods showed that the CdSe core can be located from 2D high resolution real-space or phase images[204,205]. Recently, EDX has been applied to visualize the CdSe core in a CdSe/CdS quantum dot in a 2D projection[206]. Because of the larger size of the crystals and the bullet shape, a 3D characterization is indispensable in the present case. Despite of the small difference in atomic number Z between the core ($Z_{Se} = 34$) and the shell ($Z_S = 16$), HAADF-STEM tomography is the preferred technique to investigate the location of the core. Although the use of chemical mapping such as EELS or EDX might be better suited to identify the CdSe core in the hetero-nanostructures, applying these techniques in 3D is not feasible since the required electron dose induced severe beam damage.

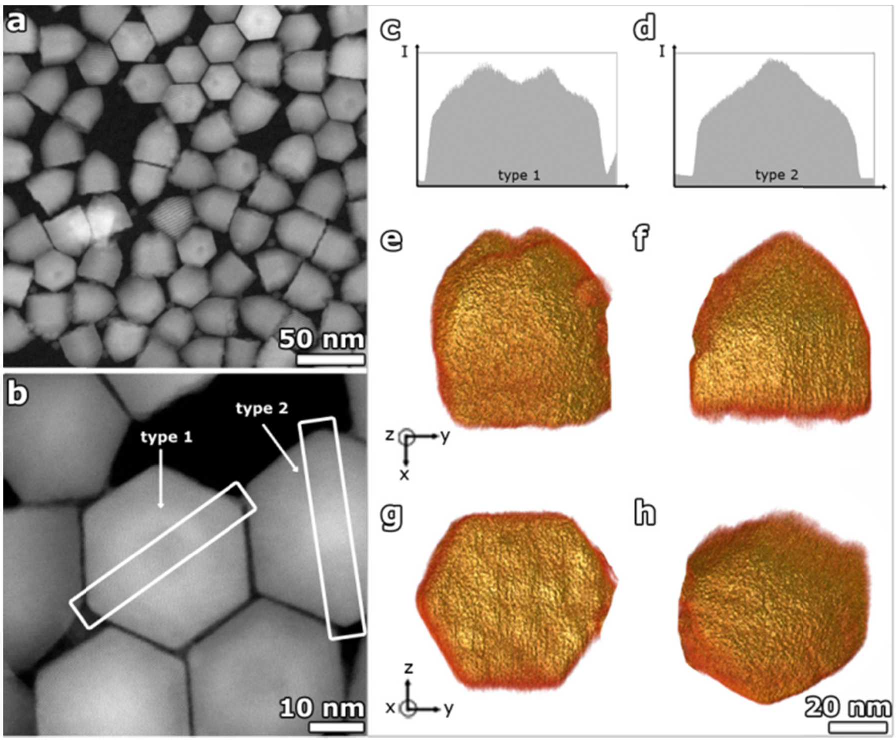

**Figure 5.1.** General shape of the CdSe (core) / CdS (giant shell) hetero-nanostructures. (a) Overview HAADF-STEM image of the CdSe (core) / CdS (giant shell) hetero-nanostructures demonstrating the hexagonal and bullet-like projections. (b) HAADF-STEM image of several CdSe/CdS hetero-nanostructures showing two types of intensity profiles: type 1 shows a lower intensity in the center of the structure, type 2 a higher intensity. (c,d) Intensity profiles acquired along the white rectangles in (b) are presented, suggesting bullets with a dip or a tip on one end. (e-h) 3D reconstructions unambiguously demonstrate the two different bullet-type crystal shapes; both have a hexagonal base (g, h), however, type 1 ends in a dip (e) and type 2 in a tip (f).

As explained in the introduction, a HAADF-STEM tomography experiment can not only provide information on the morphology but also a chemical characterization in three dimensions can be obtained. Therefore, a HAADF-STEM series was acquired over a tilt range of ± 70° with a tilt increment of 5° to investigate the core location of the CdSe core inside the hetero-nanostructure. When inspecting orthoslices through the 3D reconstruction, computed using a conventional SIRT algorithm, the CdSe core is faintly visible, therefore a correct detection of the position is difficult

(Figure 5.2.c and g). In order to better visualize the CdSe core in the CdS shell, we applied a more advanced reconstruction algorithm. As discussed in section 4.3.2 in Chapter 2, the TVM algorithm is based on the assumption that the gradient of the object under investigation is sparse[159]. As a consequence, edges in the 3D reconstruction will be enhanced. Orthoslices through the TVM reconstruction, obtained at the same position as Figure 5.2.c and f are presented in Figure 5.2.d and h. The results show that the core is not located in the center of the CdS crystal (Fig 5.2.a,b and 5.2.d,e), but closer to the tip or dip of the bullets. Previous studies on CdSe/CdS core/shell nanorods also showed an asymmetric position of the CdSe core along the nanorod axis[55,201,204,207]. Overall, the distance between the CdSe core position and the hexagonal base is comparable for both bullet shapes, suggesting a very similar growth process for both morphologies.

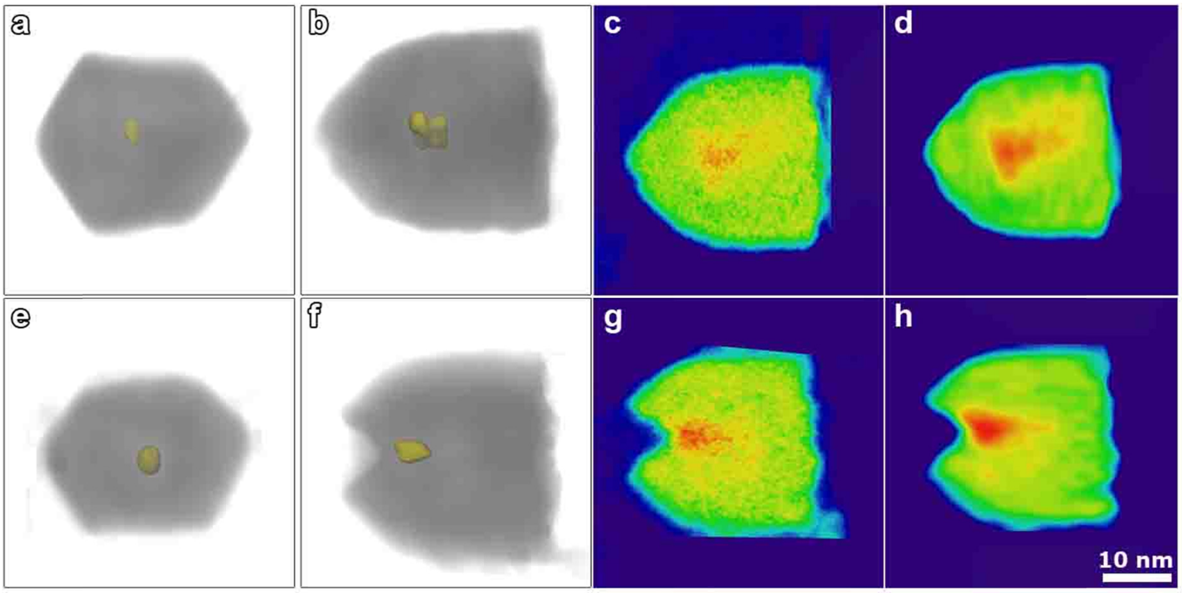

**Figure 5.2.** HAADF-STEM tomography on bullet-shaped CdSe/CdS hetero-nanocrystals to detect the position of the CdSe core. The location of the CdSe core is shown in yellow in the 3D reconstructions of the two types of bullet-shaped hetero-nanostructures, type 2 with a tip (a,b) and type 1 with a dip (e,f). The orthoslices through the conventional SIRT reconstruction of the hetero-nanostructures ending in a tip (c) and ending in a dip (g) provide a faint intensity contrast between the CdS shell and the CdSe core. When applying the TVM algorithm, the heavier CdSe core is clearly visible in the orthoslices (d and h).

### 2.3. Facet determination

As the two types of bullet-shaped nanocrystals yield a similar position for the CdSe core, the epitaxy and growth of the CdS crystalline shell is expected to be very similar for both types. In order to evaluate the surface energy of both types, the facets of the hetero-nanostructures need to be identified. Previous studies have shown that the facets of nanocrystals can be investigated by electron tomography[101,208,209]. Here, it is not straightforward because of the relatively small number of projection images in the tilt series. The lack of information will induce a more rounded shape, which hampers an unambiguous characterization of the facets from a 3D experiment. Therefore, we additionally used direct high resolution HAADF-STEM imaging to determine the facets of the CdSe/CdS bullets. Figure 5.3 shows a high resolution HAADF-STEM image acquired along the (long) [001] direction. The hexagonal arrangement of the atomic columns (Figure 5.3.c) at the base of the hetero-nanostructure demonstrates that the CdSe/CdS core/shell hetero-nanostructures have a wurtzite crystal structure. Since the wurtzite structure is non-centrosymmetric, anisotropic growth is expected, which is confirmed by the position of the CdSe core (see above). However, this is in disagreement with the principles of the successive ion layer adhesion and reaction (SILAR) method[210,211] designed for layer-by-layer growth. It is well possible, that even in the SILAR method, the growth occurs by molecular attachment of CdS units instead of Cd and S in subsequent steps[29,212,213]. This would preserve the facet polarity and anisotropy. Moreover, a slight excess of the added precursors would enable preferential growth in the polar [00-1], S-terminated direction. Next to the identification of the crystal system, the lateral facets can be examined from the high resolution HAADF-STEM image (Figure 5.3.a) and its corresponding diffractogram (Figure 5.3.b). From these images, the lateral facets are identified as {-110} planes. In Figure 5.3.d, a schematic overview is shown to support the viewing directions with respect to the hexagonal base of a hetero-nanostructure.

In order to investigate the facets that form the tip or the dip, high resolution images acquired along an edge between two lateral facets, corresponding to the [110] direction, are evaluated. In this direction, the angle between a lateral facet and a facet forming the tip can be measured. In this manner, we

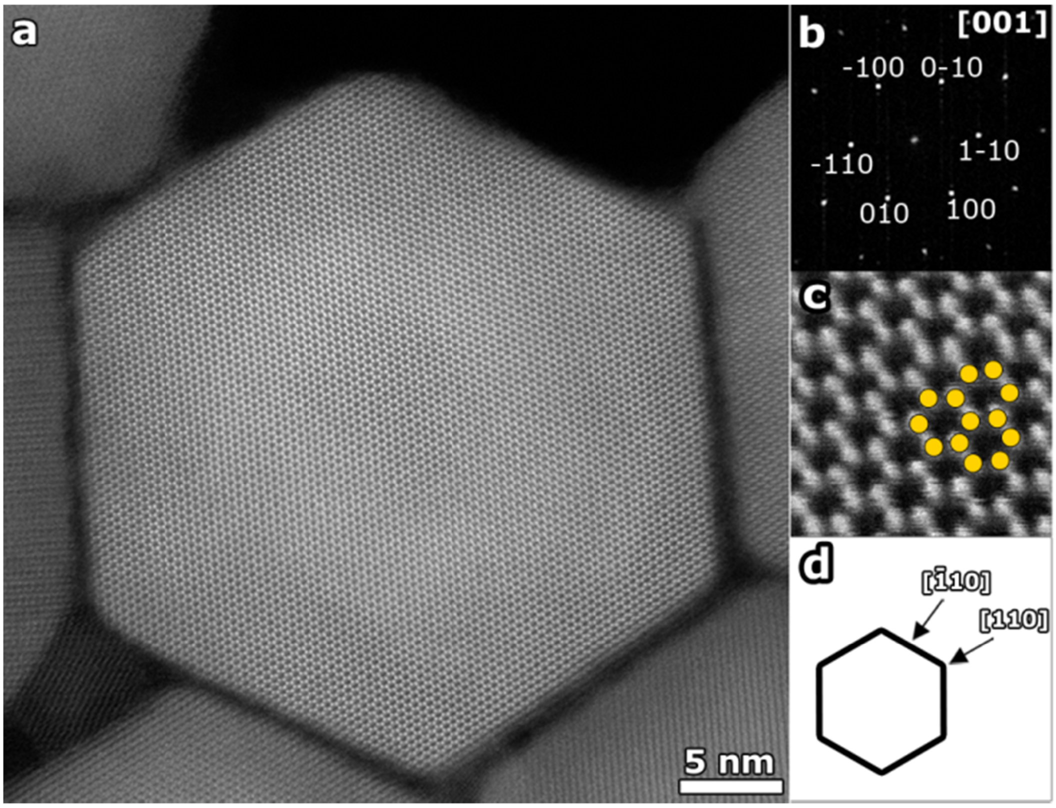

**Figure 5.3.** Atomically resolved HAADF-STEM image acquired along the long axis of the bullets. (a) High resolution HAADF-STEM image of a CdSe/CdS bullet-shaped nanocrystal with its corresponding diffractogram (b). The image acquired along the [001] direction shows the hexagonal pattern characteristic for wurtzite. (c) A more detailed view of the atomic arrangement is shown. (d) Schematic of the base of a CdSe/CdS hetero-nanostructure with indication of the [110] and [-110] viewing directions.

conclude that the facets at the tip correspond to {1-11} planes. For the type 1 CdSe/CdS bullets with a dip, the d1 and d4 facets (Figure 5.4.c) are identical to the facets forming the tip of the type 2 bullets. The dip forming facets were identified by studying the decrease in intensity in the high resolution HAADF-STEM images due to the presence of the dip. A more detailed comparison is shown in Figure 5.4.b and d. Analyzing the d2 and d3 facets in Figure 5.4.c shows that the d2 facet is parallel to the d4 facet and d3 is parallel to d1. This indicates that both types of bullet shapes have identical facets, and a comparable total surface energy.

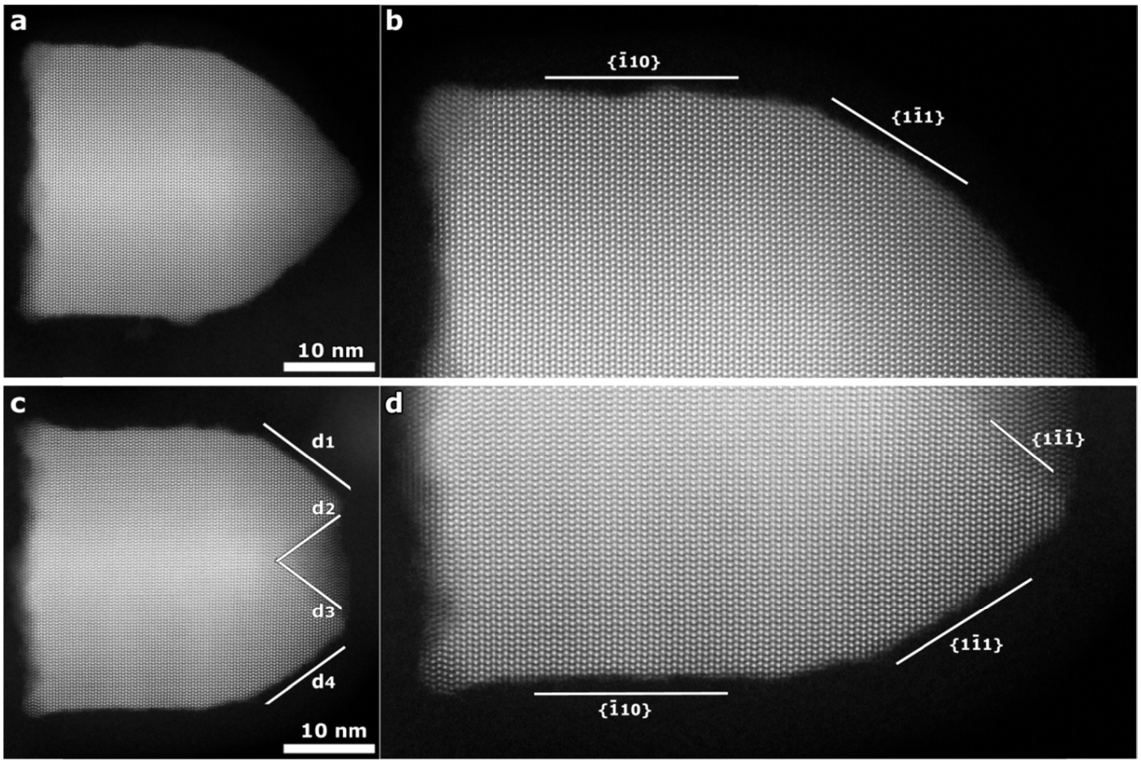

**Figure 5.4.** Identification of the facets at the tip or dip of the CdSe/CdS bullet-shaped hetero-nanostructures. (a,c) High resolution HAADF-STEM images of both types of bullet-shaped nanocrystals, with a more detailed view in (b,d). The lateral facets correspond to [-110] planes. For both types of bullet shapes, the facets originating from the lateral facets towards the dip or tip correspond to [1-11] facets. The type 1 hetero-nanostructures ending in a dip have additional facets ending in the dip, indicated as (d2 and d3). In (c) it is shown that these facets (d2, d3) are parallel to facet d1 and d4, respectively.

The complete characterization of the atomic structure and facets of the bullet-shaped CdSe (core) / CdS (giant shell) hetero-nanostructures suggest a mechanism of CdS epitaxy and growth. It was mentioned above that the growth most probably occurs by attachment of CdS units, rather than separate Cd and S layers. The presence of excess CdS molecular units allows a distinct faster growth of the S-terminated [00-1] facets in the direction of the polar c-axis[29]. An atomic simulation of the growth of the giant CdS crystal around the CdSe core is beyond the scope of the present work. Here, we present an intuitive picture, based on the atomic characterization of the bullet-shaped hetero-nanocrystals presented above, schematized in Figure 5.5.

The CdSe core has a wurtzite crystal structure, and induces wurtzite growth of the CdS shell. In the early stage of the process (Figure 5.6), epitaxial formation of CdS occurs on all facets, but the growth of wurtzite CdS in the [00-1] direction with a S-terminated facet is faster than in the opposite [001] direction terminated by Cd. This is similar to the growth of CdSe/CdS rods. Such strongly anisotropic growth rates are well documented for wurtzite type crystals[214–216]. In a later stage, the cylindrical crystal shape with hexagonal base typical for wurtzite crystals becomes increasingly pronounced. The

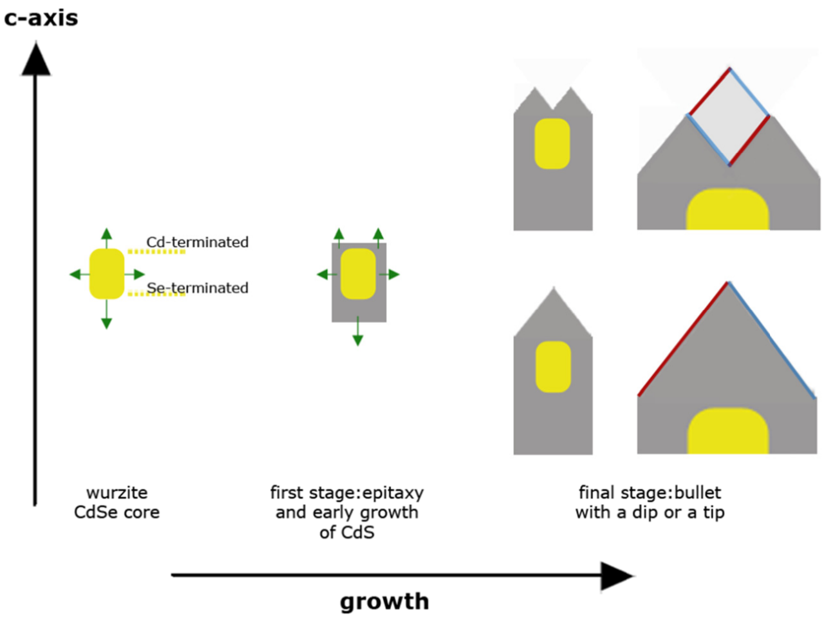

**Figure 5.5.** Scheme of the anisotropic growth of the giant CdS shell on the CdSe core. From left to right: slightly elongated wurtzite CdSe crystal core; the green arrows indicate the relative growth rates of the CdS in the [001], [00-1] and [110] directions. In the first stage (Figure 5.6), there is epitaxy and starting growth of a hexagon-based CdS crystal. Later stages show either a growth in the [001] on top of the crystal accompanied by horizontal ingrowth, resulting in a bullet with a dip; or a growth of the inward facets which result in bullets with a tip. The facets forming the dip are indicated in red and blue to show that a bullet with a tip is build up by exactly the same facets.

growth along the [00-1] is fast with respect to the opposite direction and the six lateral directions of the CdS crystal, which grow more slowly. Growth in the direction perpendicular to the c-axis can also occur inwards (arrows not shown) resulting in a bullet shape with a dip. Possibly, the dip width and depth is gradually reduced by inwards CdS growth. In any case, stable {1-11} facets present in the dip lead to a low surface energy, and slow growth. It remains ambiguous whether the type 1 and type 2 bullet-shaped hetero-nanostructures are equally stable polymorphs, or alternatively, that the type 1 bullets are an unfinished stage, finally resulting into the final bullet-shaped hetero-nanostructures with a tip. However, based on the facet characterization and equal presence of both types of morphologies, it is suggested that both types are equally stable. The end-facets at the tip indicate that the {1-11} facets are more stable than the Cd-terminated {001} facets.

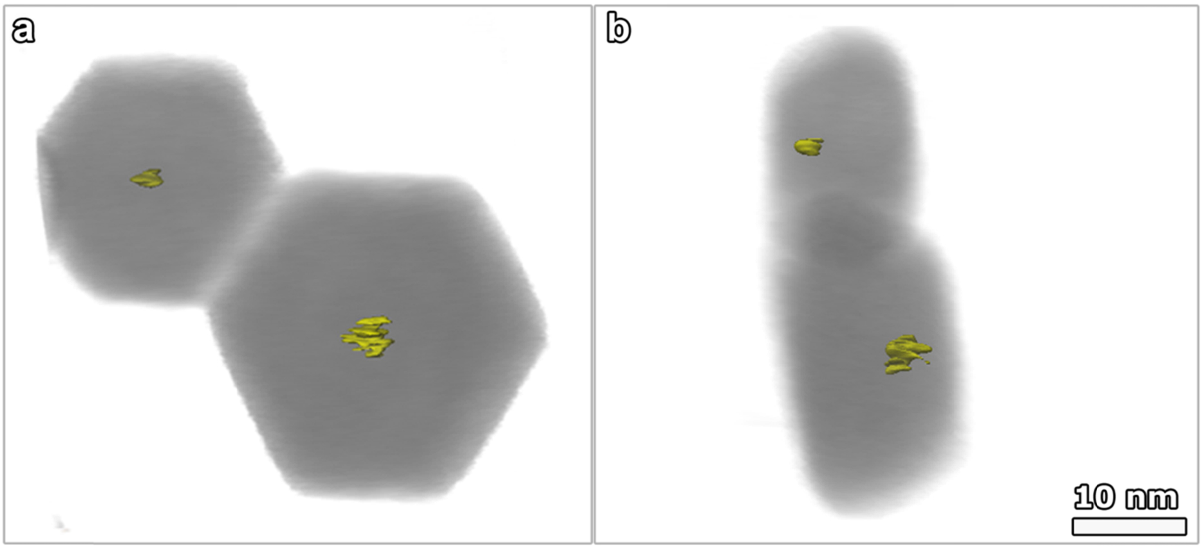

**Figure 5.6.** HAADF-STEM tomography on the first stage of the CdSe/CdS nanobullets with indication of the position of the CdSe core. The location of the CdSe core is shown in yellow in the 3D reconstructions (a,b), showing that the core is located closer to one of the basal facets.

## 3. Ternary core/shell nanostructures

The further deployment of Cd- and Pb-chalcogenides is limited by the toxicity of Pb and Cd. Therefore, a worldwide research effort to define alternative materials with comparable properties and less toxicity has been stimulated. Nanocrystals based on ternary I-III-VI semiconductors such as $CuInX_2$ are an attractive option, since their photoluminescence is tunable from the visible to the near-infrared light. Therefore, such materials are promising for applications such as light-emitting devices, biomedical imaging and solar energy conversion[62–66]. However, the synthesis of ternary nanocrystals is challenging since multiple precursor reactivities must be simultaneously controlled. Therefore, direct synthesis protocols for colloidal $CuInX_2$ nanocrystals remain still largely underdeveloped[67–71,217] and do not offer the same level of control as available for Cd-based nanocrystals. To date, it has not been possible to grow luminescent anisotropic ternary nanocrystals, or to combine two different $CuInX_2$ compounds into a single hetero-nanostructure by hetero-epitaxial overgrowth. A novel method was proposed in [207] where luminescent $CuInSe_2/CuInS_2$ (CISe/CIS) dot core/rod shell heteronanorods could be obtained by applying sequential topotactic cation exchange reactions ($Cu^+$ for $Cd^{2+}$ followed by self-limited partial $In^{3+}$ for $Cu^+$) to template Cd-chalcogenide hetero-nanostructures. During these reactions, the size, shape and hetero-architecture of the template nanocrystals should be preserved. HAADF-STEM tomography is hereby applied to study this preservation as both a structural and a chemical characterization in three dimensions are indispensable when investigating these ternary semiconductor hetero-nanostructures.

### 3.1. Characterization of the morphology

The template Cd-chalcogenide hetero-nanostructures used in this approach are the well-known CdSe/CdS nanorods, which show efficient photoluminescence at 2.07 eV and an absorption spectrum dominated by CdS transitions. In Figure 5.7.a, a HAADF-STEM image of multiple CdSe/CdS core/shell nanorods is shown. A careful observation reveals that some of the nanorods have a rather

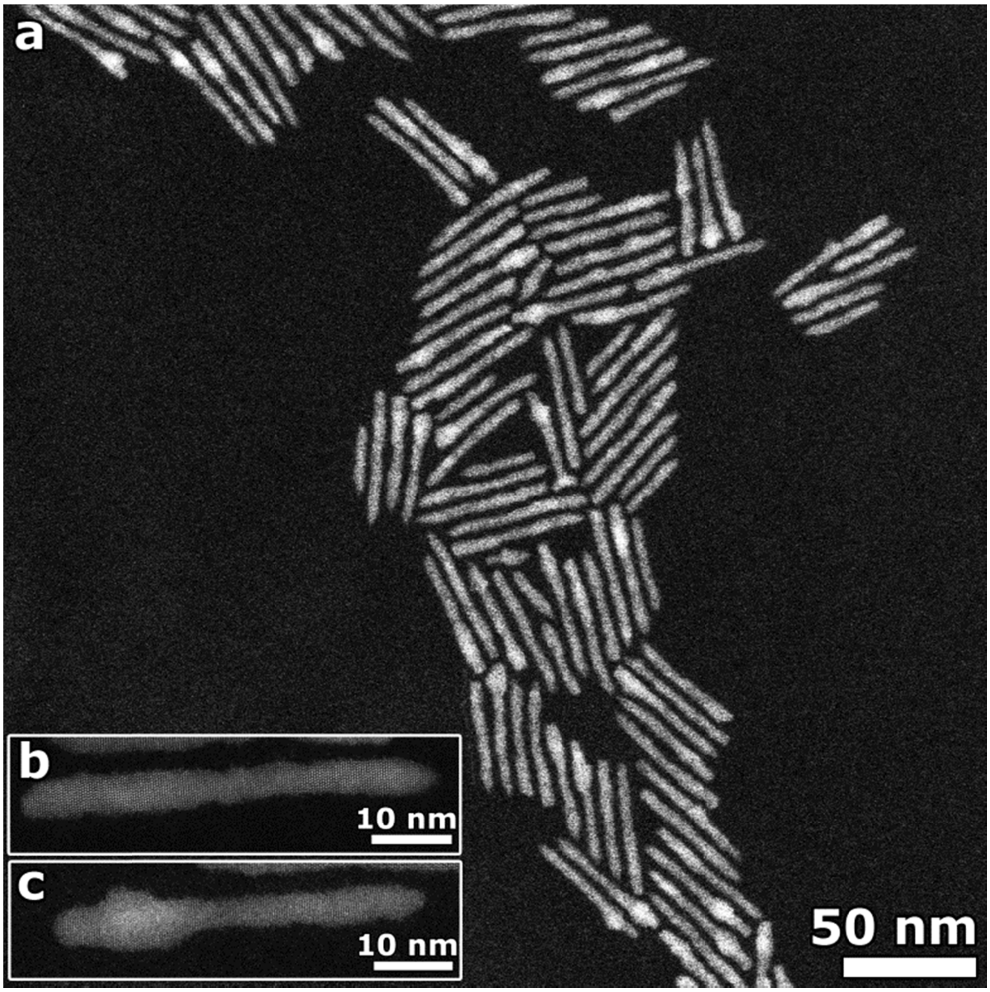

**Figure 5.7.** (a) HAADF-STEM image of multiple parent CdSe/CdS core/shell nanorods. Both nanorods with (b) a rather uniform thickness and with (c) a thicker part at one side of the nanorod is observed.

uniform thickness (Figure 5.7.b) and others have a thicker part located at one side of the nanorod (Figure 5.7.c). The size of the nanorods ranges from approximately 40 nm to 55 nm. In a first topotactic cation exchange reaction of $Cu^{+}$ for $Cd^{2+}$, the nanorods become non-luminescent and exhibit an absorption spectrum typical of Cu-chalcogenides. Afterwards, the Cu-based nanorods are subjected to a partial $In^{3+}$ for $Cu^{+}$ cation exchange that yields CISe/CIS core/shell nanorods with photoluminescence in the near-infrared light centered at 1.22 eV and an absorption spectrum that is consistent with the CuIn-chalcogenide based nanocrystals. In Figure 5.8.a and b, a HAADF-STEM image of several of the intermediate $Cu_2Se/Cu_2S$ core/shell nanorods and of the final CISe/CIS core/shell nanorods are visualized, respectively. For both the intermediate as the final products, we can observe nanorods with a more uniform thickness and nanorods which have a thicker part on one side, which were already present in the parent CdSe/CdS core/shell nanorods. After the final cation exchange reaction, a byproduct of In is formed next to the CISe/CIS core/shell nanorods. From these HAADF-STEM images at the nanoscale, the size of the different nanorods is investigated and similar sizes are confirmed. However, to study the thickness of the different core/shell nanorods high resolution HAADF-STEM imaging is most suitable, since the thickness of the different nanorods can be examined up to the atomic scale.

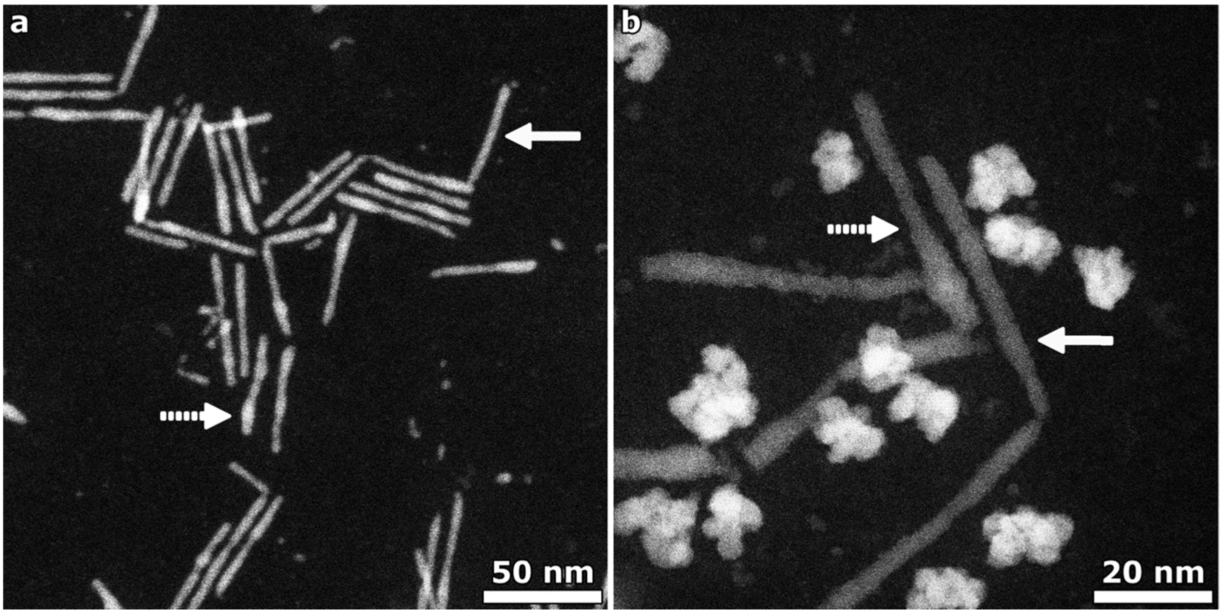

**Figure 5.8.** HAADF-STEM images of (a) the $Cu_2Se/Cu_2S$ core/shell nanorods and (b) the CISe/CIS core/shell nanorods, respectively. The full arrows indicate the presence of nanorods with a uniform thickness and the dotted arrows nanorods with a thicker part at an asymmetric position in the rod. The presence of an In byproduct can be observed as bright irregular nanostructures.

To elucidate on the lateral thickness of the nanorods, a visual inspection of the high resolution HAADF-STEM images is sufficient. In Figure 5.9.a, a high resolution HAADF-STEM image of the parent CdSe/CdS core/shell nanorods is visualized. Investigation of multiple CdSe/CdS core/shell nanorods shows that the parent nanorods have a lateral thickness of approximately 9 to 15 atomic layers, which corresponds to a thickness of approximately 2.87 to 5.02 nm. High resolution HAADF-STEM investigation indicated that the intermediate $Cu_2Se/Cu_2S$ core/shell nanorods (Figure 5.9.b) are not highly symmetrical which could correspond to the monoclinic structure (inset of Figure 5.9.b). As the nanorods are beam sensitive, a main zone could not be reached before the nanostructure was damaged, which prohibited a measurement of the thickness with atomic precision. However, we are most interested in the final product and characterized the lateral thickness of the CISe/CIS core/shell nanorods (Figure 5.9.c) as approximately 8 to 14 atomic layers thick, which corresponds to a thickness of 2.70 to 4.73 nm, approximately. One could still wonder whether the nanorods are symmetrical or that the thickness parallel to the electron beam is elongated. In order to retrieve this thickness information, atom-counting on the high resolution HAADF-STEM images is needed. To perform such atom-counting, the StatSTEM program was used to perform a model-based quantification of the atomic columns[107,178,179]. In Figure 5.10 the result of such counting for the parent CdSe/CdS nanorod is shown, from which we can conclude that the rod is symmetrical as also in that direction a maximum thickness of 15 atoms is found. From these thickness measurements, we can conclude that the size of the core/shell rods does not change by applying these sequential topotactic cation exchange reactions. Next to the investigation of the thickness with atomic precision, the crystal structure of the core/shell nanorods can be investigated by high resolution HAADF-STEM imaging. A fast Fourier Transform (FFT) analysis of the high resolution HAADF-STEM images confirms that both the parent CdSe/CdS and final CISe/CIS core/shell nanorods exhibit a wurtzite crystal structure. As the majority of the volume of the parent core/shell nanorods consists of CdS, the contribution of the CdSe core is not detected in the FFT analysis (inset of Figure 5.9.a). For the final core/shell nanorods, the same conclusion can be made as there is no contribution of the CISe core detected in the FFT image (inset of Figure 5.9.c).

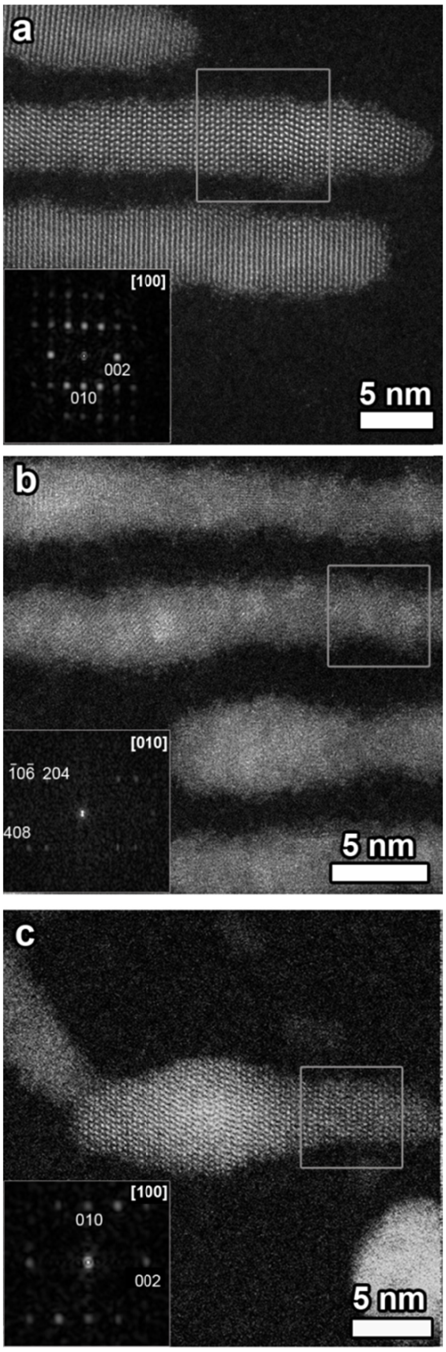

**Figure 5.9.** High-Resolution HAADF-STEM images of (a) CdSe/CdS core/shell nanorods, (b) $Cu_2Se/Cu_2S$ core/shell nanorods and (c) CISe/CIS core/shell nanorods. The rectangles indicate the regions where a diffractogram was obtained. The corresponding patterns show characteristic {010} and {002} wurtzite CdS reflections for CdSe/CdS core/shell nanorods, characteristic chalcocite $Cu_2S$ reflections for $Cu_2Se/Cu_2S$ core/shell nanorods and characteristic wurtzite CIS reflections for CISe/CIS core/shell nanorods.

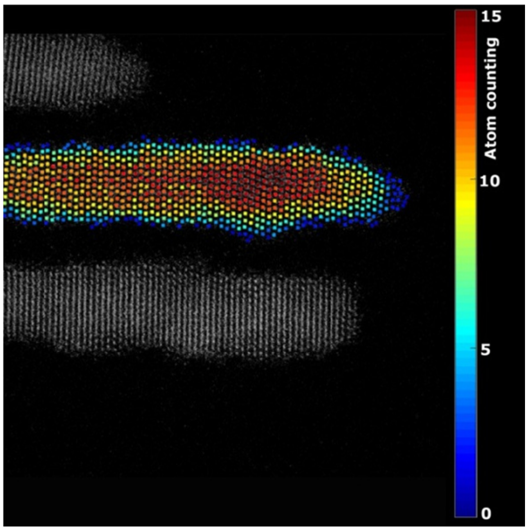

**Figure 5.10.** Atom-counting results of a parent CdSe/CdS nanorod, from which a maximum thickness of 15 atoms is calculated.

### 3.2. Identification of the core location

In Section 2.2, both the 3D morphology and the 3D position of the core of the CdSe/CdS core/shell nanobullets were successfully characterized by the use of HAADF-STEM electron tomography. As the ternary core/shell nanorods from this study have some similarities with the nanobullets, the same approach is used to investigate the exact 3D position of the cores inside the shell of the ternary core/shell nanorods. However, here, the acquisition of several images at the same position of interest caused a lot of carbon contamination, due to the ligands covering the nanorods. Therefore, the support grids were baked at 120 °C for several hours in order to remove the organic ligands from the surface of the nanorods. After this treatment, the organic contamination decreased, but also the shell of the $Cu_2Se/Cu_2S$ and the CISe/CIS core/shell nanorods was slightly altered (Figure 5.11.a and d). For all the nanorods, HAADF-STEM tilt series of 15 projection images were acquired with an angular range of -70° to +70° and a tilt increment of 10°. Typically more projection images are required for a conventional electron tomography experiment, but even after the baking treatment, there was still contamination remaining which hampered the acquisition of more projection images. Nevertheless, the positions of the cores were successfully determined and the 3D reconstructions show that the cores have an asymmetric position inside the rod (Figure 5.11.a,d,g). Additionally it seems that the cores are slightly elongated, however we cannot define the shape unambiguously because of the limited amount of projection images.

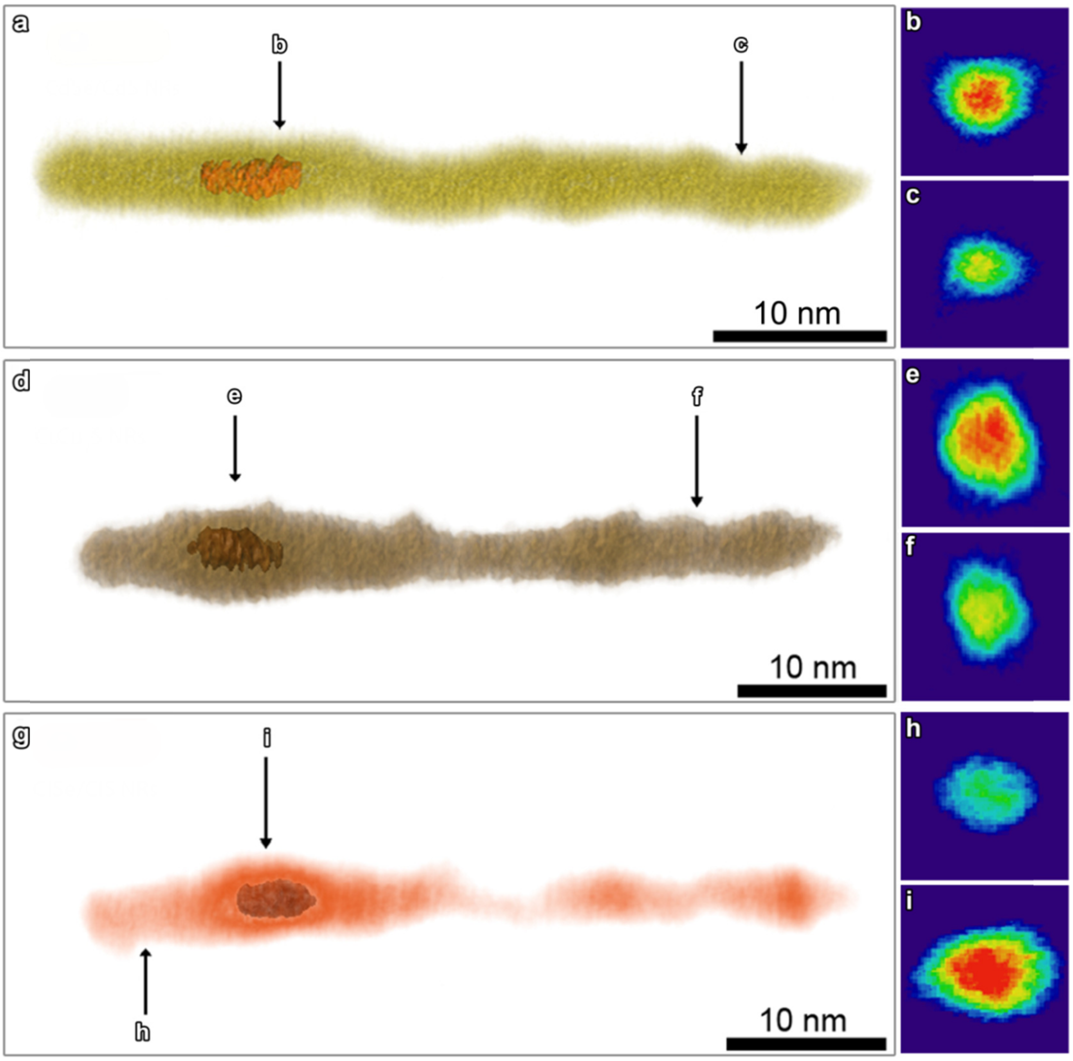

**Figure 5.11.** Visualizations of tomographic 3D reconstructions of (a) the template CdSe/CdS core/shell nanorods (yellow: CdS, orange: CdSe), (d) the intermediate $Cu_2Se/Cu_2S$ core/shell nanorods (light brown: $Cu_2S$, dark brown: $Cu_2Se$) and (g) the final product CISe/CIS core/shell nanorods (light red: CIS, dark red: CISe). Orthoslices at the positions marked with b and c for CdSe/CdS nanorods, e and f for $Cu_2Se/Cu_2S$ nanorods and h and i for CISe/CIS nanorods show the position of the Se-containing cores, due to the difference in Z-contrast ($Z_{Se}$=34 and $Z_S$=16).

## 4. Conclusion

HAADF-STEM tomography was used to characterize both the shape and chemical components in 3D of CdSe/CdS core/shell nanobullets and CISe/CIS core/shell nanorods. An important question on core/shell hetero-nanostructures is the position of the core inside the nanostructures as from this position the growth of the nanostructure is initiated. Here, an asymmetric core position was found in these semiconductor binary nanobullets and ternary nanorods. A limitation to this approach is the need for sufficient intensity difference between the chemical components. If a hetero-nanostructure consists of two or more chemical components with comparable atomic numbers, HAADF-STEM imaging or tomography will not provide any chemical information on the nanostructure. In order to study a broader variety of hetero-nanostructures, a more general technique is necessary to investigate the chemical character of these structures. In the next chapter, a 3D spectroscopic technique is introduced to extend the chemical characterization towards a broader variety of complex hetero-nanostructures.

# Chapter 6

## Energy dispersive X-ray tomography

## 1. Introduction

In the previous chapter, it was shown that by using HAADF-STEM tomography, 3D chemical information can be obtained up to a certain extent. A careful analysis of the intensities in the 3D reconstruction is required to distinguish between certain elements and hence, this is only possible when their atomic numbers are sufficiently different. Therefore, alternative chemical characterization approaches should be explored. In Chapter 2, different imaging modes in electron tomography were discussed and it was mentioned that by the use of a novel detection system, EDX tomography becomes possible. As the Super-X detection system was only developed recently[136], a thorough study on its applicability for quantitative 3D EDX is necessary. Au/Ag core/shell nanostructures will be used for this purpose since these particles are ideal to evaluate the technique since chemical information can also be retrieved using HAADF-STEM imaging and tomography.

## 2. EDX from 2D to 3D

### 2.1. 2D EDX mapping

As explained in Chapter 2, EDX can be used to map the chemical elements present in a specific nanomaterial. To summarize, the incoming electrons of the electron beam transfer energy to an inner shell electron of an atom in the specimen, creating an electron hole. A higher energy electron from an outer shell will fill up the created electron hole and an X-ray will be emitted. The energy of the X-ray will equal the energy difference between the outer and inner shell energy. Thereby, the recorded elemental spectrum is characteristic to the elements which are present in the nanostructure. Recording these generated X-rays in a TEM results in an elemental map of the investigated material as in each pixel a spectrum is recorded. The intensity $I_A$ of the characteristic X-ray peaks for an element $A$ present in the nanostructure equals to[218]:

$$I_A = \frac{C_A \omega_A Q_A s}{Z_A}, \tag{6.1}$$

with $C_A$ the weight fraction of element $A$, $\omega_A$ the fluorescence yield, $Q_A$ the ionization cross-section, $s$ the thickness of the specimen and $Z_A$ the atomic number. As the intensity of the peak and thereby the number of generated X-rays, scales with the thickness $s$ of the specimen, a 2D elemental map can in principle serve as a projection image for electron tomography, as the projection requirement seems to be fulfilled.

## 2.2. Practical aspects of EDX tomography

### 2.2.1. Detector set-up

As mentioned in Chapter 2, early attempts to perform EDX tomography were hampered by the sample-detector geometry since the EDX detector is typically placed under a specific tilt angle to the specimen[219]. The amount of detected X-rays will therefore depend on the sample position with respect to the detector. The optimal signal will be collected when the sample is tilted towards the detector, while at specific tilt angles the signal will be blocked by shadowing effects. Thereby, the first 3D EDX results were obtained on needle-shaped samples where shadowing effects are avoided during the acquisition of the tilt series[134,135].

A few years ago, a new detector geometry was introduced where four X-ray detectors are placed symmetrically around the sample[136], which is schematically shown in Figure 6.1. The aim of this Super-X detection system was to reduce the blocking of the generated X-rays by the holder with respect to the position of the holder towards the X-ray detectors. With the design and production of this new EDX detector set-up, advances in EDX tomography become within reach. However, before performing an EDX tomography experiment, the Super-X detection system needs to be thoroughly examined to confirm its usability in electron tomography, which will be discussed in the next section.

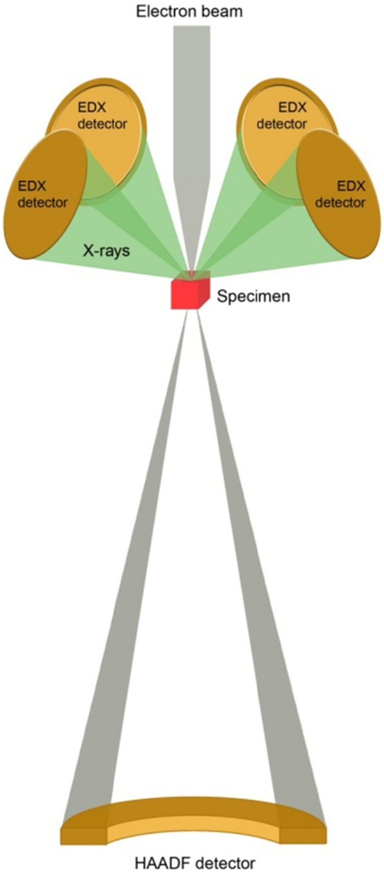

**Figure 6.1.** Super-X detection system which has four X-ray detectors symmetrically placed around the specimen. A HAADF-STEM image can be acquired simultaneously while detecting the generated X-rays.

### 2.2.2. Acquisition of tilt series of EDX maps

In the next section, a thorough analysis of the Super-X detection system is carried out to elucidate on the applicability of an EDX tilt series for tomography. In section 2.1 we concluded that the detected X-ray signal is linearly dependent on the thickness of the investigated sample. This means that in theory a 2D EDX map can serve as a projection image for tomography. However, further investigations are necessary as the signal generated by a nanoparticle should be constant throughout the full tilt series. Different acquisition approaches are examined in order to propose the optimal acquisition approach for EDX tomography.

**Acquisition methodology**

With the Super-X set-up, it is expected that the shadowing effects due to the position of the holder towards the detectors are minimized and thereby that the total amount of detected characteristic X-rays for a nanoparticle is independent of the tilt angle. This assumption, however, needs to be investigated with care, if we want to perform a reliable EDX tomography experiment. Therefore, we studied the detected X-ray counts of a nanoparticle for different dedicated microscopy holders at different tilt angles. As at all the different tilt angles, the whole nanoparticle is scanned, the total amount of characteristic X-rays should be constant. In a first experiment, we investigated the outcome for a conventional single tilt tomography holder (Fishione model 2020, Figure 6.2.a). Each 10°, an EDX map was acquired of a SiO nanoparticle from -70° to +70°. In Figure 6.2.a.1, the detected X-ray counts are visualized in function of these tilt angles for each individual detector. From this graph, it is clear that the detected X-ray signal is still dependent on the tilt angle. A clear decrease in the amount of detected X-rays at the lower tilt angles can be observed (Figure 6.2.a.2). This shows that still a large amount of generated X-rays does not reach one of the four detectors. At certain tilt angles the X-rays are blocked by the holder, therefore its geometry determines the detected X-ray signal profile. The investigation of a Si needle mounted on an on-axis tomography holder (Figure 6.2.b) confirms that shadowing effects are largely reduced when investigating a needle-shaped sample, which is visualized in Figure 6.2.b.1-2. As we are focused on the investigation of nanoparticles, the use of needle samples is not straightforward as its preparation is challenging and time-consuming[146]. Therefore, this experimental design was mimicked by attaching a regular TEM grid to the tip of the on-axis tomography holder (Fishione model 2050). The experimental set-up is illustrated in Figure 6.2.c, which shows that possible shadowing can only come from the support grid itself. In Figure 6.2.c.1-2, a reduction of shadowing effects can be observed in comparison to the use of a single tilt tomography holder, but there is still a dependence on the tilt angle. These studies have led us to a more novel dedicated tomography holder (Fishione model 2030, Figure 6.2.d), which uses the same principle as the experimental test set-up we designed. This novel holder was developed to keep the

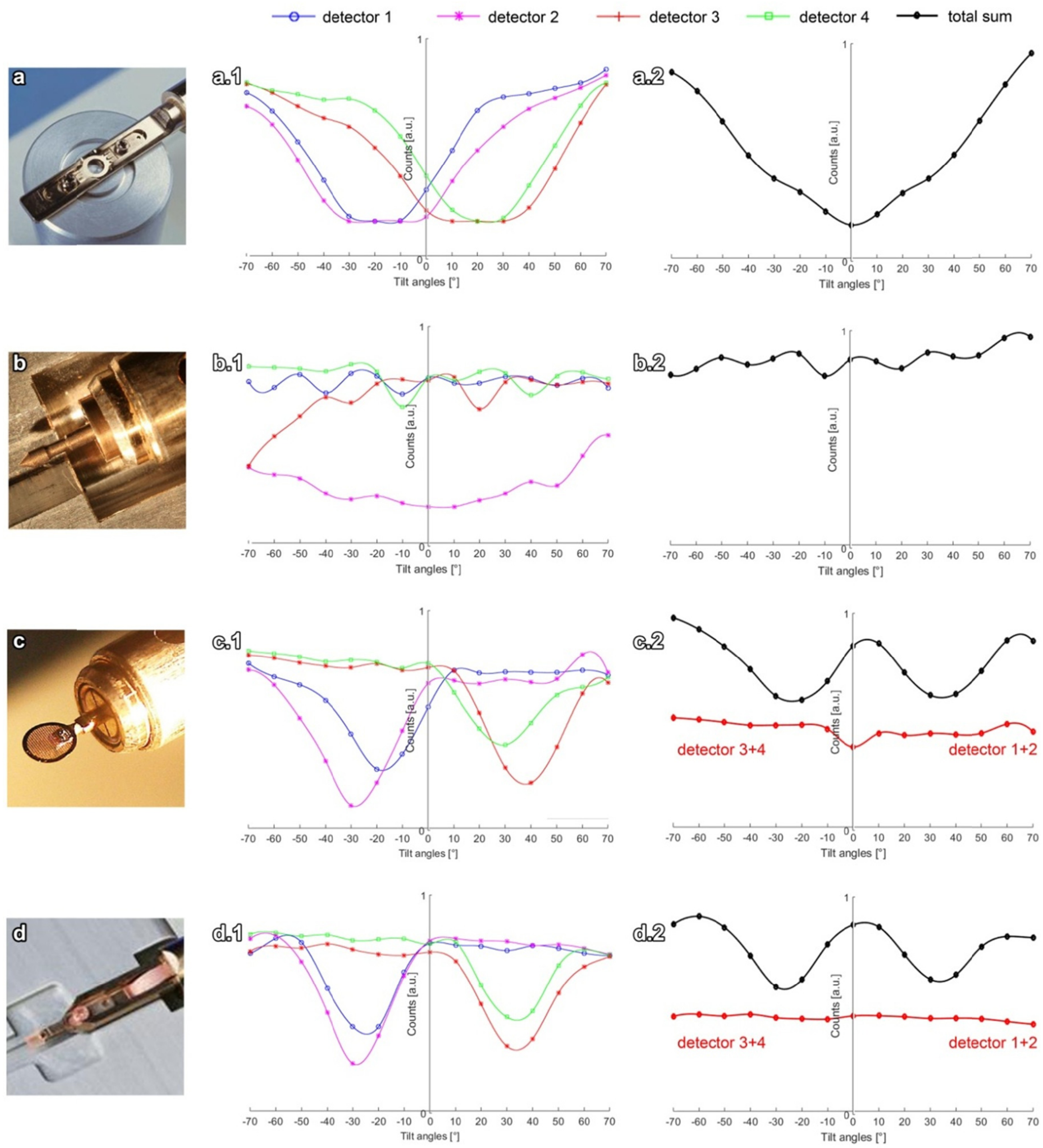

**Figure 6.2.** Detected X-ray counts as function of tilt angle. Four different tomography set-ups are evaluated: (a) a Fischione 2020 tomography holder, (b) an on-axis Fischione 2050 holder with a needle-shaped specimen, (c) an on-axis tomography holder with a support grid glued at the tip and (d) a Fischione 2030 tomography holder. The number of detected X-rays is plotted as function of the tilt angle for each detector separately (a.1, b.1, c.1 and d.1) and for the sum of all the detectors (a.2, b.2, c.2 and d.2). When the correct detectors are summed for the last two experimental set-ups, the resulting signal is independent of the tilt angle.

shadowing to a minimum; however, even here an asymmetric collection efficiency of the separate detectors is still observed as a function of tilt angle. In Figure 6.2.d.1, the detected X-ray counts for the different detectors are visualized. In order to use EDX maps as reliable input for a tomography experiment, we therefore propose to combine EDX signals of certain detectors to obtain EDX maps which satisfy the projection requirement. By combining the signal of detector 3 and 4 at negative tilt angles and the signal of detector 1 and 2 at positive tilt angles, we overcome shadowing effects and a more linear signal in function of the tilt angle is found (Figure 6.2.d.2). With this investigation, we show that even with a more advanced detection system, one should be careful with the acquisition of a tilt series of EDX maps to obtain reliable 3D EDX information.

Recently, the synergistic combination of quantified EDX maps and HAADF-STEM tomography was developed and successfully applied by Zanaga *et al* [220]. In this manner, the effect of shadowing is minimized and the spatial resolution of the 3D reconstruction is improved. The quantification of an EDX map will be explained in the next section. Another methodology was proposed by Slater *et al* [221], where a time-varied acquisition scheme is used to compensate for variations in the detected signal at each tilt angle. This approach ensures the fulfilment of the projection requirement and additionally more signal will be detected as at all times all the detectors are open. In section 3, different acquisition approaches are evaluated by their application on Au/Ag core/shell nanoparticles.

By the development of the Super-X detection system and the use of these novel acquisition approaches, the efficiency of X-ray detection has largely improved. However, the acquisition time for a single EDX map requires typically a few minutes, which is much longer in comparison to the acquisition time of a HAADF-STEM image, which requires only a few seconds. This means that an increased electron dose is necessary for the acquisition of a tilt series of EDX maps, which could lead to beam damage during the acquisition. Not only the investigated nanostructure needs to resist these long exposures, but also the support grid has to be robust to the electron beam. If the support grid is damaged during the tomography experiment (Figure 6.3), there is a possibility that the nanostructure will move during the acquisition of the tilt series. Such a movement will hamper a reliable 3D reconstruction. Therefore, only a limited number of projected EDX maps with a relatively low signal-to-noise ratio can be acquired. As a result, the need for novel advanced 3D reconstruction algorithms is emerging.

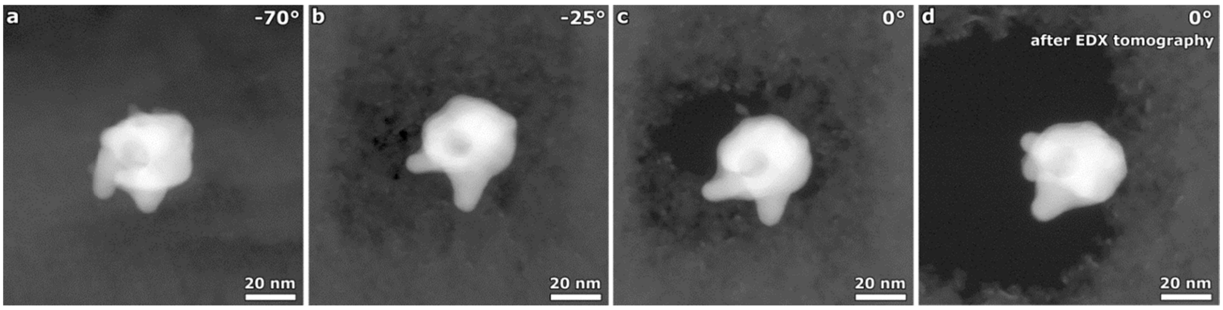

**Figure 6.3.** HAADF-STEM images acquired during the acquisition of the tilt series of an EDX tomography experiment. (a) HAADF-STEM image acquired at -70° before the acquisition of the first EDX map. (b) After the acquisition of five EDX maps, the carbon layer seems to be damaged. The HAADF-STEM image was acquired at -25°. (c,d) In the HAADF-STEM images acquired at 0° (c) during and (d) after the tomography experiment, it is clear that the nanostructure has clearly moved because of the damaged carbon support.

### Quantification of tilt series

As described in Chapter 2, an acquired EDX spectrum does not only contain the characteristic X-ray peaks but also a background signal caused by Bremsstrahlung is present. An example of an acquired spectrum is shown in Figure 6.4.a in grey. In order to retrieve the 3D elemental composition of a specific chemical element, the 2D elemental maps should be composed of only the characteristic X-ray peak from that element. Therefore, the background signal needs be removed from the detected signal (Figure 6.4.a in red). Additionally, multiple characteristic peaks can overlap and then a deconvolution of the peaks is necessary to obtain reliable 2D projection images for the chemical elements present in the investigated sample. During the quantification procedure, the spectrum of each pixel in the projection image is examined. For example when investigating a Au/Ag core/shell

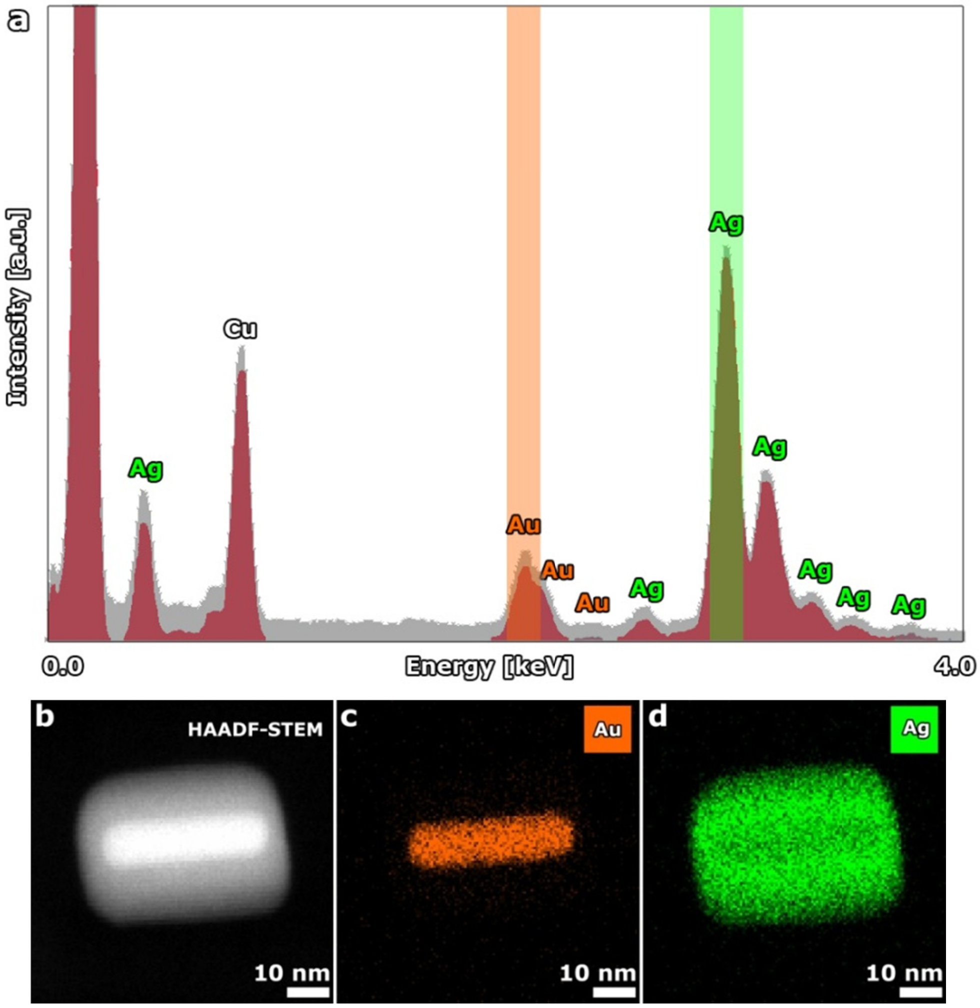

**Figure 6.4.** (a) The integrated, detected EDX spectrum for a Au/Ag rod core/shell nanoparticle is shown in grey. The spectrum which is obtained after the background subtraction is shown in red. From that spectrum, the elemental maps for Au (c) and Ag (d) are extracted. The characteristic peaks for Au and Ag which are used for the quantification are highlighted in (a) in orange and green, respectively. The corresponding HAADF-STEM projection image which is acquired simultaneously during the EDX detection is shown in (b).

nanoparticle, each pixel can either contain only Au, only Ag, both Au and Ag or none of these elements. After the quantification, the amount of Au and the amount of Ag for each pixel will be known. The result of such a quantification process is shown in Figure 6.4.c and d for a Au/Ag rod core/shell nanoparticle. As the detection system is still far from optimal, the EDX maps have a poor quality. The count rate in the maps is quite low and neighbouring pixels can differ severely. To reduce the changes in neighbouring pixels, EDX maps are often averaged to yield images with a more constant varying count rate. Remaining background pixels can be eliminated by using the HAADF-STEM images as a mask. Both the limited amount of projection images as the low signal-to-noise rate will complicate an accurate alignment of the tilt series. In the next section, we explain how a tilt series of EDX maps needs to be aligned in a straightforward and reliable manner.

### 2.2.3. Alignment of tilt series

As the detection system still suffers from quite low detection efficiency, the resulting EDX projection maps are relatively noisy. Additionally, as the acquisition time for these maps takes several minutes, we can only acquire a limited amount of projection images during the acquisition of an EDX tilt series. Therefore, these tilt series are less suitable for a conventional cross correlation alignment method, as the differences in the projected structure in two successive projection images may differ significantly. During the acquisition of an EDX map, a HAADF-STEM projection image is acquired simultaneously at each tilt angle. As a consequence, the HAADF-STEM tilt series can be aligned in a proper manner as they provide a better signal to noise ratio. After optimizing the alignment parameters for the HAADF-STEM tilt series, they can be applied on the EDX tilt series of the different chemical elements as the images are acquired at the same time. In this way, a consistent alignment of all data is obtained.

## 3. Investigation of Au/Ag core/shell nanoparticles

The different acquisition approaches, as discussed in section 2.2.2, are tested on a Au rod core / Ag cube shell nanoparticle. All the EDX tilt series were acquired with an angular range of ± 70°, a tilt increment 10° and a TVM algorithm was applied to reconstruct the tilt series. The use of TVM is beneficial as the low amount of noisy projection images will deteriorate the quality of a SIRT reconstruction. Since TVM is more robust towards low signal-to-noise ratio, artefacts in the EDX reconstruction will be reduced.

### 3.1. Qualitative results

A first experiment was applied with the use of a single tilt tomography holder. All the detectors were used for the X-ray collection and each map was collected for $180s$. A 3D visualization of the EDX tomography result is shown in Figure 6.5.a. Corresponding orthoslices through the 3D reconstruction are shown in Figures 6.5.a.1-6. As discussed in section 2.2.2, the projection requirement is not satisfied with this acquisition approach due to shadowing, but still we are able to visualize both the Au core (green) and the Ag shell (grey) from these EDX tomography reconstructions. The orthoslices through the Ag shell Figures 6.5.a.1 and a.3 show some intensity variations which could originate from violation of the projection requirement. These artefacts will hamper a reliable quantification of the 3D reconstruction.

Next, the Fishione 2030 holder was used in combination with the use of detectors 3 and 4 for the negative tilt angles and detectors 1 and 2 for the positive tilt angles. The outcome of this acquisition approach is visualized in Figure 6.5.b. This approach should minimize signal variations at different tilt angles. We can clearly characterize the Au core and the Ag shell, however some minor intensity variations in the orthoslices through the Ag shell are observed in Figures 6.5.b.1 and b.3 as was seen in the conventional approach. A careful analysis of the detected X-ray counts for this tilt series has shown that the signal still shows some fluctuations in function of the tilt angle. The position of the investigated nanostructure on the grid can affect the amount of blocking[221], therefore the acquired count rate profile in Figure 6.2.d.1-2 can vary according to the exact position of the nanostructure. Deviations from this profile will result in fluctuations when using the optimized procedure.

In the last approach, a time variation acquisition scheme was applied. The time factors were calculated based on the collected X-ray counts of the conventional approach. In this way, longer acquisition times are used at the lower tilt angles to compensate for blocking by the holder. The total acquisition time, and thereby dose, was kept constant in comparison to the first (and second) approach. In total 45 minutes were needed to acquire the full EDX tilt series. The result visualized in Figure 6.5.c shows less intensity variations in the orthoslices through the Ag shell (Figures 6.5.c.1 and c.3) in comparison to the previous acquisition approaches. We can however conclude that all the approaches qualitatively lead to a similar result as both the core and the shell can be clearly detected and reconstructed.

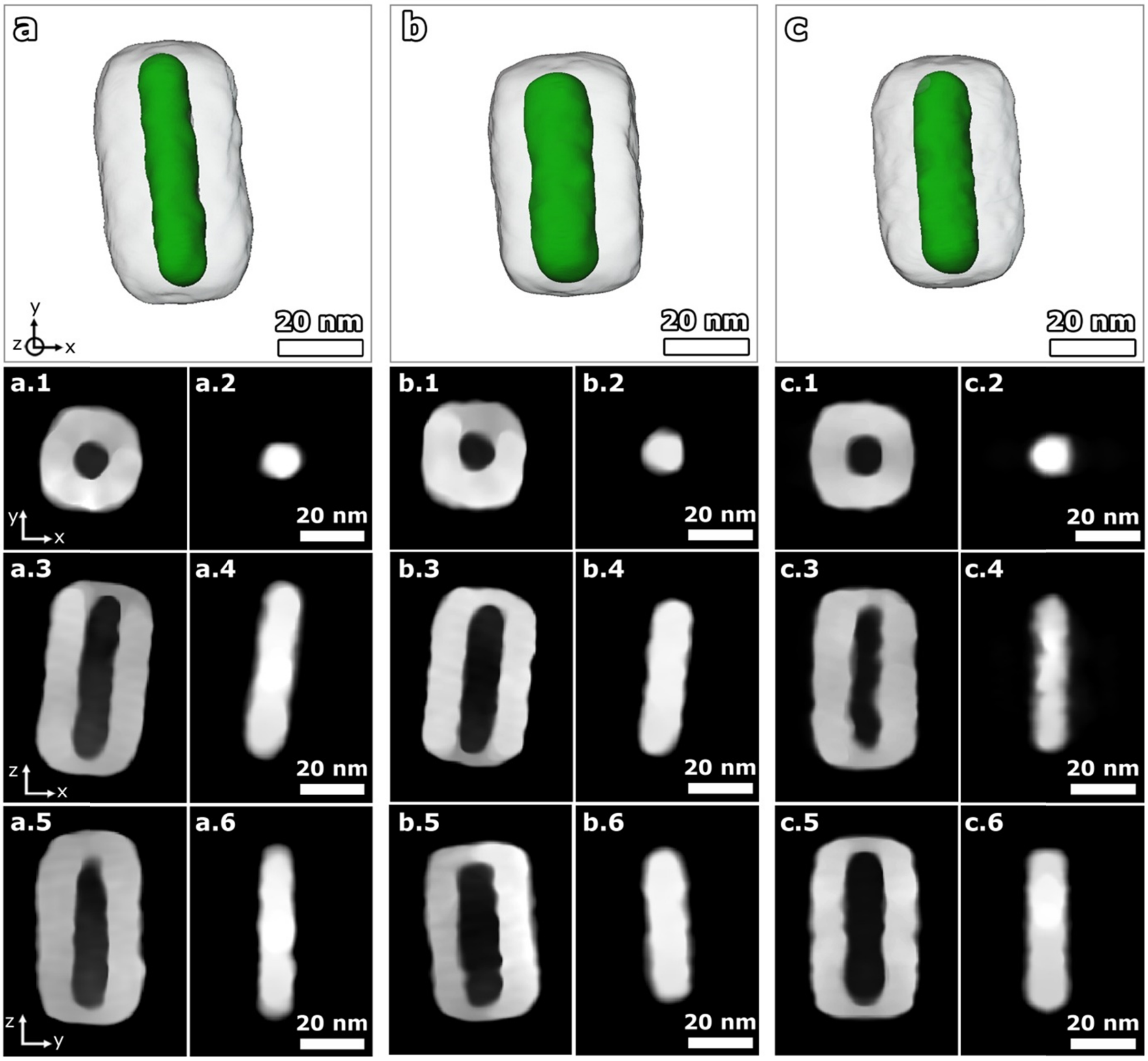

**Figure 6.5.** 3D visualizations and corresponding orthoslices of Au/Ag core/shell nanoparticles with the use of (a) a conventional acquisition approach, (b) the Fishione 2030 holder and two-by-two detectors and (c) a time variation acquisition scheme of EDX tilt series.

### 3.2. Quantitative results

To compare the outcome of the different acquisition approaches in a quantitative manner, the 3D reconstructions of the HAADF-STEM tilt series, which are simultaneously acquired with the EDX tilt series, are used as a ground truth. Since the atomic numbers of Au and Ag are significantly different and the interface between the two components is sharp, a quantification from Au and Ag is possible by thresholding the HAADF-STEM reconstruction. The shape error is introduced as a quantitative measure and corresponds to the number of voxels that are misclassified in the segmentations of the EDX reconstructions in comparison to the reconstructions of the HAADF-STEM tilt series. Both the shape error for Ag and Au can be calculated with this approach. In Figure 6.6, the outcome of the different acquisition procedures of the Ag shell is visualized. Orthoslices through the HAADF-STEM and EDX reconstructions of Ag are shown for the conventional acquisition method (Figure 6.6.a and b), the Fishione 2030 holder in combination with the use of two detectors at positive and negative tilt angles (Figure 6.6.d and e) and the time variation method (Figure 6.6.g and h). For every method, the difference reconstruction is shown in Figure 6.6.c,f and i, respectively. A total shape error of 29% is found for the conventional method. From Figure 6.6.c, it is clear that the misclassification of voxels for the Ag is located at the inner and outer edges of the shell. Using the two approaches which reduce the effects of shadowing, the total shape error is reduced with a factor of 2. For the method where the 2030 holder used in combination of the two detector set-up, the total shape error is reduced to 15%. A total shape error of 11% is found for the time variation acquisition method. The misclassified voxels are also in these reconstructions found at the inner and outer edge of the Ag shell (Figure 6.6.f and i).

The shape error was also calculated for the Au core and shows again a large reduction when the two optimized acquisition approaches are used (Figure 6.7). The shape error for Au is only 1-2% for these approaches (Figure 6.7.f and i) in comparison to 6% for the conventional method (Figure 6.7.c). Therefore, the use of these optimized procedures shows a large improvement and more reliable results

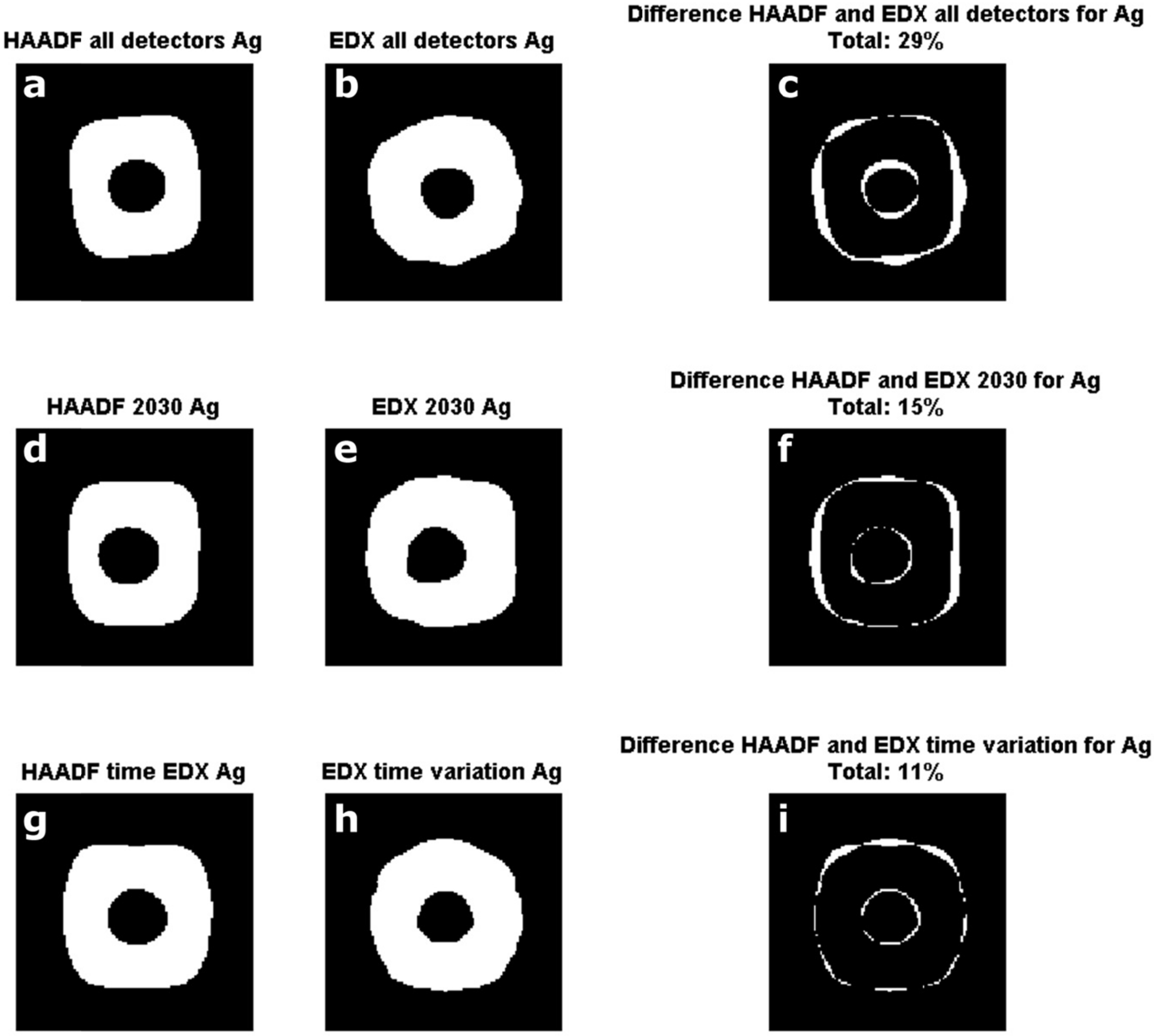

**Figure 6.6.** Orthoslices through the segmented reconstructions of the (a,d,g) HAADF-STEM and (b,e,h) EDX tilt series of the Ag shell for the different acquisition approaches: (a,b) the conventional acquisition approach, (d,e) the Fishione 2030 holder and two-by-two detectors and (g,h) a time variation acquisition scheme of EDX tilt series. (c,f,i) Orthoslices through the difference reconstructions for the three approaches and their calculated total shape error are visualized.

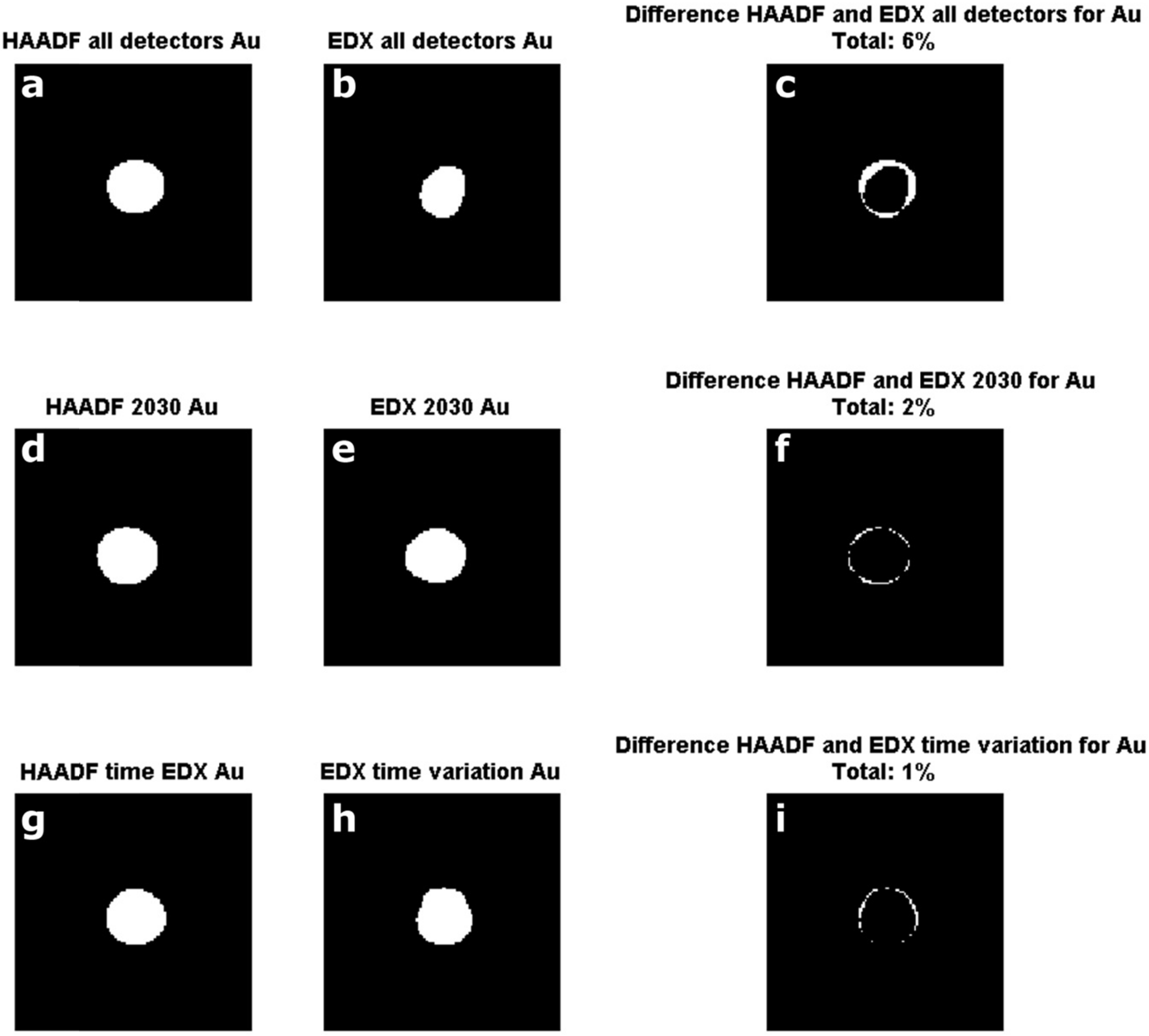

**Figure 6.7.** Orthoslices through the segmented reconstructions of the (a,d,g) HAADF-STEM and (b,e,h) EDX tilt series of the Au core for the different acquisition approaches: (a,b) the conventional acquisition approach, (d,e) the Fishione 2030 holder and two-by-two detectors and (g,h) a time variation acquisition scheme of EDX tilt series. (c,f,i) Orthoslices through the difference reconstructions for the three approaches and their calculated total shape error are visualized.

are obtained in comparison to the conventional acquisition approach, where the projection requirement is not fulfilled. The total shape error of the Ag, however, still remains quite large for these optimized procedures. Next to the projection requirement, an additional challenge is the low signal-to-noise ratio of the EDX maps, which clearly has an impact on the 3D reconstruction. In Figure 6.8, line profiles through the HAADF-STEM projection image, the EDX map and averaged EDX map are shown. From this Figure, it is clear that the quality of an EDX map is quite poor in comparison to the quality of the HAADF-STEM image. The use of averaging of the EDX map shows an improvement on the quality, however, a difference with the HAADF-STEM projection image is still visible. Improving the signal-to-noise ratio of the EDX maps will lead to an improvement of the quality of the 3D reconstruction and is therefore a future challenge. Combining HAADF-STEM and EDX tomography can lead to more reliable 3D reconstructions[220,222].

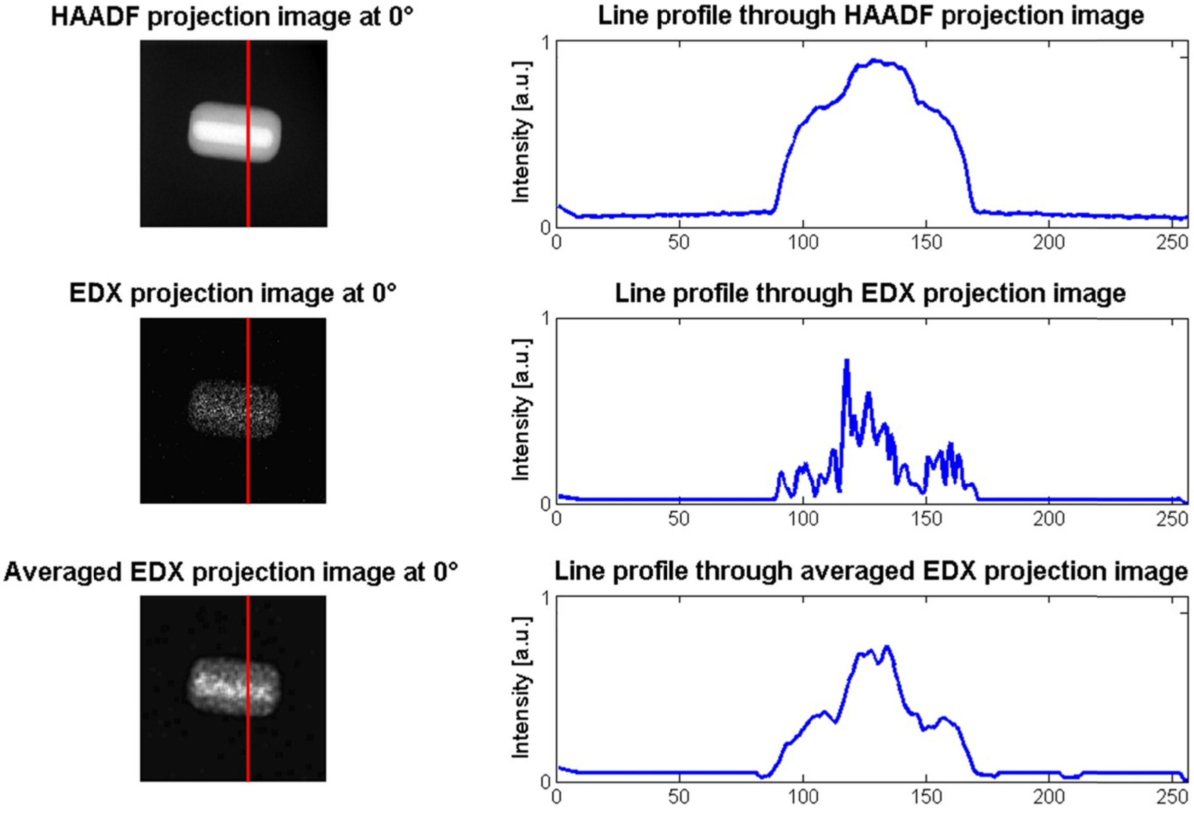

**Figure 6.8.** A HAADF-STEM projection image, EDX map and EDX averaged map at 0° are visualized. The line profiles (red) through these projection images are shown.

## 4. Conclusion

In this chapter, we have discussed the extension of EDX mapping from 2D to 3D and the challenges concerning performing a reliable EDX tomography experiment. We have carried out a careful analysis of the performance of the novel developed Super-X detection system and concluded that the acquisition procedure needs to be optimized in order to fulfil the projection requirement. Different approaches were evaluated by the application on Au/Ag core/shell nanoparticles. We have shown that a qualitative interpretation can be carried out with the different approaches –even when the projection requirement is not fully satisfied–. However, if we do not only want to know “where is what?” but also “how much?”, the development of novel reconstruction algorithms emerges. The low amount of projection images in combination with their low signal-to-ratio need to be properly dealt with, in order to obtain reliable 3D reconstructions from which quantitative results can be extracted.

# Chapter 7

## A neural network filtered back projection approach

This chapter is based on: Bladt, E., Pelt, D. M., Bals, S., Batenburg, K. J. *Electron tomography based on highly limited data using a neural network reconstruction technique*. Ultramicroscopy, 158 (2015) 81–88.

Own contribution: Responsible for all the electron tomography acquisition and analysis of 3D reconstructions.

## 1. Introduction

In the previous chapters, it was shown that electron tomography is necessary to perform a 3D characterization of nanostructures. In Chapter 3 and 5, HAADF-STEM tomography was applied to perform a structural and chemical characterization of semiconductor nanostructures. The use of EDX tomography to perform a 3D chemical characterization was investigated and optimized in Chapter 6. In general, electron tomography is often used to determine the size and shape of nanoparticles and nowadays, 3D reconstructions can even be obtained with a resolution at the atomic level[107,209]. Although these investigations provide very precise information on the nanoparticle morphology, both the acquisition of tilt series as well as the 3D reconstruction is very time-consuming and it is consequently not straightforward to acquire results in 3D that are statistically relevant, which is a major drawback e.g. when using electron tomography to optimize the synthesis of nanoparticles. This problem will be even more essential for anisotropic nanoparticles that are currently receiving a lot of attention because of the increased flexibility they provide to tune the final (optical) properties[223–225]. Since the optimization of the production of nanoparticles with a specific shape would largely benefit from statistical 3D results with a nanometer resolution, one of the emerging challenges in the field of electron tomography is to increase the throughput of 3D reconstructions of nanoparticles. At the same time, the quality of the reconstructions should be maintained and should enable one to obtain reliable and quantitative results concerning parameters such as particle size and surface morphology.

Additionally, there is a high need for advanced reconstruction algorithms in EDX tomography, which can handle a low amount of projection images. As discussed in Chapter 6, a major drawback of EDX tomography is the need for longer acquisition times, which limits the acquisition of a high number of projection images. The development of completely novel 3D reconstruction techniques will expand the possibilities of EDX tomography.

Here, we will determine the 3D shape and size of a large set of anisotropic Au nanoparticles by making effective use of a new approach for electron tomographic reconstructions that is based on artificial neural networks. The neural network filtered back projection method (NN-FBP) is a recently developed reconstruction technique that has been applied successfully to X-ray tomography[226];

however the implementation for electron tomography is completely new. The proposed method will aim to reduce the number of necessary projection images for a 3D reconstruction by a factor of 5 or more. In this manner, the acquisition time and time that is necessary for a 3D reconstruction will significantly reduce, enabling 3D results that are of statistical relevance. Afterwards, the extension of the NN-FBP algorithm towards a chemical characterization will be studied. Both HAADF-STEM and EDX tilt series will be investigated by a NN-FBP implementation.

## 2. Neural network filtered back projection method: structural characterization

The investigated sample contains Au nanoparticles yielding different morphologies: nanorods, nanotriangles, nanoprisms and nanospheres. A HAADF-STEM overview image of the sample is provided in Figure 7.1.a. Although this image only corresponds to a 2D projection of a set of 3D objects, it is already clear that different morphologies occur. Since all the investigated nanoparticles have a thickness below 100 nm, the projection requirement for tomography is satisfied[125,227]. The projection requirement was explained in section 2 of Chapter 2. A conventional electron tomography experiment was performed to characterize the different morphologies present in the sample. The outcome of this procedure for the different nanoparticles in Figure 7.1.a is visualized in Figure 7.1.b. The reconstructions are calculated using the SIRT algorithm and are based on a series of 151 images, acquired over a tilt range of ±75°. Since the quality of 3D reconstructions based on the conventional approach is predominantly determined by the number of projection images[151,154,155], these experiments are very time-consuming and require sufficient measurement time at the TEM.

The key to increasing the image quality if only a small number of 2D projections are available, is the effective use of prior knowledge in the reconstruction. By exploiting rather generic features of the particles, without assuming a specific shape or morphology, this additional knowledge is used to compute a particle shape that better approximates the true morphology. Various algorithms involving prior knowledge are currently in use in electron tomography (e.g. the DART algorithm for discrete

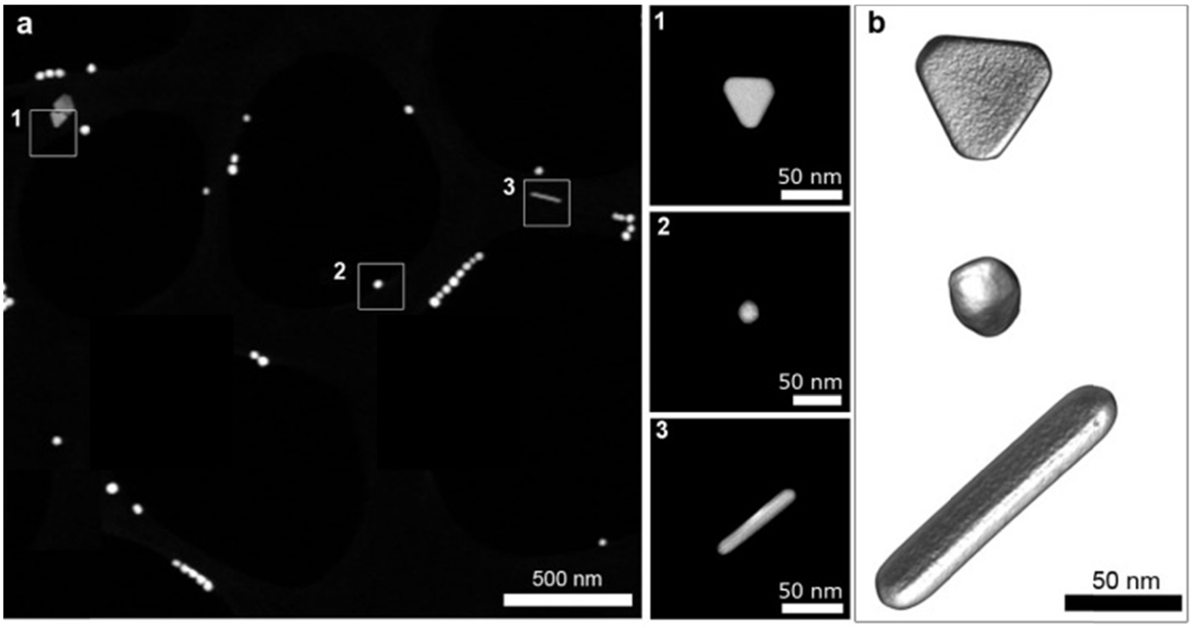

**Figure 7.1.** (a) The HAADF-STEM overview image shows the presence of several morphologies in the sample, with indication of (1) a nanotriangle, (2) a nanosphere and (3) a nanorod. (b) 3D volume renderings of the corresponding nanoparticles are presented.

tomography[228] and multiple methods for TVM[157]), where the particular prior knowledge is encoded by the user and various parameters have to be set. These prior-knowledge based methods are typically very time-consuming, which limits the throughput of 3D reconstructions that can be achieved by using them for the reconstruction. Furthermore, implementing these methods can be difficult and time-consuming as well, since they rely on advanced mathematics. The proposed alternative approach called Neural Network Filtered Back Projection (NN-FBP) was first described by Pelt and Batenburg in [226], which can effectively exploit sample characteristics to improve the reconstruction quality, while still being highly computationally efficient since it is based on a simple FBP reconstruction. Here, we apply this new technique for the first time to electron tomography data. The application of NN-FBP to electron tomography consists of two phases: (i) a *learning phase*, in which full tilt series and their corresponding reconstructions are used to calibrate the reconstruction algorithm and (ii) a *reconstruction phase*, in which large batches of limited tilt series (i.e. using fewer projections) are rapidly reconstructed. A schematic overview the NN-FBP method is given in Figure 7.2. In the next subsections, we will first briefly explain how the reconstructions are formed in the reconstruction phase, followed by an overview of how the calibration is performed in the learning phase.

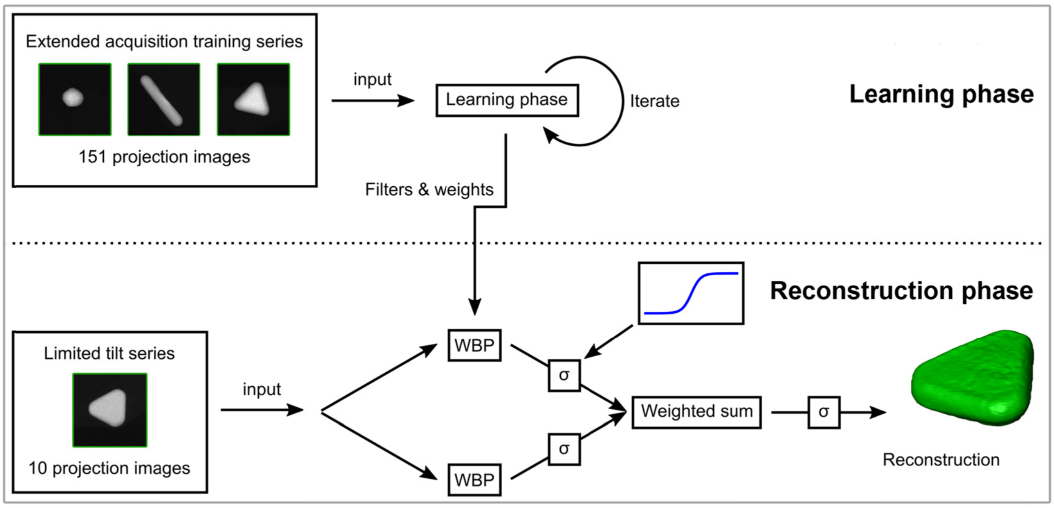

**Figure 7.2.** Schematic overview of the NN-FBP procedure. In the learning phase, the extended acquisition series are used as an input to learn filters and weights specific to the training objects. In the reconstruction phase, the learned filters are used in multiple FBP reconstructions with an additional pixel-wise nonlinear scaling operation, which are combined to obtain a single reconstruction of a limited tilt series.

## 2.1. Method

### 2.1.1. Reconstruction phase

Reconstructions obtained by a standard FBP are commonly plagued by a range of reconstruction artefacts when reconstructing from a limited tilt range and few projection angles. Streaks can be observed in the 3D reconstruction due to the limited number of projections, and the limited angular range leads to an elongation and blurring in the Z-direction. It was shown that strong improvements on the reconstruction quality from limited data can be obtained by combining a small number (e.g. 2 or 4) of FBP reconstructions, each obtained using a different filter[226].

In the reconstruction phase, the NN-FBP algorithm computes a reconstructed volume from limited projection data by combining multiple FBP reconstructions with different filters into a single reconstruction. A key ingredient of the algorithm is the application of a pixel-wise nonlinear scaling operation to each of the FBP images. Following this operation, the images are combined by taking a weighted sum of the scaled FBP images. As a final step, another nonlinear scaling operation is applied to this combined image (see reconstruction phase in Figure 7.2).

Note that without these nonlinear scaling operations, the final reconstruction can also be obtained by first creating a weighted sum of the different filters, and performing a FBP with the resulting filter, as the FBP algorithm is a linear method with respect to the used filter. Because of this, such a method will not be able to produce more accurate reconstructions than standard FBP with an appropriately chosen filter. Also, because of the nonlinear scaling operation, it is not possible to directly compare the filters of the NN-FBP method with standard filters for FBP.

By using the nonlinear scaling operation, the NN-FBP algorithm is able to reduce the artefacts that are usually present in standard FBP reconstructions when only a small number of projections are available. An example image with standard FBP, a linear combination of two FBPs, and a combination of two FBPs with nonlinear scaling is shown in Figure 7.3. As expected, the Figure shows that the linear combination is identical to a single FBP reconstruction, while the combination with nonlinear scaling is significantly more accurate.

### 2.1.2. Learning phase

The question remains how the different filters and weights have to be chosen, such that the method produces accurate reconstructions. It is shown that ideas from artificial neural network theory can be used to find optimal filters and weights[226]. Specifically, filters and weights can be learned by the NN-FBP method in a separate learning phase, in which the method is presented with high-quality reconstructions of a set of training objects. In artificial neural network theory, this technique is called supervised learning. In the learning phase, the filters and weights are iteratively adjusted until the NN-

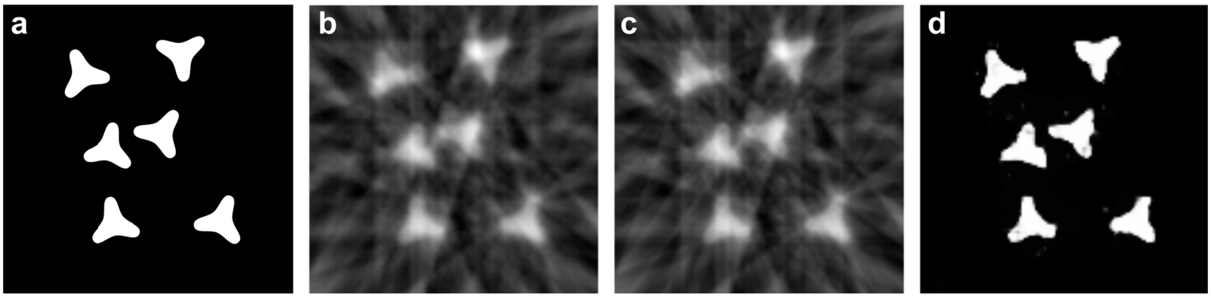

**Figure 7.3.** Three reconstructions of a phantom image from 10 projections: (a) the phantom image, (b) FBP with a single filter, (c) a linear combination of two FBP reconstructions, and (d) a combination of two FBP reconstructions with a pixel-wise nonlinear scaling operation. In each reconstruction, the weights and filters are chosen such that the mean squared error with the phantom image is minimized.

FBP reconstructions match the presented high-quality reconstructions. Afterwards, the trained filters and weights can be used to accurately reconstruct objects that are similar to the ones used for training, using only a limited number of projections. The angle distribution of the limited number of projections has to be specified during the learning phase, and the learned filters and weights will be specific to the chosen distribution. To reduce the influence of the specific angles that are chosen, NN-FBP uses angle-independent filters, i.e. the same filters are used for each projection. An important requirement of the NN-FBP method is that the reconstructed objects should consist only of materials that were also present in the training objects. When this requirement is satisfied, the NN-FBP method is able to produce accurate reconstructions, even for objects with different shapes and/or sizes as the training objects. A schematic overview of both the learning phase and subsequent reconstruction of the NN-FBP method is given in Figure 7.2.

As opposed to previous advanced reconstruction methods, specific prior knowledge is not explicitly used in the NN-FBP method. Instead, the method learns to exploit certain characteristics of the training objects by adjusting the filters and weights appropriately. Because the exploited characteristics are learned automatically by the method, it has a broader applicability than previous advanced 3D reconstruction methods. Also, since NN-FBP is based on the efficient FBP algorithm, it is computationally efficient as well, enabling high throughput of 3D reconstructions. An additional advantage is that existing implementations of the FBP algorithm can be used to easily implement the NN-FBP method. A final advantage is that it is possible to include the segmentation step in the NN-FBP method by using segmented high-quality reconstructions of the training objects in the learning phase. In this case, the NN-FBP method will reconstruct objects with voxel values that are very close to their segmented value, and the final segmentation can be performed by simple rounding to the nearest segmented value. This removes the need for manual segmentation, which can be problematic for other methods when only a limited set of projections is available. Additionally, a build-in segmentation is less subjective in comparison to a manual segmentation.

## 2.2. Results

### 2.2.1. Qualitative results

In a first experiment, tilt series of a nanosphere, a nanorod and a nanotriangle are acquired over an angular tilt range of ± 75° with a tilt increment of 1°. These three series and their 3D SIRT reconstructions are used as training input, resulting in a set of filters that will be used during the NN-FBP approach. The resulting NN-FBP algorithm is applied to a limited tilt series that was acquired from a different nanotriangle. Although only 10 projection images obtained over a range of ± 75° are used during the NN-FBP reconstruction, it needs to be pointed out that we also acquired an extended series of 151 projection images. The SIRT reconstruction of the extended dataset was used as ground truth, in order to evaluate the NN-FBP outcome. Figure 7.4.a presents a volume rendering of this full range SIRT reconstruction of the investigated nanotriangle. In all experiments, we used 200 iterations for the SIRT reconstructions, which was empirically verified to produce accurate reconstructions. The result of the NN-FBP algorithm is shown in Figure 7.4.b. It must be stressed that in this case only 10 projection images were used and that this nanotriangle was not used in the training step. It can be seen that the 3D volume visualization of the NN-FBP reconstruction is in very good agreement with the SIRT reconstruction of the full data series. The top and side facet can clearly be distinguished in the

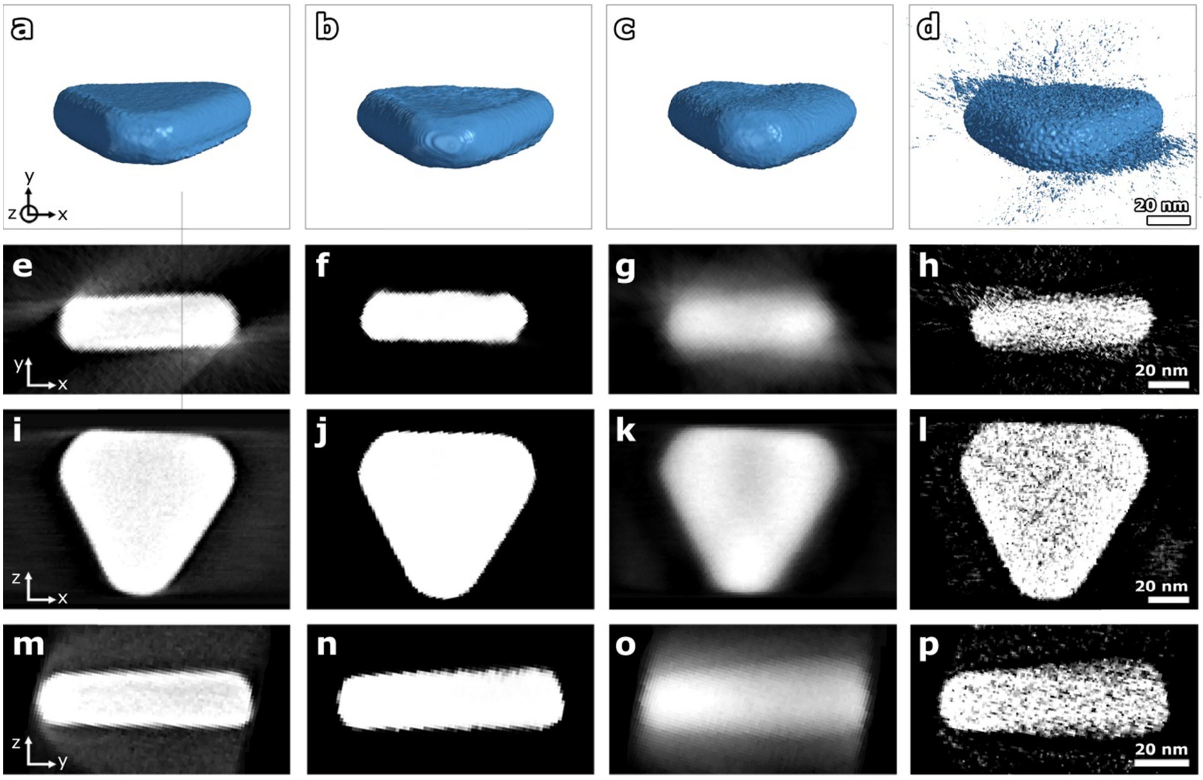

**Figure 7.4.** Reconstructed volumes of a nanotriangle using (a) the full dataset of 151 projections and the SIRT algorithm, and a limited dataset of only 10 projections using (b) the NN-FBP, (c) the SIRT and (d) the FBP algorithm. Xy, xz and yz orthoslices through the (e,i,m) full SIRT, (f,j,n) the NN-FBP, (g,k,o) the limited SIRT and (h,l,p) the limited FBP reconstructions of the nanotriangle.

corresponding orthoslices in Figures 7.4.e,i,m and f,j,n. On the other hand, when comparing the SIRT reconstruction based on the extended series with the SIRT reconstruction based on 10 projection images (Figures 7.4.c,g,k,o), it can be seen that the faceted shape is less pronounced. In the FBP reconstruction applied on 10 projection images (Figures 7.4.d,h,l,p), severe noise and streaking artefacts can be distinguished. These artefacts can be prohibitive for further analysis of the scanned object, such as volume or shape calculations. Therefore, the FBP reconstruction will be left out in the further analysis. The benefits of NN-FBP become obvious; the number of images required for a 3D reconstruction using NN-FBP is reduced by a factor of 15, but the quality is comparable to a reconstruction based on a full data series with a tilt increment of 1°.

In Figures 7.5 and 7.6, results for a nanosphere and a nanorod are presented, respectively. Here, the training of the filters was again obtained by 3 training series. For the nanosphere, extended series of the nanorod and both nanotriangles were used. The training step for the nanorod was performed by the extended series of the nanosphere and both nanotriangles. These nanostructures yield fewer facets and as a consequence, the general morphology as visualized in Figures 7.5.b,c and 7.6.b,c appear to be better preserved when using only 10 projections. However, missing wedge artefacts can be clearly seen in the orthoslices presented in Figures 7.5.f,i,l and 7.6.f,i,l. Because of such artefacts, some features of the morphology indicated by white arrows in both the orthoslices through the full SIRT reconstruction (Figure 7.5.d,g,j) and the NN-FBP reconstruction (Figure 7.5.e,h,k) are not clearly visible in the orthoslices through the limited SIRT reconstruction (Figure 7.5.f,i,l). It has to be pointed out that the NN-FBP method does not train on specific shapes as the training can be performed on different shapes than the investigated object.

### 2.2.2. Quantitative results

As a quantitative measure, a difference reconstruction for the nanosphere is constructed by subtracting the SIRT (Figure 7.7.a) and NN-FBP reconstructions based on 10 projection images (Figure 7.7.b) from the full SIRT reconstruction of the nanosphere. The threshold value for the full SIRT reconstruction is obtained from the histogram. The histogram of the limited SIRT reconstruction, however, is largely influenced by the lack of projection images, which hampers an appropriate choice for the threshold value. In Figure 7.8, comparisons are shown between the histograms of the full SIRT reconstruction (blue) and the limited SIRT reconstruction (green) for each nanoparticle. Clearly, one would have trouble choosing correct threshold values on the basis of the limited SIRT histograms. Therefore, the same threshold value as the full SIRT reconstruction is used for the limited SIRT reconstructions. Since the NN-FBP reconstructions are already segmented, no threshold value is needed for them, which makes the quantification less subjective. Both from the visualization in Figure 7.7.a, as well as the corresponding orthoslices through the difference

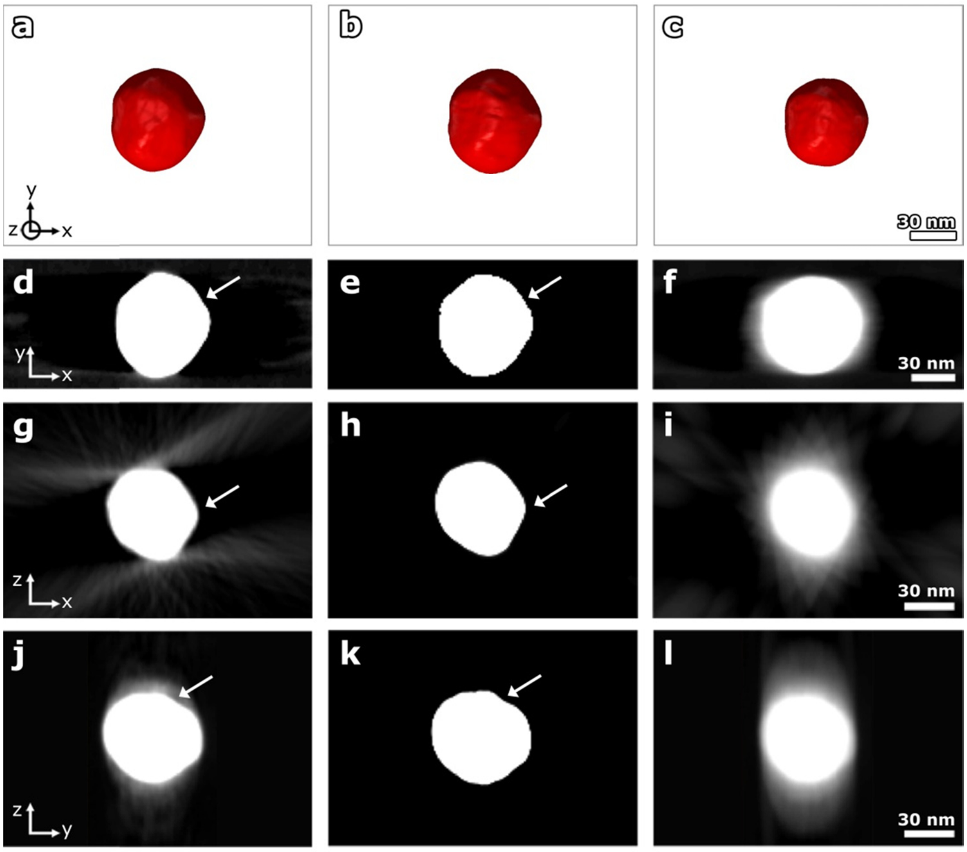

**Figure 7.5.** Reconstructed volumes of a nanosphere using (a) the full dataset of 151 projections and the SIRT algorithm, and a limited dataset of only 10 projections using (b) the NN-FBP and (c) the SIRT algorithm. Xy, xz and yz orthoslices through the (d,g,j) full SIRT, (e,h,k) the NN-FBP and (f,i,l) the limited SIRT reconstructions of the nanosphere. The white arrows indicate the presence of surface roughnesses. It is clear that these features are visible both in the orthoslices through the full SIRT as in the orthoslices through the NN-FBP reconstruction; however, in the limited SIRT reconstruction they are not detectable.

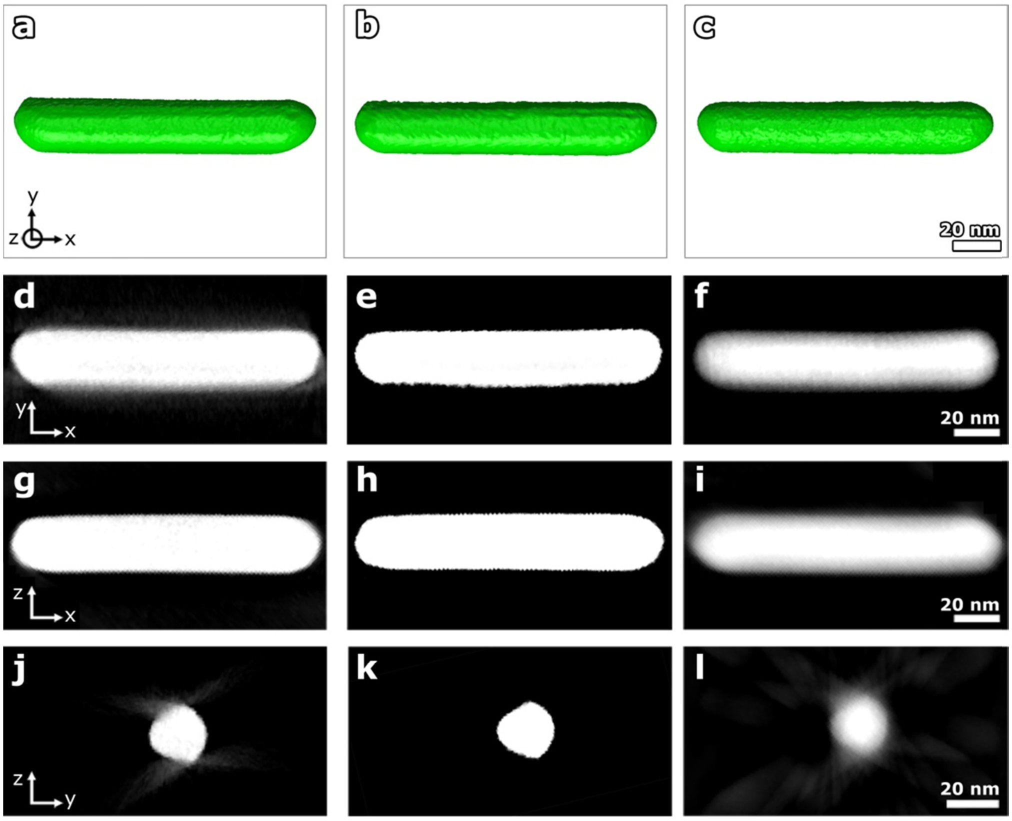

**Figure 7.6.** Reconstructed volumes of a nanorod using (a) the full dataset of 151 projections and the SIRT algorithm, and a limited dataset of only 10 projections using (b) the NN-FBP and (c) the SIRT algorithm. Xy, xz and yz orthoslices through the (d,g,j) full SIRT, (e,h,k) the NN-FBP and (f,i,l) the limited SIRT reconstructions of the nanorod.

reconstruction in Figure 7.7.c, the volume misinterpretation of the limited SIRT reconstruction is clearly detectable. The orthoslices through the limited SIRT difference reconstruction of the nanosphere show a thick white shell. Here, the larger amount of white pixels indicates a volume misinterpretation of 21.5% when using the SIRT algorithm on the dataset of only 10 projection images. From Figure 7.7.b and its corresponding orthoslices in Figure 7.7.d, it is clear that the volume reconstructed with NN-FBP on 10 projection images is close to the actual volume. The NN-FBP reconstruction has only 1.6% of volume underestimation.

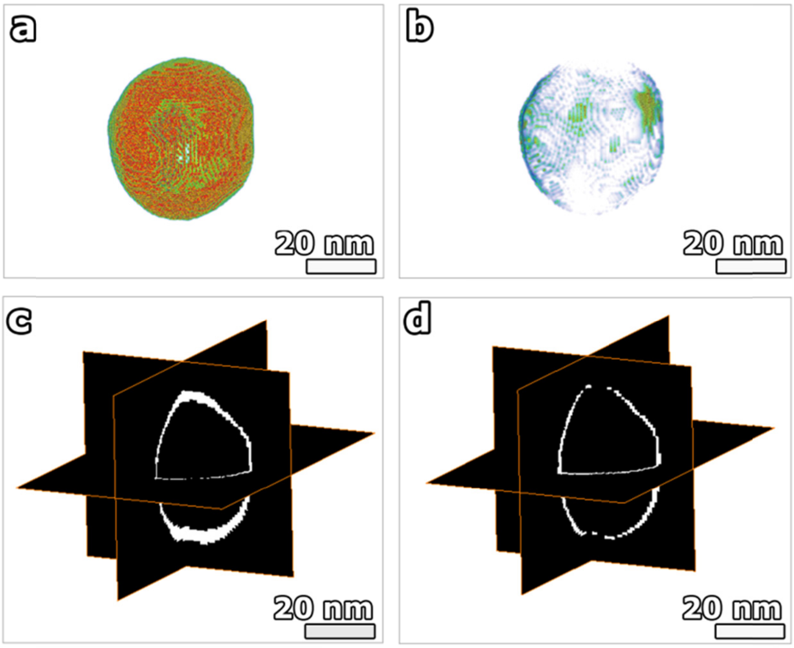

**Figure 7.7.** Difference reconstructions of the nanosphere constructed by subtracting (a) the SIRT and (b) NN-FBP reconstruction of 10 projection images from the full SIRT reconstruction representing the missing volume and its orthoslices (c) and (d), respectively. The volume misinterpretation for the NN-FBP reconstruction equals only 1.6%, which is indicated by the fine shell of the difference reconstruction. The thicker shell present in the difference reconstruction of the limited SIRT equals a volume misinterpretation of 21.5%.

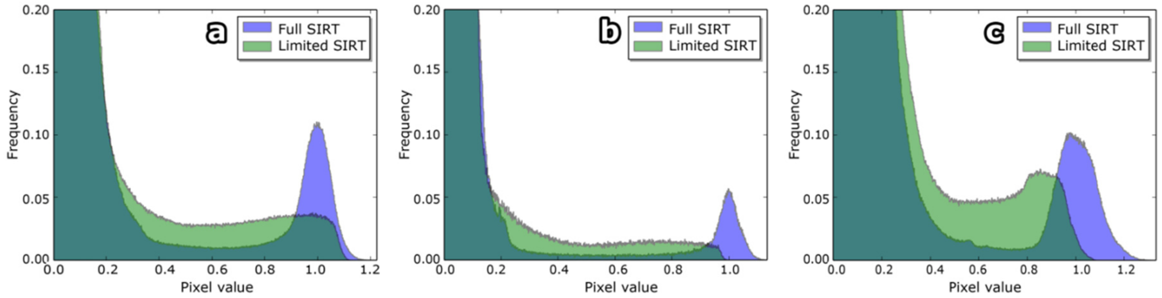

**Figure 7.8.** Histograms of SIRT reconstructions of the nanorod (a), the nanosphere (b), and the nanotriangle (c), with all 151 projections (Full), and only 10 projections (Limited). It is clear that the poor quality of the limited SIRT reconstruction hampers an objective choice of a threshold for segmentation purposes.

For the nanorod (Figure 7.9), the volume for SIRT applied to a limited dataset results in an underestimation of 13.1%. The NN-FBP reconstruction leads to a misinterpretation of only 2.3%. For the nanotriangle, the volume misinterpretation for the limited SIRT reconstruction equals 2.7%. When reconstructing the 10 projection dataset with the NN-FBP algorithm, the volume misinterpretation equals 2.4%. For the nanotriangle, the volume misinterpretation of the limited SIRT reconstruction is close to the misinterpretation of the NN-FBP reconstruction. In this case, however, the volume misinterpretation of the limited SIRT reconstruction gives a misleading result, due to a volume underestimation at the center of the nanotriangle and a volume overestimation at the tips of the nanotriangle. In general, the volume misinterpretation can be misleading due to the cancelling out of overestimation and underestimation. Clearly, the evaluation of the quality of the reconstruction can not only be based on an inspection of the volume error. Therefore, the shape error is calculated, which corresponds to the number of voxels that are labelled differently in the segmentations of the limited data reconstructions in comparison to the full SIRT reconstruction. In this manner, both the local volume underestimation at the center as well as the volume overestimation at the tips is taken into account.

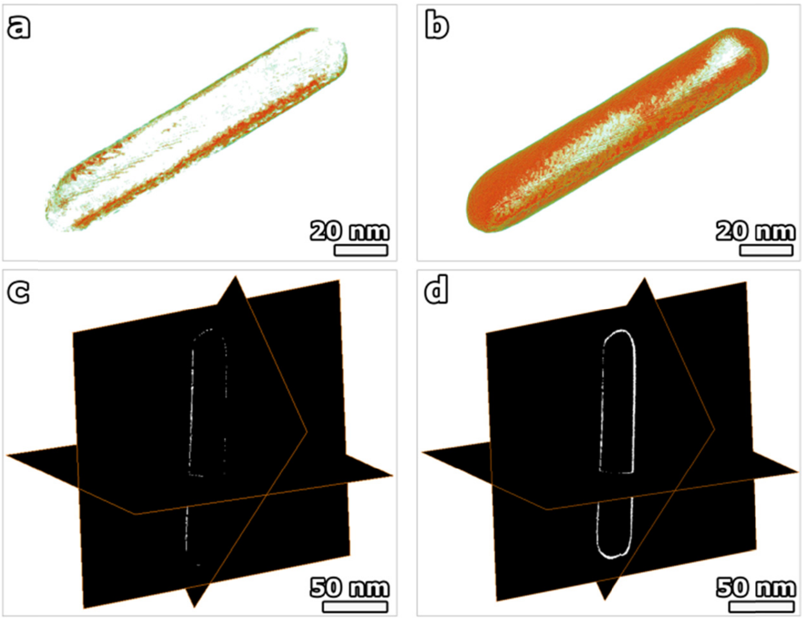

**Figure 7.9.** Difference reconstructions of the nanorod constructed by subtracting (a) the NN-FBP and (b) SIRT reconstruction of 10 projection images from the full SIRT reconstruction representing the missing volume. Corresponding orthoslices through the difference reconstruction of a nanorod using (c) NN-FBP and (d) SIRT on 10 projections are shown. The volume misinterpretation for the NN-FBP reconstruction equals only 2.3%, which is indicated by the fine shell of the difference reconstruction. The thicker shell present in the difference reconstruction of the limited SIRT equals a volume misinterpretation of 13.1%.

For the nanotriangle, there is a 16.5% shape misinterpretation for the limited SIRT reconstruction (Figure 7.10). The shape error for the NN-FBP reconstruction equals 7.5%, which is clearly smaller in comparison to the shape error of the limited SIRT reconstruction. An extended investigation of the influence of the chosen threshold value on the shape error and volume error of the limited SIRT reconstructions is shown in Figure 7.11. Note that from Figure 7.11, one can conclude that the errors depend heavily on the chosen threshold value, showing the difficulties one would have when choosing a threshold value both optimizing shape and volume error for limited SIRT reconstructions. As pointed out before, the NN-FBP method does not require a user-dependent choice of threshold value, which is an additional benefit of the technique.

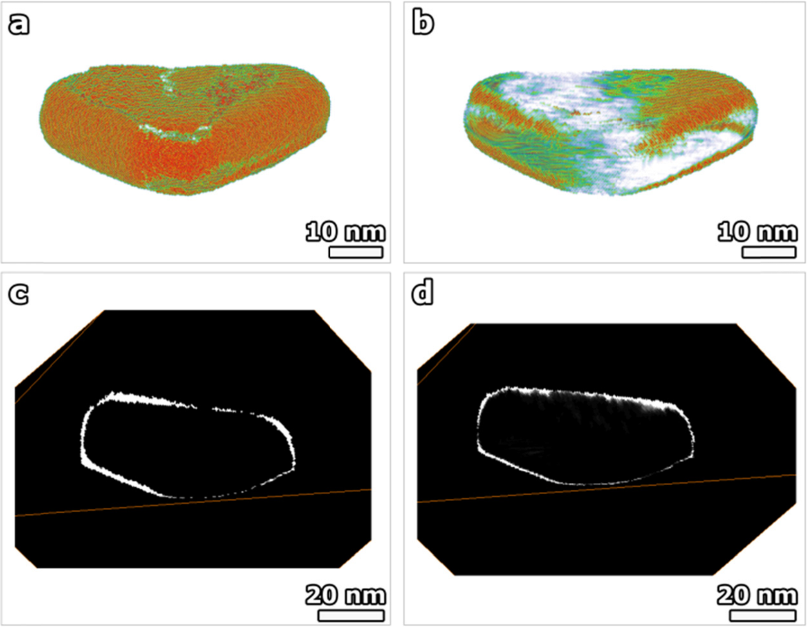

**Figure 7.10.** Representation of the shape misinterpretation, which for (a) the limited SIRT reconstruction shows a volume underestimation at the center of the nanotriangle and a volume overestimation at the tips of the nanotriangle. In (b) the shape misinterpretation for the limited NN-FBP reconstruction is visualized. (c) and (d) represent the orthoslices through the limited SIRT and NN-FBP reconstruction, respectively. The shape misinterpretation for the NN-FBP reconstruction equals 7.5%, which is indicated by the fine shell of the difference reconstruction. The thicker shell present in the difference reconstruction of the limited SIRT equals a shape misinterpretation of 16.5%.

### 2.2.3. Statistical results

In general it is difficult to obtain statistical results when applying electron tomography. As pointed out previously, the acquisition of tilt series for electron tomography is very time-consuming and a large electron dose is required in the case of small tilt increments. The NN-FBP algorithm is therefore of great interest as it can be applied to reduce the acquisition time. In addition the reconstruction time is also highly reduced as the NN-FBP algorithm is as fast as an analytical technique, nevertheless the reconstruction has a comparable quality to iterative reconstructions. In this manner, a large set of nanostructures can be investigated in an efficient approach, leading to statistical results. Using the

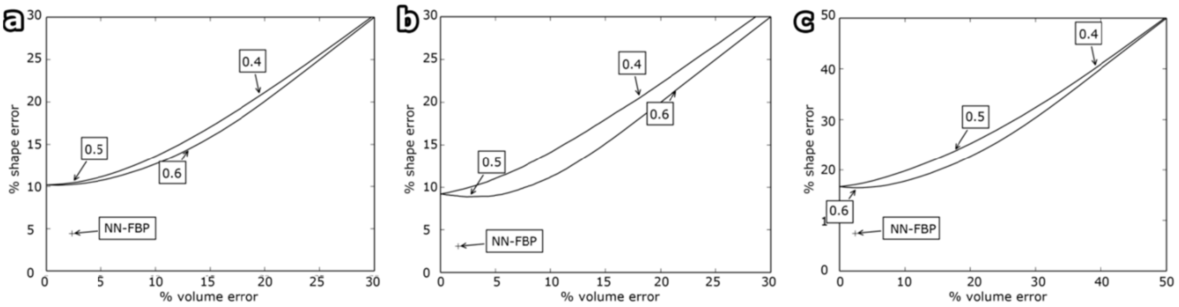

**Figure 7.11.** Plots of the relative error in the shape and the volume of segmented limited SIRT reconstructions of the nanorod (a), the nanosphere (b), and the nanotriangle (c), compared to the full SIRT reconstruction, for different thresholds of the limited SIRT reconstruction. The error in shape is defined as the number of voxels that are labelled differently in the segmentations of the limited in comparison to the full SIRT reconstruction. The error in volume is defined as the absolute value of the difference between the volumes of the segmented limited SIRT reconstruction and the segmented full SIRT reconstruction. The errors for a threshold of 0.4, 0.5 and 0.6 are indicated with arrows and intermediate thresholds are shown by a line. The errors of the NN-FBP method for each nanoparticle are also shown. Note that for each nanoparticle, the error of the NN-FBP reconstruction is closer to the origin than the error of any thresholded SIRT reconstruction.

NN-FBP procedure explained above, training was performed on a set of 20 nanoparticles, and a total of 71 nanospheres was investigated. The number of nanoparticles to train on was chosen empirically, such that there were both enough particles to use in the learning phase, and enough particles to obtain statistical results from. In Figure 7.12, the distribution of the radii of these nanospheres is evaluated as a test case for the NN-FBP algorithm. As the optical properties, such as the absorption cross-section, are dependent on the shape and size of the nanoparticles, it is of key importance to retrieve the real nanoparticle morphology. A difference of a few nanometer can already influence the outcome of the optical response[229,230]. Additionally, the synthesis procedure of the nanoparticles can be carefully evaluated. In order to investigate the reliability of the NN-FBP approach, extended tilt series of 151 images were acquired for all particles. The outcome of the NN-FBP algorithm and the SIRT algorithm, using only 10 projections, is then compared to the measurements based on the SIRT reconstruction using 151 projections. The distribution indicated in grey in Figure 7.12 presents the radii distribution for the nanospheres reconstructed using SIRT applied to limited datasets and clearly gives a different distribution in comparison to the radii distribution of the full SIRT reconstruction, which is presented in white. The average radius found in this manner equals (24.1 ± 0.59) nm, which is significantly smaller than the actual radius which equals (27.1 ± 0.25) nm, found through the full SIRT reconstructions. The radii distribution of the NN-FBP reconstruction (black), however, is in good agreement with the results extracted from the full SIRT data (white). The average radius of the NN-FBP reconstructed nanospheres equals (26.8 ± 0.29) nm. This value is in good agreement with the actual average radius and shows a clear overlap of the error bars. It is again clear that the SIRT algorithm cannot provide reliable information when limited datasets are investigated. These results confirm the reliability of the NN-FBP algorithm and demonstrate the possibility of combining electron tomography and statistical measurements.

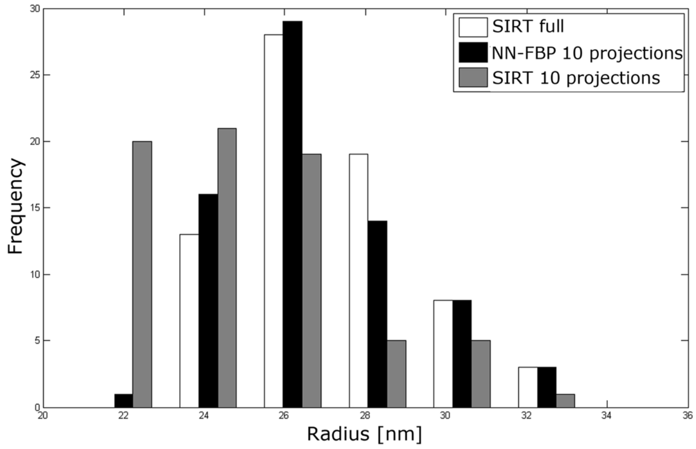

**Figure 7.12.** Distribution of the radii of nanospheres reconstructed using SIRT on full datasets of 151 projections (white), NN-FBP (black) and SIRT on limited datasets of 10 projections (grey). The distributions of SIRT full and NN-FBP 10 projections are in good agreement. When SIRT is applied on the limited datasets, a different distribution is found due to the misinterpretation of the volume.

## 3. Neural network filtered back projection method: chemical characterization

After a successful implementation of the NN-FBP method on HAADF-STEM tomography of Au nanoparticles, an extension towards a chemical characterization is aimed for. In Chapter 5, it was shown that with HAADF-STEM tomography we can perform a 3D structural and chemical characterization of core/shell nanostructures if the difference in atomic numbers is sufficiently large. To extend the chemical characterization to a broader range of nanoparticles, the use of EDX tomography emerges, which was introduced in Chapter 6. Both the NN-FBP implementation on HAADF-STEM and EDX tomography of hetero-nanostructures is discussed in the next section.

### 3.1. HAADF-STEM tomography

In this section, we discuss the extension of the NN-FBP reconstruction method for the application on HAADF-STEM tilt series of core/shell nanostructures. The implementation becomes more challenging as not only the shape needs to be retrieved in a reliable manner, but additionally the core and the shell need to be characterized. To perform an accurate characterization of the two components, it is required that they have a distinct difference in atomic number as HAADF-STEM tomography is used. The difference in atomic number will lead to a noticeable intensity variation which is required to separate one component from the other. In Chapter 5, the intensity difference between CdSe and CdS in the HAADF-STEM projection images enabled us to detect the core in these CdSe/CdS nanobullets and nanorods. Here, Au/Ag core/shell nanoparticles are used as test objects to extend the NN-FBP approach. Since Au atoms ($Z_{Au} = 79$) are much heavier than Ag atoms ($Z_{Ag} = 47$), Au will appear brighter in a HAADF-STEM image, which is illustrated in Figure 7.13. Three Au/Ag core/shell nanoparticles with a different shape are visualized in Figure 7.13. Both the growth of the shape of the Au core and the Ag shell is controlled. The three different nanoparticles from Figure 7.13 are used in this Chapter.

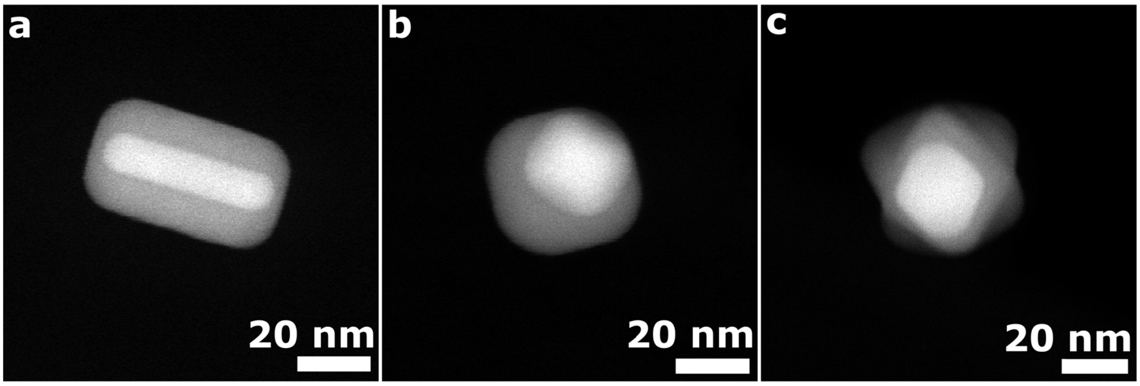

**Figure 7.13.** HAADF-STEM images of Au core / Ag shell nanoparticles with different shapes: (a) Au rod core / Ag cube shell nanoparticle, (b) Au octahedron core / Ag cube shell nanoparticle and (c) Au octahedron core / Ag star-shaped shell nanoparticle.

### 3.1.1. Method and results

The NN-FBP algorithm is again composed of a learning and a reconstruction phase, which were explained in section 2.1. During the learning phase, the algorithm is trained by the use of Au/Ag core/shell nanoparticles with a different shape. Tilt series of 151 projection images are acquired, reconstructed using a SIRT algorithm and a segmentation is performed. This last step results in a 3D reconstruction with 3 grey values, one for the background, one for Au and one for Ag. For the training, different approaches are possible to retrieve the Au and the Ag. We could either train 1 NN-FBP which will be able to reconstruct both the Au and the Ag, simultaneously. Another option is that we train multiple NN-FBPs, which each reconstruct a part of the nanostructure. For this approach, we use the different segmented SIRT reconstructions separately. Based on trial-and-error, we propose to train two NN-FBPs, one which is trained on the segmented Au core and the second NN-FBP trains on the full shape of the particle. In this manner, we obtain the Au reconstruction directly and the Ag reconstruction is calculated by subtracting the Au NN-FBP reconstruction from the full shape NN-FBP reconstruction.

After the learning phase, the two NN-FBPs are applied on different Au/Ag core/shell nanoparticles. The outcome of these NN-FBP reconstructions is evaluated by the volume error for both Au and Ag and the overall shape error, which are visualized in Figure 7.14. We have to note that the overall shape error is a collection of the voxels which are assigned to a wrong class: a Au voxel which is classified as Ag or vacuum and a Ag voxel which is classified as Au or vacuum. From these graphs, we can conclude that the volume error for Au is reduced when using the NN-FBP algorithm. For the Ag volume error, there is no general trend observed. It seems that for some nanoparticles, the use of NN-FBP is preferred, while for others a SIRT reconstruction on 11 projections seems beneficial. A second observation is that the volume errors for Ag are lower that the Au volume errors, which is observed for the limited SIRT and NN-FBP reconstructions. As described in section 2.2.2, we want to stress that the use of volume error as a quality criterion can be misleading. An overestimation and underestimation of the volume will cancel out the total volume error and can therefore give a false positive value. Therefore, we calculated, as before, the shape error which resembles all the misclassified pixels. The shape errors for the NN-FBP reconstructions in Figure 7.14 are however comparable to the errors from the limited SIRT reconstructions. A close observation is therefore necessary to comprehend these shape errors. In Figure 7.15.a-c, 3D reconstructions of a Au octahedron core / Ag cube shell nanoparticle are visualized, in which the Au core is depicted in green and the Ag shell in grey. The SIRT reconstruction of the full tilt series (151 projection images) is shown in Figure 7.15.a and its corresponding orthoslices are visualized in Figure 7.15.d,g,j. The orthoslices represent slices through the segmented volume where the Au core is identified in grey and

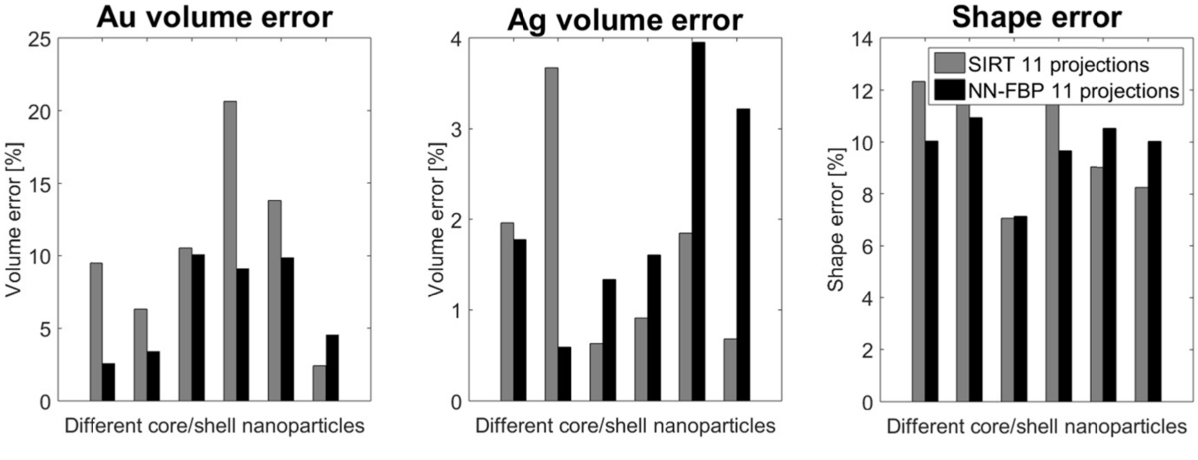

**Figure 7.14.** Volume and shape errors for different Au/Ag core/shell nanoparticles.

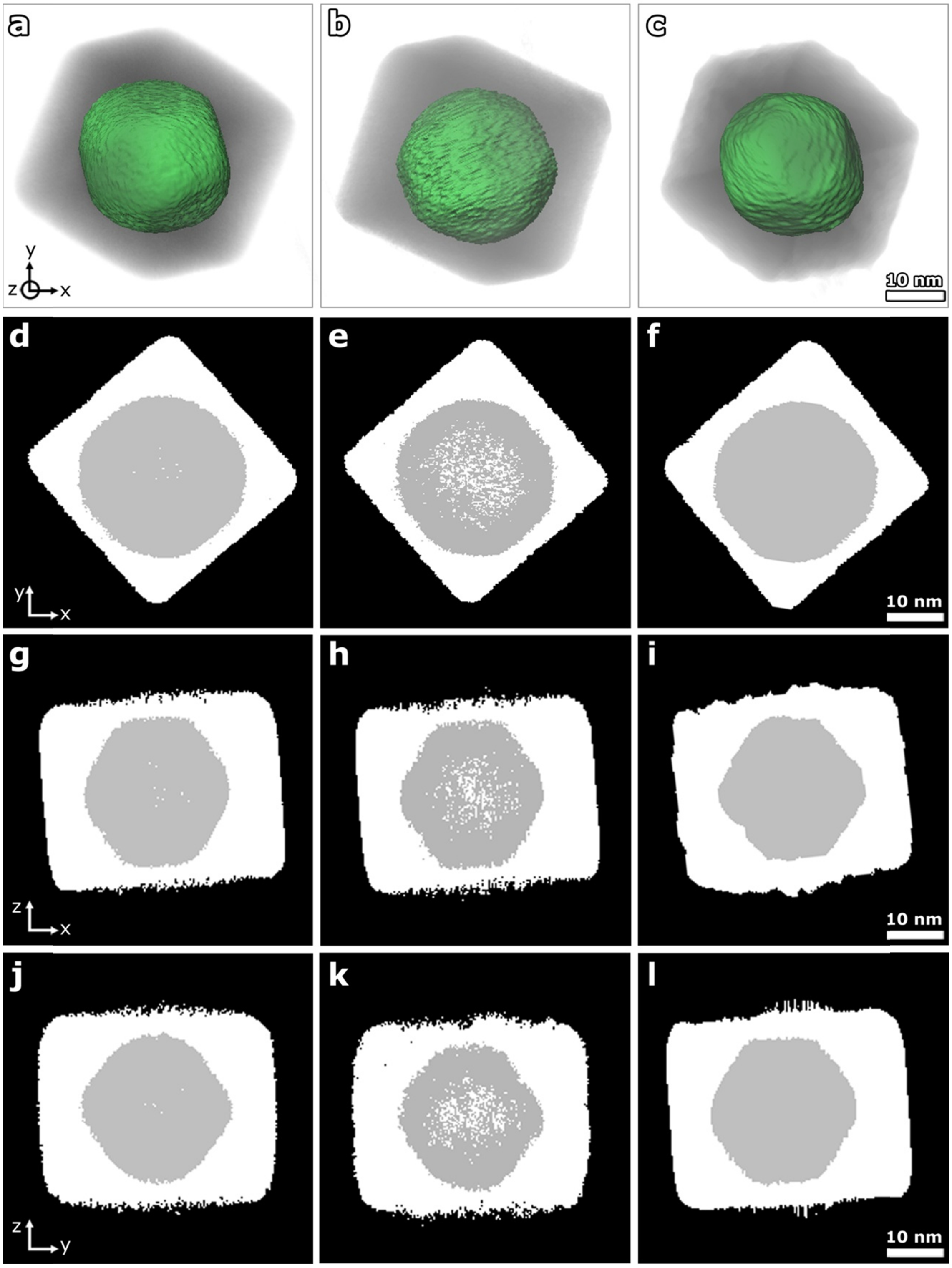

**Figure 7.15.** Reconstructed volumes of a Au octahedron / Ag cube shell nanoparticle using (a) the full dataset of 151 projections and the SIRT algorithm, and a limited dataset of only 11 projections using (b) the SIRT and (c) the NN-FBP algorithm. Xy, xz and yz orthoslices through the (d,g,j) full SIRT, (e,h,k) the limited SIRT and (f,i,l) the NN-FBP reconstructions of the core/shell nanoparticle.

the Ag shell in white. Some missing wedge artefacts in the z-direction can be observed in the xz- and yz-orthoslices (Figure 7.15.g and j, respectively). The result of the limited SIRT reconstruction is shown in Figure 7.15.b and its corresponding orthoslices are visualized in Figure 7.15.e,h,k. In these orthoslices, we notice that some Au core pixels are classified as Ag. These misclassified pixels will lead in a volume misinterpretation of the Au core and will contribute to the shape error. We can conclude that a reliable segmentation is hampered as there is no clear intensity difference between the two components. The NN-FBP reconstruction, based on 11 projections, of the Au/Ag core/shell nanoparticle is visualized in Figure 7.15.c. A visual inspection shows that the 3D NN-FBP reconstruction resembles the full SIRT reconstruction. There are no pixels in the Au core classified as Ag, which explained the shape error for the limited SIRT reconstruction. The shape error of the NN-FBP reconstruction is caused by missing wedge artefacts, which can be observed in the xz- and yz-orthoslices in Figure 7.15.i and l, respectively. The shape of the facets perpendicular to the z-direction is misinterpreted which increases the shape error. Increasing the number of projections for the training phase could result in an improvement of the 3D reconstructions, which is currently ongoing research.

### 3.2. EDX tomography

The need for novel advanced reconstruction algorithms emerges as the tilt series of an EDX tomography experiment is highly limited. In Chapter 6, it was shown that an EDX tilt series consists typically of only 15 images as the tilt increment is 10°. A critical issue regarding the use of NN-FBP for EDX tomography is the need of highly sampled training series. The Au/Ag core/shell nanostructures, which were investigated in Chapter 6 and the previous section, showed a deformation of the Ag shell after the acquisition of an EDX tilt series with a high number of maps. Therefore, these nanostructures cannot be used for the NN-FBP implementation as it is not feasible to acquire training data. Here, we investigate the NN-FBP implementation on EDX tilt series of $FeO_x$-Au nanostars as these nanoparticles are less beam sensitive in comparison to the Au/Ag core/shell nanostructures. In Figure 7.16 both a HAADF-STEM image and an EDX map of such a nanostar is shown. The $FeO_x$ core is presented in purple in the EDX map, which is however not visible in the

HAADF-STEM image. Since the Fe containing core is quite light, the electrons scattered by the core are not reaching the HAADF detector as they are scattered to lower angles. The use of EDX tomography can visualize both the $FeO_x$ core and the Au nanostar.

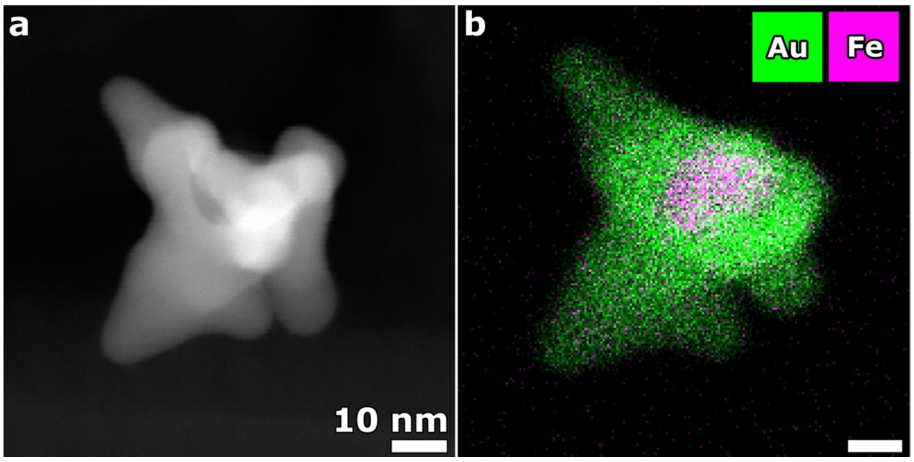

**Figure 7.16.** (a) HAADF-STEM image of a $FeO_x$-Au nanostar, in which only the Au is detectable as the $FeO_x$ is not detected due to low angle scattering. (b) Both the presence of Au (green) and Fe (purple) is confirmed by EDX mapping.

### 3.2.1. Method and results

In the first step towards a successful NN-FBP implementation for EDX tomography, two EDX tilt series of $FeO_x$-Au nanostars were acquired. The EDX tilt series, which will be used in the learning phase, have an angular range from -70° to +74° with a tilt increment of 2°, a dwell time of 15 $\mu s$ and a total acquisition time of 2 minutes. In Figure 7.17, a part of the EDX tilt series and a 3D visualization of the nanostar are shown. No alteration of the nanoparticles was observed after the acquisition of the tilt series. During the learning phase, the two tilt series of 73 projection maps are used and afterwards, the obtained NN-FBP algorithm is applied on a tilt series of 10 projections. Since EDX maps contain much more noise than a HAADF-STEM image, the NN-FBP implementation is first applied to one dataset. This means that in the learning phase the algorithm is trained on 73 projections of the nanostar and subsequently the obtained NN-FBP is applied on 10 projection images of the same nanostar. This evaluation will provide us with a best case scenario,

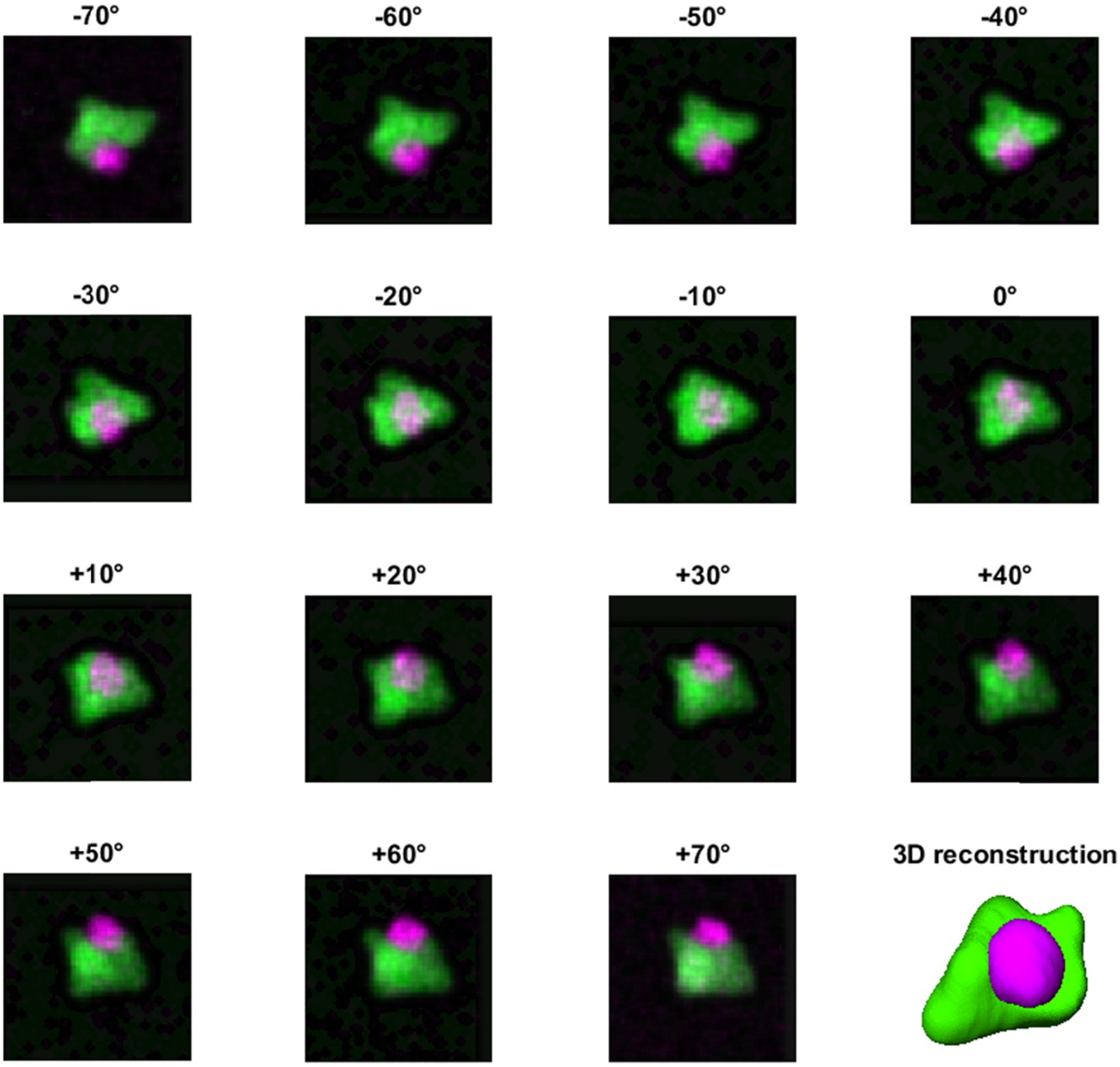

**Figure 7.17.** EDX maps of a $FeO_x$-Au nanostars visualized at distinct tilt angles. The 3D reconstruction shows the $FeO_x$ sphere in purple and the Au star in green.

from which we can optimize the methodology if necessary. In Figure 7.18, the volume and shape error for the Au reconstruction from two nanostars are presented. It is clear that the volume error is highly reduced when the NN-FBP algorithm is used to reconstruct the Au nanostar based on 10 projections. For the first nanostar, the Au volume error for the limited SIRT reconstruction equals 5.4%, which is reduced to 0.3% when using the NN-FBP algorithm. The Au volume error of the second nanostar is 4 times reduced (from 11.9% to 3.0%). As discussed previously, the shape error should be calculated as

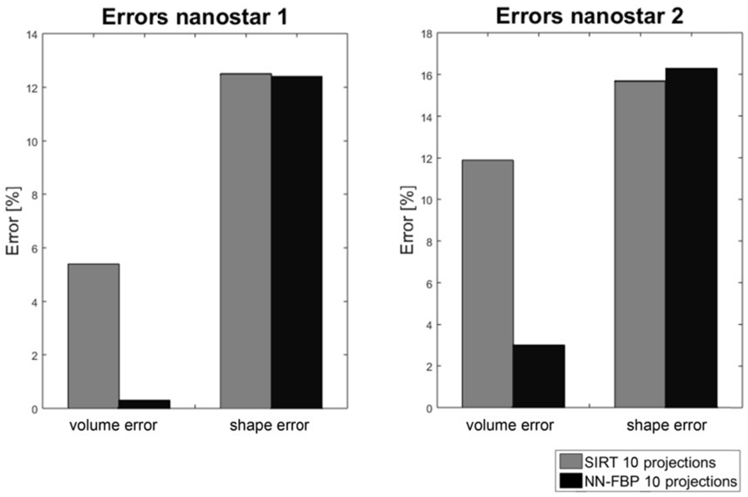

**Figure 7.18.** Volume and shape errors of the Au reconstruction from 2 FeOx-Au nanostars.

the volume error could be misleading. The shape errors are also presented in the graphs in Figure 7.18. The shape error for the limited SIRT reconstructions of the nanostars is 12.5% and 15.7%. It seems that the volume error contains both a volume under- and overestimation as the shape error is significantly higher. When the NN-FBP algorithm is used, the shape errors are comparable to the limited SIRT errors, respectively 12.4% and 16.3%.

It seems that to implement the NN-FBP algorithm on EDX tomography, more projection images need to be included in the learning phase as the shape error remains quite large when the NN-FBP is trained on only 10 projection images. As discussed in Chapter 6, EDX maps have a low signal-to-noise ratio and additionally the value of neighbouring pixels can be quite different. Therefore, the quality of the images of an EDX tilt series is much poorer in comparison to the images of a HAADF-STEM tilt series. We assume that the quality of the individual EDX maps contribute to the shape error of the NN-FBP reconstruction, which hampers a reliable 3D reconstruction.\

## 4. Conclusion

By the use of the NN-FBP reconstruction algorithm on HAADF-STEM tilt series of Au nanoparticles, we are able to yield reconstructions based on highly limited data with a comparable quality to a reconstruction based on a full data series with a tilt increment of 1°. The decrease in acquisition time and the use of an efficient reconstruction method enables us to examine a broad range of nanostructures in a statistical manner. Providing statistical information on the 3D shape of certain nanoparticles will provide the synthesis scientists with crucial information and more guided modifications can be made to the synthesis procedure. The NN-FBP algorithm also has promising prospects for the 3D investigation of beam sensitive samples, where only a limited amount of projection images need to be acquired.

The extension of NN-FBP towards a 3D chemical characterization remains challenging. The implementation on HAADF-STEM tilt series of core/shell nanostructures showed some promising results, however more fine-tuning of the filters of the NN-FBP algorithm and/or more projection images in the learning phase are necessary to minimize missing wedge artefacts. The use of NN-FBP on EDX tomography is precarious as the acquisition of a high quality tilt series for the learning phase remains challenging. We conclude that the NN-FBP reconstruction algorithm is applicable on nanostructures consisting of one element from which projection images with a high signal-to-noise ratio can be acquired.

# Chapter 8

## Outlook towards a 3D chemical characterization at the atomic scale

## 1. Introduction

Recent advances such as the development of spherical aberration correction for electron microscopy[231,232] and the development of the ChemiSTEM system[233] have provided the opportunity to chemical mapping in STEM at the atomic scale. A simultaneous acquisition of a HAADF-STEM image and the collection of either EELS[234–238] or EDX spectra[239–244] enables us to determine directly the location of different atomic columns and the chemical structure of the investigated material. The need for long acquisition times or a long dwell time at each recorded pixel have limited the materials that can be investigated by chemical mapping at the atomic level. Typically, the longer dwell time causes electron beam damage to the investigated material unless they are (relatively) resistant to electron beam irradiation. Previous studies have reported the atomic-scale mapping of slabs of materials such as GaAs, $SrTiO_3$ and interfaces such as InGaAs/InP, $SrTiO_3/PbTiO_3$ and $La_{0.7}Sr_{0.3}MnO_3/BiFeO_3$[239,241,243,245]. Chemical mapping of a nanoparticle at the atomic level by EDX remains however unexplored. Both the need for extreme stability of the microscope and the limited thickness of the nanoparticle complicate the acquisition of a high quality EDX map at the atomic scale.

Nowadays, the synthesis of ceria-zirconia nanocrystals as oxygen storage catalysts aims for a production of zirconia nanocrystals with a very thin ceria layer. The use of high resolution EDX mapping is tested to study the atomic thickness of the ceria layer. Next, the applicability of atomically resolved EDX maps for atom-counting is evaluated by the investigation of ceria nanoparticles.

## 2. Ceria-zirconia nanocrystals at the atomic scale

Ceria-zirconia nanocrystals with low ceria content are promising as catalysts for oxygen storage in a broad temperature range. The reduction of the active ceria layer around a zirconia nanocrystal towards atomically thin emerges in both an economic and geo-strategic point of view. A synthesis procedure is proposed which performs a Severe Reduction followed by Mild Oxidation treatment (SRMO) after the growth of ceria islands at the surface of the zirconia nanocrystal[246].

HAADF-STEM imaging relies on Z-contrast in the image and as the atomic numbers of Ce and Zr are quite different ($Z_{Ce}$ = 58 and $Z_{Zr}$ = 40), an intensity difference in a HAADF-STEM image could be expected. Since, the nanocrystal consists of only 2% ceria, HAADF-STEM imaging will, however, not provide us with reliable chemical information. As the characteristic peaks of Ce and Zr have very different energies, EDX mapping is a suitable technique to examine the chemical composition of ceria-zirconia nanocrystals. The low amount of Ce requires however longer acquisition times to collect sufficient signal. An acquisition time of 20 minutes with a standard electron dose for spectroscopy (approximately 200 pA) is needed to detect sufficient signal for the low Ce content. The use of EDX tomography to retrieve the 3D chemical characterization of such nanocrystals is therefore less feasible as typically 15 projection images are required (-70°: 10°: +70°). Such experiments would require mapping of 5 hours, which will possibly induce beam damage, movement of the particle and a build-up of contamination. All these factors will hamper a reliable 3D chemical characterization. As it is expected that the Ce content is present as a shell around the nanocrystal, two orthogonal EDX projections are acquired at a tilt angle of -45° (Figure 8.1.b) and +45° (Figure 8.1.d). In these EDX maps, the Zr signal is indicated in red and the Ce signal is indicated in green. It is clear from the projected maps that a thin layer of ceria is formed at the surface of the nanocrystal. An integrated line profile across the nanocrystal (Figure 8.1.e) confirms the presence of Ce at the surface. From these results we can already conclude that the SRMO treatment was successful as the ceria islands formed a surface layer around the zirconia particle.

We can however not identify the atomic thickness of this Ce layer based on these EDX maps at the nanoscale. In order to determine the thickness of this layer, atomic-scale chemical imaging is needed. Since the amount of Ce is extremely low (2%), the acquisition of an EDX map with high signal-to-noise requires a long acquisition time and consequently a high stability is needed. In Figure 8.2.a, a high resolution HAADF-STEM image of a ceria-zirconia nanocrystal is shown. There is no clear intensity difference present at the outer surface of the nanocrystal which contains Ce. The white rectangle in Figure 8.2.a indicates the region which is investigated by EDX mapping. Figure 8.2.c and d show the averaged EDX maps of the Zr and the Ce counts, respectively. The corresponding

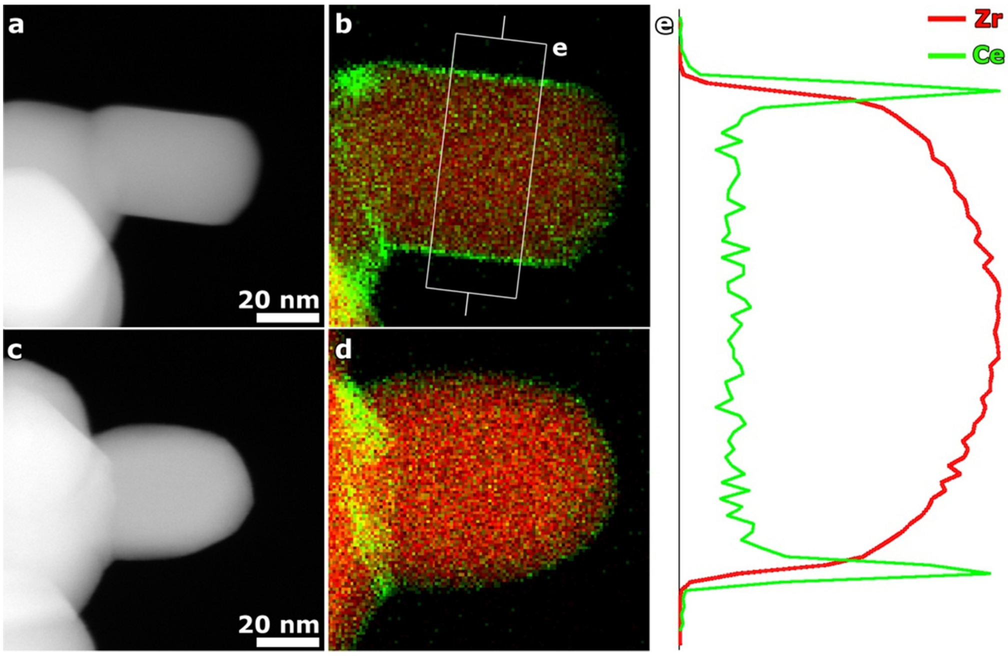

**Figure 8.1.** (a,c) HAADF-STEM projection images of a ceria/zirconia (SRMO) nanocrystal acquired at a tilt angle of -45° and +45°, respectively. In (b) and (d) the corresponding acquired EDX maps, with an acquisition time of 20 minutes, are shown. The Zr signal is indicated in red and the Ce signal is indicated in green. The orthogonal EDX maps prove that the nanocrystal is covered with a Ce containing layer. The line profile through the crystal in (e) confirms the presence of a Ce surface layer.

HAADF-STEM image is presented in Figure 8.2.b together with an indication of the direction along which the line profile in Figure 8.2.e is extracted. From this integrated line profile, it is clear that the ceria layer consists of only 2 atomic layers. Additionally, clear peaks at the position of the atomic columns of Zr can be observed in Figure 8.2.e. This result is extremely promising as it is the first EDX map at the atomic scale of a nanoparticle to our knowledge. It has to be pointed out that to acquire such a map, the nanoparticle needs to be quite robust to the electron beam as such long mapping at a very small area of the nanoparticle is intensive and can possibly result in local beam damage. This is a critical point towards the 3D chemical characterization of nanoparticles at the atomic scale.

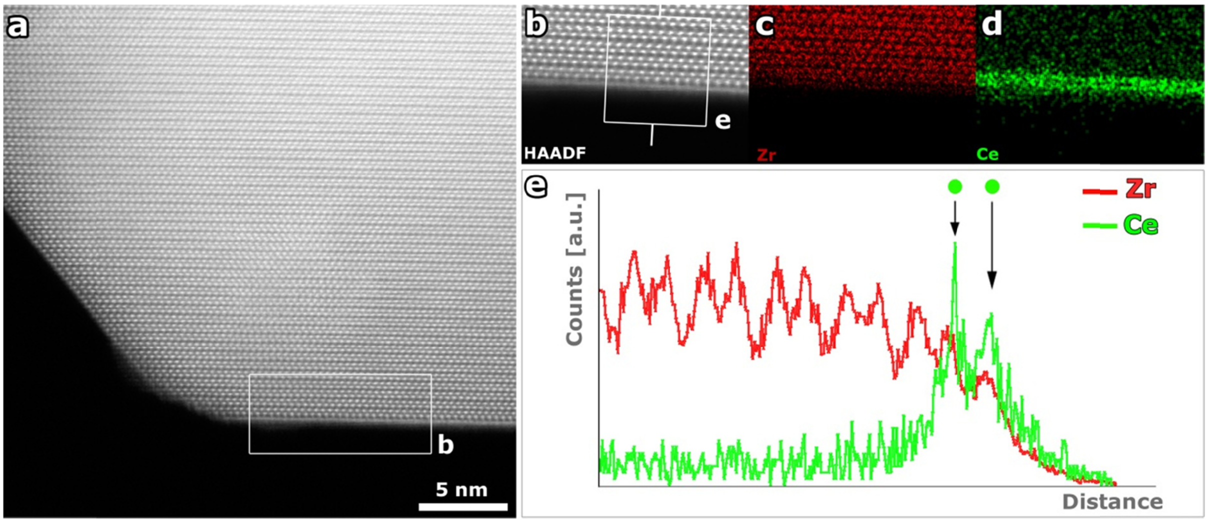

**Figure 8.2.** (a) High resolution HAADF-STEM image of a ceria-zirconia nanocrystal after SRMO treatment, where (b) indicates the location of the acquisition of the EDX map. (c) Averaged EDX maps of the Zr net counts and the Ce net counts, which shows the presence of Ce at the surface of the nanocrystal. In the corresponding HAADF-STEM image, the location of the line profile (e) is shown. (e) The line profile perpendicular to the edge of the nanocrystal indicates that the Ce containing shell consists of two atomic layers.

## 3. Extension to 3D

In the past, a 3D characterization of different nanocrystals based on a single projection image has been reported. The 3D atomic structure of an isolated Au nanocluster was obtained from a single aberration corrected high resolution HAADF-STEM image[247]. The approach was optimized by the use of statistical methods which retrieve the number of atoms in each projected atomic column in a high resolution HAADF-STEM projection image, which revealed the atomic lattice of a Ag nanoparticle embedded in an Al matrix[107]. The counting results of different HAADF-STEM projection images were used as an input for a discrete tomography algorithm; which was later on used to reconstruct a PbSe core in a PbSe/CdSe core/shell nanoparticle[106]. Recent advances have resulted in unscrambling mixed elements in a Au/Ag core/shell nanoparticle based on atom-counting[248]. So far, such statistical approaches have not yet been applied to EDX maps.

We have investigated the applicability of EDX maps as an input for atom-counting. If so, similar techniques as those for HAADF-STEM can be used to reach 3D atomic resolution by EDX. Therefore, we investigated a pure ceria nanoparticle of which both an atomic resolution HAADF-STEM image and EDX map are simultaneously acquired. In a first step (Figure 8.3.a and b), the HAADF-STEM image is used to determine both the atomic column positions and the total intensities of electrons scattered by the atomic columns, the so-called scattering cross-sections. The atomic column positions retrieved from the high resolution HAADF-STEM image can be used as starting positions for the EDX map due to the simultaneous acquisition (Figure 8.3.c). The quality of an EDX map is in general poorer in comparison to the HAADF-STEM image. If this is the case, the atomic column positions found in the HAADF-STEM image can be duplicated and used in the EDX map. Here, the quality of the EDX map of the ceria particle allowed us to fit the atomic column positions on the map itself. Afterwards, the scattering cross-sections of the EDX map can be obtained (Figure 8.3.d). A schematic procedure of this approach is shown in Figure 8.3.

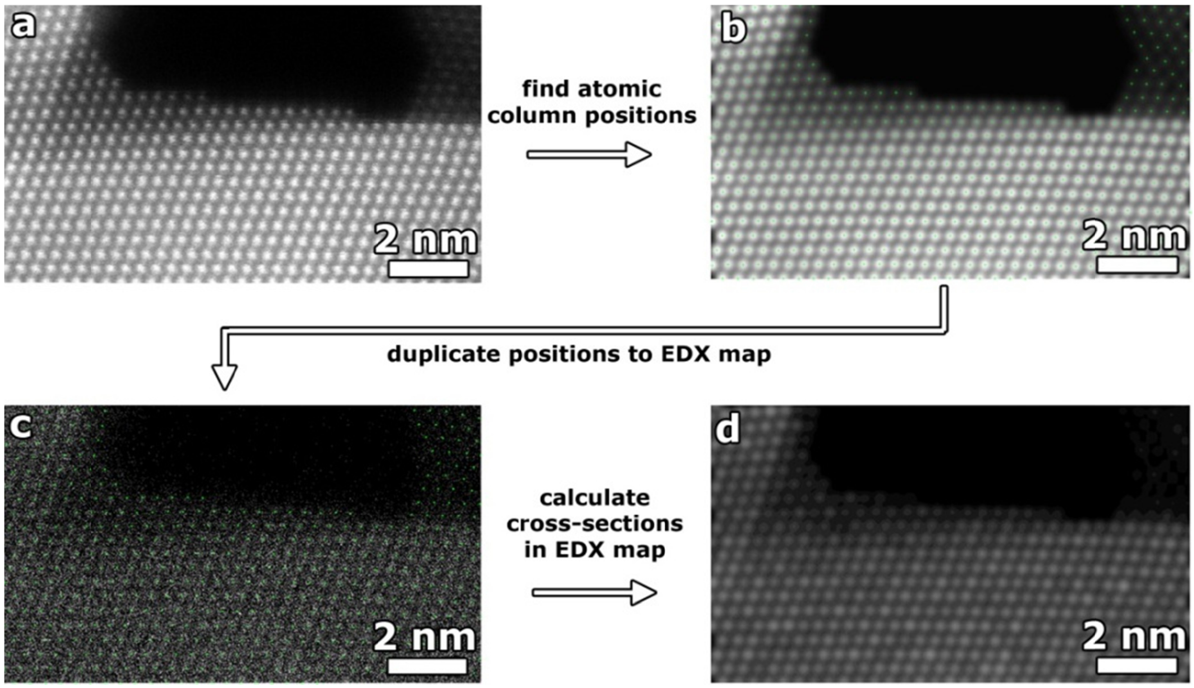

**Figure 8.3.** Schematic representation of how the atomic column positions and scattering cross-sections in an EDX map are retrieved.

Then, we can relate the cross-sections in both images to atom counts and compare both outcomes. As the use of statistical parameter estimation theory has proven to be successful on HAADF-STEM data[180], we utilize these results as the ground truth. In Figure 8.4.a, the results of atom-counting on the HAADF-STEM image is presented. The HAADF scattering cross-sections are visualized in function of the retrieved number of atoms in Figure 8.4.c, from which a linear dependence is found. The EDX scattering cross-sections depicted in blue show a comparable trend as the HAADF scattering cross-sections, which confirm the applicability of EDX maps for atom-counting. Based on this trend, the atom counts of the EDX map are scaled to match the HAADF-STEM counting results, to retrieve absolute numbers for each atomic column. We believe that this result will open up future possibilities towards the atomic resolution chemical characterization of hetero-nanostructures in 3D.

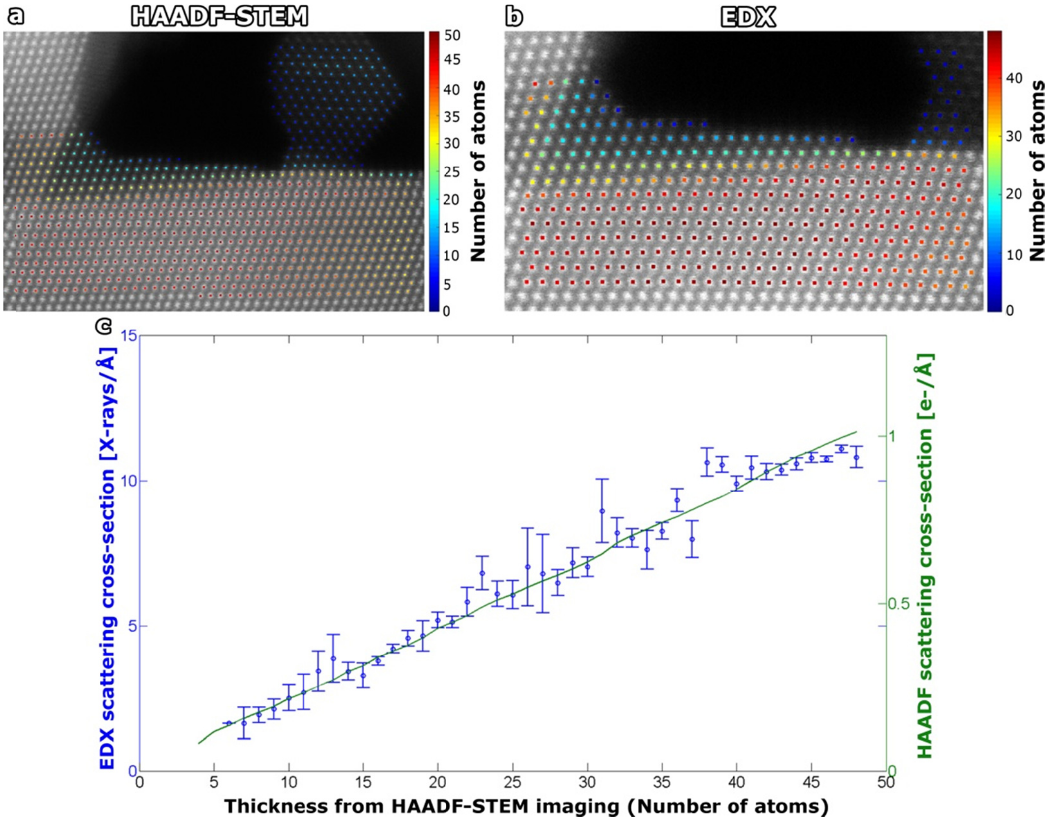

**Figure 8.4.** The atom-counting results of (a) the HAADF-STEM image and (b) the EDX map of a ceria nanoparticle are visualized. (c) The scattering cross-sections for both techniques are shown in function of the number of atoms. We have to note that the absolute number of atoms of the EDX map is scaled to match the HAADF-STEM counting results.

## 4. Conclusion

Different TEM techniques are able to resolve chemical information of complex hetero-nanostructures at the atomic level. With the use of EDX mapping, the chemical character of a broad variety of nanostructures can be examined. Here, we successfully applied EDX mapping at the atomic level, to retrieve the atomic thickness of a very thin ceria layer in a ceria-zirconia nanocrystal. Up to our knowledge, this is the first experimental result of atomic resolution EDX mapping of a nanoparticle. We confirmed the applicability of atomically resolved EDX maps for atom-counting by studying a ceria nanoparticle. We foresee great potential using this approach to enable a 3D chemical characterization of nanostructures at the atomic scale.

# Chapter 9

## Outlook

## 1. Conclusion

In this thesis, several challenges in the field of electron tomography were addressed. The application of HAADF-STEM tomography enabled us to study the helicity of CdSe nanohelices and the position of the core of several semiconductor core/shell hetero-nanostructures was obtained. The use of low-dose imaging and template-matching was applied to beam sensitive inorganic-organic nanocrystals, which revealed their native atomic structure. A neural network based reconstruction approach was successfully implemented for HAADF-STEM tilt series of Au nanoparticles. This enabled us to extract quantitative 3D information in a statistically relevant manner. The applicability of atomically resolved EDX maps for atom-counting and eventually for 3D atomic resolution tomography was also investigated in this thesis. However, remaining challenges occur:

- the 3D study of beam sensitive materials;
- the development of robust reconstruction algorithms for spectroscopic tomography;
- the 3D chemical characterization of nanostructures at the atomic level.

## 2. The study of beam sensitive materials

In Chapter 3, CdSe semiconductor nanoplatelets were successfully characterized by high resolution HAADF-STEM despite their degradation. The study of the atomic structure of perovskite nanocrystals was more challenging due to their extreme beam sensitivity. The use of high resolution HAADF-STEM enabled us to study the atomic structure of lead cesium halide perovskite nanocrystals in Chapter 4. Organolead iodide perovskites, however, could not be studied using a conventional approach, as beam damage occurred almost instantaneously. Therefore, the need of low dose imaging was required to study the nanocrystals at the atomic level. With the use of a template-matching algorithm, we were able to improve the signal-to-noise level and to retrieve the atomic structure before any degradation altered the structure. Additionally, the potential of exit wave reconstruction was discussed since it is of interest when investigating the atomic structure of the perovskite nanostructures. Less local damage occurred with the use of a TEM based technique in comparison to the damage obtained upon scanning.

The extension of this technique to 3D will require an ultrasensitive detection system to acquire focal series at different tilt angles in a time efficient manner. The drastic reduction of acquisition time will be crucial in the 3D atomic characterization studies of beam sensitive materials such as perovskite nanocrystals, porous samples or polymer based materials.

## 3. Novel reconstruction algorithms for spectroscopic tomography

The use of HAADF-STEM tomography was used in the thesis to obtain the 3D structure of nanoparticles, for example to elucidate on the helicity of CdSe nanoplatelets in Chapter 3. In Chapter 5, the location of the core of semiconductor core/shell hetero-nanostructures could be determined by 3D HAADF-STEM since a significant difference in the atomic number of the core and the shell was present. We conclude that extracting 3D chemical information is in some cases possible with the use of HAADF-STEM. EDX tomography, however, can be used as a more general approach since no restrictions on the atomic number of the elements in the hetero-nanostructure are necessary (Chapter 6). The low amount of EDX projection images in combination with their low signal-to-noise level complicates the 3D reconstructions and obtaining quantitative 3D results remain troublesome (Chapter 5).

Although very precise and local information on the 3D structure of colloidal nanoparticles can be obtained by electron tomography, a major drawback is the total duration of such experiments. Due to a combination of a long acquisition procedure and a time-consuming reconstruction process, it is not straightforward to obtain statistically relevant results in 3D. Moreover, in order to have a general understanding concerning the structure-property relation of functional nanoparticles, a large number of nanoparticles needs to be investigated.

The need for novel reconstruction algorithms which are able to yield high quality 3D reconstructions based on a limited amount of projection images is emerging. Such algorithms can open up the possibility of performing statistical analysis on 3D parameters and eventually lead to high throughput electron tomography. The extension of advanced reconstruction algorithm to obtain 3D chemical information needs some further efforts. For HAADF-STEM tilt series of hetero-nanostructures, 10 projection images were not sufficient to develop a successful NN-FBP algorithm for hetero-nanostructures. For EDX tomography tilt series, the NN-FBP approach is less suitable due to the low signal-to-noise ratio of the individual EDX projection maps. The combination of HAADF-STEM and EDX tomography is required to obtain reliable 3D chemical reconstructions from these tilt series. It has been shown that using compressive sensing, the main features in an image can still be retrieved when only 20% if the pixels in the scanned area are acquired[249]. Therefore, the use of compressive sensing should be evaluated since an amount of the pixels in an EDX map have a very low count rate.

## 4. The extension towards a 3D chemical characterization at the atomic level

In Chapter 8, we have confirmed the applicability of EDX maps for atom-counting by studying a ceria nanoparticle. This result will enable us to study the 3D chemical character of complex hetero-nanostructures in 3D at the atomic level.

A major drawback of EDX remains the need for long acquisition times. Therefore, only a limited amount of colloidal nanoparticles are suitable for EDX investigations, as others will deform or alter upon acquisition. With the development of the Super-X detection system, the detection efficiency already improved by a factor of 5 in comparison to the previous detector set-up, but it remains a limiting factor. The extension of such atomic characterization studies using EDX in 3D will be hampered by the limited detection efficiency. The acquisition of multiple atomically resolved EDX maps will therefore be hindered, which makes the application of atomic resolution EDX tomography problematic. We believe that the use of statistical parameter estimation theory to perform atom-counting on a 2D EDX map will open up the possibility to retrieve the 3D atomic resolution chemical character of nanoparticles.

# References

(1) Rosi, N. L.; Mirkin, C. A. *Chem. Rev.* **2005**, *105* (4), 1547.

(2) Zijlstra, P.; Chon, J. W. M.; Gu, M. *Nature* **2009**, *459* (7245), 410.

(3) Zijlstra, P.; Orrit, M. *Reports Prog. Phys.* **2011**, *74* (10), 106401.

(4) Dreaden, E. C.; Alkilany, A. M.; Huang, X.; Murphy, C. J.; El-Sayed, M. a. *Chem. Soc. Rev.* **2012**, *41* (7), 2740.

(5) Cao-Milán, R.; Liz-Marzán, L. M. *Expert Opin. Drug Deliv.* **2014**, *11* (5), 741.

(6) Daniel, M. C.; Astruc, D. *Chemical Reviews*. 2004, pp 293–346.

(7) Burda, C.; Chen, X.; Narayanan, R.; El-Sayed, M. A. *Chemical Reviews*. 2005, pp 1025–1102.

(8) Pérez-Juste, J.; Pastoriza-Santos, I.; Liz-Marzán, L. M.; Mulvaney, P. *Coord. Chem. Rev.* **2005**, *249* (17-18), 1870.

(9) Liz-Marzán, L. M. *Langmuir* **2006**, *22* (1), 32.

(10) Eustis, S.; el-Sayed, M. a. *Chem. Soc. Rev.* **2006**, *35* (3), 209.

(11) Sánchez-Iglesias, A.; Pastoriza-Santos, I.; Pérez-Juste, J.; Rodríguez-González, B.; García de Abajo, F. J.; Liz-Marzán, L. M. *Adv. Mater.* **2006**, *18* (19), 2529.

(12) Grzelczak, M.; Pérez-Juste, J.; Mulvaney, P.; Liz-Marzán, L. M. *Chem. Soc. Rev.* **2008**, *37* (9), 1783.

(13) Tao, A. R.; Habas, S.; Yang, P. *Small* **2008**, *4* (3), 310.

(14) Huang, X.; Neretina, S.; El-Sayed, M. A. *Advanced Materials*. 2009, pp 4880–4910.

(15) Jana, N. R.; Gearheart, L.; Murphy, C. J. *Adv. Mater.* **2001**, *13* (18), 1389.

(16) Nikoobakht, B.; El-Sayed, M. A. *Chem. Mater.* **2003**, *15* (10), 1957.

(17) Gou, L.; Murphy, C. J. *Chem. Mater.* **2005**, *17* (14), 3668.

(18) Millstone, J. E.; Wei, W.; Jones, M. R.; Yoo, H.; Mirkin, C. A. *Nano Lett.* **2008**, *8* (8), 2526.

(19) Jain, S.; Hirst, D. G.; O'Sullivan, J. M. *Br. J. Radiol.* **2012**, *85* (1010), 101.

(20) Polavarapu, L.; Liz-Marzán, L. M. *Phys. Chem. Chem. Phys.* **2013**, *15* (15), 5288.

(21) Velev, O. D.; Kaler, E. W. **1999**, *15* (11), 0.

(22) Taton, T. A.; Mirkin, C. A.; Letsinger, R. L.; Taton, T. A.; Mirkin, C. A.; Letsinger, R. L. **2016**, *289* (5485), 1757.

(23) Li, M.; Zhang, Z. S.; Zhang, X.; Li, K. Y.; Yu, X. F. *Opt. Express* **2008**, *16* (18), 14288.

(24) Wang, L.; Kiya, A.; Okuno, Y.; Niidome, Y.; Tamai, N. *J. Chem. Phys.* **2011**, *134* (5), 054501.

(25) Hunyadi, S. E.; Murphy, C. J. *J. Mater. Chem.* **2006**, *16* (40), 3929.

(26) Gómez-Graña, S.; Pérez-Juste, J.; Alvarez-Puebla, R. A.; Guerrero-Martínez, A.; Liz-Marzán, L. M. *Adv. Opt. Mater.* **2013**, *1* (7), 477.

(27) Murray, C. B.; Norris, D. J.; Bawendi, M. G. *J. Am. Chem. Soc.* **1993**, *115* (19), 8706.

(28) Alivisatos, A. P. *J. Phys. Chem.* **1996**, *100* (31), 13226.

(29) Donegá, C. de M. *Chem. Soc. Rev.* **2011**, *40* (3), 1512.

(30) Ip, A. H.; Thon, S. M.; Hoogland, S.; Voznyy, O.; Zhitomirsky, D.; Debnath, R.; Levina, L.; Rollny, L. R.; Carey, G. H.; Fischer, A.; Kemp, K. W.; Kramer, I. J.; Ning, Z.; Labelle, A. J.; Chou, K. W.; Amassian, A.; Sargent, E. H. *Nat. Nanotechnol.* **2012**, *7* (9), 577.

(31) Shirasaki, Y.; Supran, G. J.; Bawendi, M. G.; Bulović, V. *Nat. Photonics* **2012**, *7* (1), 13.

(32) Duan, X.; Lieber, C. M. *Adv. Mater.* **2000**, *12* (4), 298.

(33) Peng, X.; Manna, L.; Yang, W.; Wickham, J.; Scher, E.; Kadavanich, Andreas, Alivisatos, A. P. *Nature* **2000**, *404* (6773), 59.

(34) Ithurria, S.; Dubertret, B. *J. Am. Chem. Soc.* **2008**, *130* (49), 16504.

(35) Son, J. S.; Yu, J. H.; Kwon, S. G.; Lee, J.; Joo, J.; Hyeon, T. *Adv. Mater.* **2011**, *23* (28), 3214.

(36) Ithurria, S.; Bousquet, G.; Dubertret, B. *J. Am. Chem. Soc.* **2011**, *133* (9), 3070.

(37) Tessier, M. D.; Javaux, C.; Maksimovic, I.; Loriette, V.; Dubertret, B. *ACS Nano* **2012**, *6* (8), 6751.

(38) Bouet, C.; Tessier, M. D.; Ithurria, S.; Mahler, B.; Nadal, B.; Dubertret, B. *Chem. Mater.* **2013**, *25* (8), 1262.

(39) Chen, Z.; Nadal, B.; Mahler, B.; Aubin, H.; Dubertret, B. *Adv. Funct. Mater.* **2014**, *24* (3), 295.

(40) Ithurria, S.; Tessier, M. D.; Mahler, B.; Lobo, R. P. S. M.; Dubertret, B.; Efros, A. L. *Nat. Mater.* **2011**, *10* (12), 936.

(41) She, C.; Fedin, I.; Dolzhnikov, D. S.; Demortière, A.; Schaller, R. D.; Pelton, M.; Talapin, D. V. *Nano Lett.* **2014**, *14* (5), 2772.

(42) Son, J. S.; Wen, X. D.; Joo, J.; Chae, J.; Baek, S.; Park, K.; Kim, J. H.; An, K.; Yu, J. H.; Kwon, S. G.; Choi, S. H.; Wang, Z.; Kim, Y. W.; Kuk, Y.; Hoffmann, R.; Hyeon, T. *Angew. Chemie - Int. Ed.* **2009**, *48* (37), 6861.

(43) Li, Z.; Peng, X. *J. Am. Chem. Soc.* **2011**, *133* (17), 6578.

(44) Mahler, B.; Nadal, B.; Bouet, C.; Patriarche, G.; Dubertret, B. *J. Am. Chem. Soc.* **2012**, *134* (45), 18591.

(45) Hines, M. A.; Guyot-Sionnest, P. *J. Phys. Chem.* **1996**, *100* (2), 468.

(46) Talapin, D. V.; Mekis, I.; Götzinger, S.; Kornowski, A.; Benson, O.; Weller, H. *J. Phys. Chem. B* **2004**, *108* (49), 18826.

(47) Michalet, X. *Science (80-. ).* **2005**, *307* (5709), 538.

(48) Qian, L.; Zheng, Y.; Xue, J.; Holloway, P. H. *Nat. Photonics* **2011**, *5* (9), 543.

(49) Lee, J.-S.; Kovalenko, M. V; Huang, J.; Chung, D. S.; Talapin, D. V. *Nat. Nanotechnol.* **2011**, *6* (6), 348.

(50) Ithurria, S.; Guyot-Sionnest, P.; Mahler, B.; Dubertret, B. *Phys. Rev. Lett.* **2007**, *99* (26), 265501.

(51) Yu, Z.; Guo, L.; Du, H.; Krauss, T.; Silcox, J. *Nano Lett.* **2005**, *5* (4), 565.

(52) Son, D. H. *Science (80-. ).* **2004**, *306* (5698), 1009.

(53) Park, J.; Zheng, H.; Jun, Y.; Alivisatos, A. P. *J. Am. Chem. Soc.* **2009**, *131* (39), 13943.

(54) Talapin, D. V.; Koeppe, R.; Götzinger, S.; Kornowski, A.; Lupton, J. M.; Rogach, A. L.; Benson, O.; Feldmann, J.; Weller, H. *Nano Lett.* **2003**, *3* (12), 1677.

(55) Carbone, L.; Nobile, C.; De Giorgi, M.; Della Sala, F.; Morello, G.; Pompa, P.; Hytch, M.; Snoeck, E.; Fiore, A.; Franchini, I. R.; Nadasan, M.; Silvestre, A. F.; Chiodo, L.; Kudera, S.; Cingolani, R.; Krahne, R.; Manna, L. *Nano Lett.* **2007**, *7* (10), 2942.

(56) Mahler, B.; Lequeux, N.; Dubertret, B. *J. Am. Chem. Soc.* **2010**, *132* (3), 953.

(57) Chen, O.; Zhao, J.; Chauhan, V. P.; Cui, J.; Wong, C.; Harris, D. K.; Wei, H.; Han, H.-S.; Fukumura, D.; Jain, R. K.; Bawendi, M. G. *Nat. Mater.* **2013**, *12* (5), 445.

(58) Tessier, M. D.; Mahler, B.; Nadal, B.; Heuclin, H.; Pedetti, S.; Dubertret, B. *Nano Lett.* **2013**, *13* (7), 3321.

(59) Rabouw, F. T.; Lunnemann, P.; Van Dijk-Moes, R. J. A.; Frimmer, M.; Pietra, F.; Koenderink, A. F.; Vanmaekelbergh, D. *Nano Lett.* **2013**, *13* (10), 4884.

(60) Chen, Y.; Vela, J.; Htoon, H.; Casson, J. L.; Werder, D. J.; Bussian, D. A.; Klimov, V. I.; Hollingsworth, J. A. *J. Am. Chem. Soc.* **2008**, *130* (15), 5026.

(61) Klimov, V. I.; Ivanov, S. A.; Nanda, J.; Achermann, M.; Bezel, I.; McGuire, J. A.; Piryatinski, A. *Nature* **2007**, *447* (7143), 441.

(62) Zhong, H.; Zhou, Y.; Ye, M.; He, Y.; Ye, J.; He, C.; Yang, C.; Li, Y. *Chem. Mater.* **2008**, *20* (20), 6434.

(63) Panthani, M. G.; Stolle, C. J.; Reid, D. K.; Rhee, D. J.; Harvey, T. B.; Akhavan, V. A.; Yu, Y.; Korgel, B. A. *J. Phys. Chem. Lett.* **2013**, *4* (12), 2030.

(64) Yarema, O.; Bozyigit, D.; Rousseau, I.; Nowack, L.; Yarema, M.; Heiss, W.; Wood, V. *Chem. Mater.* **2013**, *25* (18), 3753.

(65) Kolny-Olesiak, J.; Weller, H. *ACS Appl. Mater. Interfaces* **2013**, *5* (23), 12221.

(66) Kruszynska, M.; Borchert, H.; Parisi, J.; Kolny-Olesiak, J. *J. Am. Chem. Soc.* **2010**, *132* (45), 15976.

(67) Lu, X.; Zhuang, Z.; Peng, Q.; Li, Y. *Cryst. Eng. Comm.* **2011**, *13* (12), 4039.

(68) De Trizio, L.; Prato, M.; Genovese, A.; Casu, A.; Povia, M.; Simonutti, R.; Alcocer, M. J. P.; D'Andrea, C.; Tassone, F.; Manna, L. *Chem. Mater.* **2012**, *24* (12), 2400.

(69) Stolle, C. J.; Schaller, R. D.; Korgel, B. A. *J. Phys. Chem. Lett.* **2014**, *5* (18), 3169.

(70) Wang, X.; Swihart, M. T. *Chem. Mater.* **2015**, *27* (5), 1786.

(71) Singh, A.; Coughlan, C.; Milliron, D. J.; Ryan, K. M. *Chem. Mater.* **2015**, *27* (5), 1517.

(72) Lee, M. M.; Teuscher, J.; Miyasaka, T.; Murakami, T. N.; Snaith, H. J. *Science (80-. ).* **2012**, *338* (6107), 643.

(73) Schmidt, L. C.; Pertegás, A.; González-Carrero, S.; Malinkiewicz, O.; Agouram, S.; Mínguez Espallargas, G.; Bolink, H. J.; Galian, R. E.; Pérez-Prieto, J. *J. Am. Chem. Soc.* **2014**, *136* (3), 850.

(74) Kojima, A.; Teshima, K.; Shirai, Y.; Miyasaka, T. *J. Am. Chem. Soc.* **2009**, *131* (17), 6050.

(75) Kim, H.-S.; Lee, C.-R.; Im, J.-H.; Lee, K.-B.; Moehl, T.; Marchioro, A.; Moon, S.-J.; Humphry-Baker, R.; Yum, J.-H.; Moser, J. E.; Grätzel, M.; Park, N.-G. *Sci. Rep.* **2012**, *2* (7436), 591.

(76) Jeon, N. J.; Noh, J. H.; Yang, W. S.; Kim, Y. C.; Ryu, S.; Seo, J.; Seok, S. Il. *Nature* **2015**, *517* (7535), 476.

(77) De Wolf, S.; Holovsky, J.; Moon, S.-J.; Löper, P.; Niesen, B.; Ledinsky, M.; Haug, F.-J.; Yum, J.-H.; Ballif, C. *J. Phys. Chem. Lett.* **2014**, *5* (6), 1035.

(78) Heo, J. H.; Im, S. H.; Noh, J. H.; Mandal, T. N.; Lim, C.-S.; Chang, J. A.; Lee, Y. H.; Kim, H.; Sarkar, A.; NazeeruddinMd, K.; Gratzel, M.; Seok, S. Il. *Nat Phot.* **2013**, *7* (6), 486.

(79) Zhou, H.; Chen, Q.; Li, G.; Luo, S.; Song, T. -b.; Duan, H.-S.; Hong, Z.; You, J.; Liu, Y.; Yang, Y. *Science (80-. ).* **2014**, *345* (6196), 542.

(80) Bi, D.; El-Zohry, A. M.; Hagfeldt, A.; Boschloo, G. *ACS Appl. Mater. Interfaces* **2014**, *6* (21), 18751.

(81) Yang, S.; Zheng, Y. C.; Hou, Y.; Chen, X.; Chen, Y.; Wang, Y.; Zhao, H.; Yang, H. G. *Chem. Mater.* **2014**, *26* (23), 6705.

(82) Tsai, H.; Nie, W.; Cheruku, P.; Mack, N. H.; Xu, P.; Gupta, G.; Mohite, A. D.; Wang, H.-L. *Chem. Mater.* **2015**, *27* (16), 5570.

(83) Salim, T.; Sun, S.; Abe, Y.; Krishna, A.; Grimsdale, A. C.; Lam, Y. M. *J. Mater. Chem. A Mater. energy Sustain.* **2015**, *3*, 8943.

(84) Yuan, H.; Debroye, E.; Janssen, K.; Naiki, H.; Steuwe, C.; Lu, G.; Moris, M.; Orgiu, E.; Uji-I, H.; De Schryver, F.; Samorì, P.; Hofkens, J.; Roeffaers, M. *J. Phys. Chem. Lett.* **2016**, *7* (3), 561.

(85) Yuan, H.; Debroye, E.; Caliandro, G.; Janssen, K. P. F.; van Loon, J.; Kirschhock, C. E. A.; Martens, J. A.; Hofkens, J.; Roeffaers, M. B. J. *ACS Omega* **2016**, *1* (1), 148.

(86) Moller, C. *Nature* **1958**, *182* (4647), 1436.

(87) Swarnkar, A.; Chulliyil, R.; Ravi, V. K.; Irfanullah, M.; Chowdhury, A.; Nag, A. *Angew. Chemie Int. Ed.* **2015**, *54* (51), 15424.

(88) Bekenstein, Y.; Koscher, B. A.; Eaton, S. W.; Yang, P.; Alivisatos, A. P. *J. Am. Chem. Soc.* **2015**, *137* (51), 16008.

(89) Song, J.; Li, J.; Li, X.; Xu, L.; Dong, Y.; Zeng, H. *Adv. Mater.* **2015**, *27* (44), 7162.

(90) Wang, Y.; Li, X.; Song, J.; Xiao, L.; Zeng, H.; Sun, H. *Adv. Mater.* **2015**, *27* (44), 7101.

(91) Li, X.; Wu, Y.; Zhang, S.; Cai, B.; Gu, Y.; Song, J.; Zeng, H. *Adv. Funct. Mater.* **2016**, *26* (15), 2435.

(92) Trovarelli, A. *Catalysis by Ceria and Related Materials*; Imperial College Press, 2002.

(93) Duprez, D., Descorme, C. In *Catalysis by Ceria and Related Materials*; Imperial College Press, 2002; pp 243–280.

(94) Di Monte, R.; Kašpar, J. *Top. Catal.* **2004**, *28* (1-4), 47.

(95) Kaspar, J., Fornasiero, P. In *Catalysis by ceria and related materials*; Imperial College Press, 2002; pp 217–241.

(96) Shelef, M., Graham, G. W., M. R. W. In *Catalysis by ceria and related materials*; Imperial College Press, 2002; pp 343–375.

(97) Kaspar, J.; Di Monte, R.; Fornasiero, P.; Graziani, M.; Bradshaw, H.; Norman, C. *Top. Catal.* **2001**, *16*, 83.

(98) Koster, A. J.; Grimm, R.; Typke, D.; Hegerl, R.; Stoschek, A.; Walz, J.; Baumeister, W. *J. Struct. Biol.* **1997**, *120* (3), 276.

(99) Frank, J. *Electron Tomography: Methods for Three-Dimensional Visualization of Structures in the Cell*; Plenum Press: New York, London, 1992.

(100) Wolf, D.; Lubk, A.; Lichte, H.; Friedrich, H. *Ultramicroscopy* **2010**, *110* (5), 390.

(101) Weyland, M.; Yates, T. J. V.; Dunin-Borkowski, R. E.; Laffont, L.; Midgley, P. A. *Scr. Mater.* **2006**, *55* (1), 29.

(102) Bar Sadan, M.; Houben, L.; Wolf, S. G.; Enyashin, A.; Seifert, G.; Tenne, R.; Urban, K. *Nano Lett.* **2008**, *8* (3), 891.

(103) Midgley, P. A.; Bals, S. In *Handbook of Nanoscopy*; Wiley-VCH Verlag GmbH & Co. KGaA, 2012; pp 253–279.

(104) Goris, B.; Bals, S.; Van den Broek, W.; Verbeeck, J.; Van Tendeloo, G. *Ultramicroscopy* **2011**, *111* (8), 1262.

(105) Koster, A. J.; Ziese, U.; Verkleij, A. J.; Janssen, A. H.; de Jong, K. P. *J. Phys. Chem. B* **2000**, *104* (40), 9368.

(106) Bals, S.; Casavola, M.; van Huis, M. A.; Van Aert, S.; Batenburg, K. J.; Van Tendeloo, G.; Vanmaekelbergh, D. *Nano Lett.* **2011**, *11* (8), 3420.

(107) Van Aert, S.; Batenburg, K. J.; Rossell, M. D.; Erni, R.; Van Tendeloo, G. *Nature* **2011**, *470* (7334), 374.

(108) Goris, B.; De Beenhouwer, J.; De Backer, A.; Zanaga, D.; Batenburg, K. J.; Sánchez-Iglesias, A.; Liz-Marzán, L. M.; Van Aert, S.; Bals, S.; Sijbers, J.; Van Tendeloo, G. *Nano Lett.* **2015**, *15* (10), 6996.

(109) Ruska, E., Knoll, M. *Zeitschrift für Tech. Phys.* **1931**, *12*, 389.

(110) Knoll, M.; Ruska, E. *Zeitschrift für Tech. Phys.* **1932**, *79* (9-10), 699.

(111) Pennycook, S. J. *Ultramicroscopy* **1989**, *30* (1-2), 58.

(112) Radon, J. *Reports Proc. Saxony Acad. Sci.* **1917**, *69*, 262.

(113) Cormack, A. M. *J. Appl. Phys.* **1964**, *35* (10), 2908.

(114) Cormack, A.M., Hounsfield, G. N. **1979**.

(115) Hounsfield, G. N. *J. Comput. Assist. Tomogr.* **1980**, *4* (5), 665.

(116) De Rosier, D. J.; Klug, A. *Nature* **1968**, *217* (5124), 130.

(117) Hoppe, W., Langer, R., Knesch, G., Poppe, C. *Naturwissenschaften* **1968**, *55*, 333.

(118) Hart, R. G. *Science (80-. ).* **1968**, *159* (3822), 1464.

(119) Hawkes, P. W. *J. Frank, Ed. Electron Tomogr. Three Dimens. Imaging with Transm. Electron Microsc.* **1992**, No. Plenum Press, New York, 17.

(120) Kübel, C.; Voigt, A.; Schoenmakers, R.; Otten, M.; Su, D.; Lee, T.-C.; Carlsson, A.; Bradley, J. *Microsc. Microanal.* **2005**, *11* (05), 378.

(121) Friedrich, H.; McCartney, M. R.; Buseck, P. R. *Ultramicroscopy* **2005**, *106* (1), 18.

(122) Williams, D. B., Carter, C. B. *Transmission Electron Microscopy: A Text- book for Materials Science*, 1st editio.; Springer New York, 1996.

(123) Pennycook, S. J.; Rafferty, B.; Nellist, P. D. *Microsc. Microanal.* **2000**, *6*, 343.

(124) Van den Broek, W.; Rosenauer, A.; Goris, B.; Martinez, G. T.; Bals, S.; Van Aert, S.; Van Dyck, D. *Ultramicroscopy* **2012**, *116*, 8.

(125) Midgley, P. A.; Weyland, M. *Ultramicroscopy* **2003**, *96* (3-4), 413.

(126) Midgley, P. A.; Dunin-Borkowski, R. E. *Nat. Mater.* **2009**, *8* (4), 271.

(127) Van Tendeloo, G.; Bals, S.; Van Aert, S.; Verbeeck, J.; Van Dyck, D. *Advanced Materials*. 2012, pp 5655–5675.

(128) Biermans, E.; Molina, L.; Batenburg, K. J.; Bals, S.; Van Tendeloo, G. *Nano Lett.* **2010**, *10* (12), 5014.

(129) Leary, R.; Saghi, Z.; Armbrüster, M.; Wowsnick, G.; Schlögl, R.; Thomas, J. M.; Midgley, P. A. *J. Phys. Chem. C* **2012**, *116* (24), 13343.

(130) Möbus, G.; Doole, R. C.; Inkson, B. J. In *Ultramicroscopy*; 2003; Vol. 96, pp 433–451.

(131) Bals, S.; Goris, B.; Liz-Marzán, L. M.; Van Tendeloo, G. *Angew. Chemie Int. Ed.* **2014**, *53* (40), 10600.

(132) Yaguchi, T.; Konno, M.; Kamino, T.; Watanabe, M. *Ultramicroscopy* **2008**, *108* (12), 1603.

(133) Jarausch, K.; Thomas, P.; Leonard, D. N.; Twesten, R.; Booth, C. R. *Ultramicroscopy* **2009**, *109* (4), 326.

(134) Lasagni, F A, Huertas-Olivares, I.; Holazapfel, C.; Mücklich, F. *IOP Conf. Ser. Mater. Sci. Eng.* **2010**, *7*, 012016.

(135) Lepinay, K., Lorut, F., Pantel, R., Epicier, T. In *Proceedings EMC 2012*; 2012.

(136) Schlossmacher, P.; Klenov, D. O.; Freitag, B.; von Harrach, H. S. *Micros. Today* **2010**, *18* (04), 14.

(137) Genc, A.; Kovarik, L.; Gu, M.; Cheng, H.; Plachinda, P.; Pullan, L.; Freitag, B.; Wang, C. *Ultramicroscopy* **2013**, *131*, 24.

(138) Lepinay, K.; Lorut, F.; Pantel, R.; Epicier, T. *Micron* **2013**, *47*, 43.

(139) Goris, B.; Polavarapu, L.; Bals, S.; Van Tendeloo, G.; Liz-Marzán, L. M. *Nano Lett.* **2014**, *14* (6), 3220.

(140) Liakakos, N.; Gatel, C.; Blon, T.; Altantzis, T.; Lentijo-Mozo, S.; Garcia-Marcelot, C.; Lacroix, L. M.; Respaud, M.; Bals, S.; Van Tendeloo, G.; Soulantica, K. *Nano Lett.* **2014**, *14* (5), 2747.

(141) Saxton, W. O.; Baumeister, W.; Hahn, M. *Ultramicroscopy* **1984**, *13* (1-2), 57.

(142) Radermacher, M. *J. Electron Microsc. Tech.* **1988**, *9* (4), 359.

(143) Arslan, I.; Tong, J. R.; Midgley, P. A. *Ultramicroscopy* **2006**, *106* (11-12), 994.

(144) Kawase, N.; Kato, M.; Nishioka, H.; Jinnai, H. *Ultramicroscopy* **2007**, *107* (1), 8.

(145) Ke, X.; Bals, S.; Cott, D.; Hantschel, T.; Bender, H.; Van Tendeloo, G. *Microsc. Microanal.* **2010**, *16* (02), 210.

(146) Jarausch, K.; Leonard, D. N. *J. Electron Microsc. (Tokyo).* **2009**, *58* (3), 175.

(147) Kremer, J. R.; Mastronarde, D. N.; McIntosh, J. R. *J. Struct. Biol.* **1996**, *116* (1), 71.

(148) Schoenmakers, R. H. M.; Perquin, R. A.; Fliervoet, T. F.; Voorhout, W.; Schirmacher, H. *Microsc. Anal.* **2005**, *19*, 5.

(149) Zheng, S. Q.; Keszthelyi, B.; Branlund, E.; Lyle, J. M.; Braunfeld, M. B.; Sedat, J. W.; Agard, D. A. *J. Struct. Biol.* **2007**, *157* (1), 138.

(150) Radon, Johann, P. P. C. *IEEE Trans. Med. Imaging* **1986**, *5* (4), 170.

(151) Gilbert, P. *J. Theor. Biol.* **1972**, *36* (1), 105.

(152) Lee, S.-W.; Lee, C.-L.; Cho, H.-M.; Park, H.-S.; Kim, D.-H.; Choi, Y.-N.; Kim, H.-J. *J. Korean Phys. Soc.* **2011**, *59* (4), 2825.

(153) Hsieh., J. *Computed tomography: Principles, Design, Artifacts, and Recent Advances.*; SPIE - The international Society for Optical Engineering, Bellingham, Washington, USA, 1st edition, 2003.

(154) Crowther, R. A.; DeRosier, D. J.; Klug, A. *Proc. R. Soc. A Math. Phys. Eng. Sci.* **1970**, *317* (1530), 319.

(155) Heidari Mezerji, H.; Van den Broek, W.; Bals, S. *Ultramicroscopy* **2011**, *111* (5), 330.

(156) Gregor, J.; Benson, T. *IEEE Trans. Med. Imaging* **2008**, *27* (7), 918.

(157) Goris, B.; Van den Broek, W.; Batenburg, K. J.; Heidari Mezerji, H.; Bals, S. *Ultramicroscopy* **2012**, *113*, 120.

(158) Leary, R.; Saghi, Z.; Midgley, P. A.; Holland, D. J. *Ultramicroscopy* **2013**, *131*, 70.

(159) Goris, B.; Roelandts, T.; Batenburg, K. J.; Heidari Mezerji, H.; Bals, S. *Ultramicroscopy* **2013**, *127*, 40.

(160) Sigle, D. O.; Hugall, J. T.; Ithurria, S.; Dubertret, B.; Baumberg, J. J. *Phys. Rev. Lett.* **2014**, *113* (8), 087402.

(161) Tessier, M. D.; Biadala, L.; Bouet, C.; Ithurria, S.; Abecassis, B.; Dubertret, B. *ACS Nano* **2013**, *7* (4), 3332.

(162) Biadala, L.; Liu, F.; Tessier, M. D.; Yakovlev, D. R.; Dubertret, B.; Bayer, M. *Nano Lett.* **2014**, *14* (3), 1134.

(163) Kunneman, L. T.; Tessier, M. D.; Heuclin, H.; Dubertret, B.; Aulin, Y. V.; Grozema, F. C.; Schins, J. M.; Siebbeles, L. D. A. *J. Phys. Chem. Lett.* **2013**, *4* (21), 3574.

(164) Achtstein, A. W.; Prudnikau, A. V.; Ermolenko, M. V.; Gurinovich, L. I.; Gaponenko, S. V.; Woggon, U.; Baranov, A. V.; Leonov, M. Y.; Rukhlenko, I. D.; Fedorov, A. V.; Artemyev, M. V. *ACS Nano* **2014**, *8* (8), 7678.

(165) Ko, H.; Takei, K.; Kapadia, R.; Chuang, S.; Fang, H.; Leu, P. W.; Ganapathi, K.; Plis, E.; Kim, H. S.; Chen, S.-Y.; Madsen, M.; Ford, A. C.; Chueh, Y.-L.; Krishna, S.; Salahuddin, S.; Javey, A. *Nature* **2010**, *468* (7321), 286.

(166) Radisavljevic, B.; Radenovic, A.; Brivio, J.; Giacometti, V.; Kis, A. *Nat. Nanotechnol.* **2011**, *6* (3), 147.

(167) Kwak, J.; Bae, W. K.; Lee, D.; Park, I.; Lim, J.; Park, M.; Cho, H.; Woo, H.; Yoon, D. Y.; Char, K.; Lee, S.; Lee, C. *Nano Lett.* **2012**, *12* (5), 2362.

(168) Bouet, C.; Mahler, B.; Nadal, B.; Abecassis, B.; Tessier, M. D.; Ithurria, S.; Xu, X.; Dubertret, B. *Chem. Mater.* **2013**, *25* (4), 639.

(169) Son, J. S.; Wen, X.-D.; Joo, J.; Chae, J.; Baek, S.; Park, K.; Kim, J. H.; An, K.; Yu, J. H.; Kwon, S. G.; Choi, S.-H.; Wang, Z.; Kim, Y.-W.; Kuk, Y.; Hoffmann, R.; Hyeon, T. *Angew. Chemie Int. Ed.* **2009**, *48* (37), 6861.

(170) Li, Z.; Peng, X. *J. Am. Chem. Soc.* **2011**, *133* (17), 6578.

(171) Arriagada, F. J.; Osseo-Asare, K. *Colloids Surfaces A Physicochem. Eng. Asp.* **1999**, *154* (3), 311.

(172) López-Quintela, M. A. *Curr. Opin. Colloid Interface Sci.* **2003**, *8* (2), 137.

(173) Nann, T.; Mulvaney, P. *Angew. Chemie Int. Ed.* **2004**, *43* (40), 5393.

(174) Selvan, S. T.; Tan, T. T.; Ying, J. Y. *Adv. Mater.* **2005**, *17* (13), 1620.

(175) Darbandi, M.; Thomann, R.; Nann, T. *Chem. Mater.* **2005**, *17* (23), 5720.

(176) Koole, R.; van Schooneveld, M. M.; Hilhorst, J.; de Mello Donegá, C.; Hart, D. C. 't; van Blaaderen, A.; Vanmaekelbergh, D.; Meijerink, A. *Chem. Mater.* **2008**, *20* (7), 2503.

(177) Pietra, F.; van Dijk - Moes, R. J. A.; Ke, X.; Bals, S.; Van Tendeloo, G.; de Mello Donega, C.; Vanmaekelbergh, D. *Chem. Mater.* **2013**, *25* (17), 3427.

(178) Van Aert, S.; De Backer, A.; Martinez, G. T.; Goris, B.; Bals, S.; Van Tendeloo, G.; Rosenauer, A. *Phys. Rev. B* **2013**, *87* (6), 064107.

(179) De Backer, A.; Martinez, G. T.; Rosenauer, A.; Van Aert, S. *Ultramicroscopy* **2013**, *134*, 23.

(180) De Backer, A.; van den Bos, K. H. W.; Van den Broek, W.; Sijbers, J.; Van Aert, S. *Ultramicroscopy* **2016**, *171*, 104.

(181) Van Dyck, D., Op de Beeck, M. *Optik (Stuttg).* **1993**, *93*, 103.

(182) Wang, A., Chen, F. R., Van Aert, S., Van Dyck, D. *Ultramicroscopy* **2010**, *110*, 527.

(183) Wang, A.; Chen, F. R.; Van Aert, S.; Van Dyck, D. *Ultramicroscopy* **2012**, *116*, 77.

(184) Stoumpos, C. C.; Malliakas, C. D.; Kanatzidis, M. G. **2013**, *2*.

(185) Dasgupta, N. P.; Sun, J.; Liu, C.; Brittman, S.; Andrews, S. C.; Lim, J.; Gao, H.; Yan, R.; Yang, P. *Adv. Mater.* **2014**, *26* (14), 2137.

(186) Sánchez-Iglesias, A.; Grzelczak, M.; Pérez-Juste, J.; Liz-Marzán, L. M. *Angew. Chem. Int. Ed. Engl.* **2010**, *49* (51), 9985.

(187) Liu, J. W.; Liang, H. W.; Yu, S. H. *Chem. Rev.* **2012**, *112* (8), 4770.

(188) Goldschmidt, V. M. *Ber Deut Chem Ges* **1927**, *60* (4), 1263.

(189) Yu, Y.; Zhang, D.; Kisielowski, C.; Dou, L.; Kornienko, N.; Bekenstein, Y.; Wong, A. B.; Alivisatos, A. P.; Yang, P. *Nano Lett.* **2016**, *16* (12), 7530.

(190) Altantzis, T.; Coutino-Gonzalez, E.; Baekelant, W.; Martinez, G. T.; Abakumov, A. M.; Tendeloo, G. Van; Roeffaers, M. B. J.; Bals, S.; Hofkens, J. *ACS Nano* **2016**, *10* (8), 7604.

(191) Reiss, P.; Bleuse, J.; Pron, A. *Nano Lett.* **2002**, *2* (7), 781.

(192) Mekis, I.; Talapin, D. V.; Kornowski, A.; Haase, M.; Weller, H. *J. Phys. Chem. B* **2003**, *107* (30), 7454.

(193) Xie, R.; Kolb, U.; Li, J.; Basché, T.; Mews, A. *J. Am. Chem. Soc.* **2005**, *127* (20), 7480.

(194) Zavelani-Rossi, M.; Lupo, M. G.; Krahne, R.; Manna, L.; Lanzani, G. *Nanoscale* **2010**, *2* (6), 931.

(195) Piryatinski, A.; Ivanov, S. A.; Tretiak, S.; Klimov, V. I. *Nano Lett.* **2007**, *7* (1), 108.

(196) Allione, M.; Ballester, A.; Li, H.; Comin, A.; Movilla, J. L.; Climente, J. I.; Manna, L.; Moreels, I. *ACS Nano* **2013**, *7* (3), 2443.

(197) Mangum, B. D.; Wang, F.; Dennis, A. M.; Gao, Y.; Ma, X.; Hollingsworth, J. A.; Htoon, H. *Small* **2014**, *10* (14), 2892.

(198) Htoon, H.; Malko, A. V.; Bussian, D.; Vela, J.; Chen, Y.; Hollingsworth, J. A.; Klimov, V. I. *Nano Lett.* **2010**, *10* (7), 2401.

(199) Malko, A. V.; Park, Y.-S.; Sampat, S.; Galland, C.; Vela, J.; Chen, Y.; Hollingsworth, J. A.; Klimov, V. I.; Htoon, H. *Nano Lett.* **2011**, *11* (12), 5213.

(200) Zhao, J.; Chen, O.; Strasfeld, D. B.; Bawendi, M. G. *Nano Lett.* **2012**, *12* (9), 4477.

(201) Talapin, D. V.; Nelson, J. H.; Shevchenko, E. V.; Aloni, S.; Sadtler, B.; Alivisatos, A. P. *Nano Lett.* **2007**, *7* (10), 2951.

(202) Greytak, A. B.; Allen, P. M.; Liu, W.; Zhao, J.; Young, E. R.; Popović, Z.; Walker, B.; Nocera, D. G.; Bawendi, M. G. *Chem. Sci.* **2012**, *3* (6), 2028.

(203) Christodoulou, S.; Vaccaro, G.; Pinchetti, V.; De Donato, F.; Grim, J. Q.; Casu, A.; Genovese, A.; Vicidomini, G.; Diaspro, A.; Brovelli, S.; Manna, L.; Moreels, I. *J. Mater. Chem. C* **2014**, *2* (17), 3439.

(204) McBride, J.; Treadway, J.; Feldman, L. C.; Pennycook, S. J.; Rosenthal, S. J. *Nano Lett.* **2006**, *6* (7), 1496.

(205) Bertoni, G.; Grillo, V.; Brescia, R.; Ke, X.; Bals, S.; Catellani, A.; Li, H.; Manna, L. *ACS Nano* **2012**, *6* (7), 6453.

(206) Orfield, N. J.; McBride, J. R.; Wang, F.; Buck, M. R.; Keene, J. D.; Reid, K. R.; Htoon, H.; Hollingsworth, J. A.; Rosenthal, S. J. *ACS Nano* **2016**, *10* (2), 1960.

(207) van der Stam, W.; Bladt, E.; Rabouw, F. T.; Bals, S.; de Mello Donega, C. *ACS Nano* **2015**, *9* (11), 11430.

(208) González, J. C.; Hernández, J. C.; López-Haro, M.; del Río, E.; Delgado, J. J.; Hungría, A. B.; Trasobares, S.; Bernal, S.; Midgley, P. A.; Calvino, J. J. *Angew. Chemie* **2009**, *121* (29), 5417.

(209) Goris, B.; Bals, S.; Van den Broek, W.; Carbó-Argibay, E.; Gómez-Graña, S.; Liz-Marzán, L. M.; Van Tendeloo, G. *Nat. Mater.* **2012**, *11* (11), 930.

(210) Qu, L.; Peng, Z. A.; Peng, X. *Nano Lett.* **2001**, *1* (6), 333.

(211) Li, J. J.; Wang, Y. A.; Guo, W.; Keay, J. C.; Mishima, T. D.; Johnson, M. B.; Peng, X. *J. Am. Chem. Soc.* **2003**, *125* (41), 12567.

(212) Liu, H.; Owen, J. S.; Alivisatos, A. P. *J. Am. Chem. Soc.* **2007**, *129* (2), 305.

(213) Abe, S.; Čapek, R. K.; De Geyter, B.; Hens, Z. *ACS Nano* **2012**, *6* (1), 42.

(214) Manna, L.; Milliron, D. J.; Meisel, A.; Scher, E. C.; Alivisatos, a P. *Nat. Mater.* **2003**, *2* (6), 382.

(215) Manna, L.; Wang; Cingolani, R.; Alivisatos, A. P. *J. Phys. Chem. B* **2005**, *109* (13), 6183.

(216) Moore, D.; Wang, Z. L. *J. Mater. Chem.* **2006**, *16* (40), 3898.

(217) Li, L.; Pandey, A.; Werder, D. J.; Khanal, B. P.; Pietryga, J. M.; Klimov, V. I. *J. Am. Chem. Soc.* **2011**, *133* (5), 1176.

(218) Lorimer, G. *Mineral. Mag.* **1987**, *51* (359), 49.

(219) Möbus, G.; Doole, R. C.; Inkson, B. J. In *Materials Research Society Symposium - Proceedings*; 2003; Vol. 738, pp 15–20.

(220) Zanaga, D.; Altantzis, T.; Polavarapu, L.; Liz-Marz?n, L. M.; Freitag, B.; Bals, S. *Part. Part. Syst. Charact.* **2016**, *33* (7), 396.

(221) Slater, T. J. A.; Janssen, A.; Camargo, P. H. C.; Burke, M. G.; Zaluzec, N. J.; Haigh, S. J. *Ultramicroscopy* **2016**, *162*, 61.

(222) Zhong, Z.; Goris, B.; Schoenmakers, R.; Bals, S.; Batenburg, K. J. **2017**, *174* (October 2016), 35.

(223) Glotzer, S. C.; Solomon, M. J. *Nat. Mater.* **2007**, *6*, 557.

(224) Nie, Z.; Petukhova, A.; Kumacheva, E. *Nat. Nanotechnol.* **2010**, *5* (1), 15.

(225) Guerrero-Martínez, A.; Grzelczak; Liz-Marzán. *ACS Nano* **2012**, *6*, 3655.

(226) Pelt, D. M.; Batenburg, K. J. *IEEE Trans. Image Process.* **2013**, *22* (12), 5238.

(227) Ercius, P.; Weyland, M.; Muller, D. A.; Gignac, L. M. *Appl. Phys. Lett.* **2006**, *88* (24), 243116.

(228) Batenburg, K. J.; Sijbers, J. *IEEE Trans. Image Process.* **2011**, *20* (9), 2542.

(229) Link, S.; El-Sayed, M. A. *Int. Rev. Phys. Chem.* **2000**, *19* (3), 409.

(230) Perassi, E. M.; Hernandez-Garrido, J. C.; Moreno, M. S.; Encina, E. R.; Coronado, E. A.; Midgley, P. A. *Nano Lett.* **2010**, *10* (6), 2097.

(231) Batson, P. E.; Dellby, N.; Krivanek, O. L. *Nature* **2002**, *419* (6902), 94.

(232) Dellby, N.; Krivanek, O. L.; Nellist, P. D.; Batson, P. E.; Lupini, A. R. *Microscopy* **2001**, *50* (3), 177.

(233) Schlossmacher, P.; Klenov, D. O.; Freitag, B.; Harrach, S. Von; Steinbach, A. *Microsc. Anal. Nanotechnol. Suppl.* **2010**, *November*, 5.

(234) Bosman, M.; Keast, V. J.; Garcia-Munoz, J. L.; D'Alfonso, A. J.; Findlay, S. D.; Allen, L. J. *Phys. Rev. Lett.* **2007**, *99* (8).

(235) Muller, D. a; Kourkoutis, L. F.; Murfitt, M.; Song, J. H.; Hwang, H. Y.; Silcox, J.; Dellby, N.; Krivanek, O. L. *Science (80-. ).* **2008**, *319* (5866), 1073.

(236) Allen, L. J.; Findlay, S. D.; Lupini, A. R.; Oxley, M. P.; Pennycook, S. J. *Phys. Rev. Lett.* **2003**, *91* (10), 105503.

(237) Shah, A. B.; Ramasse, Q. M.; Zhai, X.; Wen, J. G.; May, S. J.; Petrov, I.; Bhattacharya, A.; Abbamonte, P.; Eckstein, J. N.; Zuo, J.-M. *Adv. Mater.* **2010**, *22* (10), 1156.

(238) Browning, N. D.; Chisholm, M. F.; Pennycook, S. J. *Nature* **1993**, *366* (6451), 143.

(239) Allen, L. J.; D'Alfonso, A. J.; Freitag, B.; Klenov, D. O. *MRS Bull.* **2012**, *37* (01), 47.

(240) Chu, M.-W.; Liou, S. C.; Chang, C.-P.; Choa, F.-S.; Chen, C. H. *Phys. Rev. Lett.* **2010**, *104* (19), 196101.

(241) D'Alfonso, A. J.; Freitag, B.; Klenov, D.; Allen, L. J. *Phys. Rev. B* **2010**, *81* (10), 100101.

(242) Klenov, D. O.; Zide, J. M. O. *Appl. Phys. Lett.* **2011**, *99* (14), 141904.

(243) Lu, P.; Xiong, J.; Van Benthem, M.; Jia, Q. *Appl. Phys. Lett.* **2013**, *102* (17), 173111.

(244) Wang, P.; D'Alfonso, A. J.; Findlay, S. D.; Allen, L. J.; Bleloch, A. L. *Phys. Rev. Lett.* **2008**, *101* (23), 236102.

(245) Kothleitner, G.; Neish, M. J.; Lugg, N. R.; Findlay, S. D.; Grogger, W.; Hofer, F.; Allen, L. J. *Phys. Rev. Lett.* **2014**, *112* (8).

(246) Yeste, M. P.; Hernández-Garrido, J. C.; Arias, D. C.; Blanco, G.; Rodríguez-Izquierdo, J. M.; Pintado, J. M.; Bernal, S.; Pérez-Omil, J. a.; Calvino, J. J. *J. Mater. Chem. A* **2013**, *1* (15), 4836.

(247) Li, Z. Y.; Young, N. P.; Di Vece, M.; Palomba, S.; Palmer, R. E.; Bleloch, A. L.; Curley, B. C.; Johnston, R. L.; Jiang, J.; Yuan, J. *Nature* **2008**, *451* (7174), 46.

(248) van den Bos, K. H. W.; De Backer, A.; Martinez, G. T.; Winckelmans, N.; Bals, S.; Nellist, P. D.; Van Aert, S. *Phys. Rev. Lett.* **2016**, *116* (24), 246101.

(249) Béché, A.; Goris, B.; Freitag, B.; Verbeeck, J. *Appl. Phys. Lett.* **2015**, *108* (9).

# List of scientific contributions

## Papers in A1 scientific journals

Leroux, F., Bladt, E., Timmermans, J.-P., Van Tendeloo, G., Bals, S. Annular dark-field transmission electron microscopy for low contrast materials. *Microscopy and Microanalysis 19 (2013) 629–34.*

Hutter, E. M., Bladt, E., Goris, B., Pietra, F., Van Der Bok, J. C., Boneschanscher, M. P., de Mello Donegá, C., Bals, S., Vanmaekelbergh, D. Conformal and atomic characterization of ultrathin CdSe platelets with a helical shape. *Nano Letters*, *14 (2015) 6257–6262.*

van der Stam, W., Bladt, E., Rabouw, F. T., Bals, S., & de Mello Donega, C. Near-Infrared Emitting CuInSe 2 /CuInS 2 Dot Core/Rod Shell Heteronanorods by Sequential Cation Exchange. *ACS Nano*, *9 (2015) 11430–11438.*

Bladt, E., Pelt, D. M., Bals, S., Batenburg, K. J. Electron tomography based on highly limited data using a neural network reconstruction technique. *Ultramicroscopy*, *158 (2015) 81–88.*

De Schutter, B., Van Stiphout, K., Santos, N. M., Bladt, E., Jordan-Sweet, J., Bals, S., Lavoie, C., Comrie, C. M., Vantomme, A., Detavernier, C. Phase formation and texture of thin nickel germanides on Ge(001) and Ge(111). *Journal of Applied Physics*, *119 (2016) 135305.*

Berends, A. C., Rabouw, F. T., Spoor, F. C. M., Bladt, E., Grozema, F. C., Houtepen, A. J., de Mello Donegá, C. Radiative and Nonradiative Recombination in CuInS 2 Nanocrystals and CuInS 2 -Based Core/Shell Nanocrystals. *The Journal of Physical Chemistry Letters*, *7 (2016) 3503–3509.*

Tong, Y., Bladt, E., Aygüler, M. F., Manzi, A., Milowska, K. Z., Hintermayr, V. A., Docampo, P., Bals, S., Urban, A. S., Polavarapu, L., Feldmann, J. Highly Luminescent Cesium Lead Halide Perovskite Nanocrystals with Tunable Composition and Thickness by Ultrasonication. *Angewandte Chemie International Edition*, *55 (2016) 13887–13892.*

Tong, Y., Bladt, E., Aygüler, M. F., Manzi, A., Milowska, K. Z., Hintermayr, V. A., Docampo, P., Bals, S., Urban, A. S., Polavarapu, L., Feldmann, J. Starke Lumineszenz in Nanokristallen aus Cesiumbleihalogenid- Perowskit mit durchstimmbarer Zusammensetzung und Dicke mittels Ultraschalldispersion. *Angewandte Chemie*, *128 (2016) 14091–14096.*

Bladt, E., van Dijk-Moes, R. J. A., Peters, J., Montanarella, F., de Mello Donega, C., Vanmaekelbergh, D., Bals, S. Atomic structure of wurtzite CdSe (core)/CdS (giant Shell) nanobullets related to epitaxy and growth. *Journal of the American Chemical Society*, *138 (2016) 14288–14293.*

Debroye, E., Yuan, H., Bladt, E., Baekelant, W., Van der Auweraer, M., Hofkens, J., Bals, S., Roeffaers M. B. J. Facile Morphology-Controlled Synthesis of Organolead Iodide Perovskite Nanocrystals Using Binary Capping Agents. *ChemNanoMat, 3 (2017) 223-227.*

Tong Y., Bohn B. J., Bladt E., Wang K., Müller-Buschbaum P., Bals S., Urban A. S., Polavarapu L., Feldmann J. Precursor Powders-to-CsPbX3 Perovksite Nanowires: One-Pot Synthesis, Growth Mechanism and Oriented Self-assembly. *Angewandte Chemie International Edition (in press)*.

Sentosun K., Lobato I., Bladt E., Zhang Y., Palenstijn W. J., Batenburg K.J., Van Dyck D., Bals. S. Artifact Reduction Based on Sinogram Interpolation for the 3D Reconstruction of Nanoparticles Using Electron Tomography. *Submitted.*

## Conference proceedings

Kujawa, S., Goris, B., Zanaga, D., Bladt, E., Altantzis, T., Bals, S.. Towards Quantitative EDS Results in 3 Dimensions, Electron Microscopy Frontiers Conference, Thuwal

Goris, B., Freitag, B., Zanaga, D., Bladt, E., Altantzis, T., Ringnalda, J., Bals, S. Towards Quantitative EDX Results in 3 Dimensions, Microscopy & Microanalysis (M&M) Conference, Hartford

## Oral presentations

Bladt, E., Annular Dark-Field Transmission Electron Microscopy for Low Contrast Materials, IMC 2014, Prague

Bladt, E., Electron tomography based on highly limited data using a neural network reconstruction technique, European Workshop on Electron Tomography, 2015, Antwerp, Belgium

Bladt, E., Advanced characterization of colloidal semiconductor nanocrystals by 2D and 3D electron microscopy, International Conference on Fundamental Processes in Semiconductor Nanocrystals (FQDots15), Santiago de Compostela, Spain

Bladt, E., Advanced characterization of colloidal semiconductor nanocrystals by 2D and 3D electron microscopy, European Microscopy Congress (EMC2016), 2016, Lyon, France:

Bladt, E., Electron tomography based on highly limited data using a neural network reconstruction technique, European Microscopy Congress (EMC2016), 2016, Lyon, France

Bladt, E., Electron tomography based on highly limited data using a neural network reconstruction technique, Golden Jubilee Meeting of the Royal Belgian Society for Microscopy (RBSM2016), 2016, Brussels, Belgium

## Poster presentations

Bladt, E., Heidari, H., Leroux, F., Bals, S. Optimization of electron tomography for the three-dimensional study of hybrid nanoparticle assemblies, NVvM (Nederlandse Vereniging voor Microscopy) Materials Science Meeting, 2013, Utrecht, The Netherlands

Bladt, E., Heidari, H., Leroux, F., Bals, S. Optimization of electron tomography for the three-dimensional study of hybrid nanoparticle assemblies, IMC (International Microscopy Conference), 2014, Prague

Bladt, E., Pelt, D. M., Bals, S., Batenburg, K. J. Electron tomography based on highly limited data using a neural network reconstruction technique, Industrial Tomography Workshop, 2015, Antwerp, Belgium

## Prizes

Image Contest at EMC 2016 in the category “Transmission Electron Microscopy based techniques”

# Dankwoord

When an actor or actress wins a movie award, he or she always promises to keep the award winning speech short. I have no intention of making this acknowledgement short as I feel honoured thanking everyone who has helped and supported me during these four years of PhD.

Ik wil graag als eerste mijn promotor, Prof. Dr. Sara Bals, bedanken. Sara gaf me de kans om dit onderzoek te starten na het schrijven van een Bachelor en Master thesis onder haar toezicht. Ik wil Sara graag bedanken voor haar onvoorwaardelijke en aanhoudende steun tijdens al deze jaren. Ik heb veel van haar geleerd, maar ik ben haar het meest dankbaar voor de tijd die ze heeft gespendeerd om mijn presentatie skills te verbeteren. Haar professionele prestaties zijn erg inspirerend en een motivatie om zelf een succesvolle carrière te ambiëren. Dank je voor al je steun, Sara.

Graag wil ik Prof. Dr. Schryvers, Prof. Dr. Verbeeck, Prof. Dr. Van Aert, Prof. Dr. Hadermann, Prof. Dr. Lamoen, Prof. Dr. Van Dyck en Prof. Dr. Van Tendeloo bedanken voor hun steun en voor de fijne discussies.

Ik wil graag mijn juryleden, Prof. Dr. Dirckx, Prof. Dr. Batenburg, Prof. Dr. Neyts, Prof. Dr. Van Aert en Prof. Dr. Van Huis bedanken om tijd te maken voor mijn thesis te lezen. Onze discussies en jullie feedback hebben me geholpen om het proefschrift te verbeteren, dank jullie.

I would like to thank Ana and Prof. Dr. Luis Liz-Marzán for providing me with the Au and Au/Ag nanoparticles. I would like to thank Annelies, Eline, Relinde and Prof. Dr. Vanmaekelbergh for the provision of the semiconductor nanoparticles. For the challenging ternary semiconductor nanoparticles, I would like to thank Anne, Ward and Prof. Dr. Celso de Mello Donega. I very much appreciated their support and friendship during the conference in Santiago de Compostela. I would like to thank Lakshmi for the provision of the metal halide perovskites. For the very challenging, extremely beam sensitive, organic-inorganic perovskites, I want to thank Haifeng, Prof. Dr. Maarten Roeffaers and Prof. Dr. Johan Hofkens. Finally, I want to thank Carolina and Prof. Dr. José Juan Calvino Gámez for the provision of the catalytic nanoparticles.

A tremendous thank you to Daan and Prof. Dr. Joost Batenburg, with whom I had a very fruitful collaboration working on the neural network implementation. I very much appreciated all their help on this subject and I hope we will continue our collaboration.

I would like to thank Dr. Hamed Heidari and Dr. Frederic Leroux for their guidance during the Bachelor and Master thesis and for awakening my passion for TEM. I could not imagine a better team to work with.

I also want to thank my other colleagues of the tomography group for their help and support during my PhD. I want to mention a special thank you to our newest member, Hans, which has showed tremendous support during these last months while I was writing the thesis.

I want to thank all my EMAT colleagues and friends for their part in this experience. Thank you for the fruitful discussions, your support and friendship. I wished Mert, Elsa, Gerardo, Kirsten, Kristof, Dimitri, Andrea and Stuart would have stayed longer as I missed them in these last years/months/weeks/days at the end of my PhD.

Two colleagues deserve some special acknowledgement as they were closest present in this experience, which are my office mates Kadir and Roeland. I could not wish for a better office team. Thanks guys for being there all these years.

I would also like to thank Liesbet for helping me these last weeks with the layout of the thesis. I want to thank Armand for the discussions, the squash/running/swimming breaks and his friendship. I really appreciated all your help and support.

Naast professionele steun, heeft de steun van vrienden en familie me geholpen om tot deze dag te geraken. Ik wil graag mijn vriend Sam van de derde verdieping bedanken voor onze occasionele pauzes en zijn –sporadische– wijze raad. Sam, dank je voor al je steun tijdens deze jaren.

Mijn middelbare school vriendin en musicalster, Helle, heeft me altijd enorm gesteund. Haar sprankelende en immens vriendelijke persoonlijkheid maken haar en haar vriendschap uniek. Ik heb erg genoten van onze lunches in het park, waarvoor je steeds naar hier kwam. Helle, je bent een fantastische vriendin, dank je voor al je steun tijdens al deze jaren.

Graag wil ik ook het geweldige duo Annlies en Lisa bedanken om me af te leiden tijdens onze wekelijkse BBB lessen. Dank jullie voor alle leuke momenten die we samen hebben gedeeld. Ik hoop dat er nog veel mogen volgen.

Ik wil graag Steven en Ans bedanken om mij te helpen om fysiek in orde te blijven tijdens deze vier jaren. Steven, dank je om altijd on call te zijn en dank je voor je vriendschap. Ans, ik blijf op zoek naar een nieuw deeltje en probeer je later nog te bedanken tijdens een speech in Zweden.

In dit laatste deel, wil ik graag vier mensen bedanken die erg belangrijk voor me zijn. Ik wil graag mijn broer, Piet, en zus, Lola, bedanken voor hun geweldige steun tijdens deze vier jaren. Het was altijd fijn en aanmoedigend om mijn broer te horen vertellen over zijn eigen onderzoek. Ik heb altijd naar mijn grote broer opgekeken en hoop dat hij fier op me is. Mijn kleine zus is de laatste jaren getransformeerd in een geweldige zakenvrouw/onderzoeker. Haar werkethiek, harde werken en passie voor haar werk zijn kwaliteiten die ik enorm bewonder in haar. Broer, zus, dank jullie voor al de steun en om er altijd voor mij te zijn.

My lovely boyfriend, Benjamin, you are my rock. Ik kan me deze laatste vier jaar niet inbeelden zonder jou aan mijn zijde. Ik fietste elke dag met een glimlach naar huis omdat thuis kwam naar jou. Na moeilijke dagen, wist je me altijd op te beuren en me terug energie te geven. Ik kan niet uitdrukken hoeveel je voor me betekent en hoe hard je me geholpen hebt om dit punt te bereiken. Tijdens deze vier jaren hebben we geweldige reizen gemaakt, zijn we gaan samenwonen en hebben we een appartement samen gekocht. Ik hoop dat we de komende jaren samen verder groeien en ik hoop dat je aan mijn zijde zal zijn tijdens de volgende uitdagingen. Dank je voor al je steun, voor jezelf te zijn en voor je liefde. Ik zie je graag.

In this last part, I want to thank the most incredible person in my life, my mother, Elsie. Mama, er zijn niet genoeg woorden om jou te bedanken op de manier dat je verdient, maar toch zal ik het proberen. Je hebt ons geleerd om altijd hard te werken voor wat we willen bereiken. Je steunde me in al mijn keuzes en stond altijd paraat met advies. Je topprioriteit was altijd om voor ons te zorgen en ons zoveel mogelijk te steunen en dat voeldt geweldig aan. Jouw liefde heeft me altijd geholpen om hard te werken en om mijn grenzen te verleggen. Je bent de meest geweldige, sterke, gepassioneerde vrouw die ik ken en die ik bewonder. Ik had gehoopt onze band vast te leggen in mijn naam. Ook al ben ik op dit moment niet officieel Eva Bladt De Vos, weet dat ik in mijn hart een echte De Vos ben. Mama, je verdient eigenlijk een heel hoofdstuk of een heel boek, je bent geweldig en ik wil je enorm bedanken voor je aanhoudende steun. Ik hoop dat ik je trots maak en ik hoop dat je pauwenstaart open staat. Mama, ik hou van je met heel mijn hart.